University of Strathclyde Department of Electronic and Electrical Engineering

Spiral 2D Array Designs for Volumetric Imaging

Andrew Tweedie

Submitted in February 2011

for the degree of

Doctor of Engineering

Centre for Ultrasonic Engineering

Dept of Electronic and Electrical Engineering

204 George Street

Glasgow

G1 1XW

This thesis is the result of the author's original research. It has been composed by the author and has not been previously submitted for examination which has led to the award of a degree.

Signed: …….. *Date:* ……..

Contents

Acknowledgments

I would like to take this opportunity to thank my academic supervisor Professor Gordon Hayward for his guidance and support throughout the duration of this thesis. I have truly learned more than I thought I could in five years, and that is credit to his supervision.

My thanks go to the members of CUE, who have all been happy to lend a hand, and share some advice along the way.

I would also like thank my industrial supervisor Vic Murray, and the rest of the team at Alba Ultrasound, who have always supported me, despite having been so busy.

Finally, I would like to thank my parents, who supported my every step along the long road to this work's completion. I cannot begin to imagine how I could have reached to this point without their help and encouragement.

Abstract

The use of linear phased arrays in NDE inspections has recently grown, resulting in faster inspection of components. Phased arrays are also used in underwater sonar and biomedical imaging. All applications require 2 dimensional (2D) arrays, capable of volumetric imaging, to further increase scan speed, and to allow tighter focussing on targets. However, 2D arrays have not found widespread use, mainly due to the large number of elements required to implement standard periodic designs. Alternative array configurations that feature a much lower element count offer a more pragmatic solution.

This thesis investigates the design of sparse 2D arrays (i.e. using fewer elements than a periodic grid sampled at the Nyquist rate) based on geometric spiral structures, with the aim to reduce the number of array elements, and therefore transmit-receive channels required to meet a given acoustic specification. The aperiodic structure of these array designs is shown to minimise the height of sidelobes, by spatially distributing sidelobe energy, therefore avoiding artefacts in the resulting acoustic image. Furthermore, their mathematically determined position simplifies the layout of the array, and therefore its manufacture. The approach taken was to develop a logarithmic spiral structure, which is shown to minimise peak sidelobe height for a given number of array elements.

A series of design rules was created, to allow the array designer to rapidly create sparse array designs to meet an acoustic specification. The acoustic field created by these designs was modelled, and it was shown that they have lower peak sidelobe levels than equivalent random 2D array designs. A 1.5 MHz, 127 element prototype array was then designed and manufactured for NDE inspection on thick section welds, which combined a -31 dB sidelobe floor with the capability for volumetric steering.

Glossary of Terms

The following is a list of the important acronyms found in the work:

CUE	Centre for Ultrasonic Engineering, based in the University of Strathclyde
RCNDE	The UK Research Centre for Non-Destructive Evaluation
2D	Two dimensional
NDE	Non Destructive Evaluation (in some industries NDT, Non Destructive Testing, is used, with the same meaning)
CW	Continuous wave
RIM	Ralyeigh integral method
DRI	Discrete Raleigh Integral
PSF	Point Spread Function
DDF	Dynamic Depth Focussing
SNR	Signal to noise ratio
TFM	Total Focussing Method
FMC	Full Matrix Capture
TIG	Tungsten Inert Gas
PDF	Probability Density Function
FEA	Finite Element Analysis
GUI	Graphical User Interface
FFT	Fast Fourier Transform
DFT	Discrete Fourier Transform
ISLR	Integrated Sidelobe Ratio
DMJ	Dissimilar Metal Joint
LSM	Linear Systems Model
SDH	Side Drilled Hole
FBH	Flat Bottomed Hole

List of Symbols

The following is a list of the more important symbols found in the work. Less significant symbols are defined in the text as required.

a	Element aperture
b	Logarithmic spiral arm parameter
c	Wave speed
d	Element pitch
d_c	Circumferential element pitch at centre of spiral array
D	Array aperture
f	Frequency
k	Wavenumber
l	Linear array element height
L	Length of spiral arm
L_{min}	Minimum total length of spiral for a specific design
N, N_T, N_R	Number of total / transmit / receive elements
N_{arms}	Number of spiral arms
p	Logarithmic spiral pitch
P_T, P_R	Transmit / receive directivity
r	Spiral element radius
R_b	Fresnel parameter, near field far field boundary
R_{12}	Reflection coefficient between medium 1 and 2
R_{min}	Minimum element radius
S_{av}	Average sidelobe level
S_p	Peak sidelobe level
T_{12}	Transmission coefficient between medium 1 and 2
u, v	Extended angular variables
Z	Acoustic impedance
γ	Spiral element angle
δ	Angle between spiral tangent and origin
θ	Elevation angle

θ_w	Beam width
θ_s	Elevation steering angle
θ_g	Grating lobe angle
θ_{smax}	Maximum elevation steering angle
λ	Wavelength
ρ	Density
φ	Azimuthal angle
ω	Angular frequency

Chapter 1

Introduction

Ultrasound is a very useful medium for measuring the mechanical properties of a body. Ultrasonic waves are mechanical waves, which are reflected and scattered as they move though a body whose material properties, such as stiffness and density, vary spatially. By introducing an ultrasonic wave into a body, and then measuring the reflected echoes, some concept of the mechanical structure of the body can be constructed.

If the structure of the body is complex in nature, it is often necessary to selectively direct a narrow ultrasonic beam through the body, in order to differentiate between different features of its structure. Indeed, by scanning structures in this way, the received ultrasonic data can be constructed into an image, showing locations where sound was reflected, and hence where the structures' mechanical properties change. For a number of years ultrasonic imaging has been used in underwater sonar, biomedicine, and more recently in Non Destructive Evaluation (NDE) to construct images which provide information on internal structures, or in the case of sonar, underwater obstacles and targets.

In all of these applications, a device called an ultrasonic transducer is used to convert the electrical signals from the imaging system to ultrasound, and convert reflected ultrasonic waves back to electrical signals on reception. Originally, these transducers were mechanically scanned to sweep the ultrasonic beam through the imaging medium. However, in the last 40 years there has been a gradual move towards the use of phased arrays, These arrays are formed by a group of individually addressable transducers, which are capable of electronic steering and focussing of the beam. This not only simplifies the mechanical construction of the system, but allows very rapid scanning, and dynamic focusing of the beam to be achieved. These systems call for complex transmit and receive electronics, with many independent electrical channels, incorporating high power transmitters, low noise preamplifiers, fast analogue to digital converters, and programmable phase delays. The expense of producing such a system for these niche markets puts a premium on the number of transmit-receive channels. This results in the cost of a phased array system being approximately proportional to the number of channels required to form the ultrasonic beam.

Steering a beam through a single plane requires the phase of the wave front to be controlled in a single axis, and calls for a linear array of transducers, often referred to as array elements. The resolution that can be achieved by the system is proportional to the aperture of the array, and the frequency of operation. In addition, linear array elements are generally spaced at a maximum distance of $\lambda/2$ to avoid spatial aliasing. This means that for a given frequency, an increase in resolution requires an increase in array elements.

In contrast to these single axis systems, volumetric steering requires phase to be controlled in two axes, calling for a 2 dimensional (2D) array of elements, which are traditionally laid out in a periodic grid. This makes volumetric imaging systems inherently costly, since to produce a 2D system with the same aperture, and hence resolution, as a linear array system, the number of array elements required is squared. For example, in NDE, 32 element linear arrays are becoming increasingly common and affordable. To produce a 2D array with similar imaging performance would require 1,024 elements, which is larger than any NDE array controller currently on the market. Considering the cost of a 256 channel NDE array controller is over £200k as of 2010, the cost penalty on this sort of system is clear. In addition, there are a number of technical aspects such as power consumption, cabling, and size that currently limit the number of channels that can be incorporated into a practical system.

There are many aspects of volumetric scanning that make it more attractive than performing simple 2D scans:

- The system can inspect a volume of a body from a single array position, reducing or eliminating the need to mechanically scan the array.

- The whole surface of the array can be programmed to focus at a single point, producing a tighter focus and increasing signal to noise ratio (SNR).

- The incident angle of the beam can be adjusted in both axes, which is useful in NDE, where flaws can be planar, resulting in the reflected sound being directional.

These points demonstrate that there is a clear motivation to move to volumetric imaging. However, the cost and complexity of developing such a system makes it impractical for many applications, especially in NDE, where the budgets for developing such devices are limited. One potential solution would be to alter the layout of 2D phased arrays so that fewer elements could be used, reducing system cost and complexity. However, this has implications for the acoustic performance of the array, which ultimately determines the quality of the ultrasonic image. Removing elements from these dense periodic grids creates sparse arrays, which have spurious lobes in their beams, referred to as grating lobes. These lobes create artefacts in the ultrasonic image, which for many applications are unacceptable. What is required is a revaluation of the design of 2D ultrasonic arrays, so that sparse devices can be created, using fewer array elements, but which do not detrimentally impact the quality of the ultrasonic image.

The work addresses this problem by developing a range of 2D sparse arrays (i.e. using fewer elements than a periodic grid sampled at the Nyquist rate) based on spiral structures. Spirals are curves eminating from a central point, whose radius increases as they circle that point. Some spirals, such as the logarithmic spiral, fall within a larger class of structures called fractals, which are shapes which exhibit self similarity across a range of scales and rotations. Both the Archimedes spiral, and the logarithmic spiral are described in detail in Chapter 5. These properties are potentially attractive for the construction of 2D arrays:

- The array layouts that they create are aperiodic, precluding the generation of grating lobes, which are associated with periodic structures.

- They are deterministic, making them both easier to define mathematically, and to manufacture.

- Their structure is self similar, meaning that their structure remains alike across a range of rotations and scales. This avoids changes in aperture, and therefor beamwidth in different directions.

- In Chapter 5 it is shown that the the sidelobe positions produced by log spiral arrays are non overlapping, minimising the peak sidelobe height.

The overall concept of the work was to create a process for designing 2D phased arrays that would allow the designer to reduce the number of elements required to meet a given acoustic specification, compared to the number required using a standard periodic grid. It was clear at the outset that there would be a trade-off between the peak sidelobe height in the array, and the number of elements required. It was therefore necessary to find a design method which was optimised to reduce sidelobe height for a given number of elements. The approach used to create this process is described in Chapter 5.

The work was carried out as part of an Engineering Doctorate scheme, though the UK Research Centre for Non Destructive Evaluation (RCNDE). The industrial sponsor was Alba Ultrasound Ltd, a manufacturer of phased arrays, and the academic partner was the Centre for Ultrasonic Engineering (CUE) at The University of Strathclyde.

Alba's main business is the manufacture of 1-3 piezocomposite phased arrays for the sonar industry. With the current growth of the NDE industry, and its recent uptake of phased array technology, Alba sees the development of NDE arrays as a significant business opportunity. However, there is established competition in the market, and costs for standard linear arrays have fallen over the last 5 years, with current linear arrays ranging in price from £3k to £6k, as of 2011. Since Alba's

current business is the manufacture of low volume (approximately 50 per year) bespoke, high value arrays (typically from £10k to over £50k per array), it is not able to compete on cost in the current market. An attractive strategy for Alba would be to enter the market with high-end niche products, and seek to gradually move to higher volume products as production costs are reduced.

2D arrays were identified as an area where there was an industry need for array which was not being fully addressed. While competitors such as Imasonic of France offer 2D arrays in the 1 – 10 MHz frequency range, these devices cost between £10k to £30k as of 2011. In addition, these devices have their elements laid out in simple periodic grids and annuli, meaning a large number of elements are required to achieve a given specification. Alba has the capability to manufacture these devices, so could offer 2D arrays at a competitive price. Indeed, if Alba were to enter the market with a 2D array design which allowed customers to use array controllers with fewer channels, it would represent a significant competitive advantage to the company over current phased array manufacturers. In addition, such designs could also be applied to sonar applications, and some niche biomedical devices, opening further niche markets to the company.

With these opportunities in mind, the overall goal of the EngD project was to develop a novel range of sparse 2D arrays. Within this remit, the following objectives were identified:

- Investigate the design of 2D sparse arrays, with the objective of reducing the number of elements required to meet a given acoustic specification.

- Create a design process for such arrays that would allow Alba to rapidly convert a customer specification into a practical array design.

- Develop Alba's acoustic modelling capability to model the performance of these arrays.

- Develop Alba's manufacturing capability for high frequency 2D NDE arrays, and build a prototype to evaluate its performance.

The thesis contributes several key advances to the field of ultrasonic array design. First, a thorough analysis of spiral array designs, and their beamforming performance is conducted. Literature on such array layouts is sparse, and where present, is mainly focused on the fields of biomedicine [1] and radio telescopes [2,3]. Secondly, the design process developed here is unique, in that it allows functional design specifications to be rapidly translated into detailed array designs. Current literature does not fully develop this link to the functional performance of the array design, and is therfore of limited use in an industrial design process. Finally, a practical prototype is manufactured, and used to demonstrate the performance of the design in an NDE inspection. Much of the existing sparse array literature focuses on sub-sampled dense periodic grids, hypothesising that abstract patterns would be impractical to manufacture. The work demonstrates not only that spiral designs can be manufactured, but that they are well within Alba's current manufacturing capabilities.

Due to the interest in the advantages of volumetric imaging from the NDE, biomedical and sonar industries, there is a large body of research on the design of sparse 2D arrays. This is discussed in detail in Chapter 3, along with the reasons for selecting a spiral layout.

In Chapter 4 the modelling software developed during the project is discussed, along with some examples of how it has been used to model Alba's existing sonar arrays.

Chapter 5 discusses the approach taken to optimise the performance of the novel spiral arrays, assess this performance compared to more traditional designs, and outlines a set of design rules for creating such devices.

These design rules were then used to create a prototype array, for the inspection of thick section (80 mm) welds. The design, manufacture, and testing of the device are described in Chapter 6.

Finally future work is discussed in Chapter 7, before the results of the work are summarised in Chapter 8.

The following chapter introduces the concept of ultrasonic phased arrays, and the theory behind them.

Chapter 2

Phased Array Imaging Theory

Ultrasound provides a useful way of interrogating a component, body, or environment. By transmitting an ultrasonic wave into a component and monitoring the waves which are reflected back, important information about that component can be obtained. If the ultrasonic wave is tightly focused in a particular region of the component, then the characteristics of this region can be isolated from those of the rest of the component. Phased arrays offer the possibility of electronically directing this focal region to different areas of the component under test, by altering the relative phase of signals transmitted and received on array elements. As this can be done very rapidly, an acoustic image of the component can be constructed, without recourse to any movement of the transducer array, or the component.

This chapter discusses the principles behind the construction of these images, and the implications this has on the design of 2D arrays.

2.1 Introduction to phased arrays

This section gives a brief overview of phased array technology, and how it can be used to rapidly manipulate and shape an ultrasonic beam.

The lateral resolution that can be achieved with an ultrasonic system is determined by the beam width of the transducer being used to transmit and receive the sound. The beam width is inversely proportional to both the aperture of the transducer, and the frequency of operation. Due to this fact, high resolution imaging systems often employ both large apertures and relatively high frequencies. The far field continuous wave (CW) beam width of a simple rectangular aperture can be calculated using the following equation [4].

$$\theta_w = 2\sin^{-1}\left(\frac{0.44\times\lambda}{D}\right) = 2\sin^{-1}\left(\frac{0.44\times c}{D\times f}\right) \qquad \textbf{(2-1)}$$

where θ_w is the far field CW beam width in degrees, λ is the wavelength of the sound in the medium in which the wave propagates, D is the width of the aperture, c is the speed of sound in the medium and f is the frequency of operation.

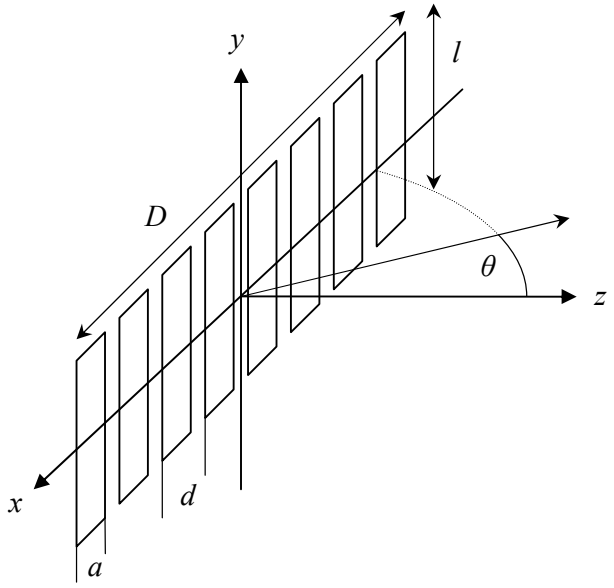

Figure 2-1 **Linear array geometry showing an 8 element linear array with element width, *a*, height, *l*, pitch, *d*, and aperture *D*. The array is plotted in *x*-*y*-*z* coordinate space, with the elevation angle θ illustrated.**

Consider the linear array shown in Figure 2-1. The beam produced by the transducer can be steered away from the transducer normal by shifting the phase of the signals on each array element, relative to their adjacent elements. The principle behind this process is demonstrated in Figure 2-2, which shows transmit steering on a linear phased array. Each element is excited with an impulse, and can be thought of as transmitting a cylindrical wavefront. In areas of the field where the phase of these waves are equal the waves are said to interfere constructively, increasing the intensity of the sound field. When no phase shifts are applied this causes a plane wave to propagate normal to the surface of the array.. By altering the phase of the

excitation signal to each element, the plane wave is formed at a new angle, and will travel to a different part of the field.

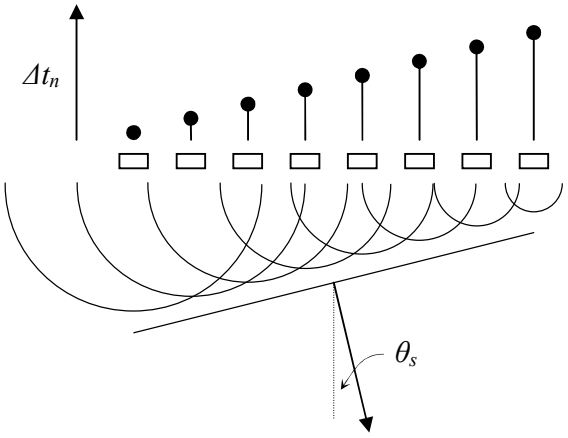

Figure 2-2 **Illustration of waves with delays Δt_n emanating from a phased array, producing a beam propagating at an angle θ_s.**

To calculate the delays required to achieve a steering angle of θ_s the following equation can be used [5].

$$\Delta t_n = n\frac{d}{c}\sin\theta_s + t_0 \qquad \textbf{(2-2)}$$

where Δt_n is the required delay, d is the element spacing of the array, and c is the velocity of propagation in the operating medium. Here, n = 0, ±1, ±2, … represents the number assigned to each element moving in both directions from the centre element 0. Finally, t_0 is made equal to the largest negative element delay, and is used to ensure that all delays are positive to preserve causality. A Rayleigh Integral Method (RIM, covered in Chapter 4) simulation of a steered ultrasonic beam is shown in Figure 2-3.

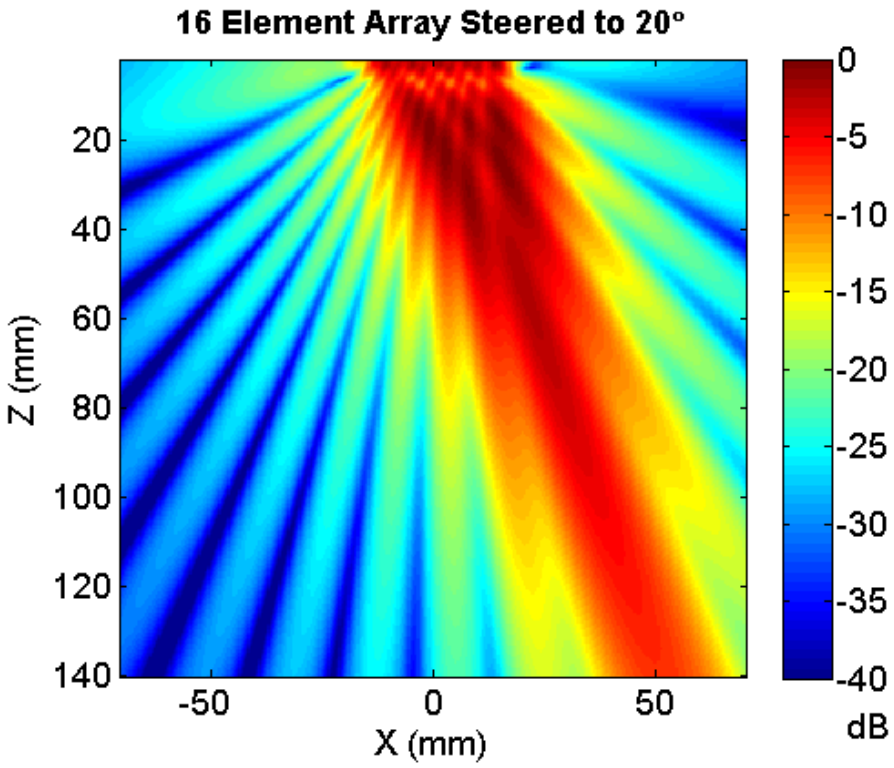

Figure 2-3 **Simulation of the acoustic field of a 1.5 MHz 16 element linear array steered to 20°, operating into steel.**

The same principles can be used to focus the beam to a point in the field. This is done by applying delays that cause the wave from each array element to arrive at the focal point simultaneously and in phase. For a linear array these delays can be calculated as follows.

$$\Delta t_n = \frac{R_f}{c}\left(1 - \left[1 + \left(\frac{nd}{R_f}\right)^2 - 2\frac{nd}{R_f}\sin\theta_s\right]^{\frac{1}{2}}\right) + t_0 \qquad \textbf{(2-3)}$$

where R_f is the focal range, and all other symbols are as previously defined. This type of focal law increases the intensity of the field at the focal point, and results in a higher contrast image than could be achieved with simple steering. A RIM simulation of a focused ultrasonic beam is shown in Figure 2-4.

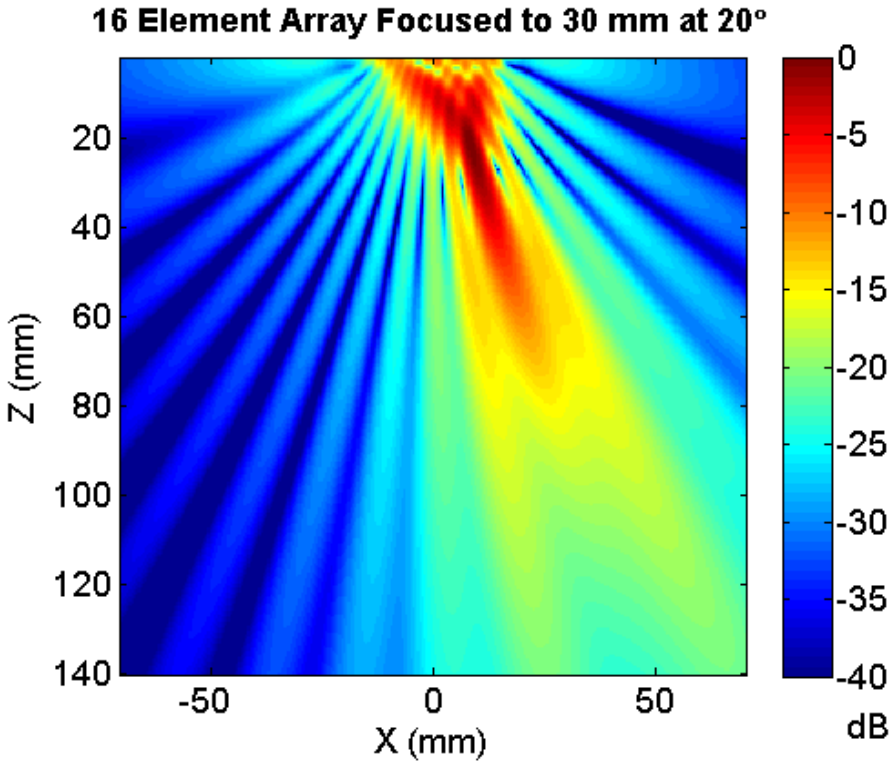

Figure 2-4 **Simulation of the acoustic field of a 1.5 MHz 16 element linear array focused to 30 mm at 20°, operating into steel.**

It should be noted that focussing is only possible in the near field, or Fresnel region [5]. Beyond this, in the far field, or Fraunhoffer region the beam shape is constant with increasing range. The range to the boundary of these two regions can be approximated with the Fresnel parameter [5].

$$R_b = \frac{D^2}{4\lambda} \qquad \textbf{(2-4)}$$

where D is the width of the transducer aperture and λ is the wavelength at the centre frequency of the transducer.

Another very important aspect of phased array design is element spacing. For a linear periodic array the Nyquist sampling criterion [6] must be satisfied to avoid the formation of grating lobes in the beam. This means that the element spacing must be less than or equal to λ/2. At spacings above this, grating lobes will be formed in the beam at some angles. Grating lobes are a form of spatial aliasing, and cause one or more aliased versions of the main beam to appear in the field. They occur at angles where the path difference between elements are integer multiples of the wavelength. The location of grating lobes in a linear periodic array can be calculated with the following equation [7].

$$\theta_g = \sin^{-1}\left(\sin\theta_s \pm \frac{n\lambda}{d} \right), \qquad n = 1,2,\ldots \qquad \textbf{(2-5)}$$

where θ_g is the angle of the n^{th} grating lobe for a steering angle of θ_s. It should therefore be noted that λ/2 spacing is only required for arrays that utilise a ±90° steering range.

In an idealised array with omni-directional elements which are under CW excitation the grating lobes produced in the array will be mirror images of the mainlobe, and have relative amplitudes of 0 dB. This is therefore a worst case condition. Under pulsed excitation, the phase of the waves interfering at the first grating lobe will be shifted by one wavelength, and this will result in a lower grating lobe amplitude. It follows that an array emitting perfect time domain impulses would have no grating lobes due to the complete separation of pulses in time at all points but the intended focus. The implications of this for the design of ultra wideband ultra sparse arrays are discussed in [8]. Grating lobe amplitude is also reduced by the limited

acceptance angle of practical array elements. However, it should be noted that when these arrays are steered to high azimuthal angles the main beam is reduced in amplitude, increasing the relative height of grating lobes, as shown in Figure 2-5. The simulation shows the directivity of a 16 element array with 9/4λ spacing, giving a grating lobe at 60°, which is -13 dB relative to the mainlobe. When the mainlobe is steered to 45° the grating lobe is 7 dB higher than the mainlobe. The elements are ~λ in width, so their beamwidth, also known as their acceptance angle, is limited.

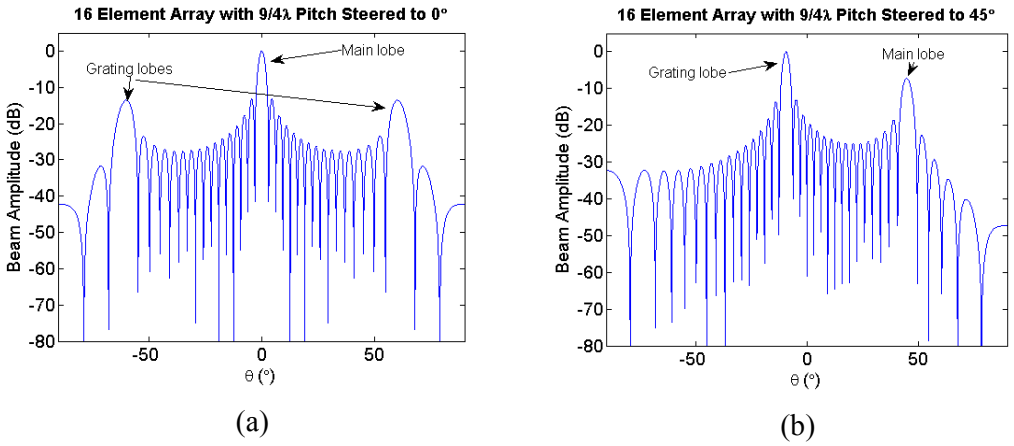

Figure 2-5 **Grating lobes in a 16 element array under different steering conditions, (a) unsteered and (b) steered to 45°.**

So far only linear 1D arrays have been discussed. However, these principles can be extended to 2D arrays, by considering the focal process in 3D space. Consider an array with the layout described in Figure 2-6. Here the subscripts *x* and *y* have been used to denote the element width and pitch in the corresponding axes.

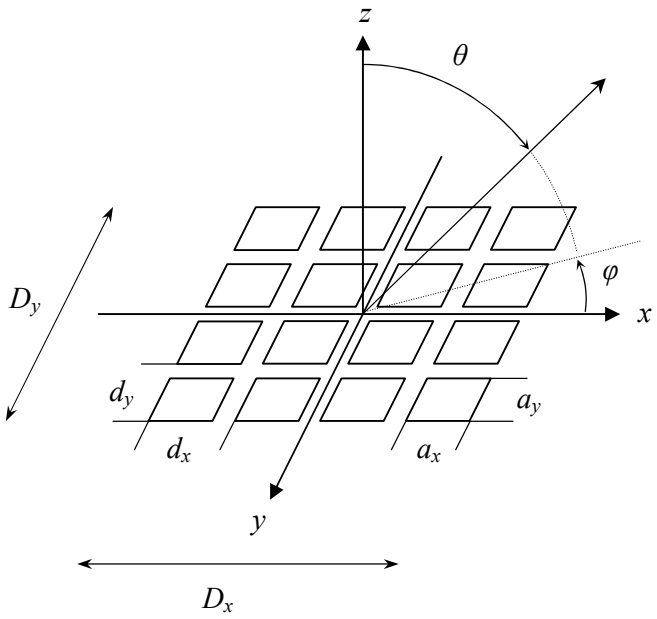

Figure 2-6 **2D array geometry showing a 16 element 2D array with element width, *a*, pitch, *d*, and aperture *D*. The array is plotted in *x*-*y*-*z* coordinate space, with the elevation angle θ, and the azimuthal angle φ illustrated.**

The far field beam hemispherical beam patterns of 2D arrays are often plotted in what is known as *u*-*v* space [7]. The parameters *u* and *v* are known as the extended angular variables, and are defined as follows.

$$u = \sin\theta\cos\varphi \qquad \textbf{(2-6)}$$

$$v = \sin\theta\sin\varphi \qquad \textbf{(2-7)}$$

where θ is the elevation angle of field points and φ is the azimuthal angle of field points. Plotting the directivity in *u*-*v* space allows the plot to be flattened for easier analysis. Examples of a 3D polar directivity plot and a *u*-*v* space directivity plot of the same 2D array are shown in Figure 2-7.

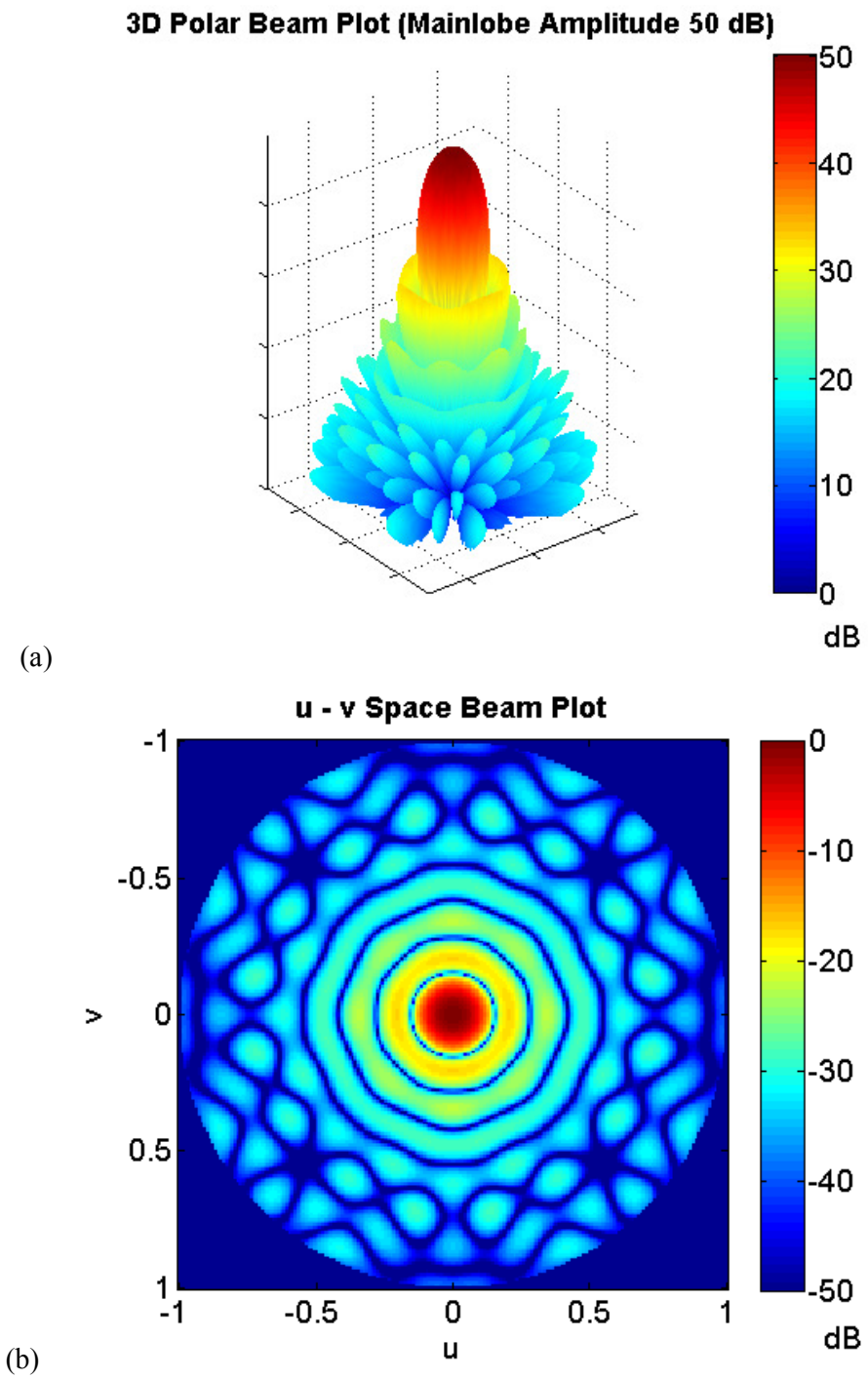

Figure 2-7 **Far field directivity of a 197 element λ/2 spaced circular grid 2D array in both (a) 3D polar and (b) *u*-*v* space. In the polar plot amplitude is represented as a function of distance from the origin.**

While Equation 2-2 can be extended for 2D grid arrays with square elements, it is convenient to consider the general case for steering and focussing, where array elements are positioned in an abstract manner.

$$\Delta t_n = \frac{(R - R_n)}{c} + t_0 \qquad \textbf{(2-8)}$$

where:

$$R_n = \sqrt{(F_x - E_{xn})^2 + (F_y - E_{yn})^2 + (F_z - E_{zn})^2} \qquad \textbf{(2-9)}$$

$$F_x = R \sin\theta_s \sin\varphi_s \qquad \textbf{(2-10)}$$

$$F_y = R \sin\theta_s \cos\varphi_s \qquad \textbf{(2-11)}$$

$$F_z = R \cos\theta_s \qquad \textbf{(2-12)}$$

F is the focal point, and E_n is the group of n element centres, each with their x, y and z coordinates in 3D space. R_n is the distance from the n^{th} element to the focal point. As before t_0 is the largest negative element delay, and ensures all delays are positive.

These focal laws allow the beam to be swept through a 3D volume, in order to build up an acoustic image. They can also focus the beam to a point in the near field to increase the contrast of the image. Apodisation is a technique which can be used to further enhance contrast, and is discussed in the next section.

2.2 Apodisation

Apodisation, sometimes referred to as shading, is a technique which is analogous to windowing in signal processing [9]. It can be used to reduce the level of sidelobes produced by a single element transducer, or transducer array. It does this at the expense of widening the main beam of the device. By reducing the sidelobe level the transducer is made less sensitive to scatterers falling outside its focal zone, and this improves image contrast.

Calculating the far field directivity of a vibrating piston is analogous to calculating the frequency response of a windowing function. This is discussed further in Chapter 4, where directivity modelling is described. This relationship offers a convenient way of analysing the effect of candidate apodisation functions.

The effect of apodisation on the simulated far field CW directivity of a 32 element, 1.5 MHz, $\lambda/2$ spaced linear array is illustrated in Figure 2-8. Directivity is calculated for both an unapodised uniformly vibrating piston, and a second device which has a Hamming apodisation function. Both directivity plots are normalised so that the mainlobe is at 0 dB, to make it easier to compare sidelobe levels and beam widths. However, it should be considered that the sensitivity of the apodised device is 5.8 dB lower, since the outer edges of the device displace less. The Hamming apodisation results in a 27 dB reduction in first sidelobe level, which is traded off against an 3.4° increase in -3 dB beamwidth.

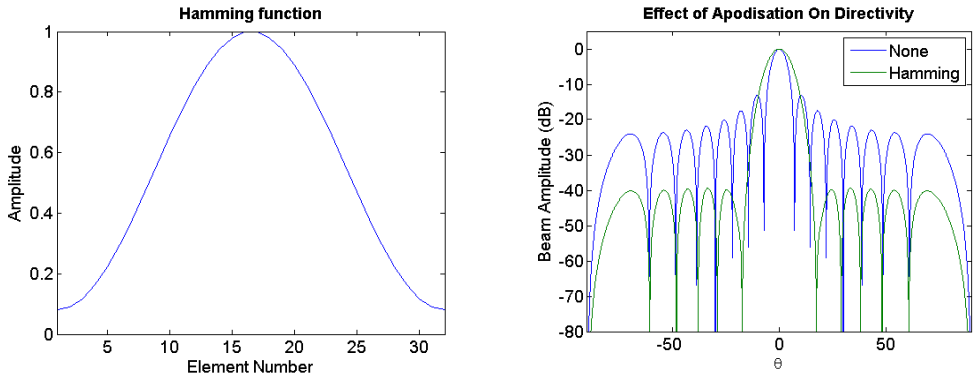

(a) (b)

Figure 2-8 **Effect of Hamming apodisation on the simulated directivity of a 32 element array, showing (a) Hamming apodisation function and (b) resulting array directivity.**

Another benefit of apodisation is a reduction in near field ripple. This is useful as the near field has many nulls where the transducer is relatively insensitive. Targets falling in these nulls can remain undetected, leading to unreliable inspections.

Figure 2-9 shows a simulated 2D field produced by the apodisation functions in Figure 2-8. The Hamming apodised device reduces the level of interference in the near field.

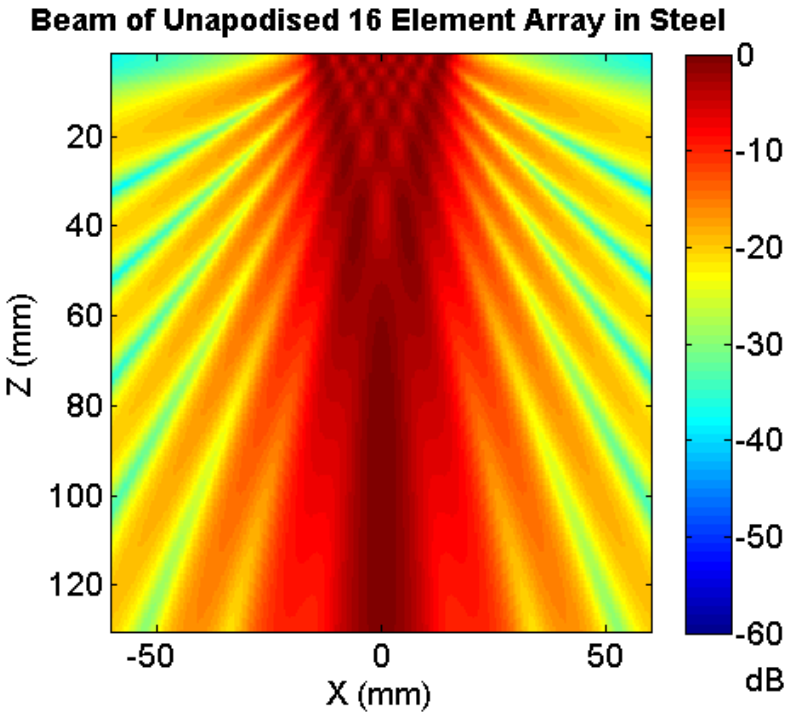

(a)

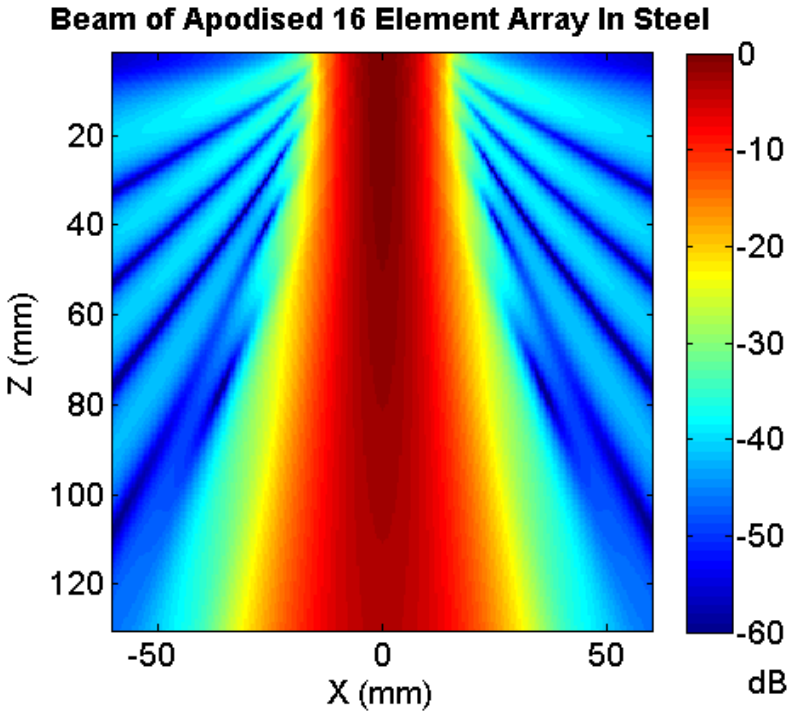

(b)

Figure 2-9 **Near field of a 16 element array, (a) unapodised and (b) Hamming apodised.**

Apodisation is also used in curved sonar arrays to reduce main beam ripple. The mechanisms by which apodisation produces these effects can be thought of as reducing the effect of the transducer's edge waves. These are emitted from the outer edges of the transducer aperture, and spread in all directions. Normally they set up an interference pattern with the plane wave which constitutes the main beam of the device. However, when apodisation is used the edges of the device vibrate with less amplitude, and the interference effects are reduced.

In practice apodisation can be realised in a number of ways. Apodisation of a linear phased array can be controlled in both transmit and receive modes, by altering the gain of the transmit and receive amplifiers. This produces an apodisation along the length of the array, and affects the azimuthal beam pattern. 2D phased arrays can use the same technique across the whole surface of the array to apodise in both axes. In order to shade a monolithic device, or the elevation direction of a linear array, a different approach must be taken. A simple tapered electrode pattern, known as a shading function, can be used to alter the cross sectional area of the element throughout its length. Alternatively a resistive electrode can be used to alter the voltage across the element's length, reducing the displacement in the lower voltage areas [10].

Apodisation can be used in conjunction with some of the main imaging algorithms, which are discussed in the following section. The methods used to create the simulations shown in this section are discussed further in Chapter 4.

2.3 Imaging algorithms

There are a variety of beamforming algorithms available for ultrasonic imaging applications. Some are well suited to a multitude of disciplines, while others have been developed for niche applications. This chapter will describe some of the best known algorithms, their advantages, and disadvantages.

2.3.1 Imaging applications

Before discussing the algorithms it is worth considering some of the special requirements of the three main ultrasonic imaging applications; NDE, biomedical, and sonar.

NDE:

- Inspections are generally conducted in stiff materials, over short distances. This means that the propagation delay for the sound is short, allowing many ultrasonic pulses to be transmitted for each image.

- Specimens do not generally change over time, so images can be built up over extended durations.

Biomedical:

- Waves travel slower in the human body than in metals, so propagation delays are longer than in NDE. Multiple ultrasonic beams can be transmitted, but the upper limit is often capped by the requirements of a real-time inspection.

- Objects in the human body, such as the heart, are constantly moving. This limits the total duration of the image acquisition.

- The human body as a medium is not homgenius, instead consisting of a plethora of types of tissue, each exhibiting their own material properties. This scatters ultrasonic waves in a complex manner, making image reconstruction more complex when compared to NDE.

Sonar:

- Waves travel relatively slowly, over very long distances, which create long propagation delays. This limits the number of pulses which can be emitted, and in most cases only a single transmitted pulse is used.

- Sonar systems often use separate dedicated transmit and receive arrays, each tailored to optimise the overall sensitivity of the system.

2.3.2 Imaging terminology

This section discusses some of the terminology used when discussing imaging algorithms: the *A-scan*, the *B-scan*, and the *Point Spread Function*.

An *A-scan* is a plot of ultrasonic signal against distance, similar to the display on an oscilloscope, but with the time scale multiplied by the propagation speed. It can be displayed as either as the raw signal, or rectified to show signal amplitude. It may be received on a single array channel, or be the processed result of beam forming over many channels. Spikes in the A-scan data can be used to identify reflections from targets in the imaging field. Figure 2-10 shows both a standard and rectified version of the same A-scan.

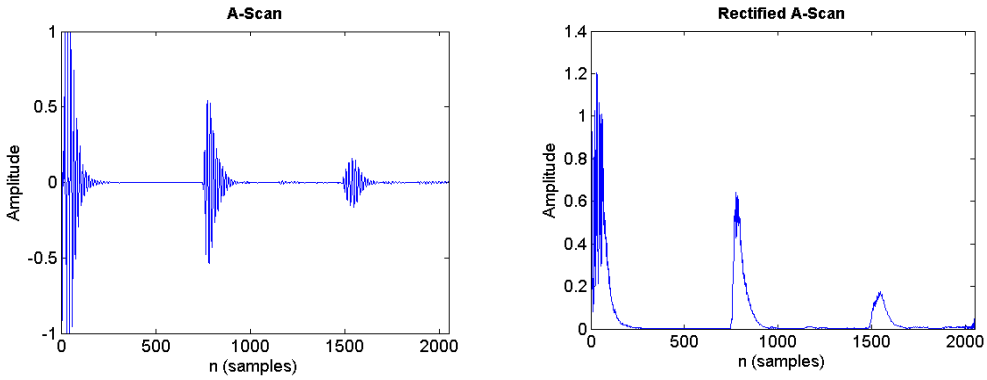

(a) (b)

Figure 2-10 **A-scans showing the excitation pulse and two reflections, (a) standard A-scan and (b) rectified A-scan,.**

A *B-scan* is a collection A-scans arranged side by side. The amplitude of the A-scan is converted to a pixel colour, or intensity to create an image. The position at which the A-scan was received is displayed on the secondary axis, so that each pixel corresponds to a point in the field. In this way a B-scan forms an ultrasonic image of the location of reflections in the field. Figure 2-11 shows an example of a B-scan.

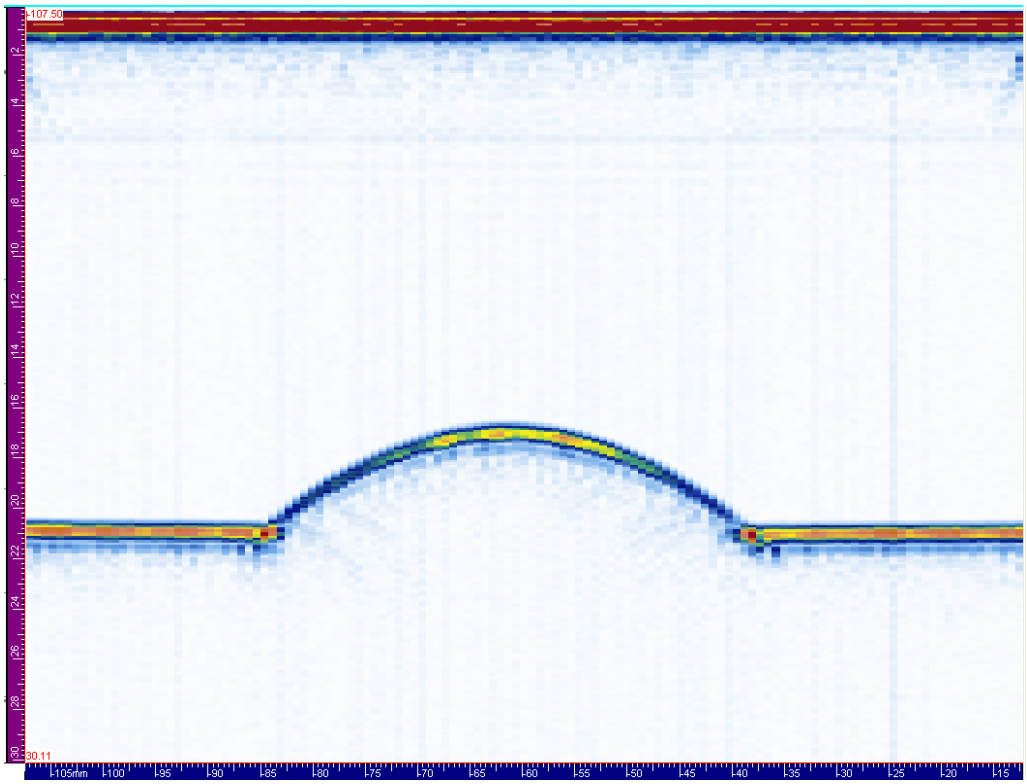

Figure 2-11 **Ultrasonic B-scan showing a weld cap on the top of a stainless steel block. The front face reflection clearly shows the profile of the cap. Scales are in mm.**

The *Point Spread Function* (PSF) is the response of an ultrasonic imaging system to a single point reflector located somewhere in the field [11]. It is a product of the imaging algorithm, the design of the phased array, and the location of the point in the field. PSF's are a convenient way of comparing the focal performance of different imaging systems. They not only measure the resolution of the system, but also the contrast that can be achieved. For example, the -6 dB width of the PSF is often used as a measure of system resolution, while the height of the main peak compared to that of the surrounding image data provides a measure of contrast.

2.3.3 Plane B-scan

The most basic scanning method used in arrays is a plane B-scan, which is illustrated in Figure 2-12. In this method a group of elements are excited simultaneously to transmit a beam into the field. Reflected ultrasonic pulses are received on the same group of elements, and are used to produce an A-scan. The active group of elements is then incremented by one element pitch along the length of the array, and the process is repeated. This method achieves a similar result as mechanically scanning a monolithic probe through the field, and recording pulse echo data. A B-scan image is then constructed from the individual A-scan images.

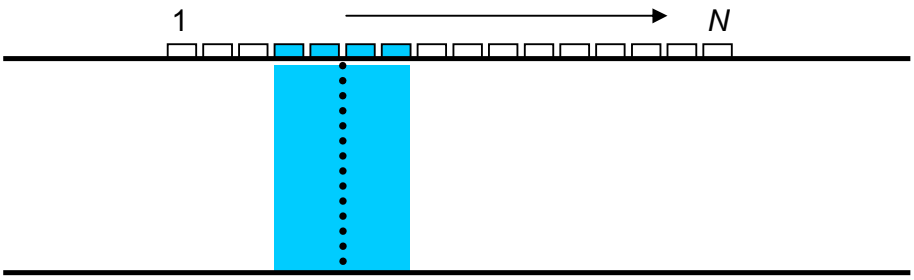

Figure 2-12 **In this plane B-scan a group of four active elements is being electronically moved across the array. Each acquisition creates an A-scan, with samples along the black dotted line. These are placed side by side to produce a B-scan.**

As there is no phasing required for this array it is often referred to as a 'scanned array', or simply a 'linear array'. Due to this, systems using this imaging mode are relatively cheap to construct, since no phase delay electronics are used, and no signal processing is required.

Plane B-scans have a number of limitations. The beam extends perpendicular to the array, so it must extend over the whole area that is to be imaged. It also employs no

focusing in plane with the array, so image resolution is limited. In addition to this, only a small fraction of the total array area is utilised for each firing.

2.3.4 Sector scan.

The sector scan is a very common method of inspection in NDE. In this imaging algorithm the beam is moved in an angular sweep about the centre of the array, as shown in Figure 2-13. The transmit pulses are phased according to the delays calculated in Equation 2-2, causing the beam to be formed along an angle θ_s from the array normal. Reflected pulses are captured on all of the array elements, and are delayed in the same manner before being summed to produce an A-scan. This process is then repeated at different angles, until the beam has interrogated the whole field. The A-scans are then constructed into a sector shaped image, often called an S-scan. The S-scan is similar to the B-scan, but the geometry of the beam path preserved.

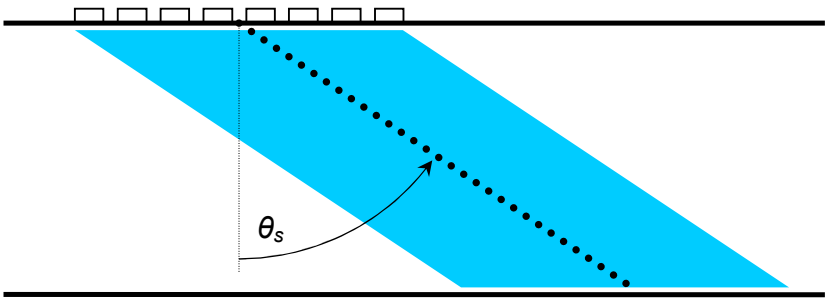

Figure 2-13 **In the sector scan phase delays are applied to the array elements to steer the beam to an angle, θ_s. At each acquisition angle an A-scan is captured with samples along the black dotted line. θ_s is then incremented to sweep the beam through the test piece.**

An advantage of the sector scan is that a large area of the object or area under inspection can be interrogated from a relatively small array. Since the beam can be steered at an angle, it can be used to inspect areas where a beam propagating normal to the surface of the object could not reach. An example of this is in cardiac imaging, where the aperture and location of the array is confined by the ribs [12].

Like the plane B-scan, the sector scan still has the disadvantage that it uses an unfocused beam, and therefore achieves relatively poor resolution. Care must also be taken to ensure that near field interference in the beam does not obscure targets which are close to the transducer.

2.3.5 Focused sector scan

The focused sector scan overcomes some of the deficiencies of the sector scan, by focusing the beam to a specified range, or depth in the image. Delays are calculated using Equation 2-3. This creates a sector image, with improved resolution at the specified range. However, resolution at shorter ranges is not improved significantly, and resolution at longer ranges decreases due to de-focusing of the beam. In NDE inspections these limitations are often overcome by performing a sector scan to interrogate the whole field, then switching to a focus scan at the appropriate range for high detail measurements. Figure 2-14 shows a focused sector scan.

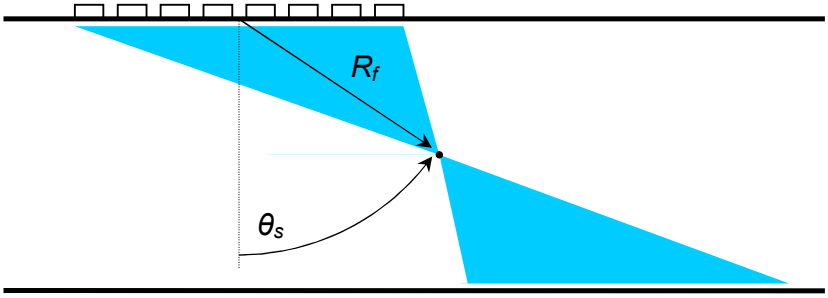

Figure 2-14 **Focused sector scan with the beam focused to a point at a range R_f, and an angle θ_s. Sensitvity and resolution is reduced in areas away from the focal point.**

A technique called Dynamic Depth Focussing (DDF) can be used to improve the performance of a focused sector scan, by focusing on more regions of the field. It is often not practical to increase the number of transmit focal laws, as this reduces the frame rate that is achievable, which is important for real-time imaging. DDF uses the same number of transmit focal laws as the sector scan and focused sector scan, but increases the number of receive focal laws. For each transmit law multiple receive focal laws are applied to the returning data, resulting in a tight focus at all ranges. There is no frame rate penalty for this, as long as the system has the computational capacity to handle the increased workload. To complement this it is essential to create a transmit pulse with a relatively flat axial beam profile, so that all areas of the sector are insonified equally. This can be achieved by applying an apodisation function to the array during transmission, to reduce near field interference effects. The approach also reduces sidelobes in the transmit beam, improving contrast. Although this method cannot achieve the same focal point resolution as the focused sector scan, resolution at all other points in the image is improved.

DDF is commonly used in biomedical imaging applications, and is growing more common in NDE inspections. It achieves a good compromise between image resolution and frame rate. One disadvantage of this method is that the divergence of the transmit beams causes the achievable lateral resolution with this method to decrease with range.

2.3.6 Synthetic aperture

Synthetic aperture, often referred to as Synthetic Aperture Focussing Technique, or SAFT is a technique developed for radar imaging systems in the 1950's [13], which has since been adapted for sonar applications. It achieves high resolution by transmitting and receiving signals from a moving platform such as an aircraft or ship, and in doing so forming a 'synthetic aperture,' which is larger than would be practical to construct as a permanent fixed array. At regular intervals along its direction of travel the system transmits a pulse on a wide-beamed transmitter, to insonify the volume which is to be imaged. A receive array records any reflected pulses, and forms an initial image of the field, as shown in Figure 2-15. The receive beamformer uses a different focal law for every pixel in the image, to achieve as high a resolution as possible. The system then repeats this process at subsequent points along its path, or 'track', each time adding the new image to the last. With each acquisition the length of the synthetic aperture grows, and resolution is improved.

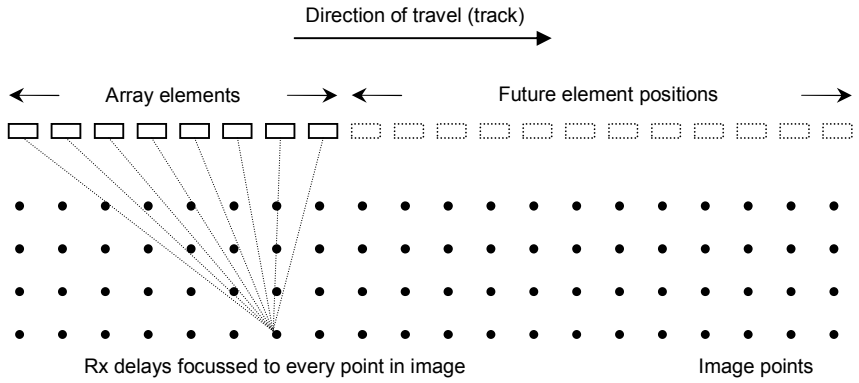

Figure 2-15 **Synthetic aperture imaging, showing an array moving along a track perpendicular to the field it is imaging. At each array position the field is insonified with a wide beam transmitter (not shown), and receive elements are focused to every point in the image. This is repeated as the array moves along the track, and the images are summed.**

Resolution is ultimately limited by the acceptance angle of the transmitter and receiver, and the accuracy of the positional information along the platform's path. An additional advantage of this algorithm is that the resolution is independent of range, as the receive aperture, and therefore the angular resolution of the system, increases with range to the target.

Since a synthetic aperture can stretch for many kilometres this algorithm allows improvements in resolution over standard systems with a fixed, permanent array. However, the algorithm can also be applied to standard arrays to take advantage of the many receive focal laws it uses. This is very useful in real time sonar applications, where propagation delays often dictate that only a single transmit pulse can be used for each image.

A disadvantage of this method is the lack of transmit beam forming. While the use of an omnidirectional transmitter allows receive beamforming throughout the whole

image, the lack of any transmit focussing reduces the Signal to Noise Ratio (SNR) of the system. Assuming that the dominant noise source in the system is uncorrelated electrical noise at the receivers, SNR for a system using transmit focusing can be shown to approximate to [14]:

$$SNR_{TF} \approx N_T \sqrt{N_R} \qquad \textbf{(2-13)}$$

where SNR_{TF} is the SNR for a system using transmit focussing, N_T and N_R are the number of transmit and receive elements respectively. For a synthetic aperture system with no transmit focus, SNR is approximately:

$$SNR_{SA} \approx \sqrt{N_T . N_R} \qquad \textbf{(2-14)}$$

where SNR_{SA} is the SNR for a synthetic aperture system with no transmit focussing. For systems which use only a single transmit pulse this represents a reduction in SNR proportional to the number of elements in the array, compared to a system that utilises all of these elements to transmit. However, it should be noted, that for applications such as NDE the dominant noise source is coherent backscatter from the medium, and not uncorrelated noise.

2.3.7 Total focussing method

Total Focussing Method (TFM) is a beamforming algorithm derived from synthetic aperture where the beam is formed purely using post processing [15]. Data capture begins by exciting the first element of the array, and receiving reflected pulses on all array elements. Then the second element of the array is excited and reflected pulses received on all array elements. This process is repeated until all of the array's elements have been use to transmit. The data set produced by this process is referred to as a Full Matrix Capture (FMC), since an independent A-scan is captured for every possible transmit receive pair in the array. A-scans are denoted $A_{tr}(n)$, where t

is the transmitting element, *r* is the receiving element, and *n* is the sample number. Receive beamforming is then applied to the FMC data to create an image which is focused at every pixel for each transmitted pulse. These images are then combined to produce an image which uses the full set of FMC data. This process is illustrated in Figure 2-16, along with an example of the structure of the FMC. It is possible to exploit some redundancy in this matrix, to reduce the amount of data storage and processing required. By assuming reciprocity, only the upper triangular section of the matrix is required, approximately halving the volume of data that must be processed.

		Receive Element					
		1	**2**	**3**	**4**	**…**	***N***
Transmit Element	**1**	$A_{11}(n)$	$A_{12}(n)$	$A_{13}(n)$	$A_{14}(n)$	…	$A_{1N}(n)$
	2	A_{21}	$A_{22}(n)$	$A_{23}(n)$	$A_{24}(n)$	…	$A_{2N}(n)$
	3	$A_{31}(n)$	$A_{32}(n)$	$A_{33}(n)$	$A_{34}(n)$	…	$A_{3N}(n)$
	4	$A_{41}(n)$	$A_{42}(n)$	$A_{43}(n)$	$A_{44}(n)$	…	$A_{4N}(n)$
	…	…	…	…	…	…	…
	N	$A_{N1}(n)$	$A_{N2}(n)$	$A_{N3}(n)$	$A_{N4}(n)$	…	$A_{NN}(n)$

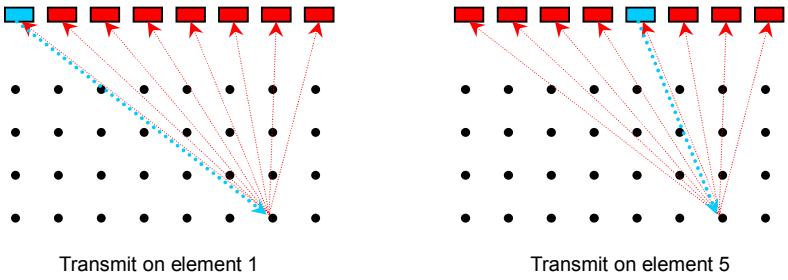

Figure 2-16 **Structure of an FMC (top), and two examples of the beamforming applied to create a pixel in the TFM image (bottom). Transmit paths are shown in blue, receive paths are shown in red.**

TFM offers a number of advantages over traditional algorithms, especially for NDE applications. It offers an improvement in image resolution over sector scans, and in many cases does not significantly increase the number of transmit pulses required. Take the example of a 128 element array performing a swept sector scan between -60°, and +60° in 1° increments. This requires 121 transmit pulses, each with the beam focussed at a specified angle. To perform TFM, an FMC would be performed,

resulting in 128 transmit pulses, but providing an image with range independent resolution. Furthermore, as the dominant noise in NDE inspections is coherent backscatter, the $\sqrt{N_T}$ reduction in SNR predicted in Equations 2-13 and 2-14 is not a major concern. This is particularly true in materials with coarse grain structures, where the multiple transmit paths inherent in TFM could be proved useful in reducing coherent noise artefacts.

There are a number of drawbacks to the TFM algorithm. The ability to capture such a large volume of data has only been made practical in recent years; this is due to increases in computing power, and data transfer rates between phased array controllers and computers. To illustrate this, an FMC on a 550 element 2D array, with 2500 samples per A-scan and 16 bit accuracy requires approximately 1.5 GBytes of storage space. To date, there are still no systems known to employ real time TFM. As with SAFT no transmit beamforming is used, resulting in higher sidelobe floors. This affects the contrast of the image, which is discussed in Section 2.4, and makes the algorithm less suitable for use with sparse arrays.

In year two of this engineering doctorate project the TFM algorithm was implemented for immersion NDE imaging using 2D arrays. Volumetric images of both side drilled, and flat bottomed holes were created, and are reported in [16].

2.4 Contrast

In the context of imaging, contrast is the difference in brightness between the dark areas of an image and the light areas. It limits the ability to detect weak target strengths which are surrounded by those with much higher target strengths. When designing an ultrasonic imaging system, and in particular the phased array, it is essential to understand the the dynamic range of the reflections which will be received, and therefore the contrast that will be required in the image.

A simple way of estimating the contrast requirements for an ultrasonic measurement is to consider the 'strength' of reflected waves from the material boundaries which exist in the field. The reflection coefficient of a plane wave travelling at normal incidence to a boundary between materials of acoustic impedances Z_1 and Z_2 can be calculated as follows [4].

$$R_{12} = \frac{Z_2 - Z_1}{Z_1 + Z_2} \qquad \textbf{(2-15)}$$

The transmission coefficient for the wave which is transmitted in material 2 is given by:

$$T_{12} = \frac{2Z_2}{Z_1 + Z_2} \qquad \textbf{(2-16)}$$

What follows is a contrast analysis for the three major ultrasonic imaging applications; biomedical, NDE, and sonar.

2.4.1 Biomedical

Using Equation 2-15 reflected signal strengths from common biomedical targets can be calculated [11], and are presented in Table 2-1.

Materials at Interface	Reflectivity (dB)
Soft tissue - air	0.0
Fat - bone	-3.2
Fat - blood	-21.3
Muscle - blood	-30.5
Muscle - liver	-40.0

Table 2-1 **Plane wave reflection coefficients at normal incidence for common biomedical material boundaries. Strengths shown are relative a total reflection [11].**

This illustrates the high contrast required for biomedical imaging, where designers prefer sidelobe floors to be as low as -60 dB. This allows a high dynamic range, logarithmically scaled image to be produced, where all of the above material boundaries can be identified. However, these examples should only be used as a rough guide, as they consider the simplified case of plane wave reflections at normal incidence. Detecting weak point scatterers in the presence of large planar reflectors with higher reflection coefficients can be significantly more challenging.

2.4.2 NDE

In NDE inspections there is typically less variation in material properties throughout the test piece, and this can simplify image analysis. A good example of this is the inspection of a steel weld using a transducer on an angled wedge. Depending on whether the inspection is carried out in air or water, and assuming that cracks in the weld are air filled, this gives the reflection coefficients shown in Table 2-2 below.

Materials at Interface	Reflectivity (dB)
Air - Steel	0.00
Water - Steel	-0.59
Rexolite - Steel	-0.99
Steel - Tungsten	-19.82

Table 2-2 **Plane wave reflection coefficients at normal incidence for common NDE material boundaries. Strengths shown are relative to a total reflection.**

The large dissimilarities between the acoustic impedance of these materials results in large reflections for almost all boundaries. A notable exception is the inclusion of tungsten particles in the weld material, which is a common defect in Tungsten Inert Gas (TIG) welds. However, it is generally considered that these defects are sub-critical, as they have a small through wall extent. They can serve as crack initiation sites, since they can create stress razors in the structure, and at this point would be easier to detect due to the reflective steel – air interface at the crack.

This simple analysis masks some important points. Consider the diagram of a water immersion inspection of a steel part shown in Figure 2-17. Here there are three important signals:

- Wave A, which travels from the transducer, is transmitted through the water – steel boundary, reflects back from a crack, and returns through the steel – water boundary back towards the transducer. This is the defect signal, and is amplitude is given by $A_A = T_{12}R_{23}T_{21}$.

- Wave B, which reflects directly from the water – steel boundary, and returns to the transducer. This is the front wall reflection, and is given by $A_A = R_{12}$.

- Wave C, which is transmitted through the water – steel boundary, reflects back from the steel – water boundary, and returns through the steel – water boundary back towards the transducer. This is the back wall reflection, and is given by $A_A = T_{12}R_{21}T_{21}$.

Wave A is the signal of interest, and wave B and C are two interfering signals, which will be received regardless of the presence of a defect. Table 2-3 shows the relative amplitudes of these reflections.

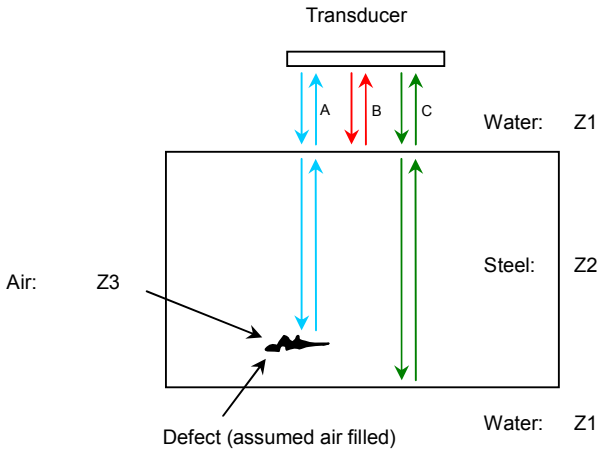

Figure 2-17 Water immersion inspection of a steel part.

Wave	Relative amplitude (dB)
A (defect)	-17.89
B (front wall)	-0.59
C (back wall)	-18.48

Table 2-3 Amplitude of reflected signals shown in Figure 2-17 relative to total reflection.

This can be considered a worst-case scenario, since at normal incidence there is a direct planar reflection from both the front and back walls. Two major observations can be made from these simple calculations:

- The large front wall reflection is almost 20 dB above any reflections from inside the component.

- While the back wall reflectivity is similar to that of a defect, defects will generally be much smaller in cross sectional area, and therefore represent a weaker target.

The first observation means that it is critical to transmit short pulses, so that the front wall reflection does not mask near surface defects. It is possible to construct transducers which emit pulses as short as three cycles of the centre frequency [8], which in general is enough to address this need.

The second observation means that the back wall reflection can create artefacts in the image at angles where sidelobes are directly reflected back to the array. This is illustrated in Figure 2-18, which shows a TFM image, captured using a 127 element spiral 2D array, operating at 1.5 MHz. This was a very early experiment carried out by the author on sparse array imaging, and more details can be found in [16]. When the beam is steered to an angle where a dominant sidelobe is directly reflected back to the array, the reflection appears in the image. This could easily be mistaken for a defect, as the user does not see any indication that it is part of the back wall. It is therefore important that sidelobes are low enough that they do not appear in the image.

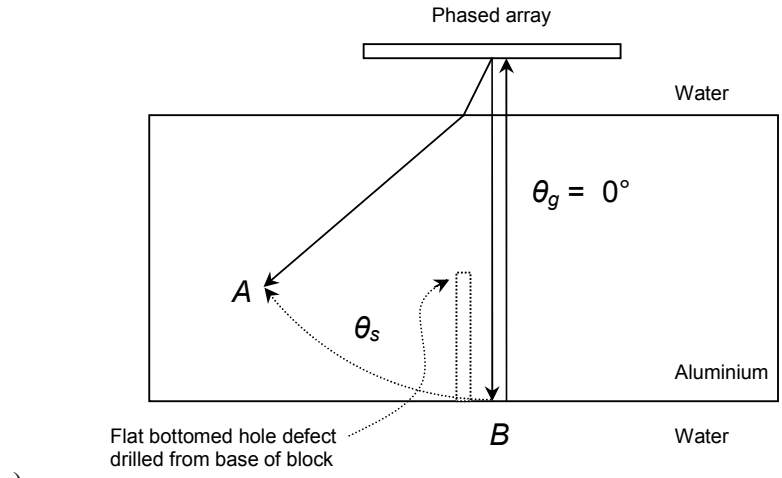

(a)

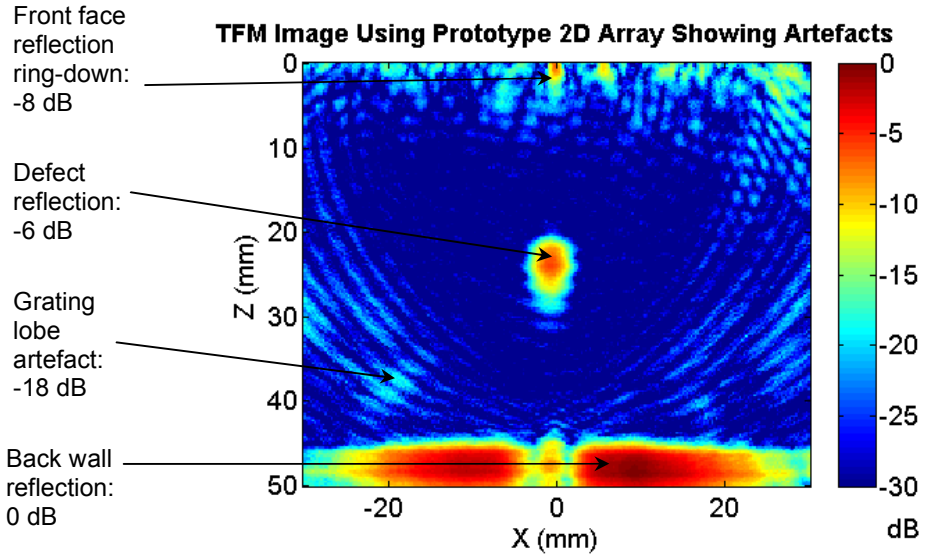

(b)

Figure 2-18 **Example of grating lobe artefacts in immersion NDE imaging. (a) shows the geometry which causes grating lobe energy from the reflection at *B* to appear in the image at *A*. (b) shows a TFM image of the test block captured with a 2D array. The light blue streaks at -18 dB are direct reflections of grating lobes from the back wall. These are only 12 dB below the defect, which is the signal of interest.**

It is clear from this example that, as the dominant reflector, the back wall reflection will play a large part in determining the sidelobe levels required in many NDE applications. The precise levels required depend on the relative size of the worst case defect when compared to the focal size of the beam. It is demonstrated experimentally in Chapter 6 that -30 dB sidelobe levels are sufficient for typical NDE inspections.

2.4.3 Sonar

In many sonar applications, such as forward look systems, the target is surrounded by open water. In this case there are no large reflectors which have the potential to obscure the target signal, and the sensitivity of the system is typically limited by signal to random noise ratio at the receiver.

Side-scan sonars are used in ocean floor topography and the location of under-sea assets. In this case the sonar must be able to resolve weak reflections from the sea bed from amidst the signals from more reflective areas. This puts tighter requirements on sidelobe levels than in forward look applications.

One major difference between sonar and the NDE and biomedical applications discussed previously are the long propagation delays encountered in sonar. This often limits real time sonar systems to a single omnidirectional transmit pulse; in this case all beamforming is done at the receiver. This limits the PSF sidelobe level that is achievable. Typical relative sidelobe levels in sonar systems are approximately -20 dB.

2.5 Considerations for 2D arrays

So far most examples have dealt with 1D arrays. However, 1D arrays are inherently limited, in that they can only electronically steer the beam in a single axis. 2D arrays offer a number of advantages:

- The ability to steer the beam in both axes, in doing so building up a volumetric image.

- The ability to achieve a tight and dynamically variable focus.

- The ability to capture this image from a single array location, eliminating the need for mechanical scanning.

In the context of NDE imaging there are two more specific benefits. If the array is scanned over the test piece in much the same way as a linear array, the test piece can be interrogated from a range of angles outside of the traditional imaging plane. This is shown in Figure 2-19, and allows the detection of out of plane defects, which is important in weld inspections. Without a 2D array, a 1D array would have to be scanned over the part many times to achieve the same coverage of the test piece.

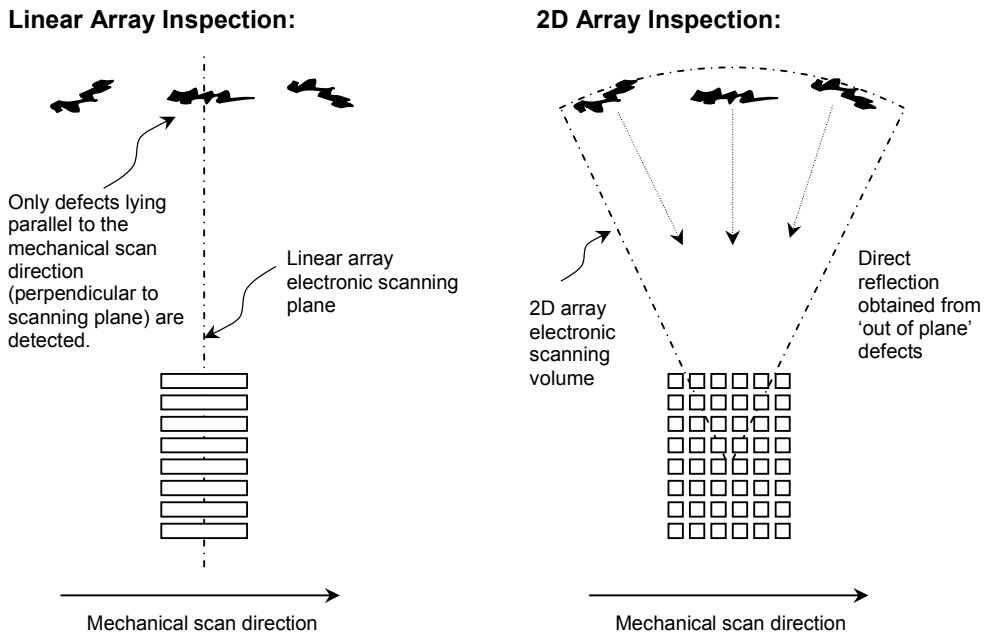

Figure 2-19 Detection of out of plane defects using a 2D array.

A second advantage is the ability to correct for refraction of sound as it enters and exits a part with complex surface curvature. Optical scanning techniques, such as the time of flight 3D scanner, can be used first to map the shape of the part which is to be inspected. The ultrasonic scanning system can then use this information to alter the delay laws of the array to accommodate variations such as weld caps, and other undesirable but often encountered surface features. This allows the inspection of these complex parts to be automated, and reduces the complexity of, for example any robotic scanning system.

Despite these advantages, 2D array technology has been slow to develop, for a number of crucial reasons:

- Number of array elements required to achieve adequate resolution is very large, increasing the cost of not only the array, but also the array controller.

- Interconnection to elements in the centre of the array is difficult, and can impair acoustic performance.

Take the example of a linear array with a 16λ aperture, as shown in Figure 2-20. The Nyquist criterion dictates that this array should have 32 elements to avoid the formation of grating lobes. If a 2D array is required with a similar resolution the simplest approach is to create a rectilinear grid with 32 elements in each axis. This squares the number of array elements required to 1,024. If the array is to have the same aperture through all azimuthal planes the corners of the array can be removed, which reduces the number of element by a factor of 3π/4. This results in a circular aperture with approximately 800 elements. For comparison, modern NDE phased array controllers typically have between 32 and 512 transmit-receive channels, and would be incompatible with such a large array. Similar numbers of elements are typically employed in biomedical and sonar imaging systems.

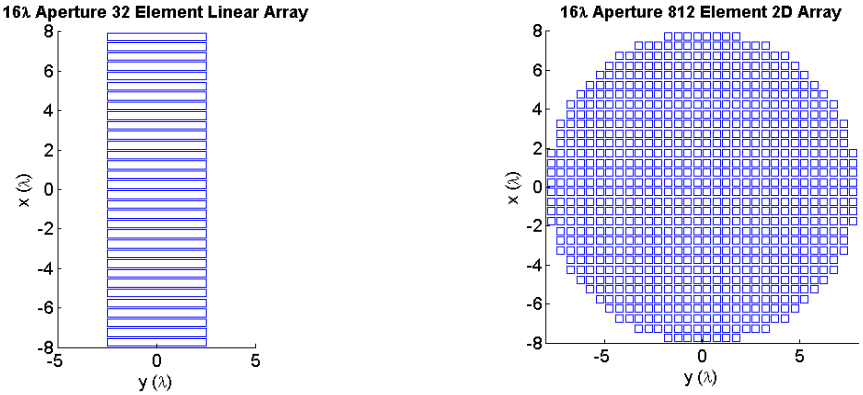

(a) (b)

Figure 2-20 **A linear array and a 2D grid array, both with 16λ apertures, demonstrating the large increase in elements required for 2D arrays, (a) linear array and (b) 2D array.**

There are a number of reasons why it is unlikely that the number of array controller channels will increase dramatically:

- The cost of the system is typically governed by the number of transmit-receive channels, with top of the range NDE units delivering 256 transmit receive channels, and costing in the region of £250,000, as of December 2010.

- Increasing the number of channels increases the thickness of cabling between the array and the controller. In practical NDE and biomedical applications this is undesirable, as the stiff cabling makes the array more difficult to manipulate accurately.

- 2D arrays are expensive due to the complexity of creating electrical interconnections to densely packed array elements, and larger arrays would further increase costs.

One solution to this problem is to use sparse arrays, which use fewer elements than the $\lambda/2$ spaced grid. Potential advantages of this approach are:

- Reduced cost of the phased array controller, due to fewer transmit-receive channels.

- Reduced cost of the phased array, due to a reduction in complexity, and easier interconnection due to the reduced density of the array.

However, these gains are generally achieved at the cost of image quality. Sparse arrays usually have higher sidelobe levels than dense arrays, as their beams often contain grating lobes. This has made them unsuitable for high resolution imaging applications, and they have seen little use commercially.

It is the aim of the work to show that sparse arrays can be constructed with sidelobes low enough to meet the requirements of volumetric NDE imaging. The next chapter discusses some of the existing techniques which can be used to design sparse 2D arrays.

Chapter 3

Sparse 2D Array Design Techniques

Moving from standard periodic arrays to a sparse array presents a design problem. While the designer of a 2D, λ/2 spaced grid needs only to know the required beamwidth to determine the aperture and element locations, there are many possibilities for sparse 2D array designs.

One common approach is to base the array on a dense 2D grid, then selectively discard elements based on some 'thinning' strategy. Although this reduces the number of possible array configurations, straight forward analysis shows the scale of the design problem. Consider the 800 element grid with a circular aperture shown in Figure 3-1, which is used to create a 128 element sparse array. The number of ways that a *k* element subset can be chosen from an *n* element set is given by the binomial distribution. That is:

$$\binom{n}{k} = \frac{n!}{k!(n-k)!} \qquad \textbf{(3-1)}$$

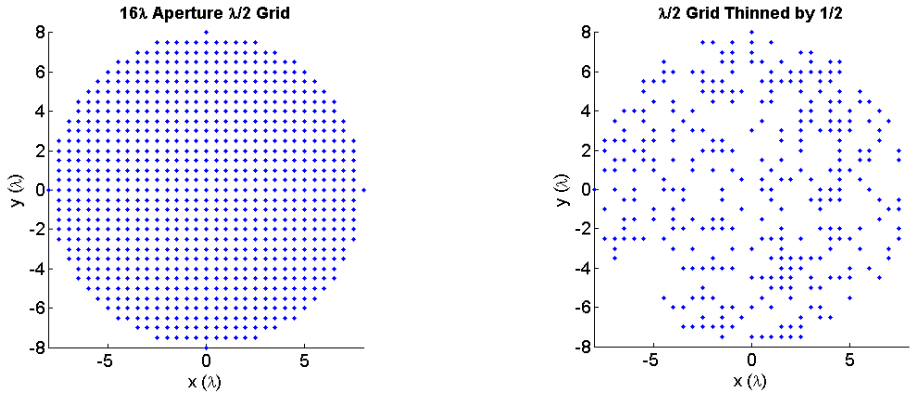

Figure 3-1 **Selective thinning of a 797 element sparse grid by removing approximately half of the elements, leaving a sparse grid of 400 elements. (a) 16λ aperture, λ/2 spaced dense array, and (b) 400 element sparse grid.**

For $n = 800, k = 128,$ Equation 3-1 gives approximately 2.197×10^{151} possibilities. To put this number in perspective, current estimates indicate that there are approximately 10^{80} atoms in the known universe. It is clear that even for this reduced problem, a design strategy which restricts the number of possible arrays is required. A review of a range of design techniques using thinning strategies is presented in [17,18]. Although thinning based approaches consider a huge number of possible array designs, they exclude many potentially useful designs from the outset. Element locations are quantised, with a step of $\lambda/2$. The present work seeks to develop a design process which affords more freedom to the positioning of array elements, while minimising the scale of the design problem. The techniques developed are discussed in Chapter 5.

The following sections describe two useful techniques for reducing the analysis of 2D arrays: the effective aperture concept and the projection slice method. Both periodic and aperiodic design techniques are then described. The primary focus of the work is on NDE applications, where most phased array controllers have combined transmit-receive channels. Unless otherwise stated the receive aperture is assumed to be the same as the transmit aperture, with all elements operating in pulse echo. However, some design techniques with different transmit and receive aperture, such as the vernier, will be discussed. Beam patterns are simulated using the Rayleigh Integral Method described in Chapter 4.

3.1 Effective aperture concept

The effective aperture concept provides a way of simplifying the transmit-receive, or 'two-way' beam pattern of an array. The effective aperture can be defined as an equivalent receive aperture that would produce the same transmit-receive beam pattern if the transmitter were a point source [14]. This allows the transmit-receive response of the system to be designed, then decomposed into separate transmit and receive beam patterns.

An expression for the effective aperture for a 1D array can be derived using the properties of the Fourier transform. The far field CW transmit-receive directivity P_{TR} can be expressed as follows:

$$P_{TR}(\theta) = P_T(\theta) P_R(\theta) \qquad \textbf{(3-2)}$$

Where P_T is the transmit directivity, P_R is the receive directivity, and θ is the angle from the array normal. It is shown in Chapter 4 that the directivity of a radiating aperture is equivalent to the Fourier transform of its element weighting. Therefore, it can be shown that the effective transmit-receive aperture of the system, E_{TR} is:

$$E_{TR}(x) = a_T(x) * a_R(x) \qquad \textbf{(3-3)}$$

Where a_T, and a_R are the element weightings of the transmit and receive apertures at position x on the array, where x is measured in wavelengths, and where convolution is denoted by the asterisk symbol. This means that the effective aperture can be calculated simply by convolving the transmit and receive apertures. This is shown graphically in Figure 3-2.

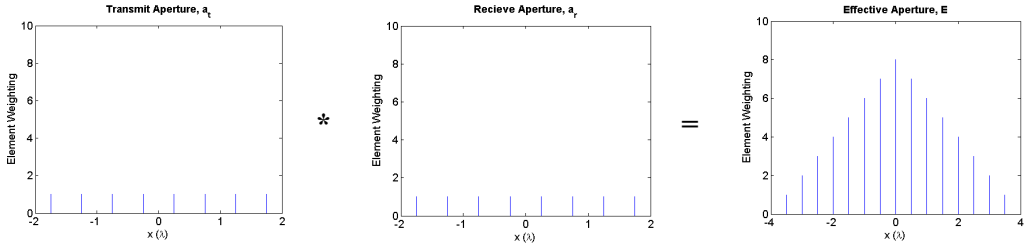

Figure 3-2 **Convolving the transmit and receive apertures to produce the effective aperture.**

This can be extended to 2D arrays, where the effective aperture is the 2D convolution of the transmit and receive apertures. This makes the effective aperture concept a useful technique for designing arrays with separate transmit and receive apertures. Vernier arrays are examples of such type of arrays.

For arrays that use the same elements for both transmit and receive the problem simplifies, and the transmit-receive beam pattern is simply equal to the square of the directivity of the common array aperture.

3.2 Projection slice method

The projection slice method provides a technique for creating a set of equivalent 1D arrays from a 2D array. It is useful as a simple method of analysing the merits of a 2D array design without having to calculate its beam pattern, which can be computationally expensive.

In the projection slice method, the equivalent 1D aperture is defined as the projection of all array elements onto a rotation of the *x-axis* at an angle φ in the plane of the array [8]. This is demonstrated in Figure 3-3.

Mathematically it can be expressed as an evaluation of the Radon transform at a single angle. If the 2D array aperture is given by the continuous function *f(x,y)*, then the Radon transform, *J*, is calculated using Equation 3-4.

$$J(\varphi, s) = \iint f(x, y)\partial(x\sin\varphi - y\cos\varphi - s)dxdy \qquad \textbf{(3-4)}$$

Where *s* is the location of the elements in the new 1D equivalent aperture.

It can be shown that the far field CW directivity of the 1D equivalent aperture is equal to that of the 2D array through the plane φ. This analysis gives rise to the concept of element shadowing. At some angles elements will overlap, and these elements are said to shadow each other. In some periodic structures this can lead to bunches of elements forming, with large gaps in between. If these gaps are large they will cause grating lobes in the beam. Designs which minimise element shadowing, like spirals and random arrays, tend to have flatter sidelobe structures [8].

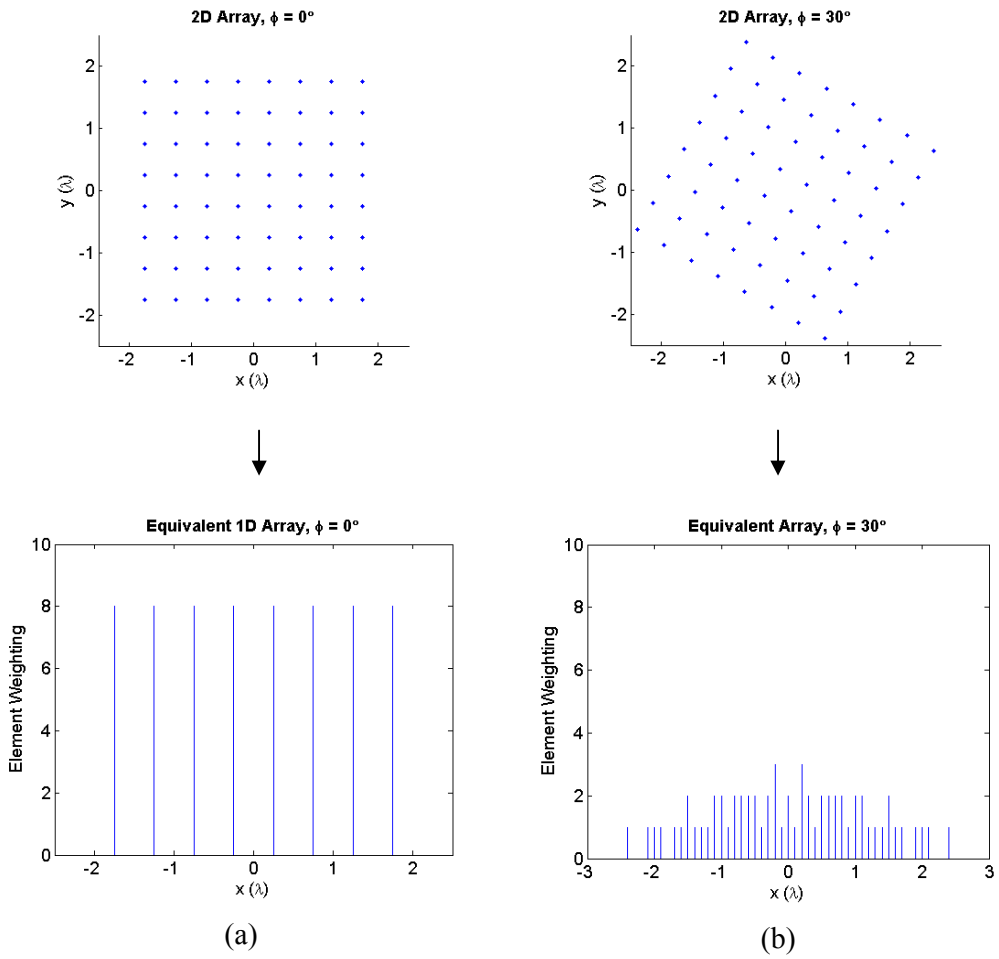

Figure 3-3 **Calculation of a two 1D equivalent arrays from a 2D grid array using the projection slice method. At 0° the grid shows a large degree of element shadowing, with groups of 8 overlapping elements, while at 30° there is much less element shadowing, with a maximum of 3 overlapping elements, (a) 0° and (b) 30°.**

3.3 Periodic sparse arrays

Periodic sparse arrays are the most straight forward to design, as they heavily reduce the size of the problem space that the designer faces. Typically the designer must choose a periodic pattern, the spacing of the elements in the pattern, and the aperture which the pattern covers.

While they are simple, periodic sparse arrays often suffer from aliasing, which creates grating lobes in the beam. Notable exceptions to this are annular designs, which undergo less element shadowing than grid arrays.

3.3.1 Grid arrays

Many dense 2D arrays consist of rectilinear grids of elements with an element spacing of approximately $\lambda/2$. One method of reducing the number of elements in a 2D array is to increase the element spacing. However, the periodic nature of these grids means that for spacings greater than $\lambda/2$ aliasing will occur and grating lobes will be formed in the beam, with their proximity to the mainlobe decreasing as element spacing is inceased. Under CW operation these lobes are approximately equal in strength to the mainlobe, making these arrays of very little use in imaging applications.

Figure 3-4 shows the layout of a 2D sparse grid with a circular aperture of 16λ, and an element spacing, d, of 1.3λ. Grating lobes appear in the beam at ~50°, as predicted by Equation 2-5. The grid contains 121 elements.

While the pulse echo performance of 2D sparse grids is poor, they do serve as a building block for vernier arrays, which are described in Section 3.3.3.

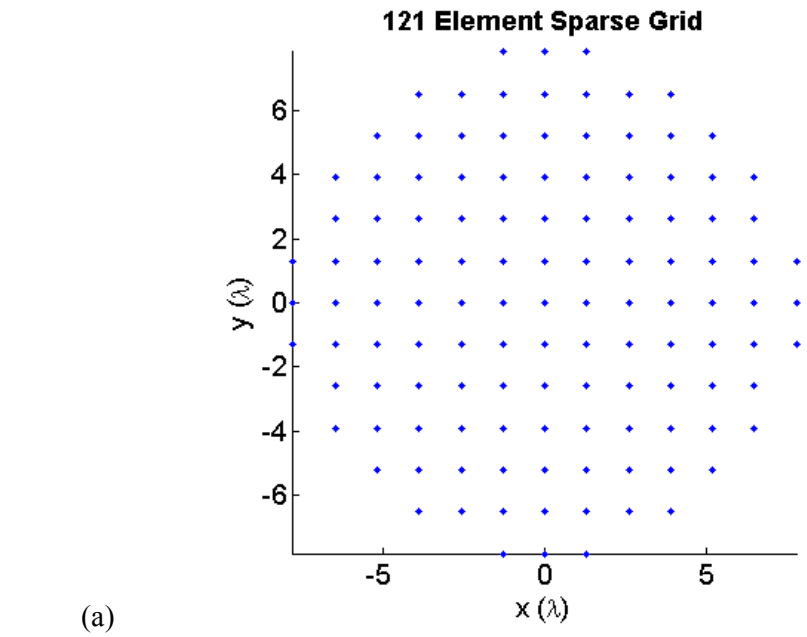

(a)

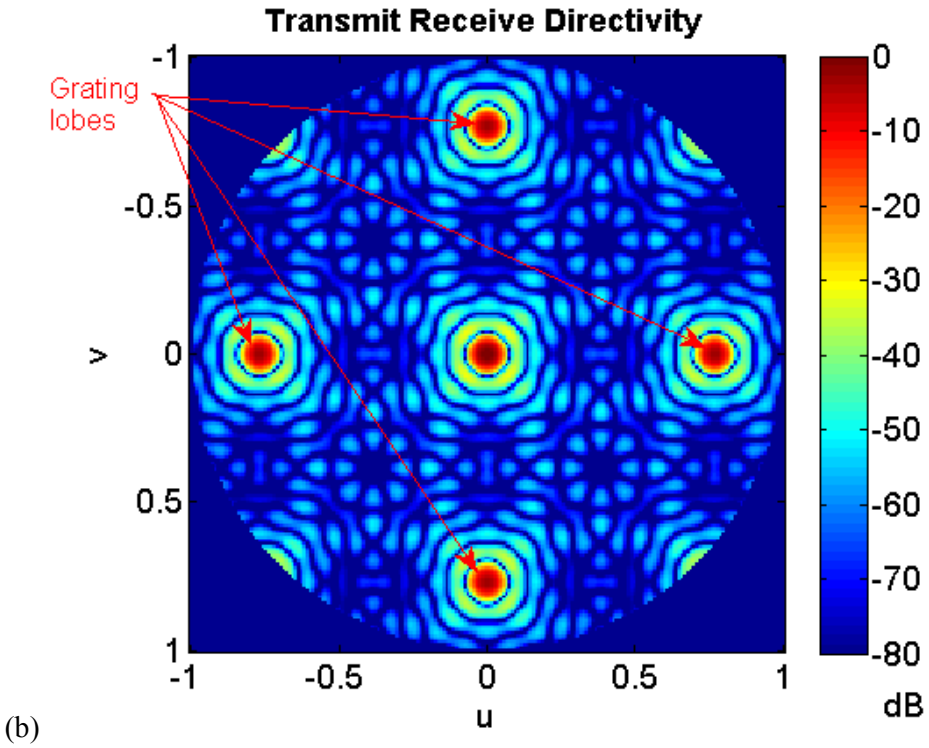

(b)

Figure 3-4 **Sparse grid array and its CW transmit-receive directivity when d = 1.3λ, (a) array layout, (b) array directivity.**

3.3.2 Segmented annular arrays

Segmented annular arrays are derived from annular arrays, which are capable of axial focussing, but not lateral steering. By segmenting each annulus into a series of elements both steering and focusing can be achieved. This forms an array which is periodic in a polar sense; elements have a radial spacing, d, and a circumferential spacing, e [19]. This is illustrated in Figure 3-5, along with the CW far field transmit-receive directivity for $d = 1.3\lambda$, $e = 1.3\lambda$. This array has 136 elements. When compared to the sparse grid array the grating lobe energy is spread around a circle, once again at ~50°. The grating lobe levels are lower than in the sparse grid, due to this spreading, at approximately -20 dB. This is because there are fewer rotational angles, φ, with dominant element shadowing.

A common design technique is to specify the same pitch in both circumferential and radial dimensions ($d = e$). Both dimensions produce a ring of grating lobes, and by doing this both rings are pushed out to the maximum angle possible for a given number of elements.

Although the grating lobe levels are reduced in comparison to grid arrays, they are still much higher than that required for good contrast resolution. As with sparse grids, segmented annular arrays can be used to form vernier transmit-receive pairs, which are discussed in the following section.

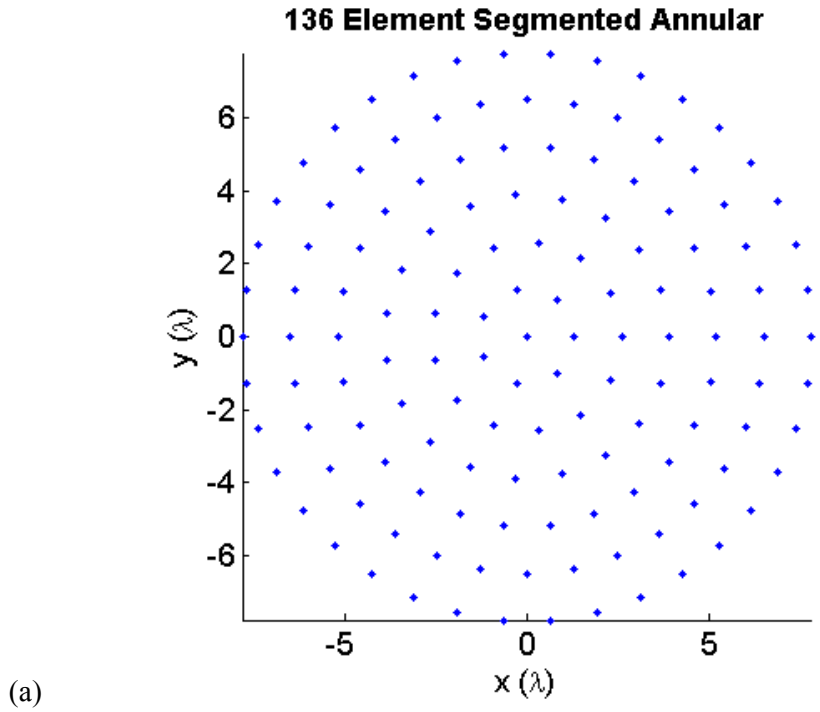

(a)

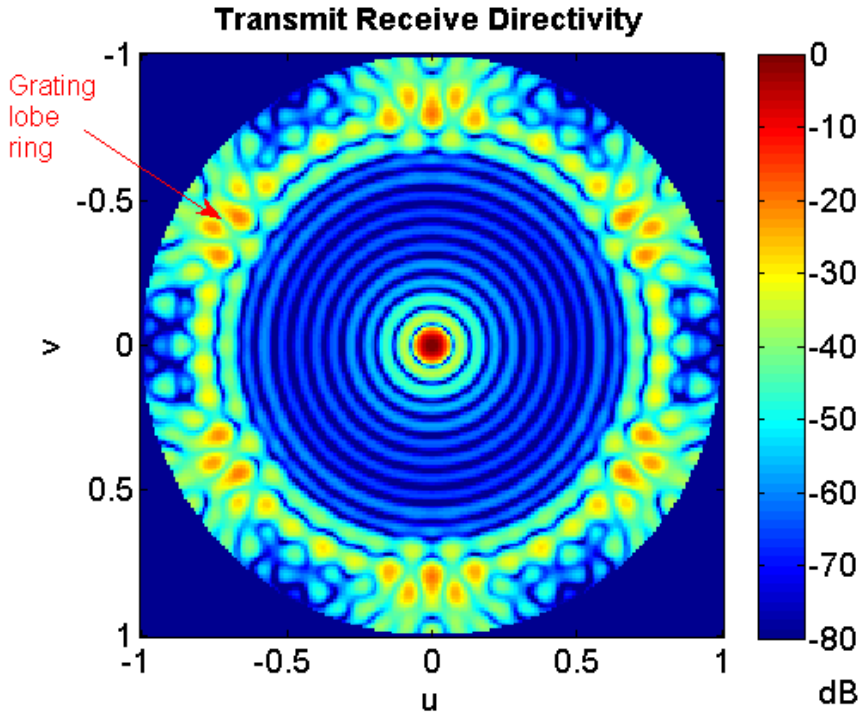

(b)

Figure 3-5 **Sparse annular array and its CW transmit-receive directivity when $d = 1.3\lambda$ and $e = 1.3\lambda$, (a) array layout and (b) array directivity.**

3.3.3 Vernier arrays

Vernier techniques for constructing sparse arrays with low sidelobes have been widely reported in the literature [17,18,20,21]. The technique utilises separate transmit and receive apertures, which are both periodic in nature. Poles in the transmit directivity are positioned at zeros in the receive directivity, and vice versa, which cancel out, reducing the overall sidelobe level. This is effectively due to the multiplicative nature of the pulse-echo process [17]. The effective aperture concept (Section 3.1) is a useful aid when designing vernier arrays, since it allows the transmit-receive beam pattern to be optimised.

Vernier arrays can be created by removing elements from dense arrays in a process called 'thinning'. A, sparseness factor, p_s, is used to modify the the inter-element pitch in both the transmit and receive apertures. Taking the example of a grid array with element spacing d, the transmit and receive pitches, v_t and v_r, are calculated as follows.

$$v_t = p_s \times d \qquad \textbf{(3-5)}$$

$$v_r = (p_s - 1) \times d \qquad \textbf{(3-6)}$$

Higher values of p_s result in a sparser array design, with p_s = 3 being the first value that features sparse designs for both apertures. Figure 3-6 shows a design where p_s = 3, which is based on a λ/2 spaced grid with a 16λ circular aperture. The transmitter has 93 elements, and the receiver 203. The simulated CW far field directivity of both the transmitter and receiver is presented, along with the transmit receive beam pattern. Peak sidelobes levels are -33 dB, and the design produces a low sidelobe floor of -70 dB.

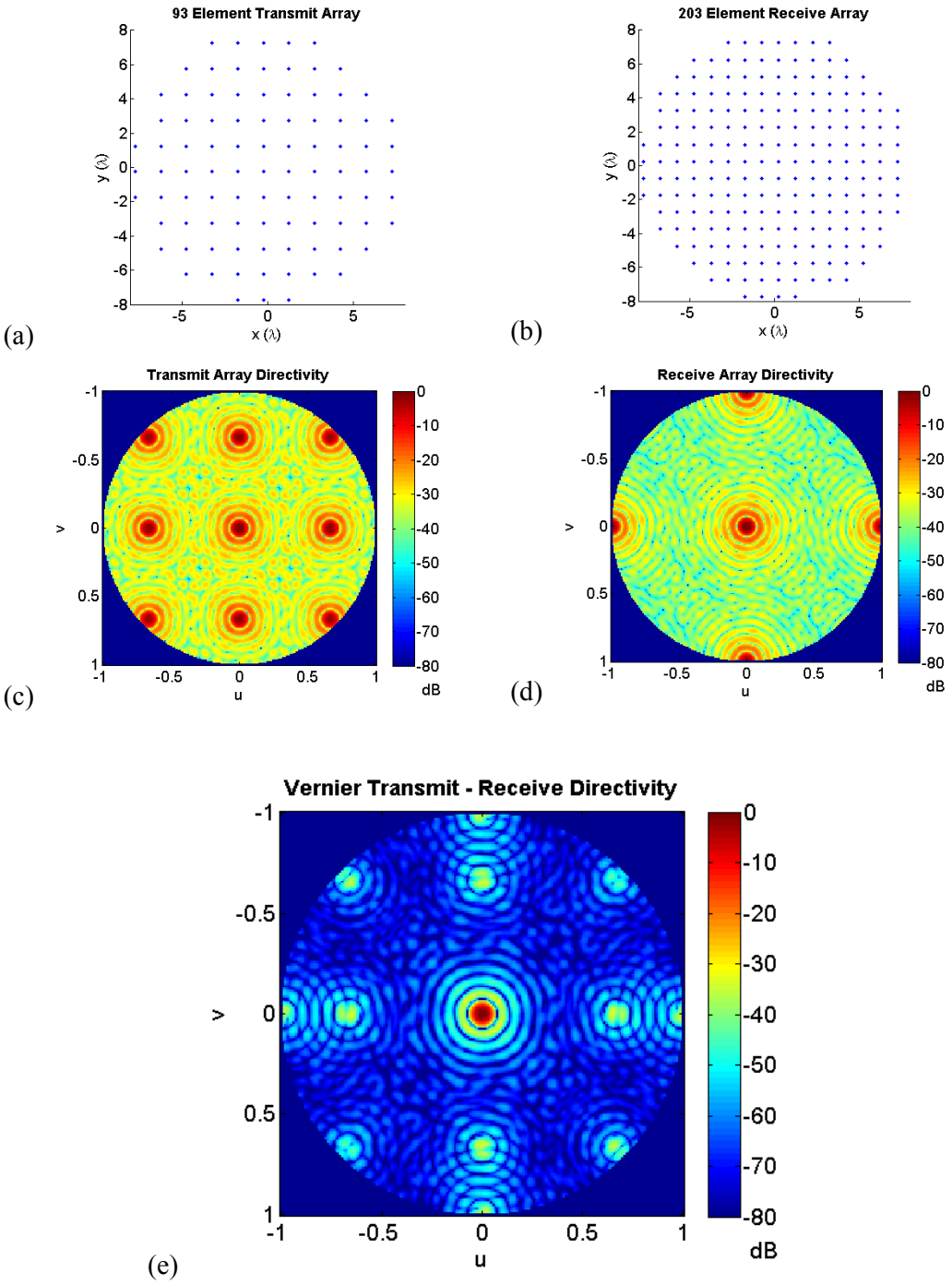

Figure 3-6 **Vernier array design based on a λ/2 spaced grid for p_s = 3, (a) transmit array, (b) receive array, (c) transmit directivity, (d) receive directivity and (e) transmit-receive directivity.**

While vernier sparse arrays can be effective at suppressing sidelobe heights, they are restricted in that they require different transmit and receive arrays. In addition to this, some elements are required only for transmission, some for only reception, and some in pulse-echo. This complicates element interconnection and transmit receive circuitry. Most NDE array controllers use channels which operate in both transmit and receive. This means that to operate a vernier array the total number of channels required must be considered. In the example presented here there are 24 overlapping elements, so the design requires a total of 272 elements. Without separate transmit-receive channels this approach leaves many channels 'turned off' in transmit or receive, underutilising the capabilities of the array controller.

Despite this, vernier techniques may be of use in biomedical and sonar applications, where the array system can be tailored to the specified application, or in NDE where a suitable array controller is available.

3.4 Aperiodic sparse arrays

The previous section demonstrated that periodic sparse arrays have grating lobes in their beams. Aperiodic designs avoid the formation of grating lobes, as the spacing between elements varies across the array. This spreads the grating lobe energy across the field, lowering the peak sidelobes.

Aperiodic designs fall into two categories: random designs, and deterministic designs. These are discussed in the following sections.

3.4.1 Random arrays

In a simplest form a random 2D array is a collection of elements whose locations are chosen from a set of independent random variables. If the elements are located at points $E_n = [x_n , y_n]$, then the values of x_n and y_n can be described by some probability density function. In practice many of these arrays are often generated, their performance simulated, and the best design is chosen. This creates an array that benefits from the aperiodicity of its statistically random array locations, but avoids the very poor designs that can implicitly be created using this method. For example, a truly random array could theoretically have all of its elements in the same location, and would simply behave like a point source. Better designs tend to have well distributed elements, with low element shadowing, and have a sidelobe floor in their beam patterns, sometimes referred to as a pedestal. An example of a random array and its beam pattern are shown in Figure 3-7. The first sidelobes are at -22 dB, while the outer peak sidelobes are at -27 dB.

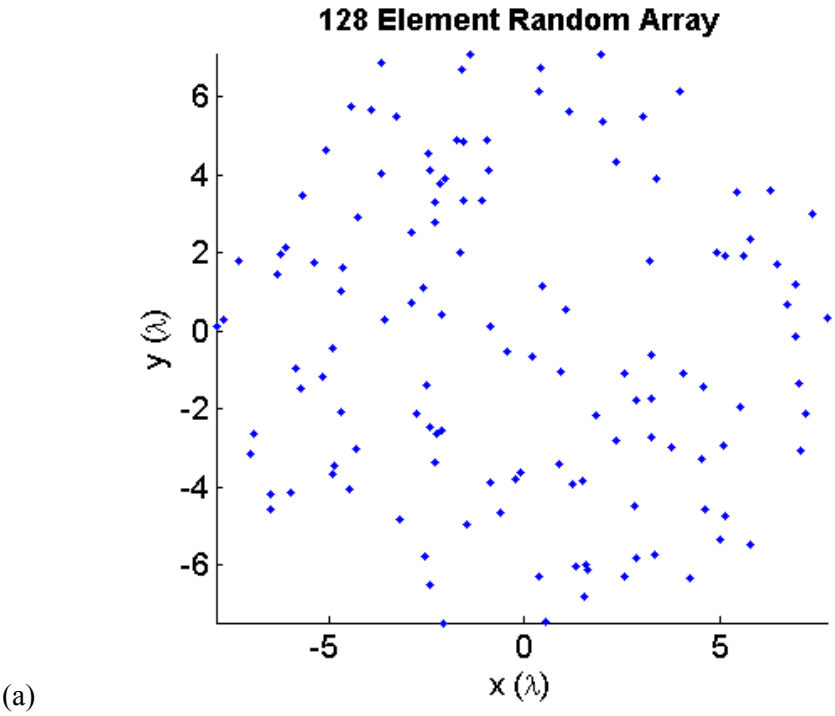

(a)

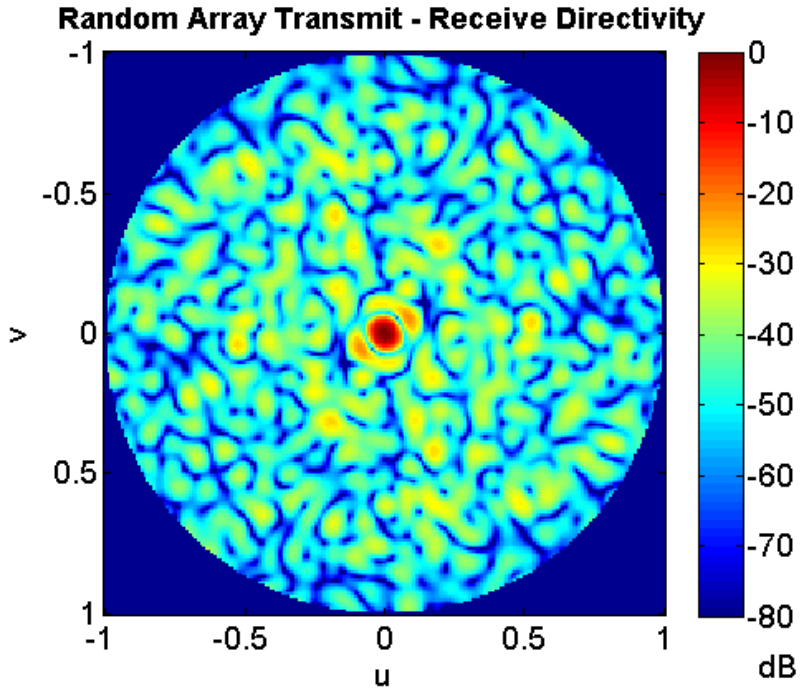

(b)

Figure 3-7 **128 element random array and its transmit – receive beam pattern, (a) array layout and (b) directivity.**

Due to their statistical design process, the performance of random arrays is best analysed in a probabilistic manner. It is relatively simple to express the average sidelobe level for an N element array, but a more useful measure is peak sidelobe level. A method for estimating the peak sidelobe level is presented by Steinberg [22], and is outlined here.

The far field beam pattern of a 2D array can be calculated by taking the 2D Fourier transform of its surface displacement. If each element is assumed to be a delta function at p_n the beam pattern $f(u,v)$ is:

$$f(u,v) = \sum_{n=1}^{N} \exp\left(-ik\left(x_n u + y_n v\right)\right) \qquad \textbf{(3-7)}$$

where $k=2\pi/\lambda$, the wavenumber. To simplify the analysis no steering will be applied to the array.

The first step is to calculate the average sidelobe level. The element locations are assumed to be described by a uniform probability density function, the array elements are isotropic, and excitation is CW. Waves from all elements arrive in phase at the mainlobe, so its amplitude will be relative to N. At all other points in the field the relative phasing of the elements is random, giving a relative root-mean-square (rms) amplitude of $N^{1/2}$. The mean power at these locations is the square of the rms amplitude, so the relationship between sidelobe power and mainlobe power is:

$$\frac{P_{side}}{P_{main}} = \frac{N}{N^2} = \frac{1}{N} \qquad \textbf{(3-8)}$$

The average sidelobe level in the array, S_{av}, in dB relative to the mainlobe is given by:

$$S_{av} = 10\log_{10}\left(\frac{1}{N}\right) \qquad \textbf{(3-9)}$$

To derive an estimate for peak sidelobe height, the probability density function (PDF) of the sidelobe pattern must be known. By applying the central limit theorem (*N* approaching infinity) the quadrature components of the complex beam pattern in the sidelobe region can be assumed to be normally distributed. Therefore, the magnitude of the beam pattern follows a Rayleigh distribution, of the form:

$$q(A) = \frac{2A}{N}\exp\left(\frac{-A^2}{N}\right) \qquad \textbf{(3-10)}$$

where A is the magnitude of the beam pattern. The probability, α, that an arbitrary sample of the sidelobe region exceeds some threshold A_0 is given by the integral:

$$\alpha = \int_{A_0}^{\infty} q(A)dA = \exp\left(\frac{-A_0{}^2}{N}\right) \qquad \textbf{(3-11)}$$

A more useful measure for array design is the probability that no sidelobes will exceed A_0, which is *1* - α. If this is given the symbol β, and n independent samples are taken, then it can be calculated with the following expression:

$$\beta = \left[1 - \exp\left(\frac{-A_0{}^2}{N}\right)\right]^n \qquad \textbf{(3-12)}$$

Rearranging Equation 3-12 for A_0, and assigning $B = A_0/N$ gives:

$$B = -\ln\left(1-\beta^{1/n}\right) \qquad \textbf{(3-13)}$$

B is an estimator of the power ratio of the peak sidelobe relative to the average sidelobe, when n points across the array are sampled. It is appropriate to sample each sidelobe in the beam pattern, so a measure for the number of lobes is required to define n. Steinberg shows that due to the Fourier relationship between the array aperture and its beam pattern, the area of an individual sidelobes is approximately λ^2/D^2, where D is the width of the aperture. There is 180° symmetry in the hemispherical beam pattern, making its total area $\pi/2$. Therefore when no steering is applied to the beam, the number of sidelobes is approximately:

$$n = \frac{\pi}{2}\frac{D}{\lambda} \qquad \textbf{(3-14)}$$

This can be combined with Figure 3-8 to produce a statistical estimate of the peak sidelobe level relative to the average sidelobe level. However, this estimate is downward biased, since it is unlikely that these samples will be located at the peak of a lobe. Steinberg uses derivatives obtained from a Taylor series expansion of the power of the beam pattern to estimate the increase in B required to give a more accurate estimate of the peak values. This approach ignores terms higher than the second order, since these have little effect on performance. This increase is assigned B_p, and is given by:

$$B_p = B + 1 + \frac{2}{B} \qquad \textbf{(3-15)}$$

The peak sidelobe level in the array, S_p, in dB relative to the mainlobe is given by:

$$S_p = 10\log_{10}\left(\frac{B_p}{N}\right) \qquad \textbf{(3-16)}$$

The effect of N on both the average sidelobe level and the peak sidelobe level estimator is shown in Figure 3-8. An aperture of 16λ is used, and confidence intervals of 99.9%, 50%, and 0.1% are shown. Sidelobe power varies linearly with N, and peak sidelobe levels are between 7.5 and 12 dB higher than average levels, depending on the confidence level used. These results agree with the array shown in Figure 3-7, which has one – way sidelobes of -11 dB. One anomaly in the predictions is for the peak sidelobes of very small arrays with high confidence levels, where the peak sidelobe rises above the mainlobe level. At small values of N the central limit theorem is a poor assumption, and in reality peak values will remain lower than the mainlobe.

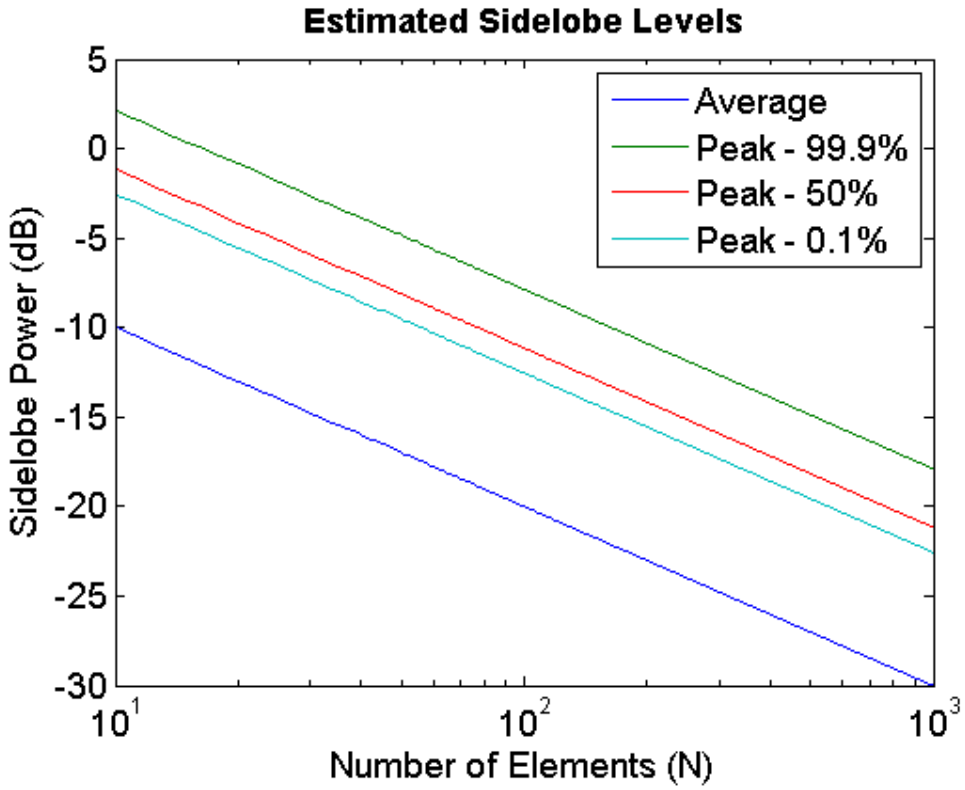

Figure 3-8 Average and peak sidelobe heights for random sparse 2D arrays.

It can be seen in Equation 3-16 that the peak sidelobe level increases with the square of the array aperture in wavelengths. Thus, an increase in aperture, or frequency will increase S_p. Other factors which affect sidelobe level, but which have not been considered here are:

- Steering angle – this moves more sidelobes into the visible region of the beam, increasing the chances of a large peak.

- Non isotropic elements – so far array elements have been approximated as point sources radiating isotropic spherical waves. In reality array elements have a finite size, and therefore have a non uniform directivity. This reduces the height of lobes near the outside of the beam. For small values of θ_s this decreases S_p, while for large values it is increased.

- Array bandwidth – temporal spreading of the transmitted pulses under wideband operation reduces coherent build up of sidelobes, reducing S_p.

While these factors to affect peak sidelobe levels, their effect is minimal compared to the previously mentioned variables [22]. This probabilistic approach is compared to simulated results in Chapter 5, and the correlation is shown to be good.

While creating random arrays in this manner can provide suitable sidelobe levels, the random nature of the array construction can cause problems for device fabrication. The random array shown in Figure 3-7 illustrates some of these issues:

- Elements can group together, experiencing higher cross talk than isolated elements. This will reduce their acceptance angle, and alter the shape of the beam, increasing sidelobe levels at high values of θ_s.

- Electrical interconnection to elements is made more complex, due to the completely random nature of the array. Some random arrays with tight bunches of elements may make reliable interconnection impossible.

- Near field performance of the array will be less predictable than with periodic arrays. Areas of the field closest to sparsely populated areas of the array may have large nulls.

To address some of these issues, a binned design approach can be taken [23]. The array is broken up into *N* areas, or bins, as shown in Figure 3-9. Each bin contains an array element, which is positioned within the bin according to some PDF. This could be a uniform PDF, or a more restrictive function such as a Gaussian, provided the element remains in the bin. Bin structures are typically grids, but can in theory be annular, or a general tessellated structure. By having some knowledge of the structure of the array, interconnection problems can be reduced and bunching can be avoided.

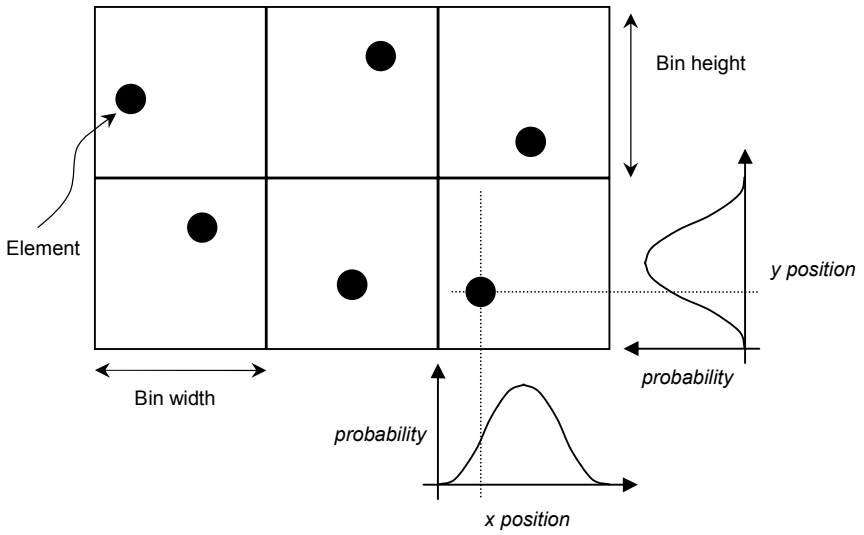

Figure 3-9 **Binned array design approach. PDFs used in both the *x* and *y* axes to determine element location within the bin.**

Binned arrays retain some of the properties of their underlying structure, and the more restrictive the PDF, the more these properties influence the beam. Take the example of an array based on a grided bin structure, where the elements are positioned using a Gaussian distribution, *G(r)* given by:

$$G(r) = \frac{1}{\sqrt{2\pi\sigma^2}} \exp\left(\frac{-r^2}{2\sigma^2}\right) \qquad \textbf{(3-17)}$$

where r is the radius of the element from the centre of the bin, and σ is the standard deviation or element radius. An alternative would be to employ a Cartesian approach, using a Gaussian distribution to define the element location in both x and y. This would marginally alter the layout, allowing elements to take up positions in the

corners of the bins. The difference between these approaches is considered relatively insignificant the polar approach has been employed for the purposes of this thesis. As σ tends to zero the array becomes a sparsely populated periodic grid, with grating lobes in its beam. As σ is increased the grating lobes are spread out, and a sidelobe pedestal begins to form around them. The beam patterns of binned arrays are often characterised by low sidelobe levels close to the mainlobe, which rise to a higher sidelobe plateau at higher elevation angles. A 137 element random binned array with $\sigma = \lambda/4$ is illustrated in Figure 3-10. Peak sidelobes are -16.5 dB, at the locations where grating lobes would form in a sparse grid, which is higher than the random array. However, the elements are much more uniformly spaced, aiding manufacture.

Binned array design is therefore a compromise between retaining the useful properties of the underlying periodic structure, and avoiding the formation of grating lobes by introducing a sufficient degree of randomness.

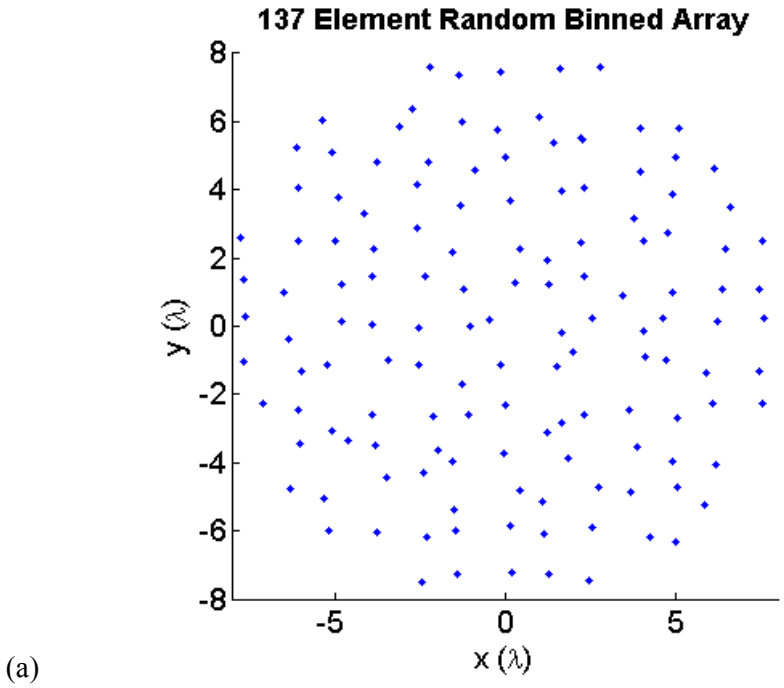

(a)

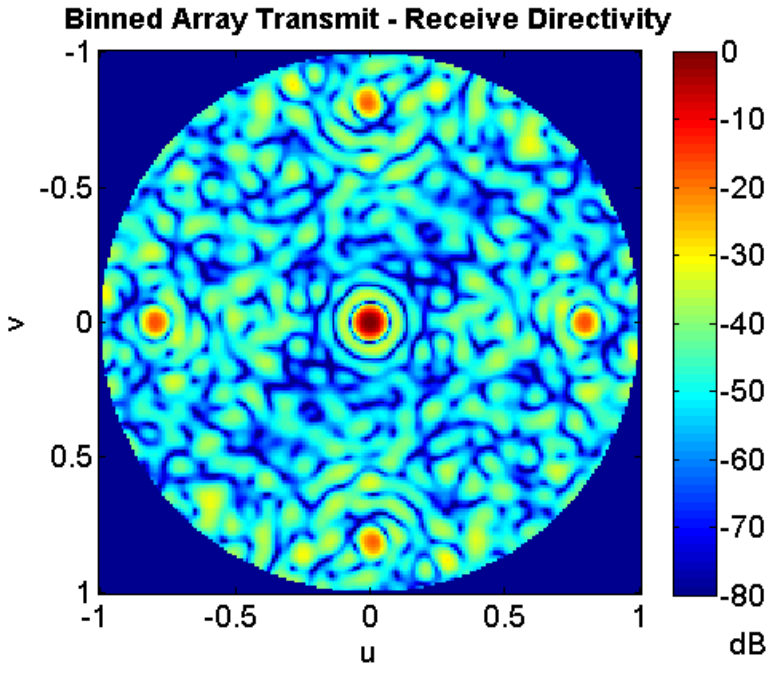

(b)

Figure 3-10 **Behaviour of a binned random array, (a) array layout and (b) transmit - receive beam pattern.**

3.4.2 Aperiodic deterministic arrays

Aperiodic deterministic arrays share many properties with random arrays due to the absence of a periodic structure. However, since they are defined using a deterministic approach they are not random. These arrays offer the potential of lower peak sidelobes than random arrays, plus the advantage of allowing more control over the separation and placement of elements, to ease the problem of electrical interconnection.

One aperiodic deterministic design of particular interest is the spiral array. It has already been reported in the literature, showing a 10 dB reduction in sidelobe performance over random arrays under simulated wideband conditions [1]. However, only one array is investigated with no discussion of design considerations. In addition to this the array is operated in a vernier fashion, with the elements in the single spiral arm alternating between transmitters and receivers. This may not be suitable for all applications, since it requires an array controller with separate transmit and receive channels.

Spirals have many interesting properties, and are already used in a variety of antenna and array applications. Spirals have been used in antenna design since the late 1950's to create wideband antennas for radio and microwave applications. They are capable of achieving constant gain, impedance, and beamwidth over a wide bandwidth, while retaining a compact design [24]. This is achieved by virtue of the spiral's self similarity; it has similar structures over a range of scales, corresponding to a range of wavelengths. A range of designs have been investigated, including logarithmic and Archimedian spirals [25]. Bandwidth ratios of 20:1 have been demonstrated, and these are generally limited by manufacturing techniques and practical size constraints [24].

More recently, spirals have been used to construct parts of the Square Kilometre Array (SKA), which when complete will be the world's largest aperture synthesis radio telescope. This type of radio telescope uses the rotation of the earth to create a much larger synthetic aperture. Acquisitions can last up to 12 hours. The SKA will

operate over a frequency range of 70 MHz to 30 GHz, and will have a peak angular resolution of several milliarcseconds [2]. To achieve this, it will require an aperture of $>10^7$ wavelengths, or approximately 2000-3000 km. To create such a large array a sparse design is required. Previously aperture synthesis telescopes produced images with peak sidelobes levels of approximately -20 dB [3]. The SKA will produce an image with a 120 dB dynamic range at 1.4 GHz, achieved using a combination of array design and signal processing. The outer reaches of the aperture will consist of a 5 armed spiral, which will build up a much denser synthetic array as it moves through the sky. The spiral design helps to avoid overlapping samples in the synthetic aperture, which is similar to the designs produced using the effective aperture concept, and the projection slice method. One additional benefit of using spirals is that the communications infrastructure used to gather signals from the outlying stations can be routed along the spiral arms, greatly simplifying its layout, and reducing costs.

Spirals possess some useful properties which make them attractive for creating ultrasonic phased arrays:

- Logarithmic spirals are examples of fractal structures due to their self similarity. This means that in a single structure there are a variety of scales and periodicities, spreading sidelobe energy over the *u*-*v* plane.

- Multi-armed spirals have rotational symmetry, which in turn create rotationally symmetric beam patterns. This simplifies the analysis of new designs, and further smoothes the beam pattern.

- The multi-armed layout offers opportunities for routing electrical interconnections in plane with the array, as opposed to directly through the backing structure. This could lead to a reduction in array cost, and an increase in robustness.

Due to their potential to deliver sparse designs with suitable sidelobe heights for ultrasonic imaging, spiral arrays will be the main focus of the work. The properties of various spiral structures, and their suitability for array design will be discussed in detail in Chapter 5. Examples of possible spiral designs are shown in Figure 3-11.

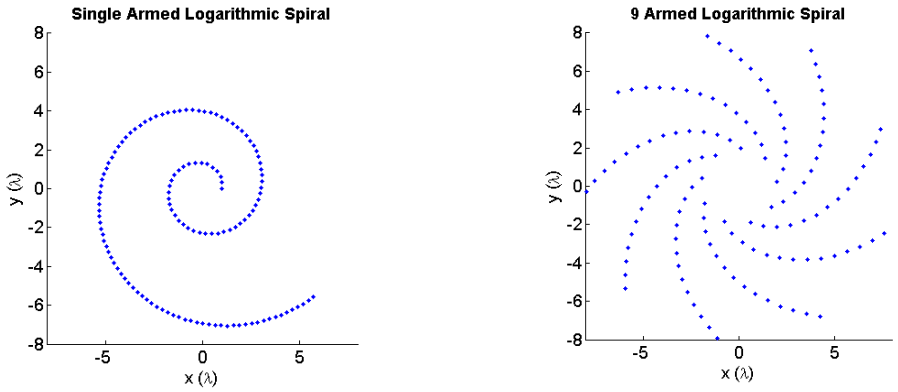

(a) (b)

Figure 3-11 **Examples of logarithmic spiral array designs, (a) single armed 128 element design and (b) 9 armed 126 element design.**

There are certainly many more possible deterministic functions which may prove useful in the design of aperiodic ultrasonic arrays. Penrose tilings are nonperiodic tiled structures generated by an aperiodic set of prototiles [26]. These tilings represent one of the simplest tiling structures capable of achieving an aperiodic pattern. They can also produce structures with rotational symmetry. However, it is not immediately obvious how these structures could be employed in an ultrasonic array. Penrose's original design contains 6 different prototiles, so unless some sort of sampling strategy is used there would be multiple element sizes and shapes used in the array.

Another alternative to spirals would be to use branching structures. These structures appear frequently in nature, and form the basis of objects such as trees, lungs and

blood vessels. Many of these objects have high fractal dimensions, and by the nature of the branching structure exhibit self similarity. However, it is unclear as to how these structures could be used to create an ultrasonic array without creating wide variation in element density across the aperture.

Spiral structures have already been shown to be suitable for producing ultrasonic arrays. However, very little literature exists on their design, manufacture, and imaging capability. The work described in this thesis will focus on advancing the field of spiral array design, by developing new design techniques, simulating the arrays' performance, and ultimately obtaining experimental imaging results.

Chapter 4

Acoustic Field Modelling Software

One of the most difficult aspects of sparse two dimensional (2D) array design is the huge number of possible element configurations for any given array specification. It would be impractical to attempt an empirical design process, as the cost and time of prototyping would be excessive. Therefore, in order to arrive at an optimal design, the capability to model the acoustic field produced by a proposed array design is essential. In this chapter an assessment of the available modelling techniques is presented, followed by a detailed description of the selected modelling process.

4.1 Overview of available field modelling algorithms

There are a wide variety of techniques available for modelling the structure of the field produced by ultrasonic transducers. These include both analytical, and numerical techniques, and offer varying degrees of complexity, accuracy, and execution speed. What follows is a brief description of available models.

4.1.1 Analytical models

Before the abundance of powerful desktop computers, analytical models were the only practical approach to modelling acoustic fields. Analytical models make a number of simplifications in order to arrive at a more tractable expression for calculating field properties, at the expense of a narrowed scope of use.

The advantage of this simplified approach is that these models highlight important cause and effect relationships to the designer, which are often masked in more complex numerical modelling techniques. In addition, analytical models execute very rapidly, making them useful in optimisation problems.

The main disadvantage of this approach is lack of flexibility. Solutions are generally restricted to simple shapes, such as pistons or bars, and the field limited to an axial strip, or an arc in the far field. In addition to this, most models consider only continuous wave operation.

4.1.2 Rayleigh integral method

The Rayleigh integral method (RIM) is based on Rayleigh's second integral, which relates the velocity potential at a point in an external field, to the normal velocity of an arbitrary radiating surface [27]. It can be used for analytical work, but in its discrete form it can be used to numerically calculate the pressure developed in an arbitrary field by a vibrating surface. This makes it very useful for both the design and experimental analysis of transducer designs. In its most basic form it considers single frequency excitation (also known as continuous wave, abbreviated CW), but using inverse Fourier techniques it can be extended to consider pulsed excitation [28]. The most common method assumes that the radiating surface is surrounded by an infinite rigid baffle, which is valid for most practical transducer applications, where the device is enclosed in a stiff metal housing. Surface velocity information can be input from the following sources:

- Simple piston-like vibration can be assumed for basic theoretical analysis.
- Finite element analysis can be used to model the transducer structure, creating a more realistic surface velocity map.
- Surface velocities can be measured experimentally using laser vibrometry.
- Individual surface points can be made to approximate the far field performance of a vibrating array element, by applying directionality to the element. This is discussed in Section 4.2.4.

When expressed as a continuous integral the Rayleigh integral takes the following form [29]:

$$P(\vec{y}) = 2i\omega\rho_0 \int_S G(|\vec{y} - \vec{x}|)\, v_n(\vec{x}) dS \qquad \textbf{(4-1)}$$

where,

$$G(r) = \frac{e^{-ikr}}{4\pi r} \qquad \textbf{(4-2)}$$

$\vec{x}$ and $\vec{y}$ denote the transducer and field surfaces respectively, i, ω, ρ_0 and k are respectively, the imaginary unit, the angular frequency in radians per second, the density of the field medium and the wave number. P, v_n and S denote respectively the field pressure, the surface normal velocity, and the set of all points on the radiating surface.

The integral can be converted to discrete form, for use in numerical computer modelling. The radiating surface is approximated as a group of omnidirectional point sources. The Discrete Rayleigh Integral (DRI), or the 'simple source method' [30] as it is commonly known, takes the following form:

$$P(g) = \frac{i\rho_0\omega}{2\pi} \sum_j A_E \frac{e^{-jkr_j}}{r_j} v_j \qquad \textbf{(4-3)}$$

where the points q_j are the points on the radiating surface, and g is a point in the field. P and v_j are respectively the acoustic pressure at g, and the velocity at the centre of the j^{th} point on the surface. A_E is the area of the point g, k is the wavenumber, and r_j is the distance between g and q_j.

The main advantages of this method are as follows:

- It is quick to evaluate on modern desktop PC, and is also simple to implement.

- Arbitrary surface shapes can be simulated allowing curved and focused transducers to be modelled.

- It can accept surface data from both modelled and experimental inputs.

- It can generate arbitrary field shapes, such as planes, hemispheres, or receiving transducers.

The main disadvantage of the approach is that it simulates devices under CW operation. This is acceptable for sonar devices, which tend to be operated at low bandwidths, but is inaccurate for NDE and biomedical applications, which generally use pulses with bandwidths over 60%. However, the CW beam at the centre frequency of a pulsed device is generally the worst case assessment of sidelobe levels. This is because in the pulsed case each point on the surface only radiates for a finite amount of time, so there are points in the field which do not undergo constructive interference. This makes the DRI a useful technique for quickly comparing the merits of different array designs.

In order to add further flexibility to the method, a process of simulating the fields of wideband devices had been developed. This is accomplished by calculating fields at each frequency of interest of the device and performing an inverse Fourier transform at each point in the field. This method is covered in detail in Section 4.2.2.

4.1.3 Spatial impulse response method

The spatial impulse response method is a convenient way of calculating acoustic fields radiated by wideband devices, and is used extensively in medical ultrasound. It is a time domain approach, which calculates the Point Spread Function (PSF) of scatterers in a homogeneous medium. The spatial impulse response is calculated by integrating Dirac functions radiated from a set of points across the surface of the transducer [31]. In this way it is effectively a time domain equivalent of the Rayleigh integral method described in section 4.1.2. To find the PSF, the spatial impulse response is convolved with the time domain response of the transducer under consideration.

The main advantage of this technique is its ability to model devices under pulsed operation. This, coupled with its direct calculation of an object's PSF, makes it well suited to simulating imaging in media with many point scatterers as is often the case in biomedicine. The method does not naturally accommodate apodisation, but can be extended to do so [31].

The main disadvantage of this method is the relative complexity of calculating CW fields. First, the spatial impulse response must be calculated. This data is then converted to the frequency domain via the Fourier transform, and the component at the desired frequency selected. Since it is often more intuitive to consider CW beams at the conceptual design stage, this complexity is undesirable.

4.1.4 Angular spectrum method

The angular spectrum method is a technique that was originally developed for analysing optical wave propagation [32], but has also been extensively used in acoustics. In its basic form it is a CW model, but it can be extended to model pulsed operation.

First, the complex pressure at a grid of points on the surface of the transducer is sampled. The 2D Fourier transform of this field is then calculated which decomposes the field into a spectrum of plane waves. These planes waves can then be propagated to a plane some distance into the field by multiplying the spectrum by a complex phasing matrix. The pressure across this field can then be calculated by taking the inverse Fourier transform of the propagated spectrum.

The method is capable of propagating waves in both the forward and backward directions through the field, and has therefore been used to analyse the surface displacements of transducers from their radiated fields [33]. The main disadvantage of this method is the lack of flexibility afforded by the Fourier transform. This transform limits the method to analysing planar devices and fields, which have been sampled using evenly spaced grids. This makes it unsuitable for modelling curved devices, and abstract array layouts. However, by using the Fast Fourier Transform (FFT), it can be calculated very quickly, and is used in Chapter 5 to analyse continuous spiral patterns.

4.1.5 Finite element analysis

Finite element analysis (FEA) is a technique which has become common-place in a wide variety of applications ranging from structural analysis to air flow in gas turbine engines. It is particularly useful for solving wave propagation problems, and is used for ultrasonic, mechanical and electromagnetic simulation. It is a numerical technique where a structure is broken into many small sections, called elements. Elements are connected at nodes, and at each of these nodes a series of partial

differential equations describe physical interactions within the system. By making the elements small, these equations can be simplified to ordinary differential equations, reducing the computation required. There are a variety of computational methods which can be used to approach a finite element problem. Explicit time domain solutions are well suited to simulating ultrasonic wave propagation, as they are less computationally intensive than implicit solutions when analysing wideband signals propagating over many wavelengths [34].

Alba routinely uses a time domain finite element package called PZFlex© [35], for modelling the performance of its arrays. This code is capable of modelling both the performance of the array's microstructure, and the shape of the field it produces. Of all the modelling techniques discussed, this method is considered the most accurate approach to characterising array performance, as the surface displacement of each array element under pulsed excitation is considered. This gives a realistic assessment of how the design of the transducer microstructure affects the acceptance angle of the array.

The main disadvantage of finite element modelling is the relatively long execution time, when compared to the previously discussed models. The scenarios considered in the work would require a large 3 dimensional model of the array, coupled with a second field extrapolation model to calculate the field. It is anticipated that a model of these dimensions would take around an hour to execute. This would make it unsuitable for use in a cost function, which may be called many thousands of times. In addition, the discretised representation of the structures being modelled can lead to dispersion of waves travelling over many wavelengths.

4.1.6 Selection of algorithm

The discrete RIM was selected for use in this project, and also for sonar modelling use in Alba. The major reasons for this choice were its flexibility, speed of execution, and the excellent agreement with experimental results that was achieved in initial results.

In Alba, this method is supported by time domain finite element modelling, and analytical linear systems modelling of transducer structures.

4.2 Field modelling process and capabilities

The modelling capability developed during this project had two main goals. The first was to provide a way to model the acoustic field produced by novel 2D array designs. The second was to support Alba's sonar design by modelling a wide variety of sonar devices. This section describes the functionality of the modelling environment that was developed, along with some examples of its simulated fields.

4.2.1 Basic model

The modelling package was based around the Rayleigh Integral Method (RIM), which is described in Section 4.1.2. It was implemented in the Matlab© environment, allowing the model to be coded at a high level, minimising its complexity. To keep the package as flexible as possible it was constructed in a modular manner, from a series of software functions. The functions were called from a top level script file, and fall into one of five categories:

- Discrete Rayleigh integral function
- Transducer generator function
- Field generator function
- Apodisation generator function
- Focal law generator function.

In this way code could be re-used for multiple problems, which minimised the amount of time required to create new models. For example, to change the transducer in the simulation from a planar array to a curved array, the designer has

only to change the transducer generator function. This is important, as over the course of the project, Alba broadened its range of transducers to include new geometries and shading functions. A block diagram of this approach is shown in Figure 4-1.

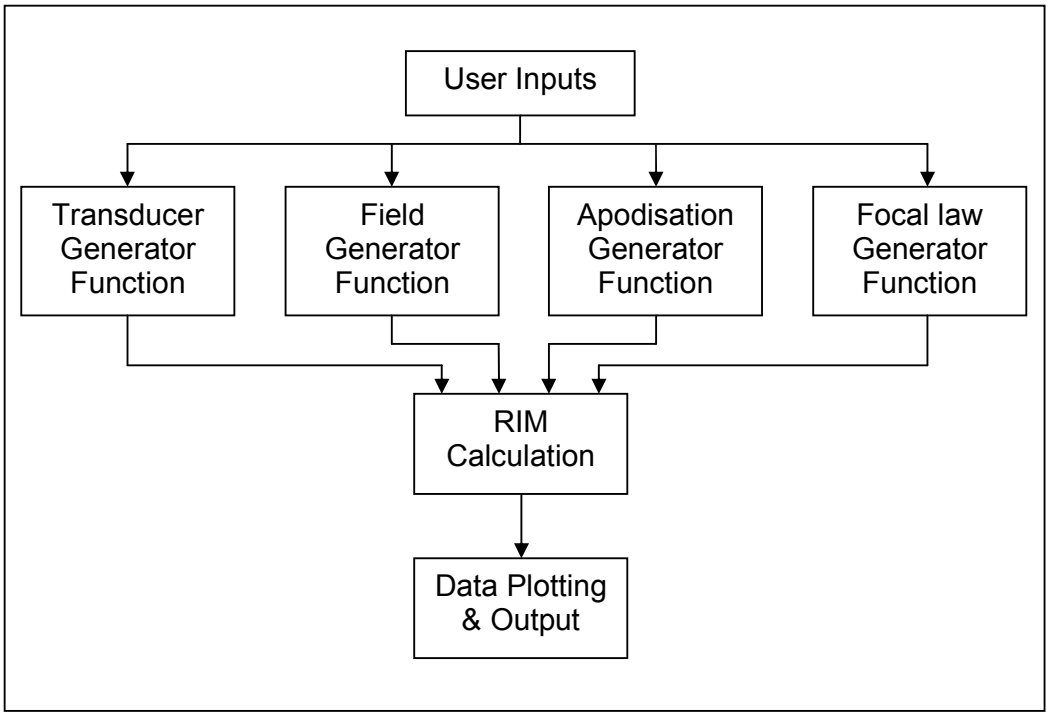

Figure 4-1 Block diagram of modelling package, showing modular elements.

The discrete Rayleigh integral is at the core of the calculation. While largely unchanged through most of the models, the code was adapted to better suit certain situations. The following options were available:

2D: Spreading was changed from the default 3 dimensional spherical setting to cylindrical for 2D calculations. This assumes that the unmodelled dimension is infinite.

This code executes more quickly due to its lower dimensionality.

Vectorised calculation: Calculations are performed as vectors, which speeds calculation. This is more memory intensive than the looped model, so is better suited to small problems.

Looped calculation: Calculations are performed in a loop, which takes longer than a vectorised calculation. However, less memory is used, so this mode is best suited to large calculations.

Multi frequency: Version for analysing pulsed excitation, described fully in Section 4.2.2.

The transducer generator function is used to create a set of points representing the transducer surface. These points are treated as omnidirectional point sources by the DRI. Points can form simple lines, grids, more complex curved surfaces, or abstract shapes. All points are considered to be of the same size. Examples of transducer geometries include:

- 2D and 3D representations of linear arrays
- 2D arrays
- Curved arrays
- Faceted arrays.

Examples of these transducer geometries are shown in Figure 4-2.

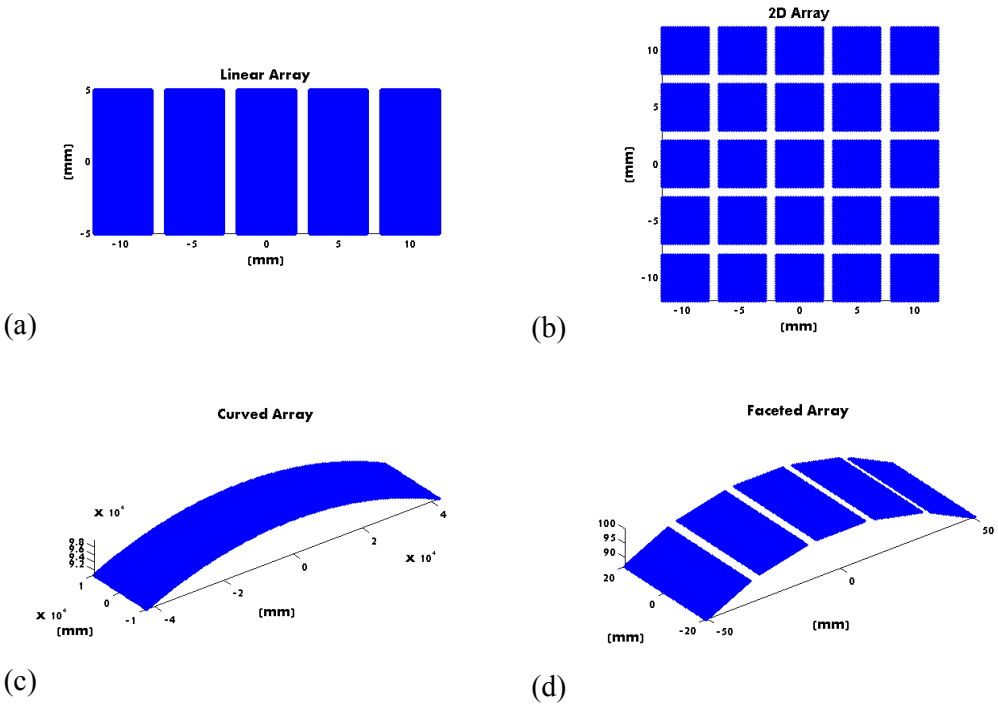

Figure 4-2 **Examples of transducer geometries that can be generated in the modelling package, (a) linear array, (b) 2D array, (c) curved array and (d) faceted array.**

Similarly, it is desirable to simulate different cross sections of the field which these transducer geometries produce. The field generator function creates observation points where the pressure of the transducer is calculated. Far field observation points are used for sonar devices, as this is the region in which these devices usually operate. For NDE devices a cross sectional slice is often used to simulate near field focusing. Supported geometries are:

- Far field arc
- Far field hemispherical
- Cross sectional 2D surface

- 3 dimensional volume

- Arbitrary surface.

Examples of these field geometries are shown in Figure 4-3.

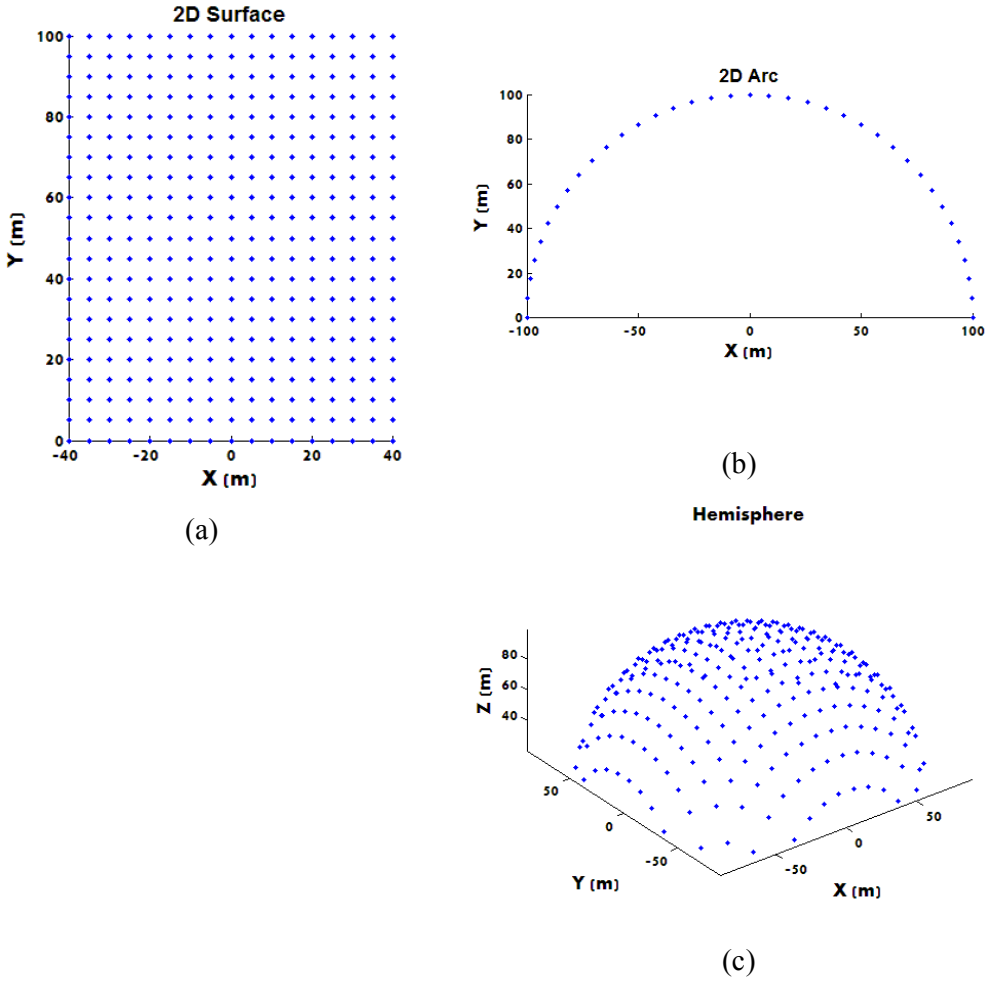

Figure 4-3 **Examples of field geometries that can be generated in the modelling package, (a) 2D surface, (b) 2D far field arc, (c) 3D far field hemisphere.**

Many arrays use apodisation functions in order to reduce the sidelobe levels in their beams. Apodisation functions can be applied either mechanically, by changing the shape and size of the array elements, or electrically, by changing the amplitude of the excitation signal to each element. The apodisation generator function can model both of these scenarios, by adjusting the vibrational velocity of each point on the arrays surface. This can be done in groups to simulate electrical apodisation of array elements, or to points within an element to change the element's shape. Examples of apodisation functions are shown in Figure 4-4. The effects of apodisation on array performance were described in detail in Chapter 2.

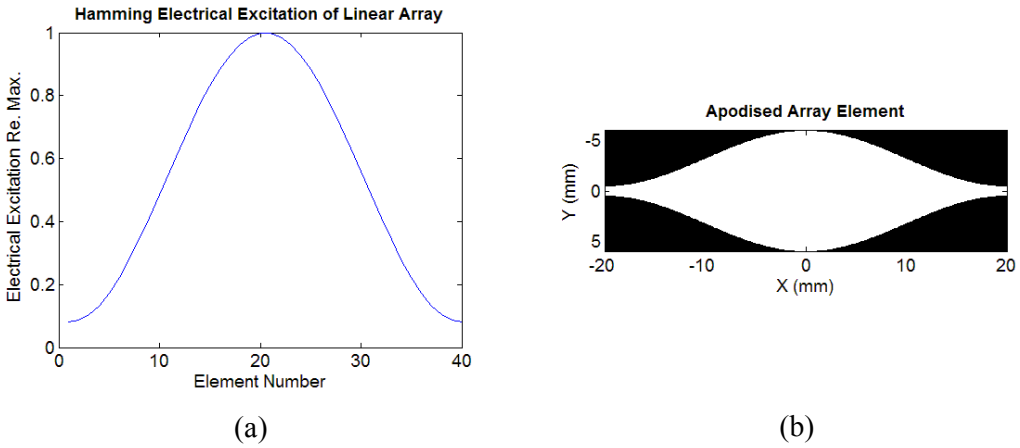

(a) (b)

Figure 4-4 **Examples of apodisation functions which can be generated within the modelling package, (a) Hamming function electrically applied across all array elements and (b) Hamming shaped electrode applied to a single array element.**

It is essential that the software is capable of simulating a wide range of focal algorithms, as various techniques are employed across the sonar, NDE and biomedical fields. As such, the focal algorithm block can accommodate any set of customised delay laws. Focal laws were discussed in detail in Chapter 2. For sonar simulations a simple far field steering law was used, while for NDE simulations the array was focused in the near field.

The modular approach is well suited to modification, and this has allowed further development of the models. Two models with graphical user interfaces (GUIs) have been developed, so that users who are unfamiliar with the Matlab© environment can also use them as design tools. These models are described in section 4.2.5.

An example of the calculated directivity of a single element device is shown in Figure 4-5. It shows the mainlobe, and the sidelobes which are present in the far field CW simulation.

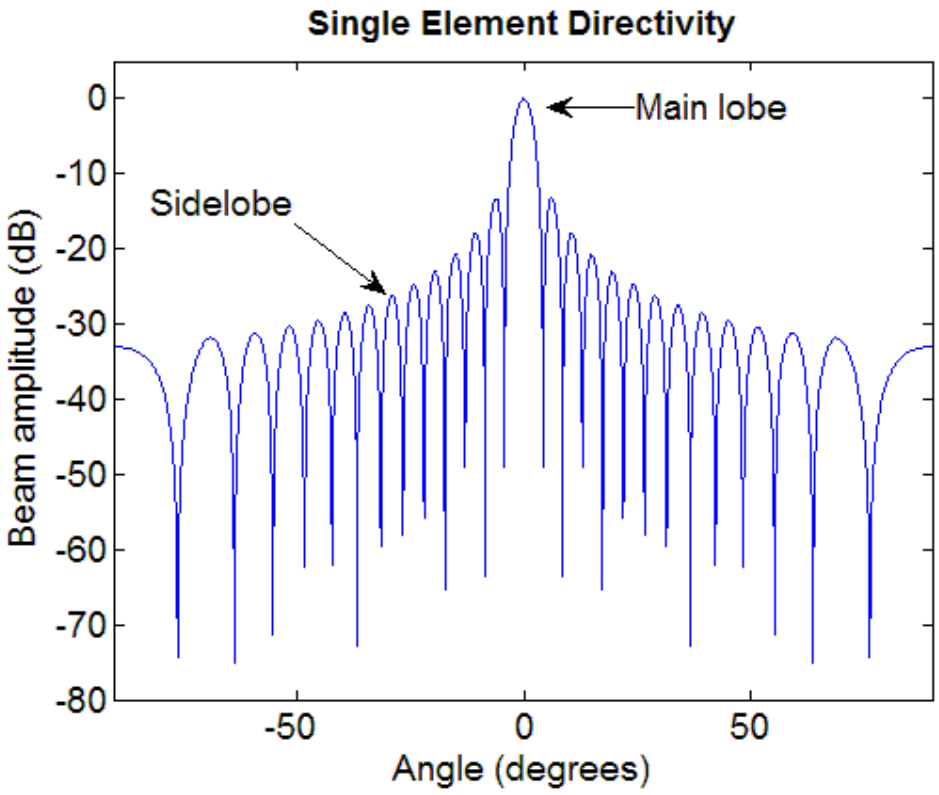

Figure 4-5 **Directivity of a single element device, showing mainlobe and sidelobes. Amplitude scale is in decibels relative to mainlobe height.**

Figure 4-6 shows a 2D cross sectional field of the same device. This illustrates the near field interference pattern, and the last maximum, which is generally regarded as the boundary between the near and far fields.

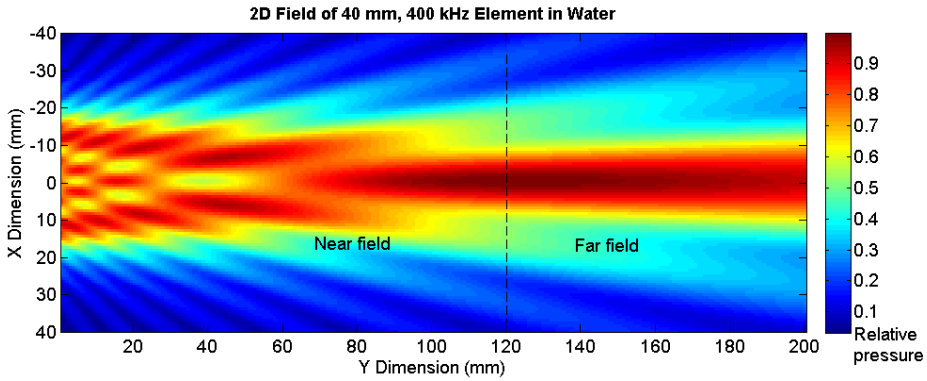

Figure 4-6 **2D cross sectional field of a 400 kHz, 40 mm wide single element device, showing both near and far field regions. Scale is linear relative to maximum pressure.**

4.2.2 Pulsed beam model

Although in basic form the DRI is a very flexible tool for simulating acoustic fields, it is limited to simulating devices under CW excitation. This is acceptable for modelling sonar devices, which are usually driven with tone bursts of 10 or more cycles. However, in NDE and biomedical applications transducers are generally driven with much shorter pulses, and high bandwidth devices can emit fewer than 3 cycles. The acoustic field produced by these devices under pulsed excitation differs significantly from narrowband devices, as energy is spread in the temporal dimension, limiting the formation of sidelobes [8].

While there are other models, such as the spatial impulse response method (see section 4.1.3), which are better suited to modelling pulsed devices, it is desirable to build a pulsed modelling capability into the modelling framework which has already

been developed. Therefore, it was decided to use inverse Fourier techniques to adapt the DRI model to model wideband excitation. Although this is a computationally intensive method, it was not required to be incorporated into cost functions and called many thousands of times. It was used as a final assessment of array performance under more realistic excitation conditions. The algorithm developed during this project has the following features:

- It is integrated within the modular CW modelling framework, and is therefore very flexible.

- It uses an analytical linear systems transducer model [36] to generate the transducer impulse response. This makes it simple to generate realistic transducer pulse shapes, rather than working with simple tone bursts and impulses. The linear systems model considers ceramic and composite transducer structures, backing layers, acoustic matching layers, and electrical loading.

- It can simulate wave propagation, and display the results as a series of time frames, or an animation.

- By taking the maximum pressure reached at each field point as the waves propagate, a plot of the maximum acoustic field pressure can be created. This is useful for comparison to CW pressure plots.

The principle of the model is described in the block diagram shown in Figure 4-7, which shows how an individual time frame is generated. The user specifies an excitation signal in the time domain. This is Fourier transformed, then multiplied by the impulse response of the transducer, which is obtained from the analytical transducer model. At this point the spectrum can be thresholded, by discarding frequencies where the signal is below a predetermined level. This level is set low enough to provide accurate reconstruction of the wave, with -40 dB being the default

setting. This approach greatly reduces computation time. At frequencies with non-zero signal level the CW beam profile of the transducer is calculated using the DRI method. This creates a series of complex beams, which are first phase shifted, then summed together, to create a beam profile at a specific time instance. The phase shift applied to each frequency is calculated using the time reference of the frame that is being calculated, as shown in Equation 4-4.

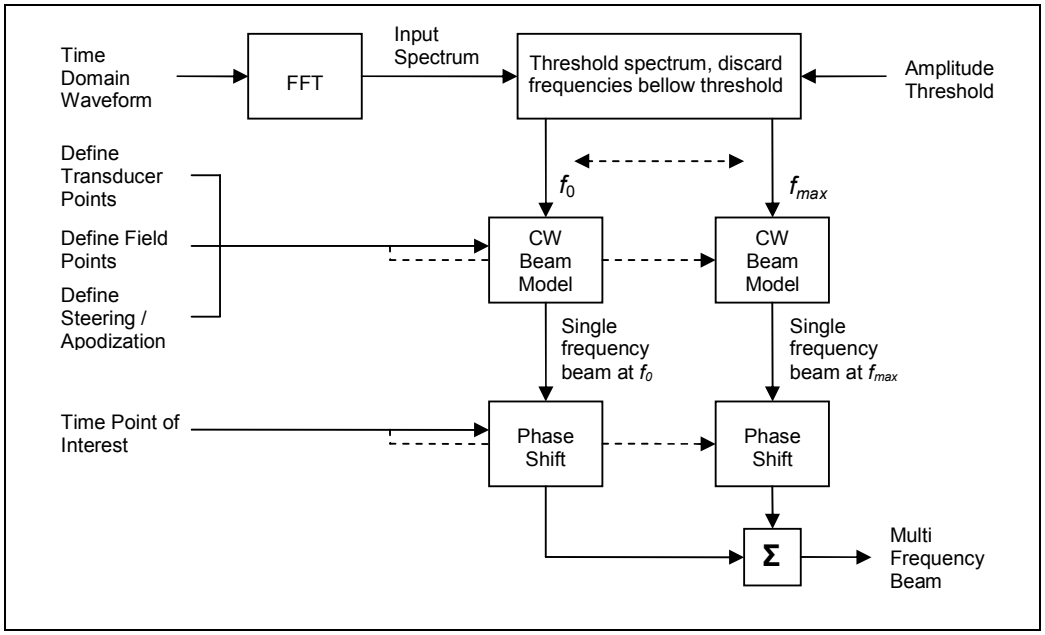

Figure 4-7 Block diagram of the pulsed beam model.

$$\varphi_f(f) = 2\pi f t_s \qquad \textbf{(4-4)}$$

where φ_f is the phase shift for the frequency component f, and t_s is the time shift of the modelled frame with reference to the beginning of the excitation signal.

Mathematically, this method is very similar to an inverse Fourier transform, and can be expressed in the following manner:

$$P_w(g) = \frac{1}{N_f} \sum_f e^{-j\varphi f} P_{CW}(f, g) \qquad \textbf{(4-5)}$$

where P_w is the pressure at a point p in the field under pulsed excitation, P_{CW} is the CW excitation at frequency f and point g, and N_f is the number of frequency points in the calculation.

It is important that a two sided spectrum be used throughout the calculation to ensure a real pressure field is output. However a simplification can be made, by simulating the CW fields at frequencies up to half of the Nyquist frequency, then summing them with their complex conjugates. This approach avoids duplication of data at the computationally intensive field simulation step, but yields the same result as the standard method.

Certain steps must be taken to avoid artefacts occurring in the modelled output. The calculation is cyclical, with a periodicity equal to the length of the input excitation signal, t_d. This means that when the time shift is equal to the signal duration, the pressure wave returns to the origin in the model. This also means that the wave's position at $t_s = 0$ is the same as its position at $t_d = 0$. The following steps are taken to avoid these issues:

- The excitation is padded with zeros so that its duration is longer than the time taken for the wave to fully traverse the field, ensuring that the time shift will never equal the signal duration.

- The impulse response generated using the transducer model is windowed with a Hamming function to avoid discontinuities in its spectrum at half the sampling frequency. This has the additional effect of smoothing the transmitted pulse, by removing the odd harmonics generated by the transducer.

Figure 4-8 shows three time frames from a single element device, along with a plot of the maximum pressure at each field point. Both plane and edge waves can be identified in the images. The plane wave is the main pulse that emanates from the centre of the device, travelling directly away from the transducer. Edge waves are generated by the discontinuities at the edge of the device, and spread as cylindrical waves. There is no near field interference pattern, due to the short duration of the pulse.

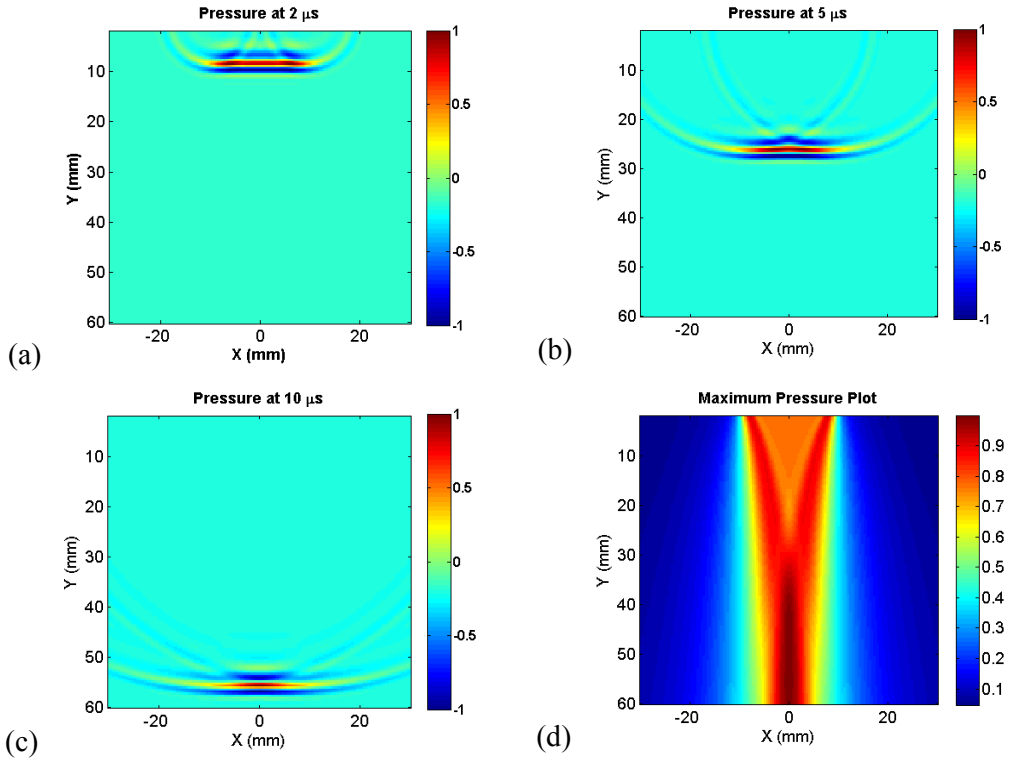

Figure 4-8 **2D Model of the pulsed excitation of a single element device showing three time frames. The device is 20 mm wide, operating at 1.5 MHz, with a 60% fractional bandwidth, and excited with a single cycle sine wave. The velocity in the field is 5,900 m/s, approximately that of steel. Colour scales show pressure relative to the maximum, (a) 2.5 μs, (b) 5 μs, (c) 10 μs and (d) maximum pressure**

4.2.3 Fields in multiple media

The Huygens-Fresnel principle [37] states that every point of a wave front may be considered the source of secondary wavelets, which spread out in all directions at the wave propagation speed. By utilising this principle the DRI can be used to simulate the refraction that occurs when a wave propagates across the boundary of two media with different wave propagation speeds. This approach is useful for calculating the fields of transducers mounted on angled wedges, or used in a water immersion inspection of a metallic component.

The field produced by the transducer in the first medium is calculated along the boundary between the media. These boundary points are then considered as sources, which re-emit the wave into the second medium. A grid of field points is created in this medium, and the pressure at these points is calculated (Figure 4-9).

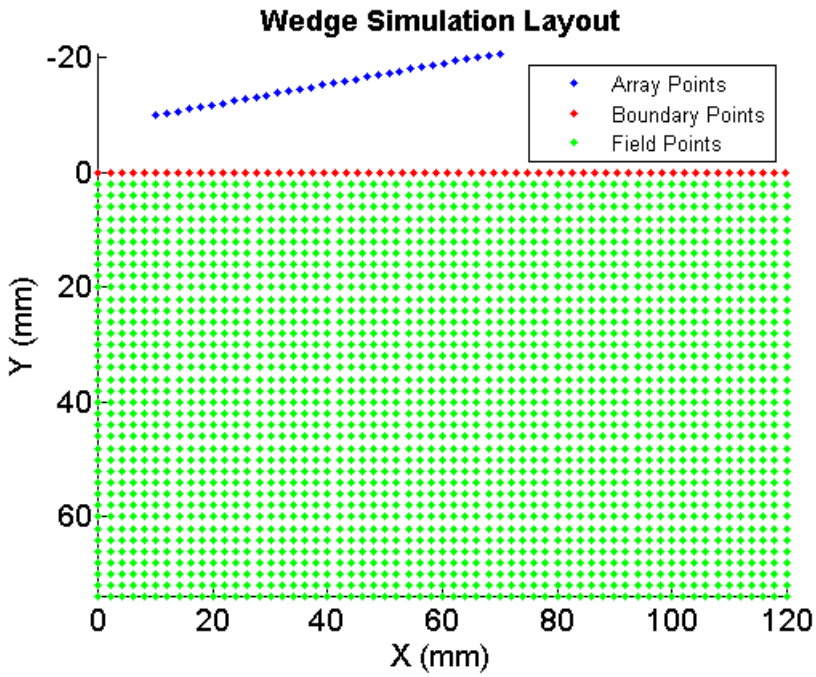

Figure 4-9 **Diagram showing transducer array points, boundary points, and field points for simulation of a transducer mounted on a wedge, and projecting sound into a second medium.**

It should be noted that for acoustic wave propagation problems this method makes some approximations. When a boundary between two solid materials is considered an incoming longitudinal wave will experience mode conversion, with some of its energy being transmitted into the medium as a shear wave. This means that for longitudinal waves approaching the boundary at oblique angles, only a fraction of the transmitted energy remains in the longitudinal mode. Formulaic approximations exist for the plane wave transmission coefficients for various wave mode combinations [4]. However, these expressions use the angle of incidence of a wave to calculate the amplitudes and angles of the longitudinal and shear components generated in the destination material. The DRI model does not preserve this angular information, since contributions from all angles are summed at the boundary, and this precludes the use of these transmission coefficients. For these reasons, results produced using this approach should be treated with care to ensure that unwanted modes are not generated, and that the amplitude of the beam is not overestimated.

An example of the calculated pressure field of a phased array mounted in a water wedge, transmitting into steel is shown in Figure 4-10. The beam is focussed at 45°, and a range of 40 mm, the simulation indicates that while this is indeed the area with the highest field intensity, there are areas in both the near and far field which have intensities greater than -6 dB.

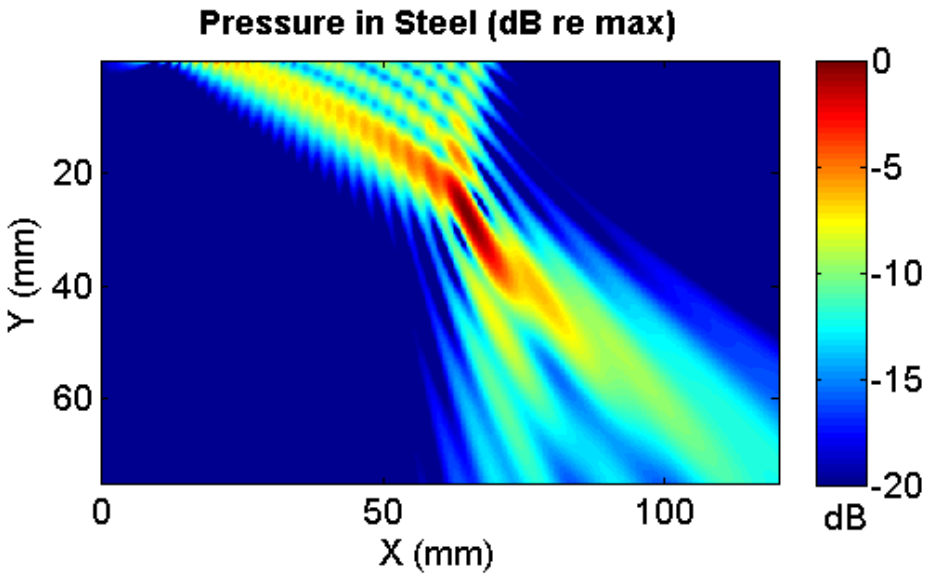

Figure 4-10 **Acoustic pressure field of 1.5 MHz, 32 element phased array mounted in a water wedge, transmitting into steel. The beam has a 45° angle in the steel, and is focussed to a range of 40 mm from its index point.**

4.2.4 Element directivity

In the standard RIM, array elements consist of a collection of omni-directional point sources. This is convenient for small models, but for modelling large 2D arrays it is very computationally intensive. Therefore, it is desirable to represent the element as a single point, with a directionality which mimics that of a real array element. For array elements consisting of simple shapes this can be achieved using analytical models for far field directivity. These are very quick to evaluate, and can be integrated into the existing DRI model. For additional speed, a lookup table can be created with the directivity coefficients.

For the case of a linear array, elements can be approximated as continuous line sources, with a width a in wavelengths. The far field radiation pattern, or directivity, across an arc with a constant radius can be evaluated using Equation 4-6.

$$P_L(\theta) = \frac{\sin(\pi a \sin(\theta))}{\pi a \sin(\theta)} \quad \textbf{(4-6)}$$

where P_L is the relative pressure in the far field at an angle θ relative to the normal, and a is the diameter of the element in wavelengths.

This can be extended to consider a rectangular element in a 2D array, with dimensions a_x by a_y. The far field radiation pattern, P_R, over a hemisphere defined in spherical coordinates is given by [38]:

$$P_R(\theta,\varphi) = \frac{\sin(\pi a_x \sin(\theta)\cos(\varphi))}{\pi a_x \sin(\theta)\cos(\varphi)} \frac{\sin(\pi a_y \sin(\theta)\sin(\varphi))}{\pi a_y \sin(\theta)\sin(\varphi)} \quad \textbf{(4-7)}$$

where φ, is the rotational angle around the array normal, and all other symbols are as previously defined.

The far field radiation pattern produced by a circular piston in an infinite baffle can be calculated with the following analytical expression [39].

$$P_C(\theta) = \frac{2J_1(\pi a \sin(\theta))}{\pi a \sin(\theta)} \quad \textbf{(4-8)}$$

where P_C is the relative pressure in the far field at an angle θ relative to the normal, a is the diameter of the piston in wavelengths, and J_1 is a first order Bessel function of the first kind.

In order to implement this method a vector between the field point and the array element point is calculated. The angle between this vector and the array element normal is then calculated, and used as an input to the analytical directivity

calculation. The calculated directivity is then used to scale the pressure contribution to the field point from that element.

For this method to be accurate none of the calculated field points should lie in the near field of the array elements, since the far field approximation is not valid there. This does not significantly limit its use, since for most applications array elements are less than a wavelength in width, so have a negligible near field length.

As with the standard DRI, this method assumes each element moves in a uniform piston-like motion, and is surrounded by an infinite rigid baffle. For elements mounted in a soft, lossy filler this is a poor approximation. These fillers are often employed to reduce mechanical cross-talk between array elements. Alternatively, the exterior elements in the array may vibrate less than the interior element, due to clamping from the surrounding passive material. In these situations the following approach must be taken:

- A displacement function should be selected which approximates the element's surface displacement as closely as possible. A Hamming function provides a suitable approximation when the element is clamped at the edges, and cannot vibrate freely. Alternatively, for more complex scenarios, displacement data from a finite element model, or experimental measurements can be used. This data should cover both the element, and the surrounding area of the transducer which is being displaced.

- The far field directivity of this displacement function is then calculated using the DRI. This can be done using a 2D calculation, which is very quick to execute.

- The actual far field directivity of the 2D surface is then calculated by multiplying the displacement function's directivity by the directivity of the analytical circular piston, shown in Equation 4-8.

This process exploits the equivalency between the RIM and the Fourier transform, by using the convolution theorem, where multiplication in the frequency domain is equivalent to convolution in the time domain. This process is summarised in Equation 4-9.

$$P_E(\theta) = P_C(\theta)\ P_S(\theta) \qquad \textbf{(4-9)}$$

where P_E is the directivity of the element, P_C is the directivity of a circular piston, P_S is the directivity of the surface function, and θ is the angle from the transducer normal to the point in the field.

Using this method the fields of transducer arrays with many hundreds of elements can be simulated in under a minute on a desktop PC.

4.2.5 Graphical user interface

A pair of models with Graphical User Interfaces (GUIs) were developed, to make the RIM model more accessible to the rest of Alba's design team. These models were written in Matlab©, and use the functions from the basic RIM to perform calculations. User inputs were captured using a simple dialogue box, and displayed in graphical plots. There are also options to save the modelled data as a text, or image file.

Both models calculate a CW pressure field. The first model considers single element devices, and has the following features:

- Apodisation can be applied by loading in a greyscale bitmap image with relative velocity values between 0 and 255.

- A 3D hemispherical directivity is calculated and displayed in a surface plot. A plane slice through the centre of the device can be selected, and displayed in a separate 2D plot.

- The 2D plot can also display default 0° and 90° slices.

- Data can be saved as an image of the 3D hemispherical plot, or text files containing the 2D slices.

Images of the single element model's interface and its outputs can be seen in Figure 4-11.

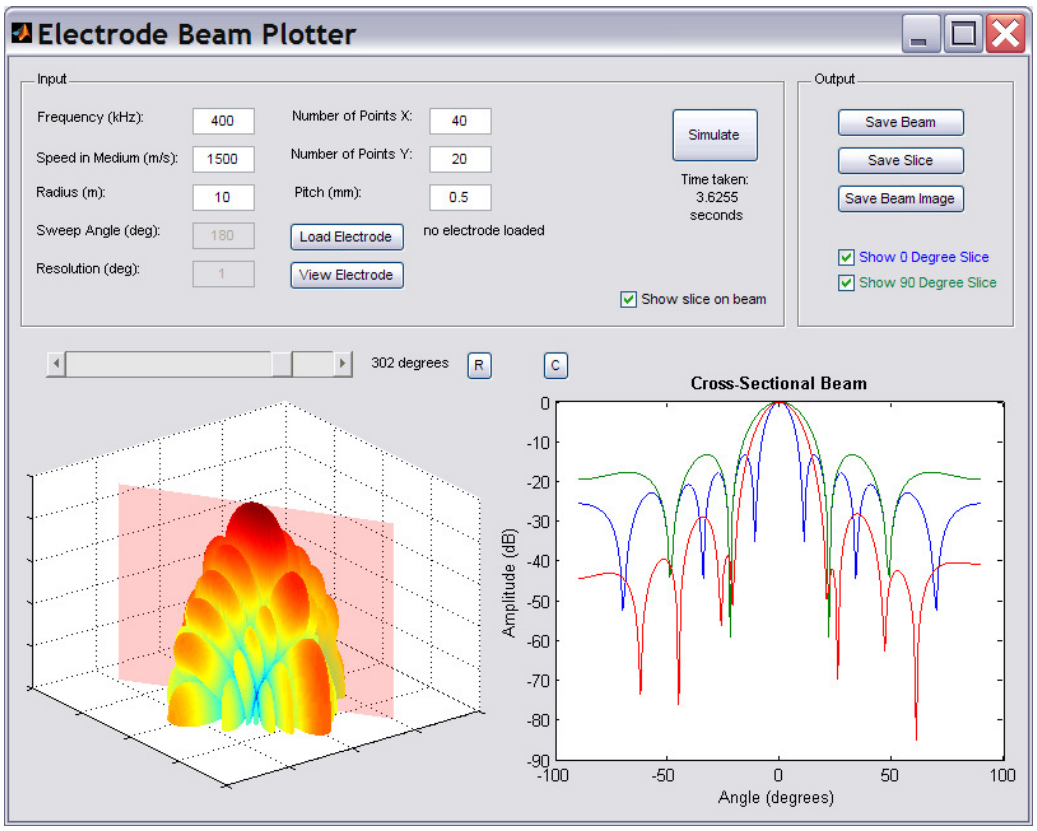

Figure 4-11 **Screen snapshot of the single element model GUI. Inputs are captured in the panel at the top left, while the outputs are selected at the top right. A hemispherical beam pattern is shown at the bottom left, and cross sections of this can be displayed at the bottom right.**

A second model was created to simulate planar, curved and faceted linear arrays. This model has the following features:

- The user can select between planar, curved and faceted arrays, and define the array geometry using simple inputs such as inter element pitch, radius of curvature, and array arc length.

- A schematic of the array design is displayed to the user, which can be rotated and scaled for easy viewing.

- Each element in the array can be given its own apodisation function, using a bitmap image. This allows not only mechanical apodisation of individual elements to be modelled, but also electronic apodisation across the length of the array. This is very useful for curved and faceted arrays, which often use shading functions to reduce mainlobe ripple.

- The directivity of the array is calculated in an arc, usually in the far field. This is displayed in a graphical plot, and can be output as a text file for export to other programs.

Images of the array model's interface and its outputs can be seen in Figure 4-12.

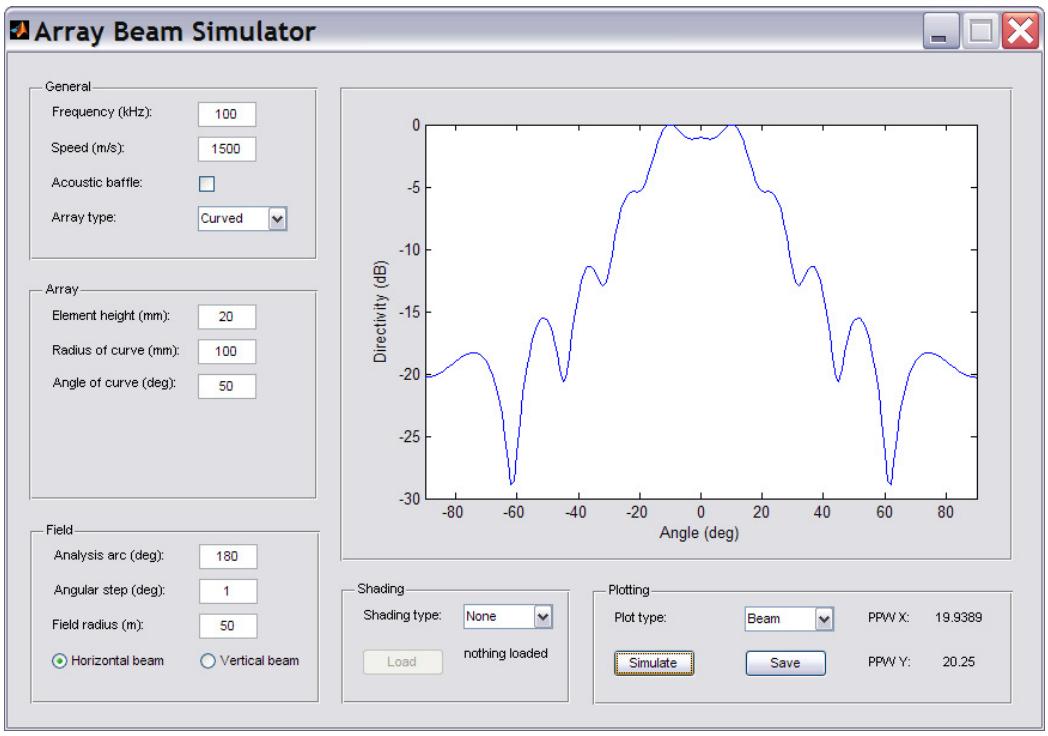

Figure 4-12 **Array model GUI. The panels on the left allow a variety of array geometries to be input. The plot on the right shows the far field directivity of a curved array, displaying some mainlobe ripple. Shading, plotting and outputs are controlled on the bottom panels. An image of the array, or the shading function can also be displayed.**

4.2.6 Comparison with experimental measurements

The models described in the previous sections have been used extensively in Alba to accelerate transducer development. By providing the capability to accurately model the far field directivity of sonar transducers, the number of prototypes required to arrive at a successful design has been reduced. The models have been particularly useful in the design of curved devices, which have more complicated beam patterns than planar arrays.

The field modelling software is most powerful when it can be used to predict the performance of a proposed array design. When doing this it is commonly assumed that the transducer will vibrate in a piston-like manner, as the exact surface displacement is unknown. While this is an approximation it has been found that these simple models are effective at predicting key acoustic attributes, such as beam width, worst case sidelobe heights, and mainlobe ripple. This is demonstrated in the following comparisons between simulated and experimental results.

In Figure 4-13 a curved sonar projector array, with two planes of directivity illustrated. The CW directivity of this array was simulated through the plane of the curve, which is often referred to as the horizontal directivity, and is shown in Figure 4-14. The beam structure around the mainlobe and first sidelobes show very good agreement with experiment. Table 4-1 shows the -3 dB beamwidths and 1st sidelobe levels, which are very similar. The noise level in the experimental measurement is approximately -35 dB.

Figure 4-15 shows the same data, but this time two array elements have been excited, extending the length of the curve. Once again, the experimental data shows good correlation with the simulation, especially around the mainlobe. Beam width and mainlobe ripple is shown in Table 4-1.

Finally, directivity in the plane perpendicular to the curve of the array, also known as vertical directivity, is shown in Figure 4-16. The agreement is good, and the data is presented in Table 4-1. It should be noted that the experimental data for this array is asymmetric, with higher sidelobe levels at 60 ° than at – 60 °. This is due to the presence of additional array elements on the positive side of the array, which act as a soft baffle. The other side is bordered by the housing, which acts as a rigid baffle, and does not interfere with device operation.

In general the agreement between these simple models and experimental measurements is good around the mainlobe. This is the most important and tightly controlled region of the beam, which makes the models a useful design tool. At wide

angles the agreement is poorer, since these areas are more sensitive to ripple in the surface displacement, and the material surrounding the array. To better consider the beam pattern at wide angles, measured or modelled surface displacements could be used. However, sidelobes at these wide angles are lower than peak sidelobes levels, and designers can generally ignore them.

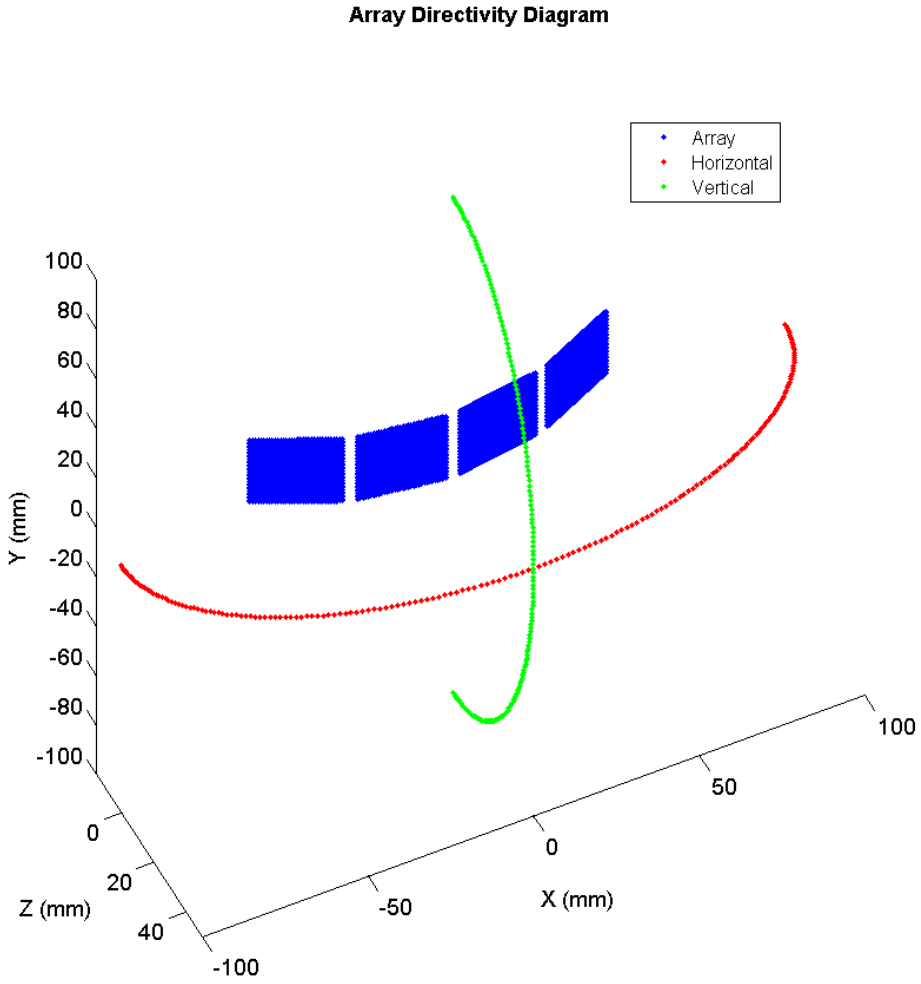

Figure 4-13 **Diagram showing a curved array (blue), and illustrating the arcs of horizontal (red) and vertical (green) directivity.**

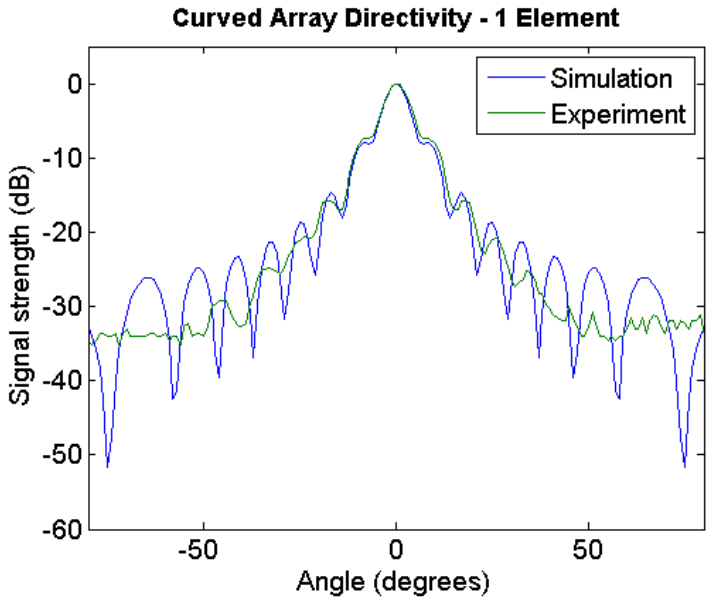

Figure 4-14 **Simulated and measured horizontal directivity of a single element from a curved sonar projector.**

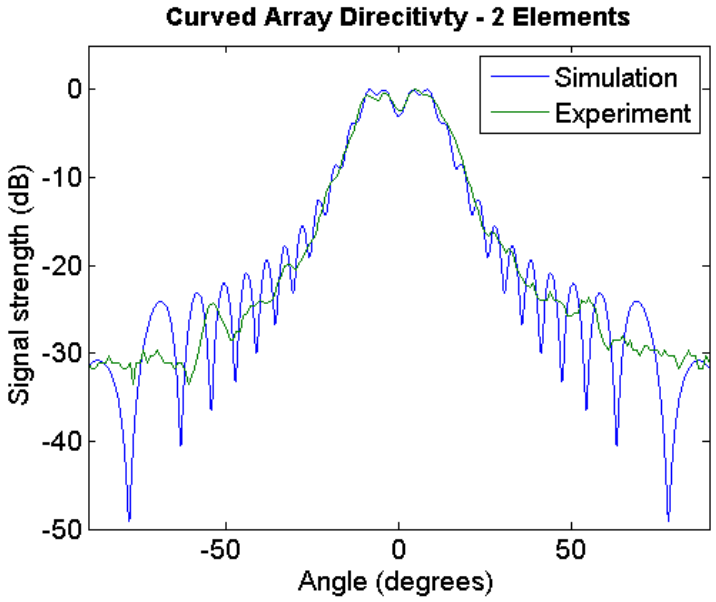

Figure 4-15 **Simulated and measured horizontal directivity of two elements from a curved sonar projector.**

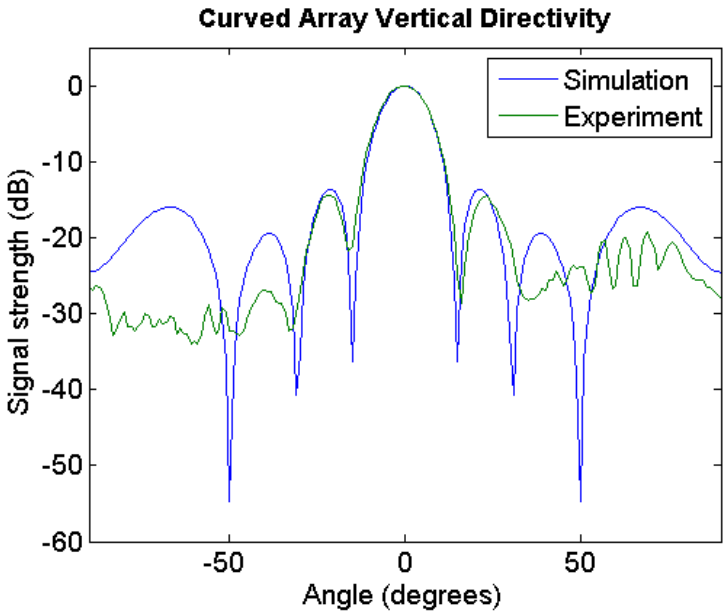

Figure 4-16 **Simulated and measured vertical directivity of a curved sonar projector.**

Data	-3 dB Beam Width	1st Sidelobe Height	Mainlobe Ripple
1 Element Horizontal Simulation	6.6 °	-7.45 dB	-
1 Element Horizontal Experiment	6.9 °	-7.98 dB	-
2 Element Horizontal Simulation	22.4 °	-	-3.0 dB
2 Element Horizontal Experiment	24.5 °	-	-2.45 dB
Vertical Simulation	12.8	-13.66	-
Vertical Experiment	13.7	-14.39	-

Table 4-1 **Comparison of key performance criteria between simulations and measurements.**

4.3 Summary of Acoustic Field Modelling

The acoustic field modelling software developed as part of this thesis has been described. It has been shown that the models consider a wide range of transducer designs, observation fields, and excitation functions. Finally the excellent correlation between simulated and experimental results was shown.

The user interface checks user inputs are valid, and in the case that they are not, returns them to a default value. This allows the software to be used more reliably by Alba's acoustic design engineers. In order to make the software more robust, and aid training, further documentation is required. The required improvements are described in detail in Chapter 7.

This software is now an integral part of Alba's transducer design process. It also provides a foundation for the investigation of novel sparse array designs. The following chapter uses this model to analyse the performance of novel spiral arrays, in order to arrive at a design process which minimises peak sidelobe height.

Chapter 5

2D Spiral Array Design Technique

A major barrier to the adoption of spiral 2D arrays is the lack of standard design techniques, and an understanding of the performance that can be achieved.

This section describes a novel design technique which has been developed for 2D spiral arrays. It first discusses the design variables, and the analytical methods used to arrive at an optimum design. The performance of the resulting spiral designs is then characterised, and compared to that of more standard array designs. Finally, the practicality of the spiral designs is discussed, along with an analysis of their most suitable applications.

5.1 Spiral Functions

While many types of spiral functions can be described mathematically, two appear to possess the most suitable properties for 2D array design. These are the logarithmic spiral, and the Archimedean spiral, which are described in the following sections. In addition to the points listed in Chapter 1, both have arms which rotate around a single point, and can be scaled to provide an approximately uniform distribution of elements over a 2D aperture. Both are continuous functions, and therefore must be sampled according to some strategy to create a practical array of discrete elements forming an ultrasonic array design.

It will be shown through further analysis that the logarithmic spiral has more advantageous properties for array design, particularly its aperiodic spacing between successive arms. The logarithmic spiral is therefore chosen as the main subject of this investigation into sparse 2D array design.

5.1.1 Archimedes spiral

The Archimedes spiral is named after the Greek mathematician Archimedes, who described it in his book *On Spirals* [40]. Its defining characteristic is that a point moving along the spiral away from the origin moves at a both a constant angular and radial velocity. It is described by the following equation:

$$r = a + b\gamma \qquad \textbf{(5-1)}$$

where r and γ are the radius and angle of the array elements. a rotates the spiral around the origin, and b controls the pitch between successive arms. A consequence of the constant radial and angular velocities of the spiral is that the pitch between arms is periodic, and equal to $2\pi b$. An example of an Archimedes spiral is shown in Figure 5-1.

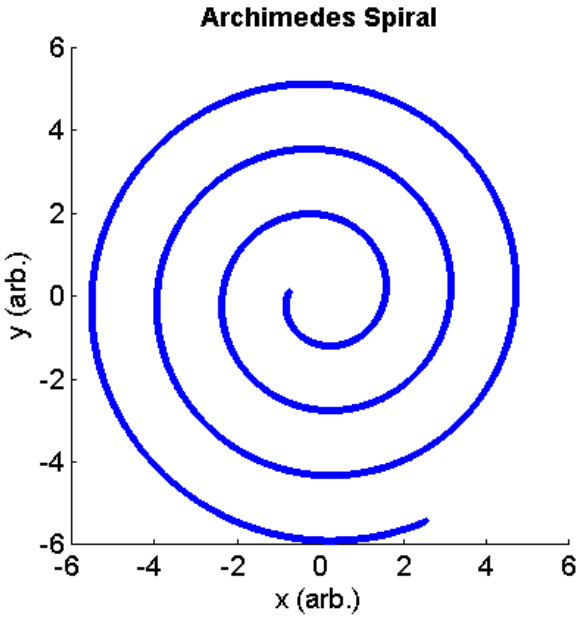

Figure 5-1 **An Archimedes spiral with *b* of 0.25. The periodic spacing created between successive turns can be clearly seen.**

It is demonstrated in this chapter that Archimedes spirals produce relatively poor sparse array designs. The main reason for this is the periodic spacing between successive arms, which results in associated grating lobes. The poor simulated results obtained from Archimedes spirals indicate that not all spirals create good arrays, and emphasises the advantages of the aperiodic spacing of log spirals arms.

5.1.2 Logarithmic spiral

Logarithmic spirals, or log spirals, are found in many natural structures, including the shells of molluscs, the arms of a spiral galaxy [41], and the approach of a hawk to its prey [42]. The log spiral has a number of unique properties, which have been found useful during the course of the work for constructing 2D arrays. An example of a single-armed log spiral is shown in Figure 5-2.

It is believed that the scaling property of the log spiral is what makes it so common in the natural world; large structures can be constructed in a log spiral form by simply adding scaled sections of the original [43].

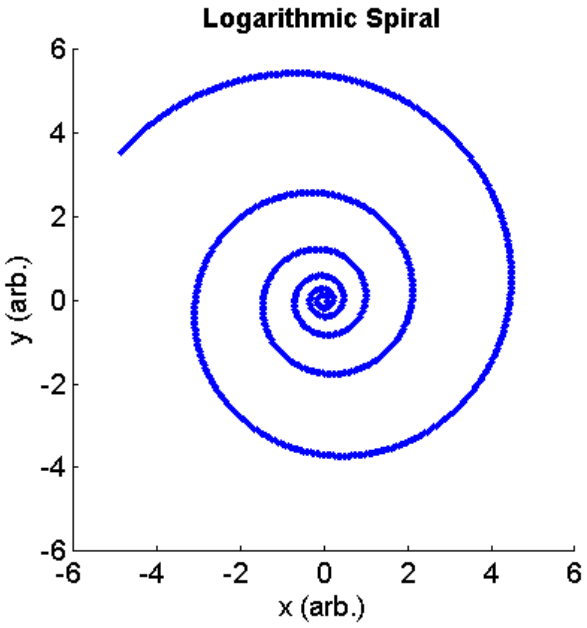

Figure 5-2 **A single-armed logarithmic spiral. The spacing between successive turns follows a geometric series.**

Some of the unique properties of the log spiral are:

- The distance between successive turns of a log spiral arm follow a geometric progression. This creates an aperiodic structure, since the gap between successive arms is constantly growing. It will be shown that this property helps to avoid the formation of grating lobes.

- The angle, φ, between the tangent and a line to the radius is the same for all points on the arm. This is one of the defining properties of the log spiral. It is shown to be useful in spreading sidelobe energy evenly, creating a flat sidelobe floor.

- Log spirals are self-congruent under all similarity transformations, meaning that they can be scaled and rotated to yield the same shape. As such, log spirals are found in fractal structures such as the Mandelbrot set [44].

- The length from a point on a spiral arm to the origin is finite, even though the spiral circles the origin an infinite number of times along this path. The distance between two points on an arm is simple to calculate, making design of arrays with particular inter element spacing possible.

When expressed using polar coordinates, r and γ, a log spiral can be defined as:

$$r = ae^{b\gamma} \qquad \textbf{(5-2)}$$

Equation 5-2 can be rearranged for γ, showing the logarithmic relationship which gives the spiral its name.

$$\gamma = \frac{1}{b}\ln\left(\frac{r}{a}\right) \qquad \textbf{(5-3)}$$

The constants a and b control the shape of the spiral that is produced. a rotates the spiral around the origin, while b alters the angle of the spiral arm. δ, the angle between the tangent of the spiral arm and a line to its radius is given by Equation 5-4 below.

$$\delta = \tan^{-1}\left(\frac{1}{b}\right) \qquad \textbf{(5-4)}$$

The pitch, p, is the compliment of δ, and is given in Equation 5-5 below.

$$p = \frac{\pi}{2} - \delta \qquad \textbf{(5-5)}$$

As b approaches 0, δ tends to 90°, and the spiral becomes a circle. Conversely, as b approaches ∞, δ tends to 0°, and the spiral becomes a radial straight line.

Figure 5-3 shows a single armed log spiral with δ and p illustrated. As the only effect of a is to rotate the spiral around the axis it can be discounted as having no effect on the performance of 2D arrays. It should be noted however, that in multi-armed spirals successive arms are obtained by varying a. Multi-armed spirals are shown in Figure 5-4. Multi armed spirals may prove useful in array design by altering the distribution of the elements, and are more fully investigated in Section 5.5.

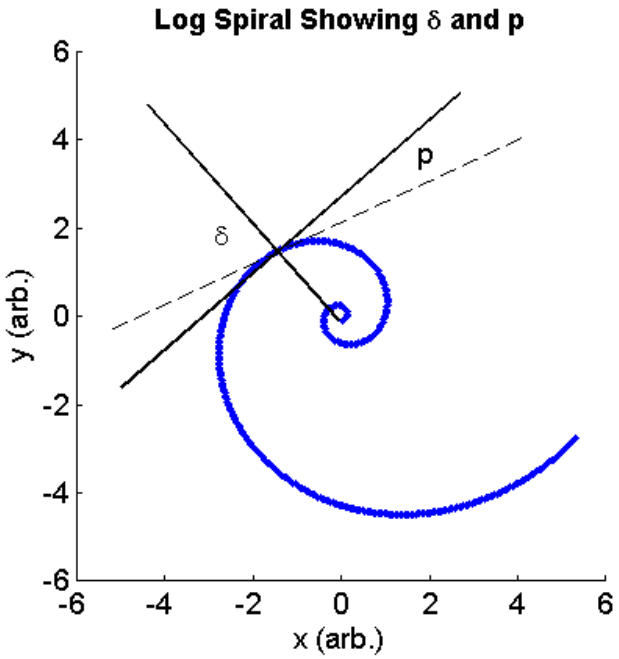

Figure 5-3 **Single armed log spiral with δ and pitch, p, illustrated.**

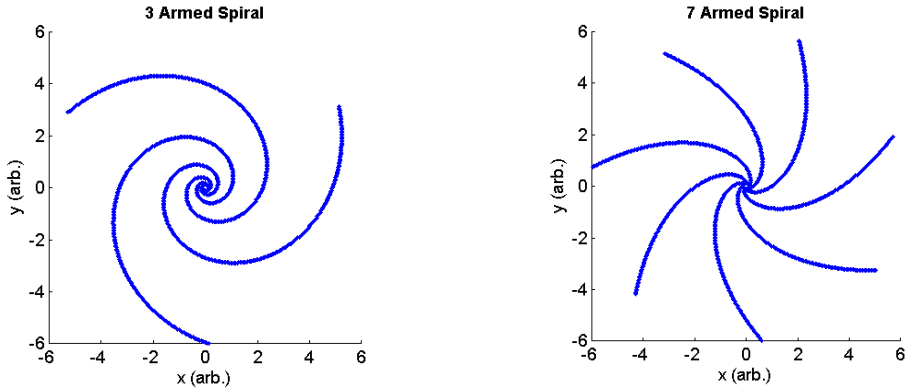

Figure 5-4 **Examples of multi-armed log spirals: (a) 3 armed log spiral with a 30° pitch; (b) 7 armed spiral with a 55° pitch.**

When designing spiral arrays it is useful to know the distance between two points, positioned on a spiral arm. This allows the spiral arm to be sampled at known intervals by positioning elements at discrete points along its length. The length of a log spiral arm, L, at an angle γ_1 is given by:

$$L(\gamma_1) = \frac{a\sqrt{1+b^2}}{b} e^{b\gamma_1} \qquad \textbf{(5-6)}$$

Equation 5-2 can be substituted into Equation 5-6 to create an expression for L at a radial point r_1.

$$L(r_1) = r_1 \frac{\sqrt{1+b^2}}{b} = \frac{r_1}{\cos(\delta)} \qquad \textbf{(5-7)}$$

To create a sampled design it is necessary to know the distance between two points r_1 and r_2 on the spiral. This distance is referred to as ΔL, and is calculated as follows, using Equation 5-7:

$$\Delta L = L(r_2) - L(r_1) = \frac{(r_2 - r_1)}{\cos(\delta)} \qquad \textbf{(5-8)}$$

Log spirals are the main focus of the work, and represent its main contribution to the field. A log spiral design process has been created to produce array designs with low sidelobes over a wide range of array densities. They are therefore presented here as an alternative to random, grid, and annular designs.

5.2 Design variables

When a designer sets out to create a 2D array there are a number of variables which must be considered. Consider an array which is designed to operate under CW excitation in the far field. At a functional acoustic level the following specifications are likely to be required:

- The -3 dB beam width of the mainlobe, θ_w.
- The maximum elevation steering angle, θ_{smax}, which will be applied.
- The number of elements in the array, N.
- The peak sidelobe level, S_p.

In this analysis it will be assumed that the first three specifications are known to the designer, and the object is to create an array with the lowest possible S_p. Other measures of array performance are discussed in Section 5.13, but since image contrast is generally limited by S_p, it is the main measure considered.

The designer must determine values for the following variables in order to minimise S_p for a log spiral array:

- The number of spiral arms, N_{arms}.
- The curvature of the spiral arms, defined by the pitch, p.
- The aperture of the array, D.
- The minimum radius of elements on each spiral arm, R_{min}.

- The spacing of the array elements, d.

- The aperture of the array elements, a.

The following sections focus on analysing how S_p varies with each of these variables. Design rules are then developed using a combination of empirical and analytical techniques. These are intended to aid the array designer, and remove the need for numerical simulation during the design process. Where possible, the effect of each variable is separated, to avoid the analysis of multivariate problems.

5.3 2D FFT for continuous analysis

An analysis tool is required to investigate how the performance of a log spiral is affected by the variables discussed in the previous section. The approach taken here is to separate the underlying spiral function from the sampling method used to create an array with discrete elements. Sampling of the spiral is then considered separately. For this approach to be effective,, an efficient method of analysing the performance of continuous spirals is required.

Chapter 4 describes the Discrete Rayleigh Integral (DRI) based modelling software that has been developed to characterise the acoustic field produced by arbitrary array designs. While this approach is well suited to accurately modelling these designs, it has a number of limitations for the analysis of log spiral functions:

- It takes approximately 4 seconds to model the CW far field directivity of a 128 element array, on a PC with a 2.6 MHz Core 2 processor, running Matlab 7.0. While this is adequate for the analysis of individual array designs, it is not well suited to analysing the design problem, where many thousands of designs may be simulated.

- It considers arrays with discrete elements, so cannot analyse a continuous spiral function.

- It considers many realistic attributes of the array such as element size, steering, and focussing. However, these details are not required for measuring basic performance characteristics of continuous spirals, so a simpler model is more suitable.

A simpler way to analyse the performance of a continuous spiral function is to use the Fourier Transform, in a similar way to the Angular Spectrum Method (described in Chapter 4). Consider the form of the Fourier transform, and the expression for the far field directivity of a linear array with periodically spaced elements [22]:

$$F(f) = \int_T f(t)\exp(-i2\pi ft)dt \qquad \textbf{(5-9)}$$

$$F(u) = \int_{\frac{D}{\lambda}} f\left(\frac{x}{\lambda}\right)\exp\left(-i2\pi\left(\frac{x}{\lambda}\right)u\right)d\left(\frac{x}{\lambda}\right) \qquad \textbf{(5-10)}$$

where $F(u)$ is evaluated over the range -1 to 1. By separating Equations 5-9 and 5-10 into their components a number of equivalencies can be established:

- $t \leftrightarrow \frac{x}{\lambda}$: Time is equivalent to the element position in wavelengths.

- $f \leftrightarrow u$: Frequency is equivalent to the reduced angular vector.

- $T \leftrightarrow \frac{D}{\lambda}$: The duration of the time domain signal is equivalent to the aperture of the array in wavelengths.

As calculations will be carried out numerically in Matlab, the Discrete Fourier Transform (DFT) is used, and evaluated using the Fast Fourier Transform (FFT) algorithm. This discrete representation requires that the spiral is sufficiently well sampled to avoid aliasing, and to properly resolve the spiral arms. However, the speed of the FFT ensures that sufficient sampling can be used while keeping run time to a minimum. The DFT of the discrete sequence $x[n]$, of length N, is:

$$X[k] = \sum_{n=0}^{N-1} x[n] \exp\left(\frac{-i2\pi kn}{N}\right) \qquad (5\text{-}11)$$

where $X[k]$ is the N point DFT, with k/N cycles per sample. The last point in the DFT therefore has ~1 cycle per sample. One sample per wavelength is equivalent to a θ of $\pi/2$, and is therefore corresponds to a u of 1. To obtain the portion of the beam between u = -1 to 0, a sampling period of $\lambda/2$ can be used. This gives frequencies up to u = 2, but due to the Nyquist sampling theorem [45] these are aliased, as they are above twice the sample frequency. The region from u = 1 to 2 is therefore equivalent to u = -1 to 0, and can be shifted, as shown in Figure 5-5.

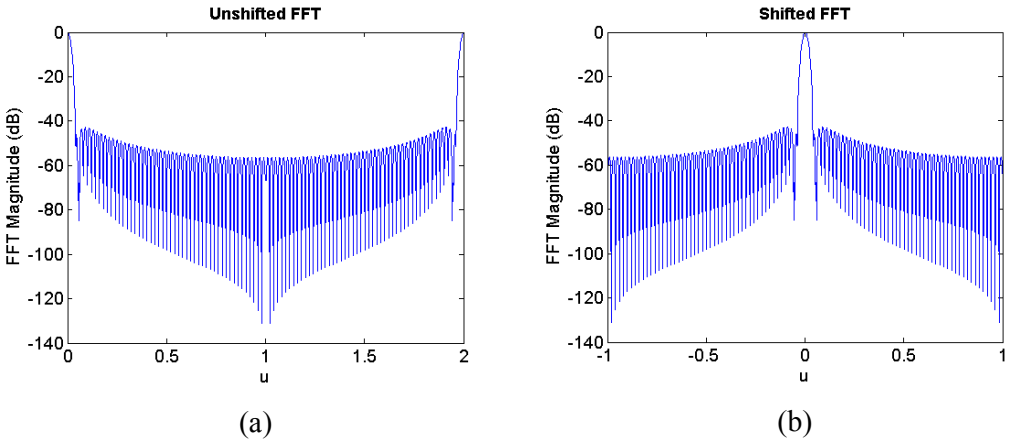

(a) (b)

Figure 5-5 **Performing an FFT on an array sampled at λ/2 produces an output which ranges between *u* = 0 to 2. By exploiting the aliasing in this beam pattern, the right half of the spectrum can be shifted down to the range *u* = -1 to 0, to give a beam pattern covering the full angular space in front of the transducer, (a) unshifted FFT, (b) shifted FFT.**

It is often attractive to use more than a λ/2 sampling period to provide a more accurate representation of a detailed array pattern. In this case only K samples of $X[k]$ are required, where K is the length of the aperture in wavelengths:

$$K = \frac{2D}{\lambda} \qquad \textbf{(5-12)}$$

This approach can be extended to use the 2 Dimensional Fast Fourier Transform (2D FFT) to evaluate the performance of an $x - y$ grid of points describing a 2D array in $u - v$ space. This is equivalent to performing the FFT in the x direction, then applying the FFT to the result [46], but this time in the y direction. The process to go from an image of the array to the far field directivity is illustrated in Figure 5-6. It should be noted that the sidelobe pattern produced is itself spiral in shape, which is discussed further in Section 5.6.

To smooth the beam pattern in the *u*-*v* plane, and ease interpretation, the image of the array can be padded with zeros. This effectively increases *D*, and therefore the number of points *K* that are included in the beam pattern.

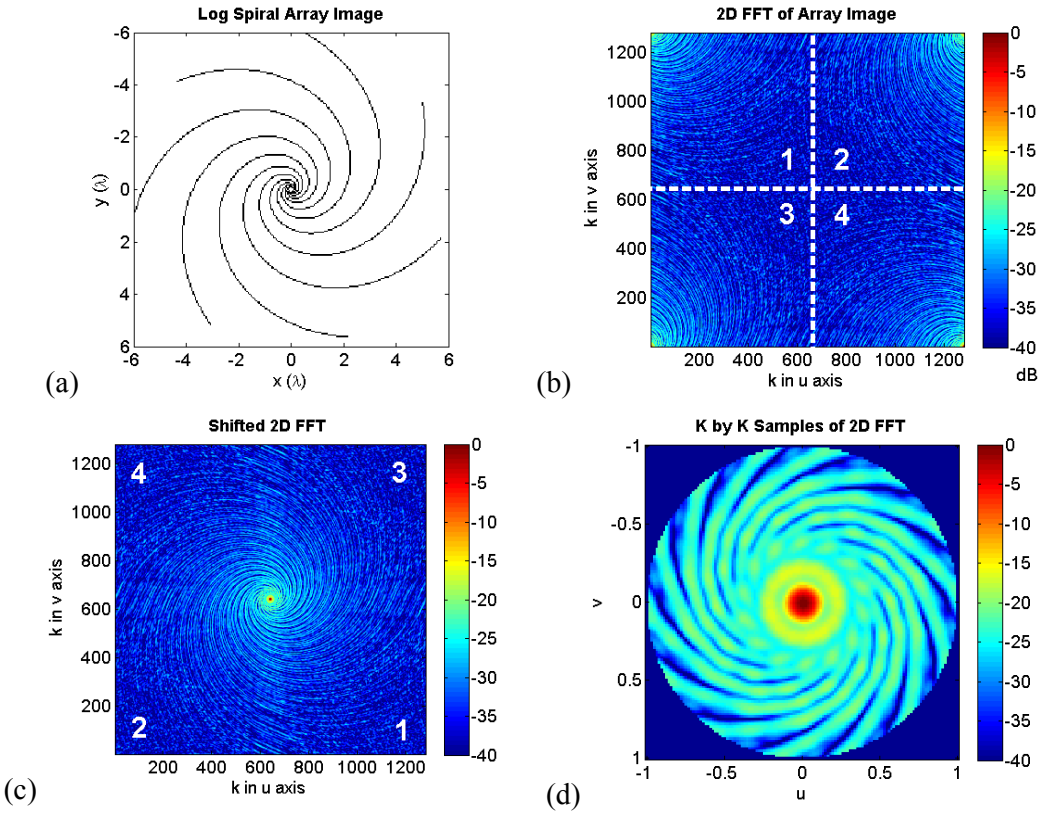

Figure 5-6 **The process of creating a far field beam pattern begins with an image of the array (a), which in this case has a 12λ aperture. A sample rate of λ/20 has been used to increase the spatial resolution of the image. The 2D FFT is shown before (b), and after (c) the data is shifted to group the mainlobe components at *u* = *v* = 0. Finally, only *K* samples from the centre of the image is used to construct the beam pattern (d). Areas outside the unit circle do not correspond to real angles, and are set to zero amplitude.**

The FFT exploits redundancy in the standard DFT algorithm, making it quicker to compute. A beam pattern for a 12λ aperture, with 20 samples per λ can be calculated in approximately 100 ms. This provides adequate resolution to resolve the spiral function to within half a wavelength of its centre, and is fast enough to examine several hundred spiral designs per minute. The designs with best performance can then be sampled to create arrays with discrete elements, and analysed in more detail using the DRI method.

5.4 Radon projection slice

Chapter 3 described how the projection slice method could be used to calculate the 1D equivalent array of a 2D array over an angular sweep. The same method is useful for analysing the degree of shadowing in continuous spiral arrays. The Radon transform [47] is a very fast method of performing this analysis, and can accept the same grid based image of a continuous array as the 2D FFT. Since the beam pattern has a two-fold rotational symmetry an angular sweep running from 0 to 180 degrees fully characterises the array. To illustrate the results produced by this analysis the following shapes, each with a 12λ aperture, are analysed below:

- A continuous disc.
- A sparse grid, with a 1.2λ spacing.
- A three armed continuous log spiral.

The images created for these designs are shown in Figure 5-7, and their Radon transforms are shown in Figure 5-8.

The continuous disc represents an idealised response for an array design. The Radon transform is constant across all angles, and takes the form of a semi circle with no nulls or peaks. This results in a far field beam pattern which does not vary with φ.

The Radon transform produced by the sparse grid is typical of grid designs. Angles of φ of 0 and 90° are perpendicular to the x and y axes respectively. At these angles there is a high level of element shadowing and the elements bunch together into discrete locations on the 1D equivalent array. These bunches of elements are separated by the pitch of the array. These are the angles where the maximum sidelobe levels occur, along with grating lobes if the spacing is greater than λ/2. At other angles there is less element shadowing, resulting in lower sidelobes, and

suppressing grating lobes. This analysis indicates that the grid design is inherently inefficient, as elements are not well distributed across the $s - \varphi$ space of the transform.

The spiral design produces a number of distinguishing features. There are noticeable lines of shadowing which run across all angles in the sweep. These lines correspond to the points where the spiral arms are running directly towards the analysis angle. However the position of these peaks in the 1D equivalent array varies linearly with φ, so they do not appear in the same position at every angle. Furthermore, they are geometrically spaced due to the separation between successive arms, so do not have underlying periodicity. In this example the aperture of the 1D equivalent array varies slightly with φ. This is mainly due to the spiral only having three arms, and would be less of an effect as the angular separation between the arms was decreased.

Overall, the spiral design varies relatively little with the analysis angle φ, even though the spacing between the arms is relatively large. This would seem to indicate that it has underlying properties which make it efficient as a basis for sparse array designs.

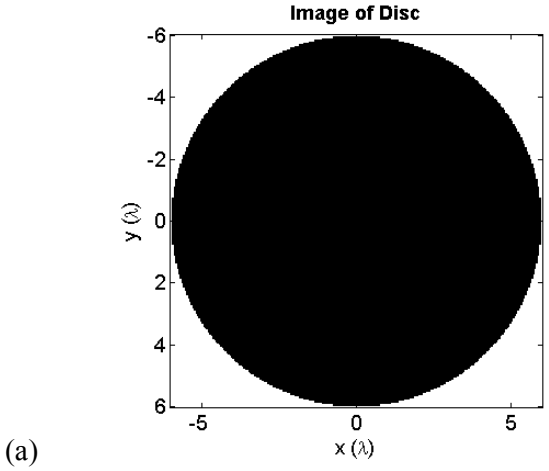

(a)

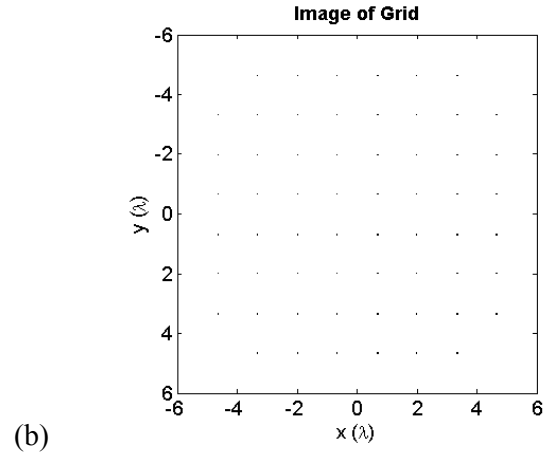

(b)

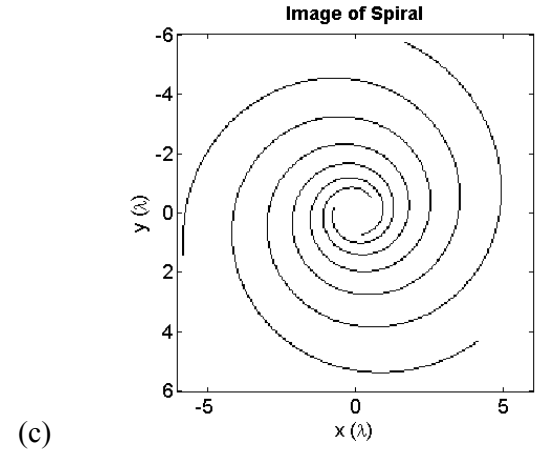

(c)

Figure 5-7 **Images generated to represent array layouts, (a) disc, (b) sparse grid and (c), log spiral.**

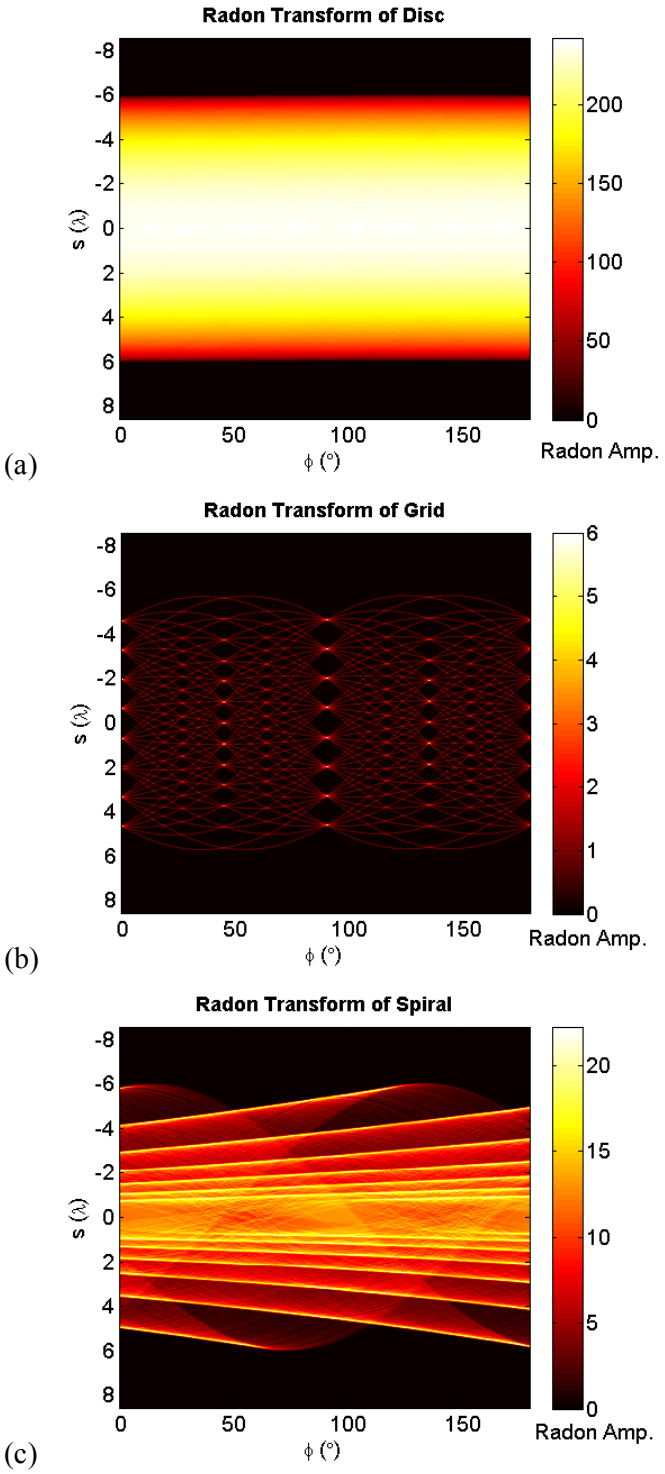

Figure 5-8 **Radon transforms of (a) continuous disc, (b) sparse grid and (c) a log spiral.**

5.5 Number of arms

To design effective and efficient spiral arrays some strategy is required to select the appropriate number of arms. It is clear that for a given spiral arm design, adding more arms will increase the length of the array, and for a given sampling strategy, the number of elements required. However, it is not immediately clear what the optimum number of arms will be when length is kept the same, and arm design is varied. This section investigates this problem, by beginning with the most intuitive spiral design in terms of analysis, and then building up to more complex designs.

To begin with, consider a single armed log spiral, where $\varphi = 0°$, producing a straight arm. The aperture, D is 12λ, and the starting radius of the arm is 0, which produces a 6 λ spiral arm. The arm is represented by a continuous line of points, creating an array image with a resolution of λ/20, on which the 2D FFT is performed to produce a beam pattern. The array and its beam pattern are shown in Figure 5-9.

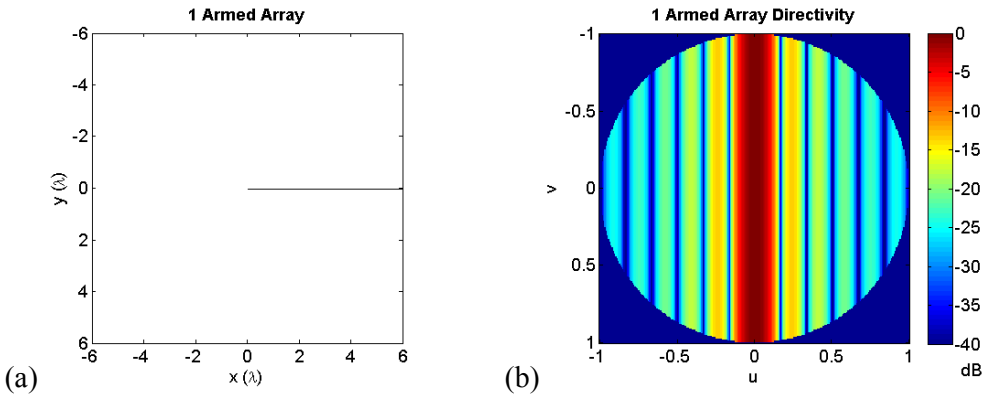

Figure 5-9 **Directivity of a single straight armed, continuously sampled log spiral (a) array layout and (b) far field directivity.**

As expected this design behaves like a linear array, with a wide beam in the *v* axis, and a narrow beam in the *u* axis. This analysis can be extended to arrays with arms ranging from 2 to 7, as shown in Figure 5-10 and Figure 5-11.

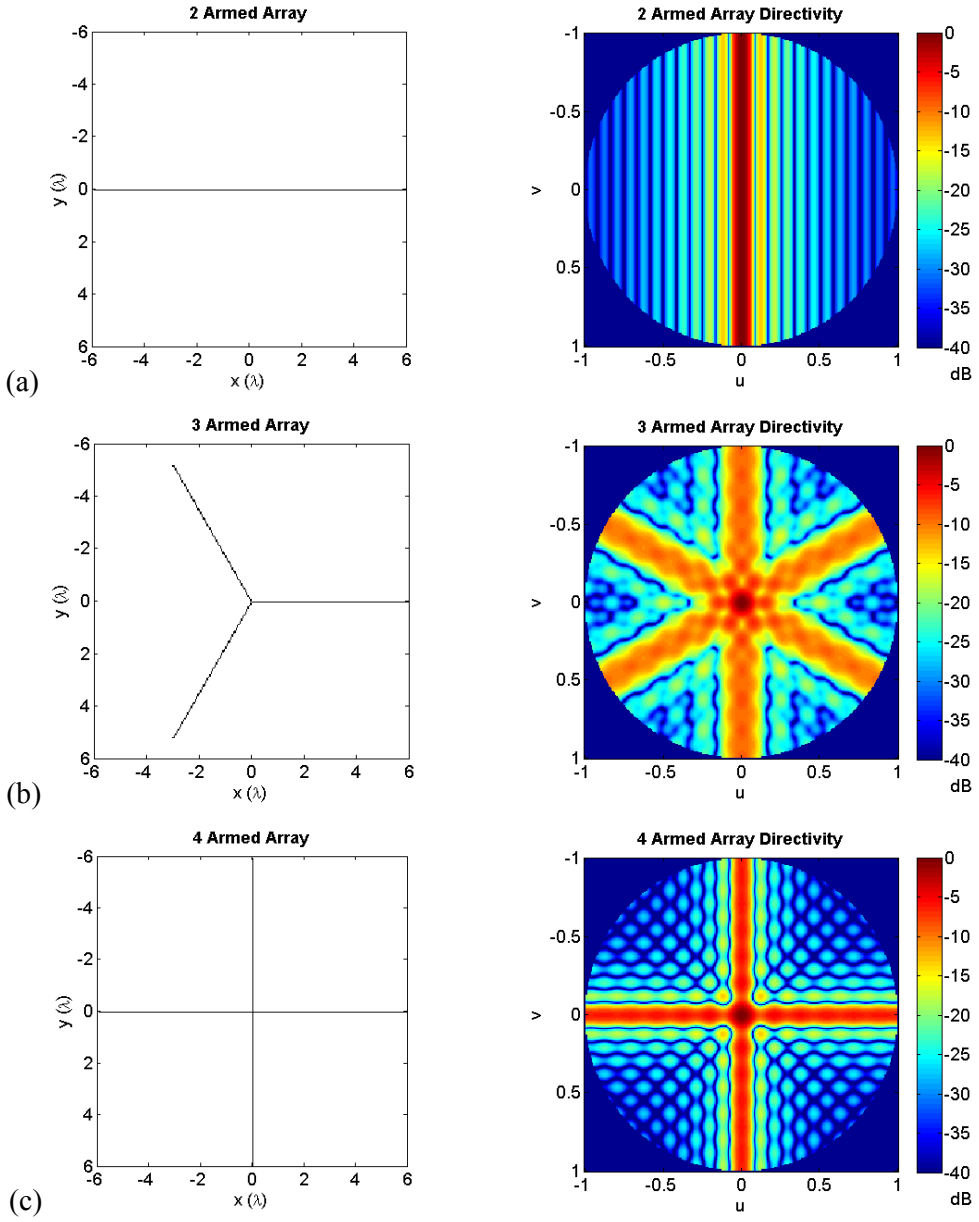

Figure 5-10 **Straight armed log spiral arrays and their directivities. The left column shows array designs, while the right column shows their directivities, (a) 2 armed array, (b) 3 armed array and (c) 4 armed array.**

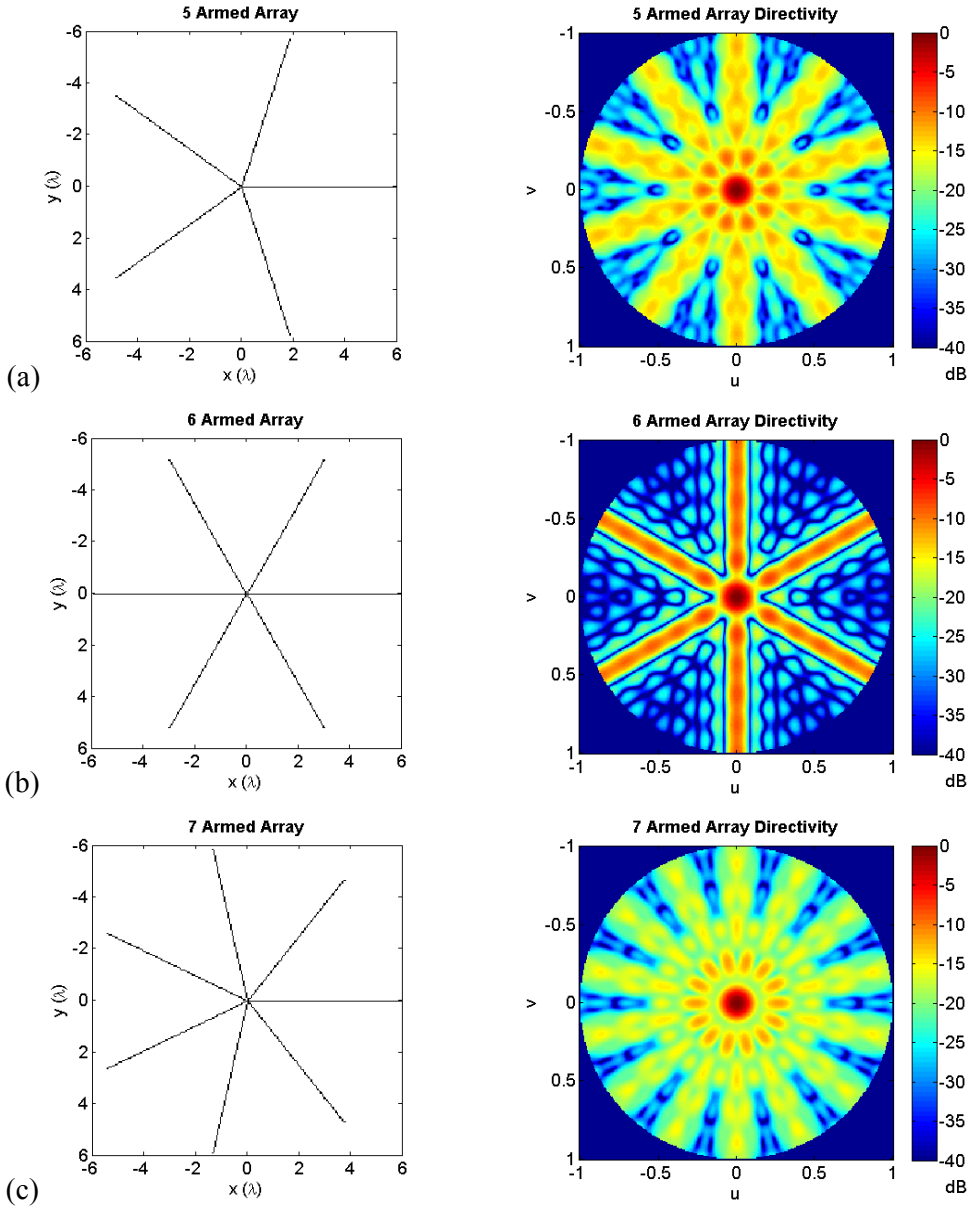

Figure 5-11 **Straight armed log spiral arrays and their directivities. The left column shows array designs, while the right column shows their directivities, (a) 5 armed spiral, (b) 6 armed spiral and (c) 7 armed spiral.**

It is clear from these examples that arrays with an odd number of arms have an advantage over those with an even number. Each spiral arm is omnidirectional in the plane perpendicular to its length, as is evidenced in the 1 and 2 arm designs. In arrays with even numbers of arms, every arm has an arm on the opposite side of the array, which will create a line of sidelobes in the same plane. This further increases element shadowing, with many elements lying in a straight line. This is in contrast to odd designs, where the only overlap between the sidelobes associated with each spiral arm is in the centre of the beam. As a result, the number of visible sidelobe lines in an odd armed array is twice the number of arms, while in even armed arrays it is equal to the number of arms.

Sidelobe heights in these designs cannot be directly compared, as the array length is proportional to the number of arms. However, it is clear that for both odd and even armed designs, increasing the number of arms reduces peak sidelobe height.

The width of the sidelobe lines remains the same, with even armed designs having narrower lobes due to the overlap in the design. This has two effects as the number of arms is increased:

- The sidelobe lines begin to spread out and fill the angular plane, creating a flat sidelobe floor.

- The inner portions of the sidelobe lines begin to overlap, creating a ring of raised sidelobes, as shown in the 5 and 7 armed designs.

This very simple analysis has illustrated the sidelobes produced by straight arms, and how these sidelobes build up when multiple arms are constructed into multi armed spiral arrays. However, these designs are not optimal, as they have a high degree of element shadowing. This can be illustrated by taking the Radon transform of the 7 armed spiral shown in Figure 5-11. This is shown in Figure 5-12.

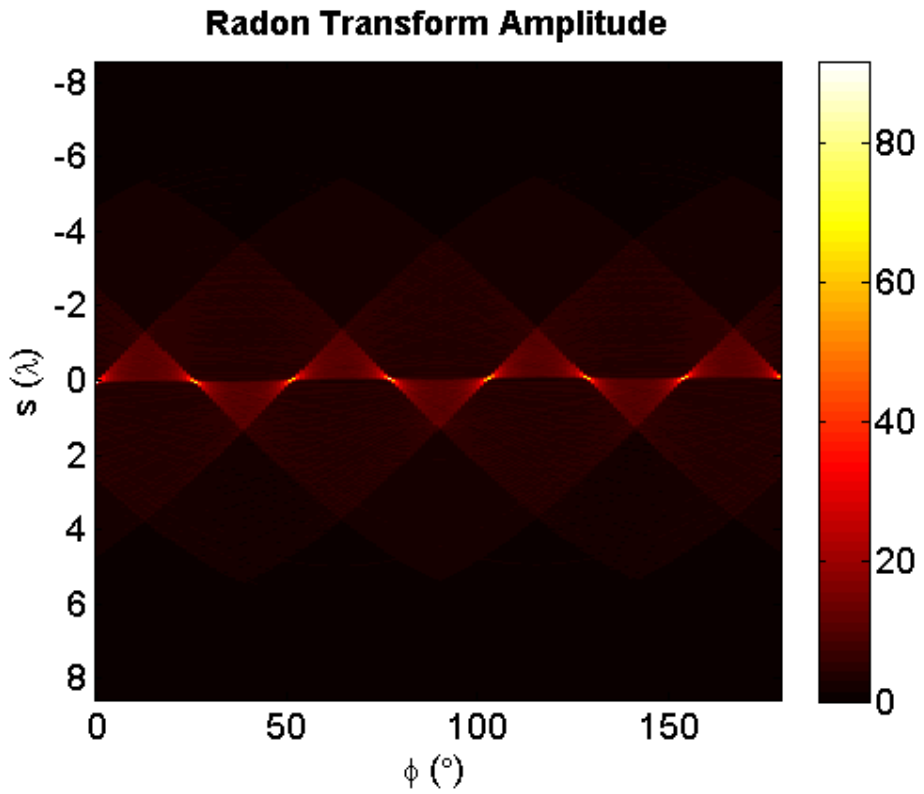

Figure 5-12 Radon transform of 7 armed, continuous log spiral with a 12λ aperture.

The Radon transform has 7 points with very strong amplitudes, which correspond to rotational angle where one of the spiral arms is perpendicular to the *s* axis, and are summed to a single point. This indicates a high level of element shadowing. In the directivity simulations these angles correspond to lines of dominant sidelobes.

Key design points discussed in this section were:

- Spirals with odd numbers of arms out perform those with even numbers, due to non overlapping sidelobes.

The next step is to consider the effect that curving the arms has on the sidelobe structure. This is discussed in the following section.

5.6 Curvature of Spiral Arms

The previous section simplified the analysis of log spiral designs by considering spirals with straight arms. However, these are only a small subset of the many spiral designs which can be realised. This section begins by analysing the directivity of a single, continuous spiral arm as its curve is increased. It then looks at the effect of combining multiple curved spiral arms into a multi armed spiral.

In Figure 5-13 and Figure 5-14 a series of continuous log spiral arms are shown, with pitches of 90°, 75°, 40°, 20°, and 5°. The 2D FFT is then used to calculate the directivity of the arms, and this is presented alongside the spiral images. The outer aperture of the arrays are 12λ, and the length of the spiral arms increases from 6λ on the straight (90°) arm, to 69λ on the 5° arm. Theoretically the arms circle the origin an infinite number of times as they approach it, however, in practice, the resolution of the image limits the number of spiral turns which are seen. In the 1/20λ sampling used in these images, the $p = 5°$ has 7 turns which can be resolved.

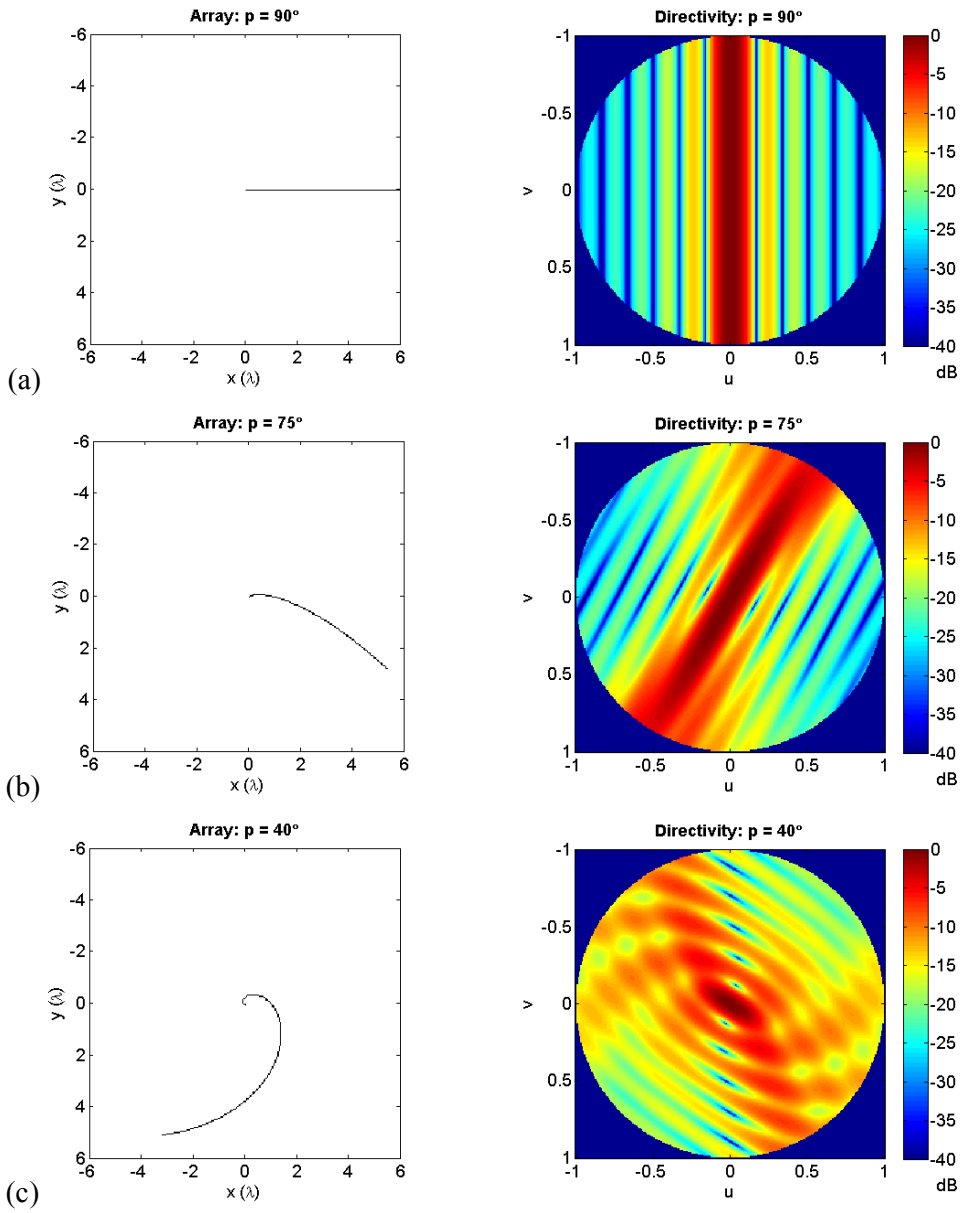

Figure 5-13 **Performance of single arm log spirals with *p* ranging from 90° down to 40°. The left column shows array designs, while the right column shows their directivities, (a) *p* = 90°, (b) *p* = 75° and (c) *p* = 40°.**

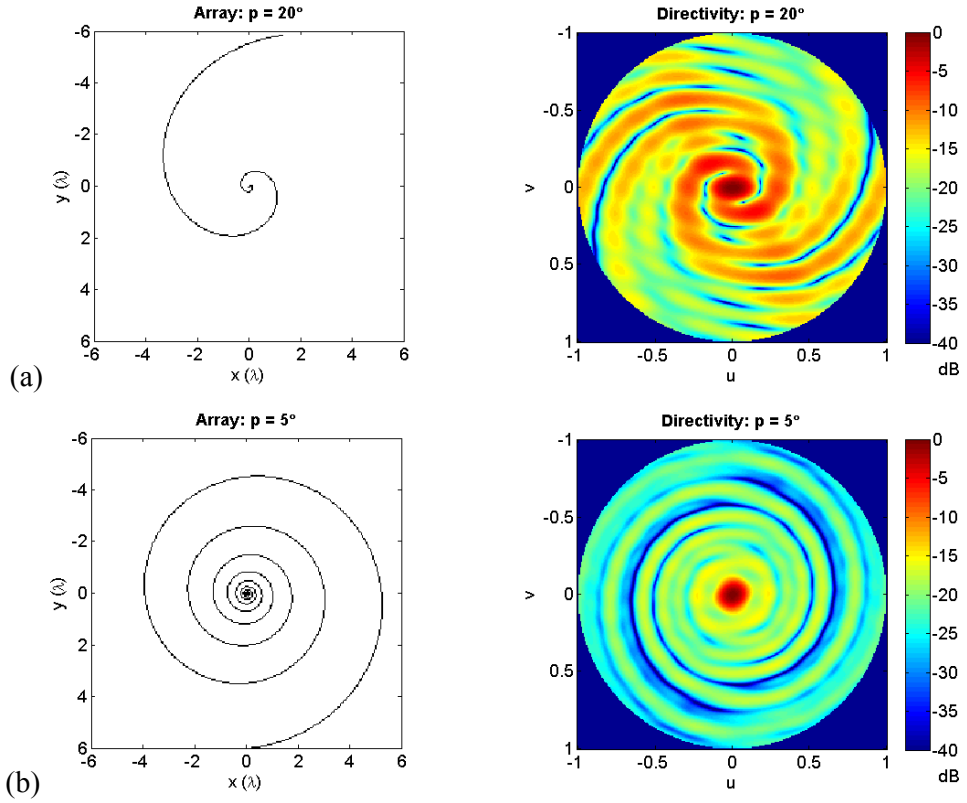

Figure 5-14 **Performance of single arm log spirals with *p* ranging from 20° down to 5°. The left column shows array designs, while the right column shows their directivities, (a) *p* = 20° and (b) *p* = 5°.**

As with the results in the previous section, the straight armed design is omnidirectional in the *v* axis, creating a wide arcing mainlobe in space. As the pitch is decreased this wide mainlobe begins to spread out, diminishing its strength, as shown in the 75° design. At 40° the a series of distinct sidelobes begin to form, and by 5° there is a well defined mainlobe, surrounded by a relatively flat sidelobe region which peaks at -16 dB.

A very important property of the sidelobes produced by a log spiral arm is that the dominant sidelobes themselves travel outward from the mainlobe in a spiral pattern.

This can be seen in the 20° example, and can be further illustrated by overlaying a rotated and flipped version of the spiral on top of its beam pattern (Figure 5-15).

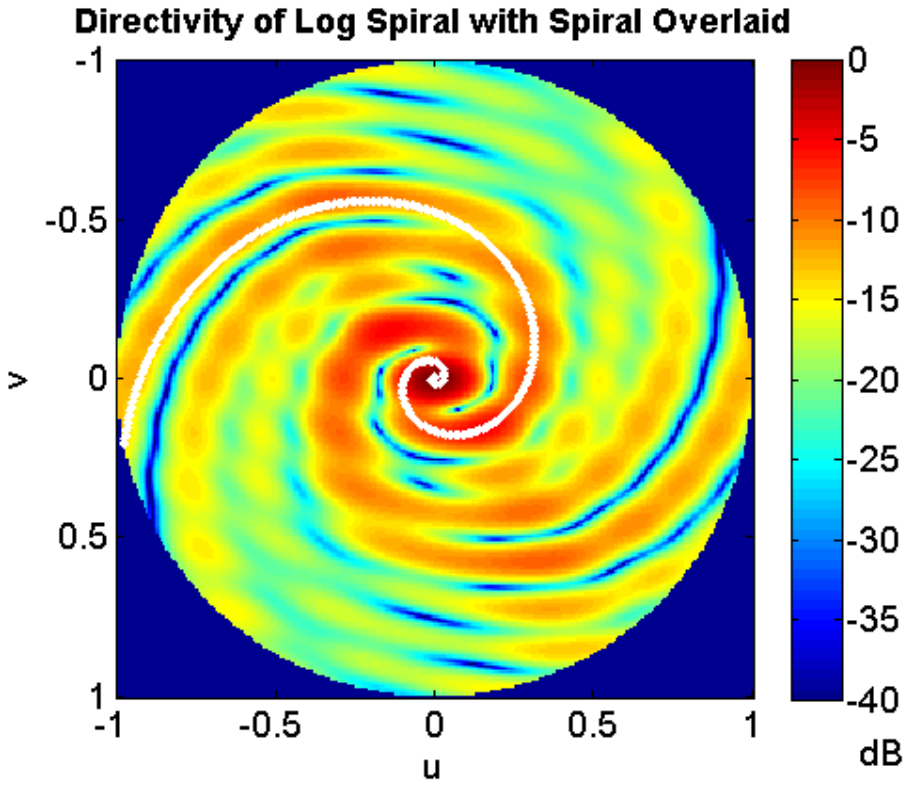

Figure 5-15 **Directivity of continuous log spiral with p = 20°, showing a sidelobe pattern which follows the same patterns as the spiral. A rotated and flipped spiral function is overlaid in white for comparison.**

Two spiral patterns of sidelobes can be seen in the beam plot, with 180° of rotation between them. This structure avoids the lines of dominant sidelobes overlapping as the pitch of the spiral is decreased, and length of the spiral increases. In addition to this, if spiral arms are added to the design with a constant angular spacing, only arms that are 180° from each other will have directly overlapping sidelobes. This can only occur in spirals with even number of arms, which have already been shown to be inferior to odd spirals.

To further illustrate this, a 3 armed log spiral with $p = 20°$ is shown in Figure 5-16. As none of the peak sidelobes directly overlap, the sidelobe structure remains relatively flat. The few peaks that do exist appear close to the mainlobe where the sidelobes are wide enough to overlap, in a similar manner to that seen with the straight armed spirals in Section 5.5.

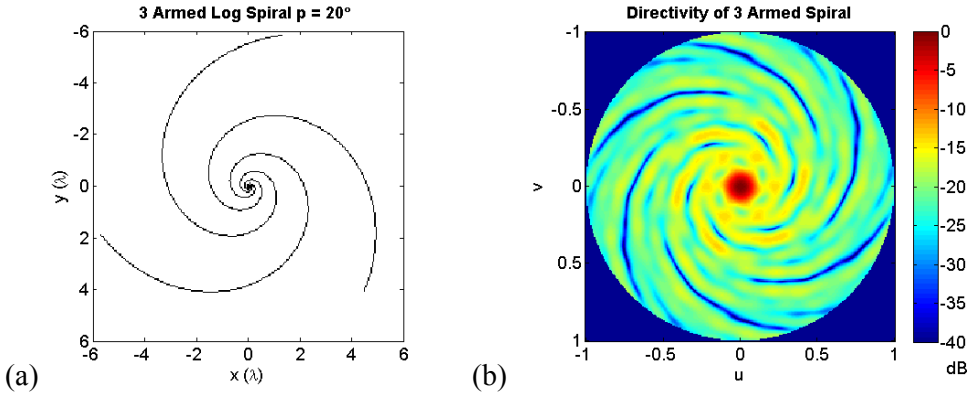

Figure 5-16 Performance of 3 armed log spiral with $p = 20°$, (a) array design and (b) array directivity.

A projection slice analysis using the Radon transform further illustrates the merits of the log spiral for array design. The Radon transform of the single armed, $p = 5°$ log spiral from Figure 5-13 is shown in Figure 5-17. While distinct lines of element shadowing can be seen, these occur at aperiodic intervals across the equivalent 1D apertures. This avoids the build up of distinct grating lobe angles in the directivity.

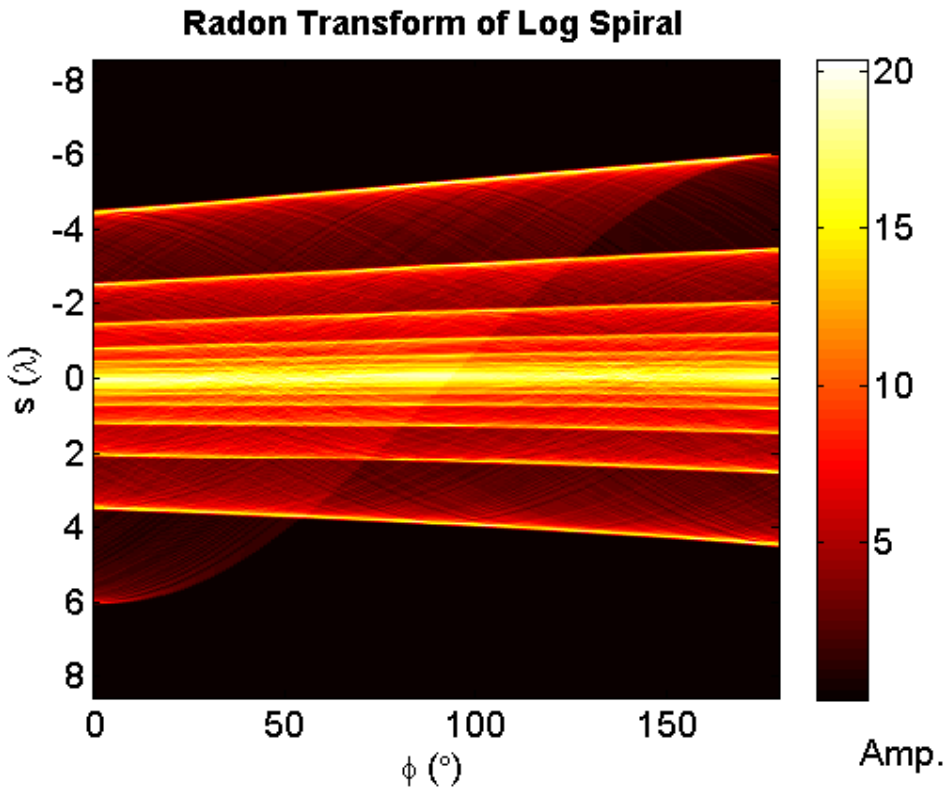

Figure 5-17 Radon transform of single armed $p = 5°$ spiral.

When a similar analysis is performed on the Archimedes spiral it can be clearly seen that the log spiral is the superior design. In Figure 5-18 a single armed Archimedes spiral is shown, with $b = 0.265$ giving it a length of approximately 69λ, which was calculated numerically. This makes it the same length as the log spiral in Figure 5-16. There is a distinct band of sidelobes in the directivity, created by the periodic spacing between the arms of the array. This periodic spacing can be clearly seen in the Radon transform of the array. To remove these lobes, the spiral would require more turns, which would make it longer than the log spiral equivalent, making the Archimedes spiral a less efficient, and more expensive design. For this reason the Archimedes spiral designs will not be investigated any further, and the work will focus on logarithmic spiral designs.

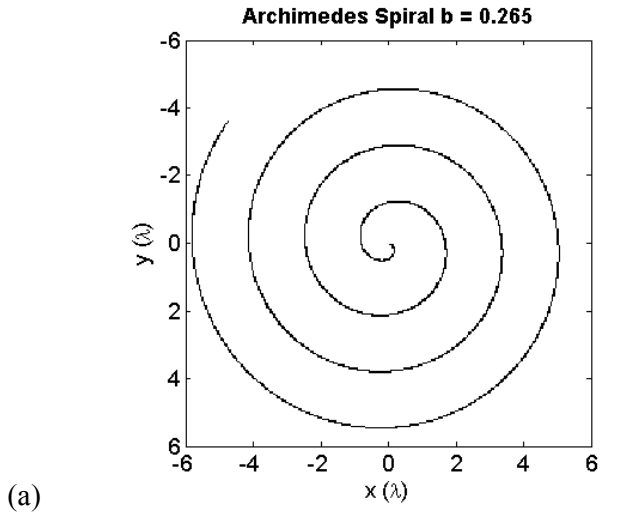

(a)

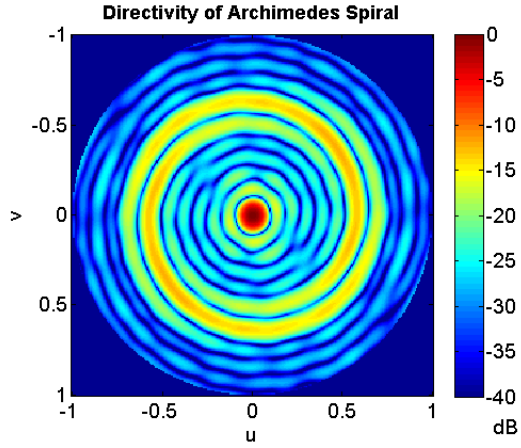

(b)

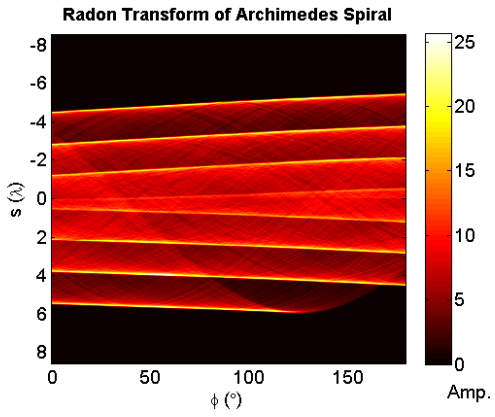

(c)

Figure 5-18 **Analysis of single armed Archimedes spiral with $b = 0.265$, (a) array design, (b) far field directivity and (c) and Radon transform.**

The shape of the sidelobe structure created by the log spiral arms suggests three distinct design approaches may be considered:

- Create a single armed spiral with as many turns as can be practically achieved with the elements available.

- Create a multi armed spiral that has many arms, each with very little curvature.

- Between these two extremes there exists a wide variety of available designs, as the number of arms is traded off against arm length. This trade off will be discussed in Section 5.10.

Key design points discussed in this section were:

- Log spirals are more effective at spreading sidelobes than Archimedes spirals.

- Log spirals avoid overlapping sidelobes across a range of lengths, as additional arms are added, if an odd number of arms is used.

5.7 Minimum Element Radius

It is clear that in order to create a practical multi armed spiral array a minimum element radius, R_{min}, must be specified, to avoid overlapping elements at the array's centre. However, doing so creates a gap in the centre of the array, where no elements are located. This alters the distribution of the array elements, and will have an effect on the shape of the acoustic beam produced. The projection slide method can be used to characterise this change in element distribution, and is used here to develop a strategy for optimising the minimum radius.

The first step is to characterise the 1D equivalent array for $R_{min} = 0$. To do this a simple 12λ aperture, 2 armed design with $p = 90$ is used, which produces an array pattern which is a straight line. The Radon transform of the array is calculated, and the 1D equivalent arrays are then averaged across all φ to produce a characteristic radial distribution for the array. This is shown in Figure 5-19.

The resulting distribution has a strong peak in the centre, which then tapers away to the outside. To test if this distribution is representative of all log spiral designs, the same method is used to calculate distributions for series of log spiral designs. The designs are shown in Figure 5-20, along with their element distributions.

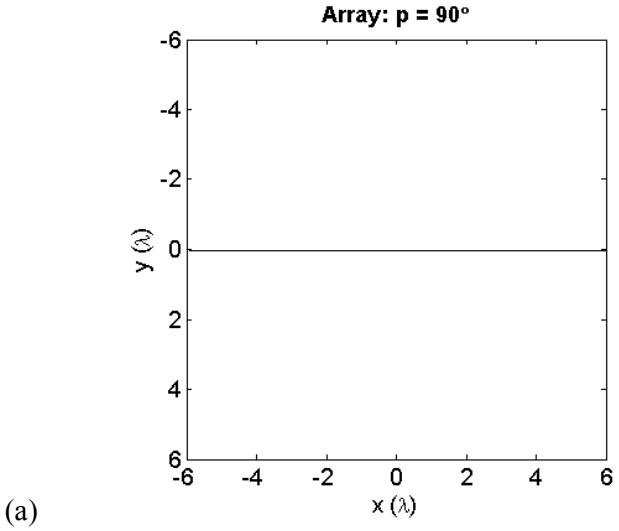

(a)

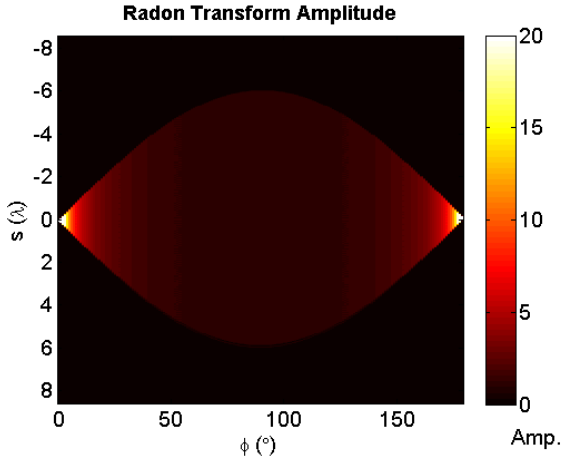

(b)

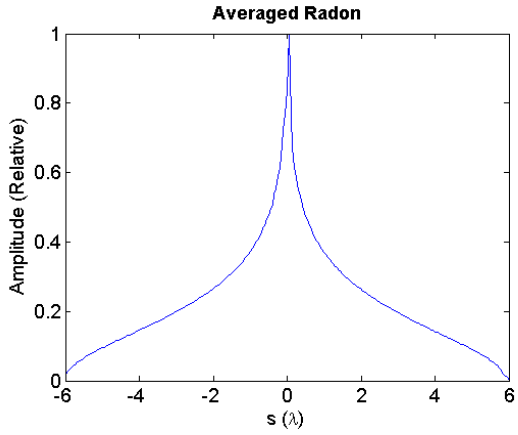

(c)

Figure 5-19 **Analysis of 2 armed, p = 90° array, (a) array design, (b) Radon transform and (c) average 1D equivalent array with amplitude normalised to its peak.**

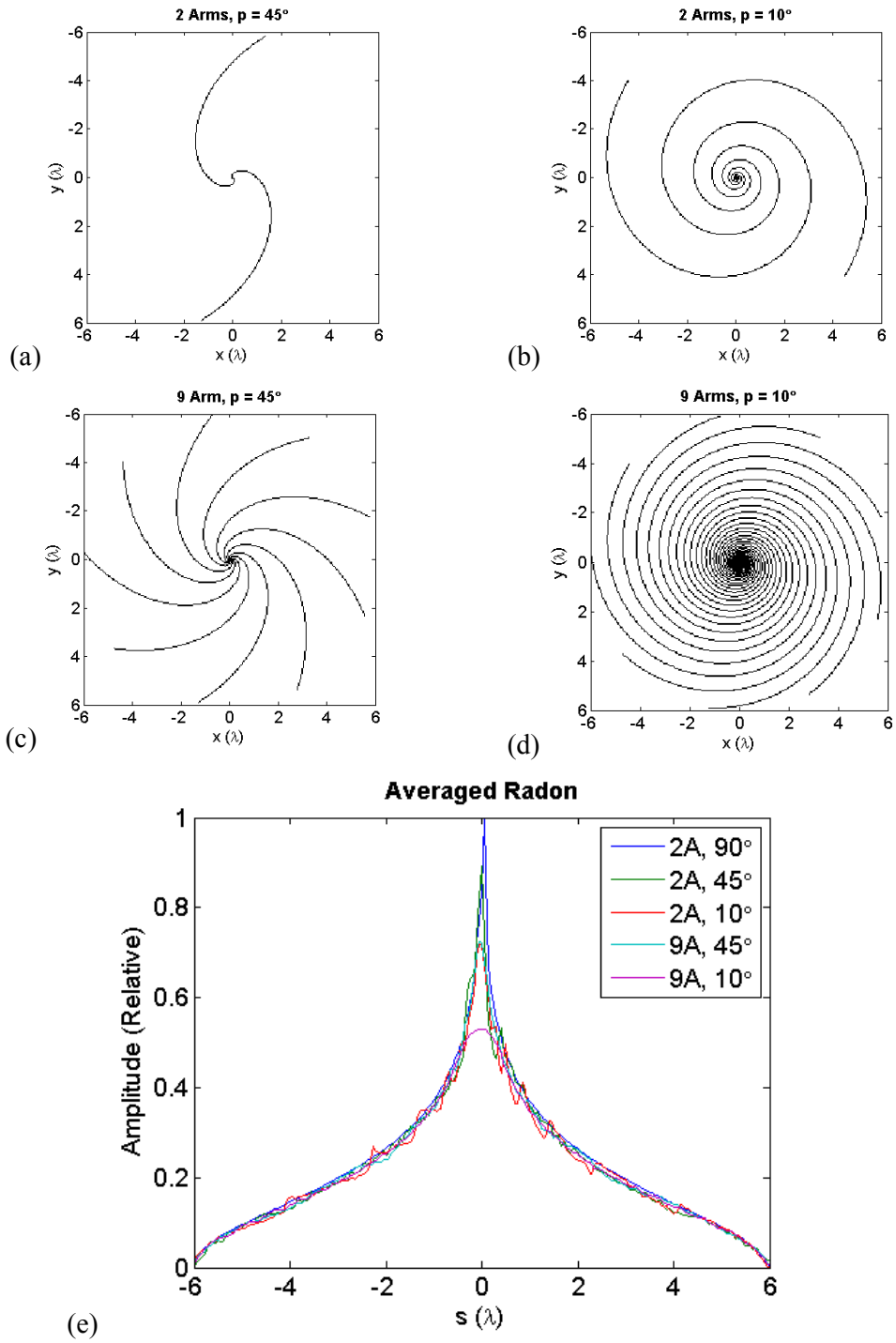

Figure 5-20 **Radial element distribution of a range of multiarmed log spirals, all showing similar distributions, (a),2 armed p = 45°, (b) 2 armed p = 10°, (c) 9 armed p = 45°, (e) 9 armed p = 10° design and (e) radial element distribution of the spirals.**

There is very little change in the radial distribution across these designs. The only significant change is for the 9 armed, $p = 10°$ design, which has a smaller peak in the centre. This is due to the arms overlapping at the centre of the array image. This artefact could be removed by increasing the resolution of the image, or allowing the amplitude of the image to be greater than one for overlapping elements.

The lack of change with number of arms is expected, as each arm has the same radial distribution, so adding additional arms will only increase the amplitude of the result. The lack of change in distribution with pitch is notable. While increasing the pitch increases the length of the arm, the logarithimic spacing between successive arms maintains the overall distribution. The fact that this distribution remains constant is useful when creating a design process, as it allows the minimum radius to be separated from all other variables, simplifying its analysis.

To evaluate the influence of R_{min} on maximum sidelobe height, the beam pattern associated with radial distribution is calculated. Figure 5-21 shows the distribution and beam pattern for an R_{min} of 0 and 2 λ. A 24 λ aperture is used to make more of the sidelobe structure of the distribution visible. The 2λ gap in the centre of the array removes the peak in the distribution, and replaces it with a shallow dip in element density. The maximum sidelobe is -16.5 dB for the 0λ reference design, and -23.5 dB for the 2λ design. The change has negligible effect on beam width.

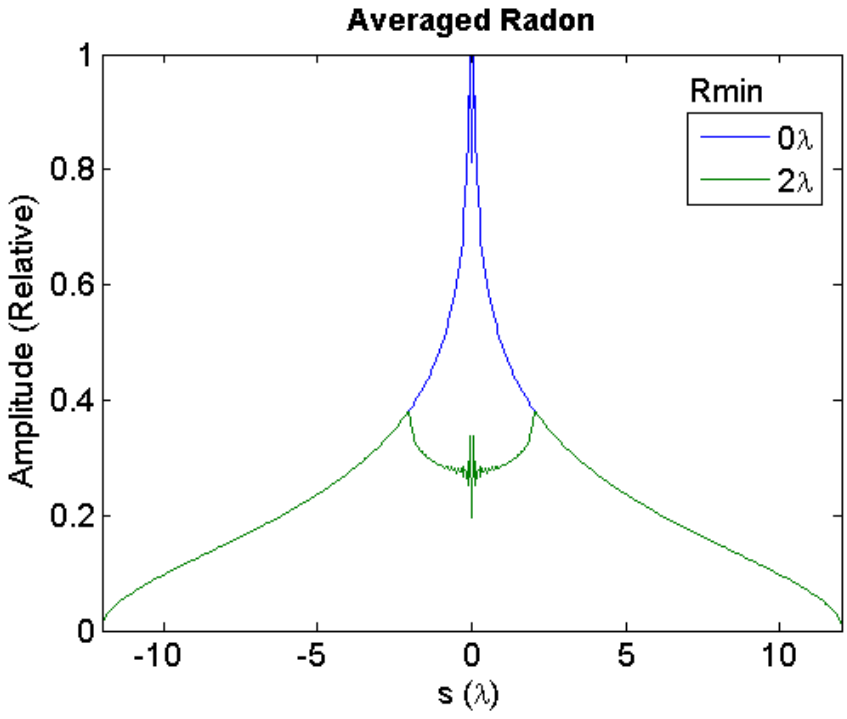

(a)

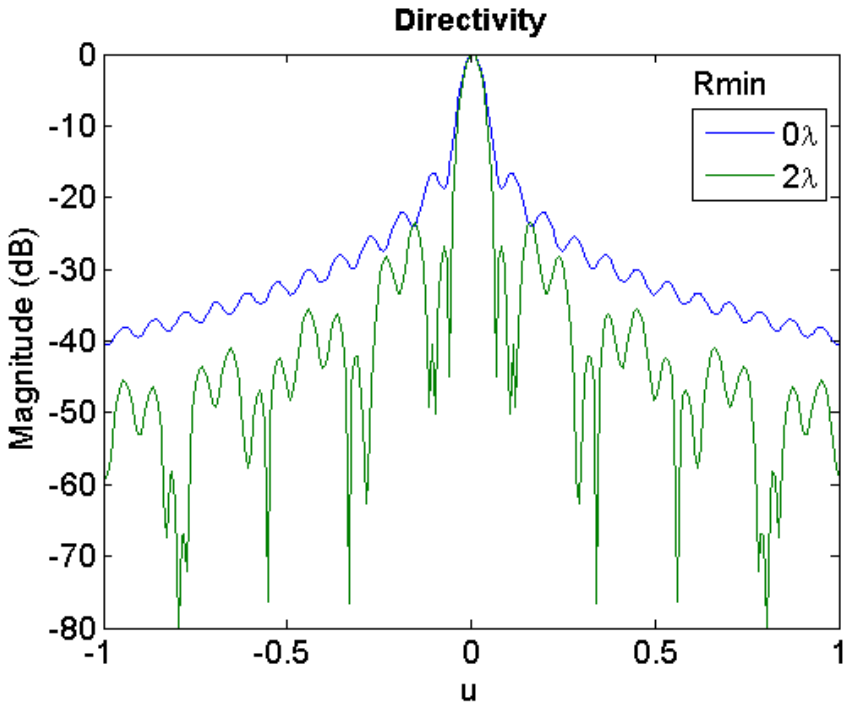

(b)

Figure 5-21 **Directvity of 24λ aperture array with 0 and 2λ R_{min}, (a) array distribution and (b) array directivity.**

R_{min} was then varied over a range from 0 to 4λ to find the value that minimises peak sidelobe level. The change in peak sidelobe with R_{min} is shown in Figure 5-22. There is a single minimum, with the sidelobe height rising either side, and a small deviation in the slope of the graph at 2.5λ. The shape of the distribution changes as R_{min} is varied, creating complex sidelobe patterns, so this deviation is not considered unusual.

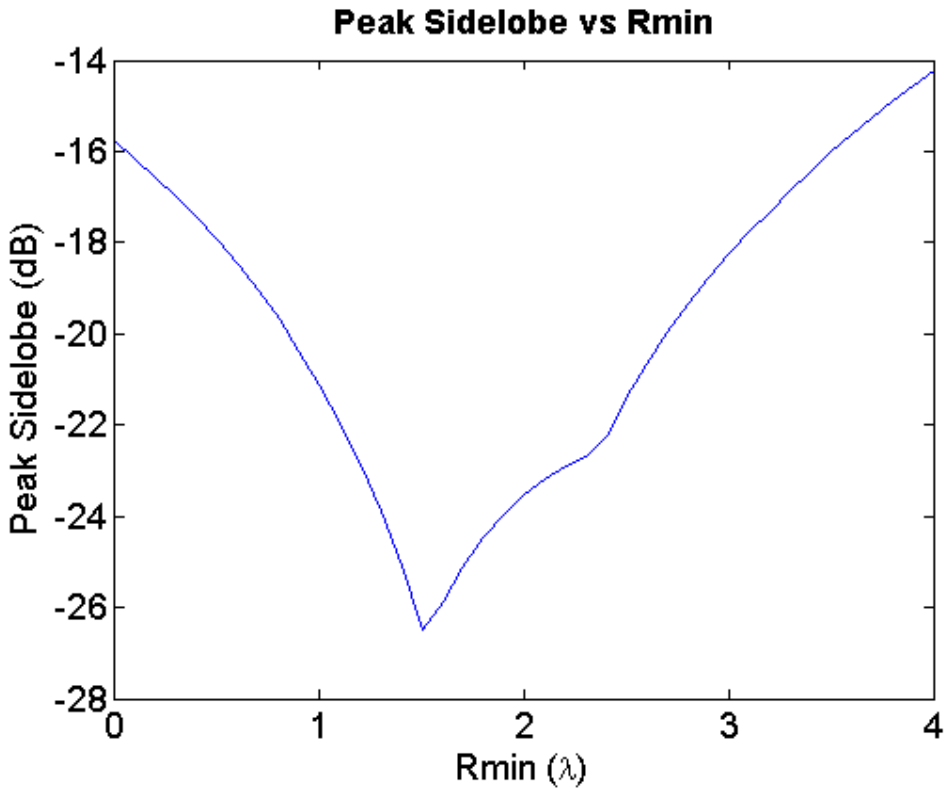

Figure 5-22 Variation of peak sidelobe level in a 24λ aperture array with R_{min}.

The minimum in the graph occurs at R_{min} = 1.5λ, producing a peak sidelobe height of -26.8 dB. The distribution and directivity for this design are shown in Figure 5-23.

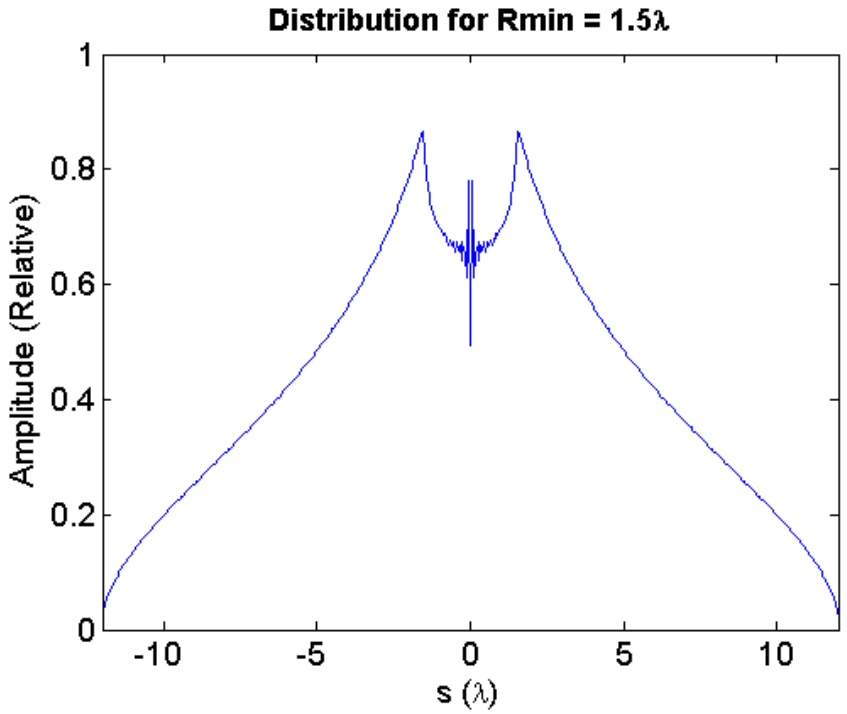

(a)

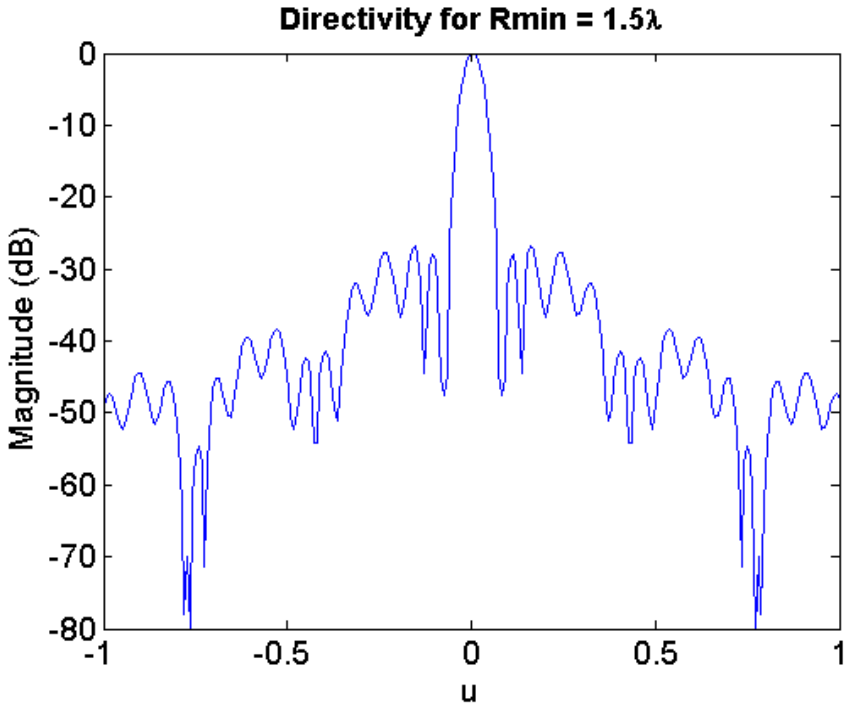

(b)

Figure 5-23 **Directivity of a 24λ aperture array with R_{min} = 1.5λ, (a) array distribution and (b) array directivity.**

In relation to the array aperture, D, the minimum element radius, R_{min}, is therefore:

$$R_{\min} = 1.5 = \frac{D}{16} \qquad \textbf{(5-13)}$$

To confirm that this rule is applicable to a 2D spiral array, an 11 arm log spiral with a pitch of 10°, and an aperture of 24λ is considered. This has a total arm length of 665λ, so is a relatively dense design, and will suppress sidelobes associated with the sparseness of the spiral structure. An image of the array, along with its Radon transform and directivity is presented in Figure 5-24.

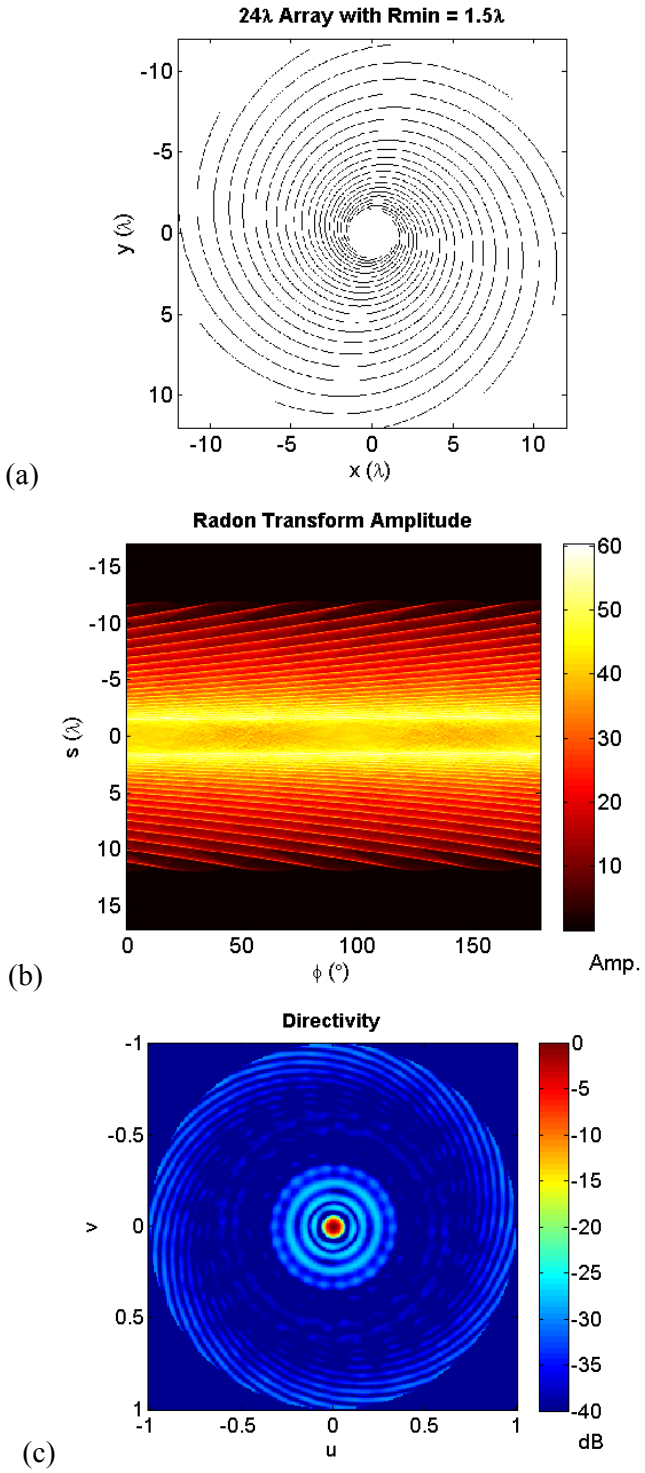

Figure 5-24 **Analysis of an 11 arm log spiral array with a 24λ aperture and a pitch of 10°, (a) array design, (b) Radon transform and (c) array directivity.**

The Radon transform of this dense design is relatively uniform, and this is reflected in the low sidelobes in the directivity. The sidelobe floor that remains around the centre of the array is a result of the fundamental distribution of the log spiral, and is at -26.5 dB, very close to the expected level.

Another useful measure that this analysis can provide is the relationship between beamwidth, θ_w, and aperture, D, for the optimised distribution. The -3 dB width of the beam in reduced angular space is inversely proportional to the aperture width, with a scaling constant k_b, as shown in the following equation:

$$\sin\left(\frac{\theta_w}{2}\right) = \frac{k_b}{D} \qquad \textbf{(5-14)}$$

where D is in wavelengths. Equation 2-1 gives the -3 dB beamwidth of a linear array element with a uniform aperture, and has a k_b of 0.44. In a similar way Equation 4-8 can be solved numerically for the -3 dB beamwidth of a circular piston, giving a k_b of 0.51 [48].

$$\theta_w = 2\sin^{-1}\left(\frac{0.51}{D}\right) \qquad \textbf{(5-15)}$$

The 24λ array shown in Figure 5-24 has a beamwidth of 3.0°. Inserting these values into Equation 5-14 and solving for k_b gives a value of 0.63. Therefore, the beamwidth of a spiral array with R_{min} selected using Equation 5-13 is:

$$\theta_w = 2\sin^{-1}\left(\frac{0.63}{D}\right) \qquad \textbf{(5-16)}$$

These results are significant, as they provide very simple design rules for not only the optimum minimum element radius, but also the aperture required to achieve a

specified beam width. Furthermore, if the required element size is known it also allows the maximum number of arms which avoid overlapping elements to be calculated. This is considered in Section 5.10. While Equation 5-13 is a useful guideline for setting R_{min}, there are situations where the required density of the array may cause elements to overlap. In this case R_{min} can be adjusted, as discussed in Section 5.11.

It should be noted that beamwidth will increase with steering angle, inline with the reduction in effective aperture. If the designer wishes to specify the worst case beamwidth, then it is the worst case effective aperture which must be considered at the design stage. Effective aperture is discussed further in Section 6.2.

Key design points discussed in this section were:

- The value for R_{min} which minimises peak sidelobe level is the same for all combinations of N_{arms} and p. It is non zero, so it avoids overlapping elements. It is inversely proportional to D, and is given in Equation 5-13.

- The lowest peak sidelobe level achievable with this distribution is -26.8 dB, which is a limit for the log spiral.

- The beamwidth produced by this distribution is given in Equation 5-16.

5.8 Spacing of elements

So far the spiral designs that have been analysed are continuous functions. However, in practice phased arrays are made up of discrete elements, each driven with a different phase delay. It is therefore important to design some method of sampling these continuous functions to yield practical arrays of discrete elements. In doing so there are two contradicting goals:

- The system should be sampled with sufficient accuracy so that the beam pattern of the array is unaffected.

- The number of elements should be minimised to reduce array and overall system cost.

Two strategies to do this are proposed. The first is to use periodic sampling, while the second is to use aperiodic logarithmic sampling.

To decide which method is most appropriate for log spiral arrays, simple continuous array designs will be modelled, and the position of any grating lobes or sidelobes due to undersampling will be assessed. To do this the RIM will be used, as it allows the acoustic beam to be steered off centre. This will allow the worst case sidelobe structure to be evaluated, which is where the beam is steered to its maximum steering angle, θ_{smax}. One-way directivity will be simulated in the far field under CW excitation, and each element will be approximated as an omnidirectional point source.

As mentioned in Chapter 2, the Nyquist sampling theorem requires that a sample period of $\lambda/2$ is used to avoid grating lobes in the beam. A 32 element linear array, with a $\lambda/2$ spacing is shown in Figure 5-25, alongside a logarithmic array with the same number of elements and the same aperture. The position of the log spaced elements, x_{log} is calculated from that of the linearly spaced elements, x_{lin} as follows:

$$x_{\log} = \frac{D}{\log_e(D+1)} \log_e\left(x_{lin} + \frac{D}{2} + 1\right) - \frac{D}{2} \qquad \textbf{(5-17)}$$

where D is the aperture of the linear array, and x_{lin} ranges from $-D/2$ to $D/2$. This produces a logarithmically spaced array with the same number of elements, over the same range. The directivity of both arrays is also shown in Figure 5-26 with steering angles of 0° and 90°.

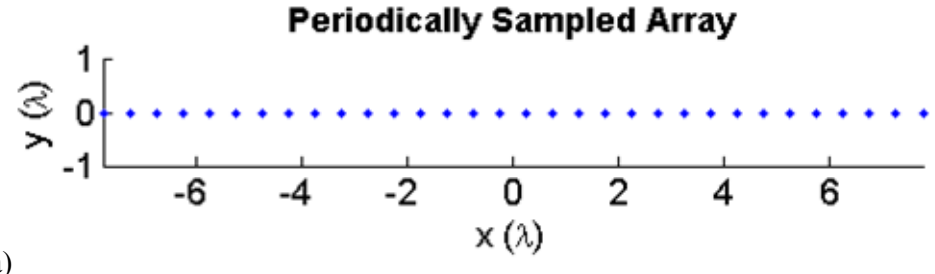

(a)

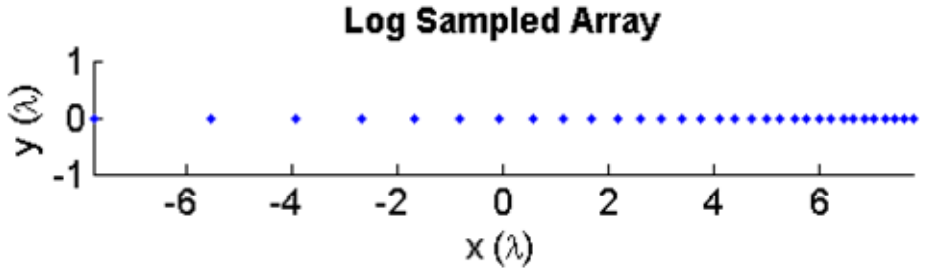

(b)

Figure 5-25 **Layouts of 32 element 1D arrays, both covering a 16λ aperture. The elements are omnidirectional points represented as blue diamonds, (a) linear sampling and (b) logarithmic sampling.**

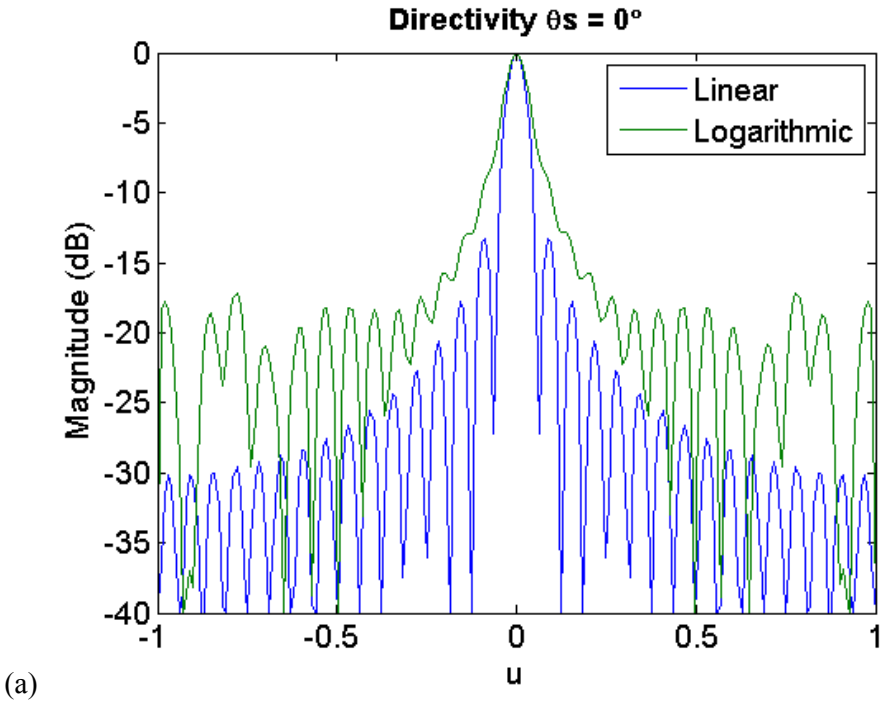

(a)

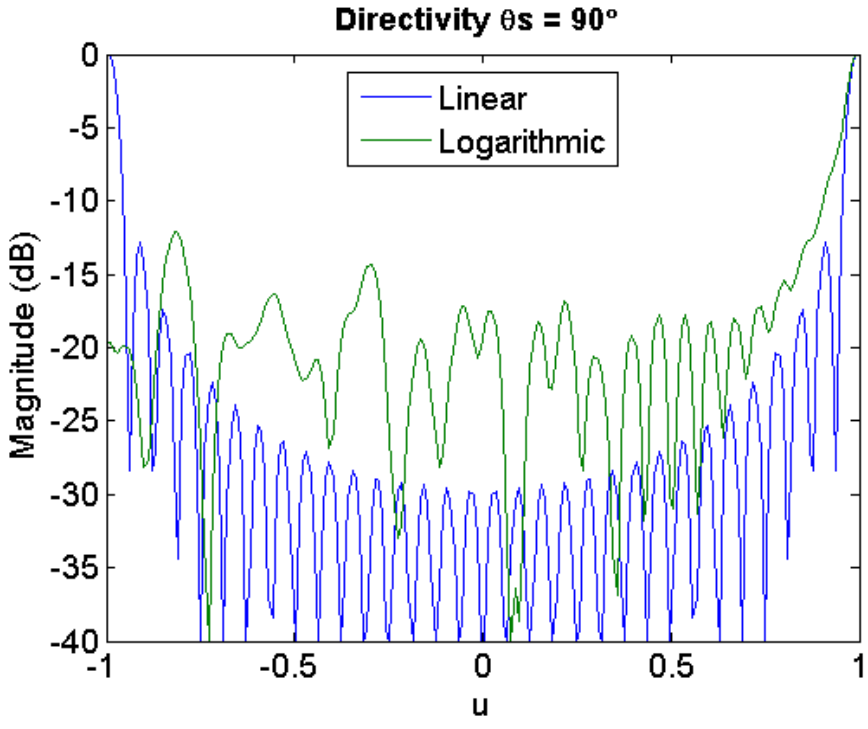

(b)

Figure 5-26 **Directivities of the arrays shown in Figure 5-25 with varied θ_s, (a) 0° and (b) 90°.**

The periodically sampled array has a sidelobe structure which decays smoothly to a minimum of -30 dB. As predicted in Equation 2-5 it produces a grating lobe at -90° when steered to +90°. Practical devices with finite element widths would not generate a signal at these extreme angles, so this design is considered to be free of grating lobes for practical purposes.

The aperiodic distribution in the logarithmically sampled array avoids any grating lobes, even when steered to 90°. However it has higher sidelobes levels with a peak at -12 dB, and a floor immediately adjacent to the mainlobe of approximately -17 dB. These sidelobes are higher than those generated by the distribution of the log spiral function, and if a spiral was sampled in this manner would be the dominant lobes. It is therefore recommended that a linear sampling strategy is used with log spiral arrays to avoid impinging on their performance.

To apply periodic sampling along the length of the spiral arms Equation 5-8 was rearranged to calculate the radial spacing vector r from a set of linearly spaced points x along the spiral arm. If x ranges from 0 at the start of the arm to x_{max} at its end, then r is calculated as follows:

$$r = \frac{bx_l}{\sqrt{1+b^2}} + R_{\min} \qquad \textbf{(5-18)}$$

x_{max} is the length of the arm over the portion sampled in the array, and is calculated using Equation 5-8. The angular points along the arm are then calculated using Equation 5-3.

As the log spiral arms are curved it is necessary to confirm that linear sampling will behave in a predictable manner. It is expected that the grating lobes associated with the sampling period would be spread in a circle around the mainlobe at an angular distance predicted by Equation 2-5. To confirm this a 9 armed log spiral with a 12λ aperture and a pitch of 20° was simulated. For comparison two different sampling

periods were used; the first was sampled at λ/2 intervals, while the second was sampled at λ intervals. The arrays are shown in Figure 5-27, along with their directivities when they are steered to $\theta_s = 90°$, $\varphi_s = 0°$. The minimum element radius is 0.75λ, calculated using Equation 5-13. The λ/2 sampled array uses 288 elements, while the λ sampled array uses 153 elements. Rounding the number of elements in an arm to the nearest integer causes the number required for λ/2 sampling to be slightly less than double that of the λ sampled array. These arrays and their directivities are compared in Figure 5-27

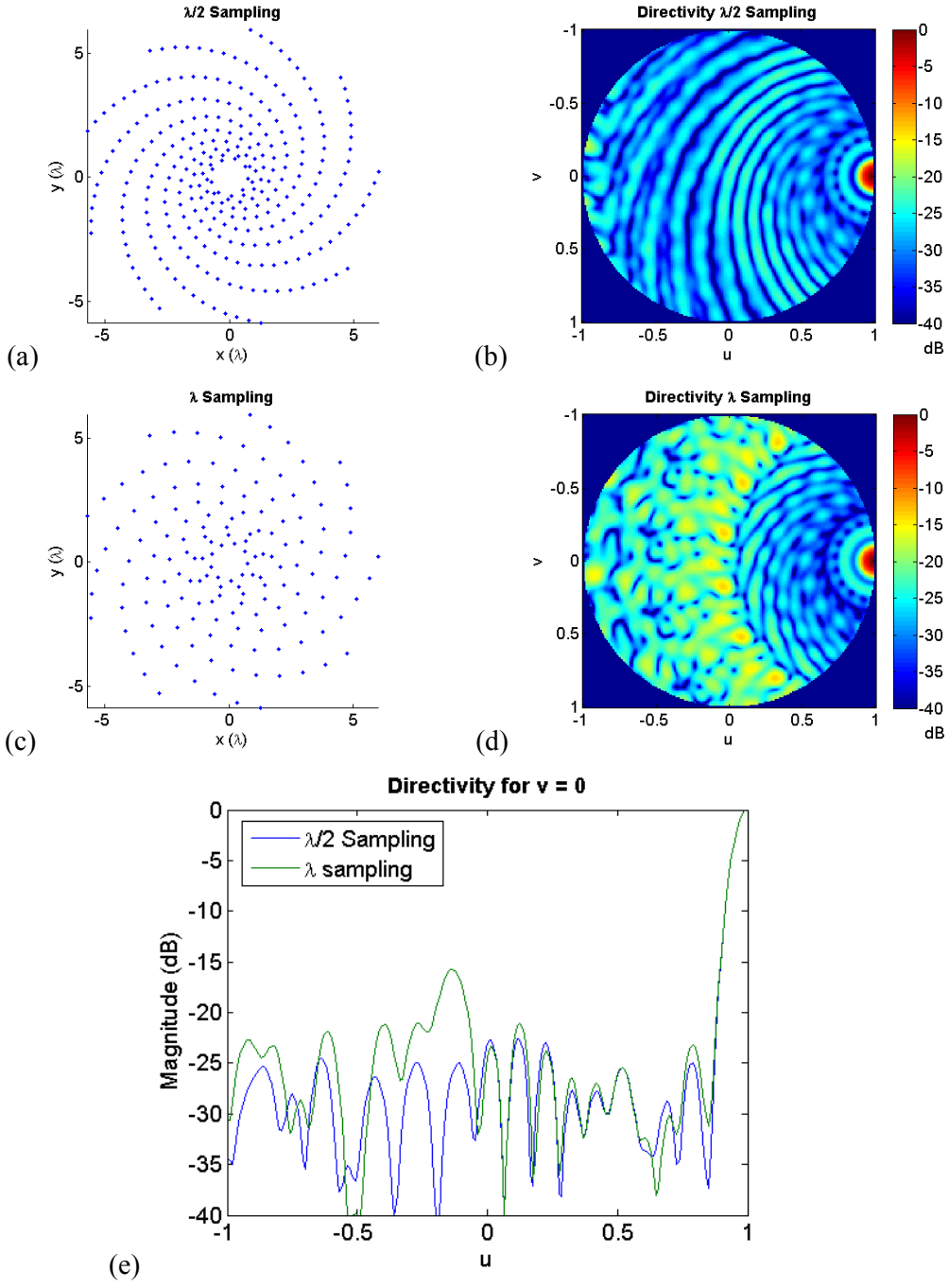

Figure 5-27 **9 armed log spirals shown alongside their directivities for $\theta_s = 90°$. The spirals are sampled with with two different spacings, (a), (b) λ/2 spaced array and directivity, (c), (d), λ spaced array and directivity And (e) slice of both directivities through $v = 0$.**

As expected the λ sampled design has a higher sidelobe level, with a peak of -15.8 dB at u = -0.035, or -2°. This sidelobe appears slightly out of the v = 0 slice, but can be seen on the u-v plane plot. It is 9.1 dB higher than the peak sidelobe in the λ/2 sampled design of -22.6 dB. This is slightly outside the angle of 0° predicted by Equation 2-5, but this error can be attributed to the complex interference pattern created by the array structure. The equation is sufficiently accurate to be used as a design guidline, since.maximum steering angles are generally specified in tens of degrees.

Substituting 90° for θ_g, and 1 for n in Equation 2-5, and rearranging for array pitch, d, the pitch required to avoid grating lobes is obtained:

$$d = \frac{\lambda}{1+\sin(\theta_{s\max})} \qquad \textbf{(5-19)}$$

This gives a pitch of λ for a maximum steering angle of 0° (no steering), which rises to λ/2 for a steering angle of 90° (full hemisphere).

For very sparse designs under sampling using a linear approach, or even using aperiodic sampling strategies may be of use. However, to realise the full performance of the continuous log spiral functions that have been derived, linear sampling according to Equation 2-5 should be used. This allows a discrete array to be created from a continuous spiral function, without increasing sidelobe height within the steered range. The optimal size for the elements in this discrete array is discussed in the following section.

Key design points discussed in this section were:

- To achieve the performance of a continuous log spiral using discrete elements a linear element spacing along the length of the arms should be used.

- The required pitch should be calculated in the same manner to a linear array using Equation 5-19.

- Linear sampling along the arm is converted into radial points using Equation 5-18.

5.9 Element size and shape

So far the elements in the array have been assumed to be omnidirectional point sources. However, in practice array elements must cover a finite area. Large elements are more sensitive, but produce a narrower beam pattern. Small elements have a wide beam pattern, but have lower sensitivity.

A second consideration is the shape of the array element. Since most 2D arrays are in the form of grids, array elements are often made rectangular in shape. However, this gives them an aperture which varies with rotation, corresponding to a change in the directivity. This can be avoided by using circular elements, which have constant aperture. Equation 4-7 and 4-8 give the directivities of rectangular and circular apertures respectively. Figure 5-28 shows simulations of both a square and a circular aperture with a_x, a_y, and a all equal to 1.5 λ.

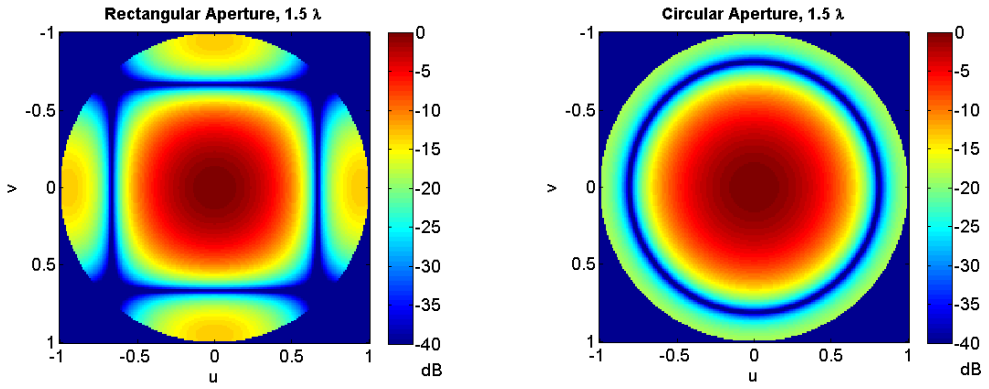

Figure 5-28 **Simulated directivities of array elements with apertures of 1.5 λ, (a) square element and (b) circular element.**

In the case of the rectangular element, the -3 dB beam width is decreased by a factor of $\sim\sqrt{2}$ for rotational angles of φ = 45°, while the beam width of the circular

element remains constant. It is therefore recommended to use circular elements for volumetric imaging applications to avoid narrowing the steerable angle of the array for angles of $\varphi = 45°$.

Rectangular elements offer some advantages for use with 1-3 piezocomposite arrays (see Chapter 6), since they conform to the underlying structure of the composite. This allows the designer to avoid pillars which are only partially electroded, and the associated lateral movement in the device that these can induce. However, for spiral array design element locations do not conform to a grid structure, so even rectangular elements may not align with the pillar structure. The solution pursued here is to ensure a high pillar aspect ratio, creating many pillars per element, and ensuring the effect of partially electroded pillars is minimised. The alignment of the electrode with the underlying pillar structure is discussed further in Chapter 6. This approach allows the use of circular elements, and their associated directivity benefits.

The effect of the limited beamwidth of array elements is to reduce the strength of the mainlobe as it is steered to larger elevation angles. Figure 5-29 shows directivities of a 9 armed, 12 λ aperture log spiral with 162 elements. The first directivity is with omnidirectional elements, while the second is with 1.5 λ circular elements. The array is steered to an elevation of 60°. The large elements have the effect of increasing the relative height of the peak sidelobe from -17.4 dB to -10.6 dB.

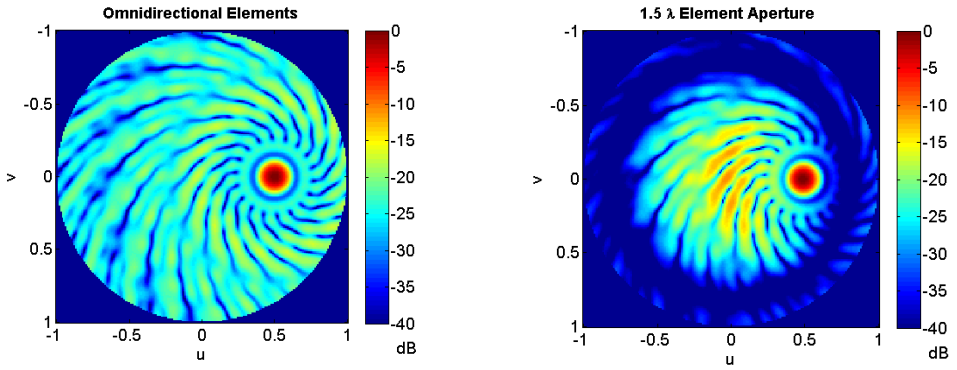

Figure 5-29 **Directivity of a 9 armed log spiral, (a) omnidirectional elements and (b) circular elements, with aperture 1.5 λ.**

To avoid this increase in sidelobe height, and the resulting loss in contrast, the aperture of array elements must be carefully chosen so that the increase in sidelobe height at the maximum steering elevation is acceptable. This can be done using Equation 5-15. One final practical consideration which is especially important for spiral arrays is that the elements should not overlap. In some cases, especially in multi armed spirals, it may be necessary to reduce the size of array elements to avoid overlap at the centre of the array.

Key design points discussed in this section were:

- Circular elements are well suited for volumetric imaging, as they have rotationally uniform directivities.

- Array sensitivity is proportional to element size, but increasing element size limits the maximum steering angle. Equation 5-15 can be used to asses the increase in sidelobe height for a specified element size and maximum steering angle.

5.10 Optimum Number of Arms

The previous sections have described efficient methods for determining the minimum radius of log spiral array elements, their spacing, and their size. It has also been made clear that an odd number of spiral arms is most efficient, and that sidelobe height can be reduced by increasing the length of the array. What remains is to characterise the optimum number of arms for a given length of spiral.

It is clear that for a given length of log spiral a number of design solutions exist. As the number of arms in the spiral is increased, the pitch of the design can also be increased to maintain the overall length of the spiral. In this section the peak sidelobe height is used as a performance measure to determine the best strategy for selecting the number of arms in a spiral design.

There is a lower limit for the length of a spiral with N_{arms} arms, which occurs when p = 90°, and the arms are straight. Below this length, L_{min}, no designs exist for that value of N_{arms}. L_{min} is calculated as follows:

$$L_{\min} = N_{arms}\left(\frac{D}{2} - R_{\min}\right) \qquad \textbf{(5-20)}$$

Substituting in R_{min} from Equation 5-13 this becomes:

$$L_{\min} = N_{arms}\left(\frac{D}{2} - \frac{D}{16}\right) = \frac{7N_{arms}D}{16} \qquad \textbf{(5-21)}$$

There are practical limits to the minimum pitch and the maximum number of arms to avoid overlapping elements, and these are discussed later in the section.

Consider a series of log spirals each with an aperture of 12 λ, and a total length of 64 λ. Rearranging Equation 5-21 to calculate N_{arms} gives an answer of 12.19, meaning

that the maximum number of arms that could be supported is 12. Since it has been shown that odd numbers of arms result in lower sidelobes the maximum number of arms that should be used is 11.

Figure 5-30 and Figure 5-31 show designs with odd values of N_{arms} ranging from 1 to 11, alongside their directivities. The arrays images are continuous spirals created on a $\lambda/20$ grid, and the directivities are calculated using the 2D FFT. The peak sidelobe levels for each design are shown in Figure 5-32.

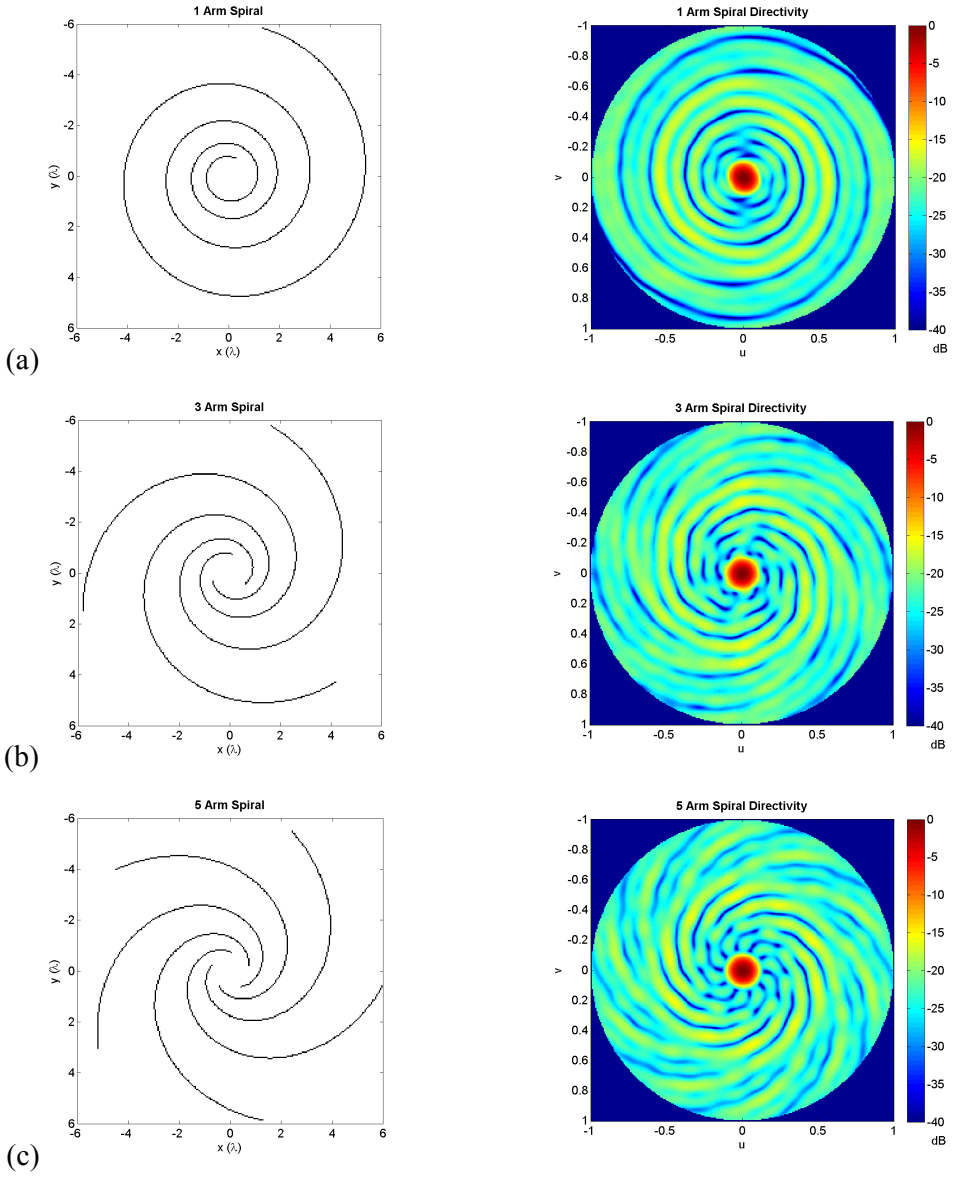

Figure 5-30 **Directivity of log spiral arrays with 12 λ apertures, and 64 λ total lengths. The number of arms in each design is odd, varying from 1 to 5. The left column shows array designs, while the right column shows array directivities, (a) 1 armed, (b) 3 armed and (c) 5 armed.**

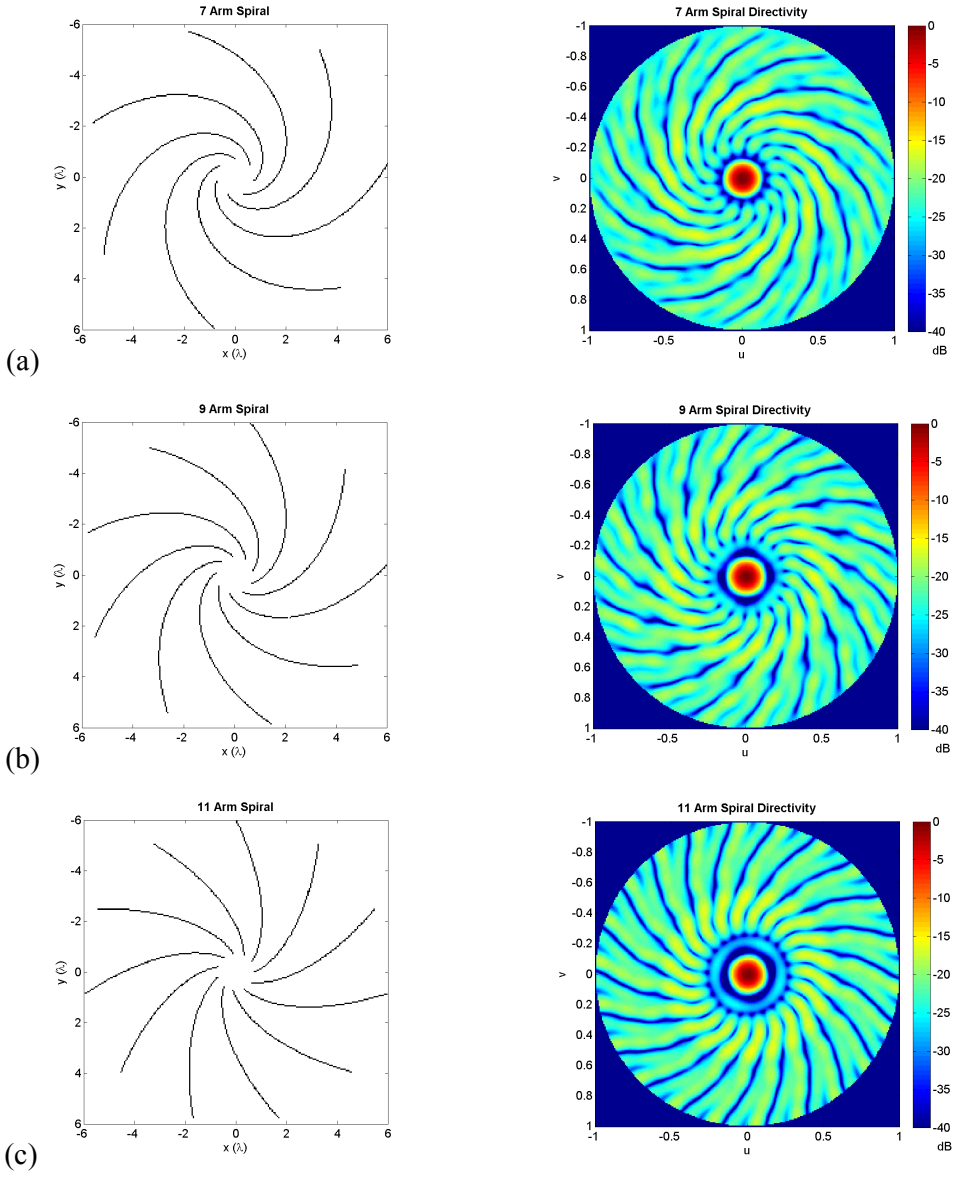

Figure 5-31 **Directivity of log spiral arrays with 12 λ apertures, and 64 λ total lengths. The number of arms in each design is odd, varying from 7 to 11. The left column shows array designs, while the right column shows array directivities, (a) 7 armed, (b) 9 armed and (c) 11 armed.**

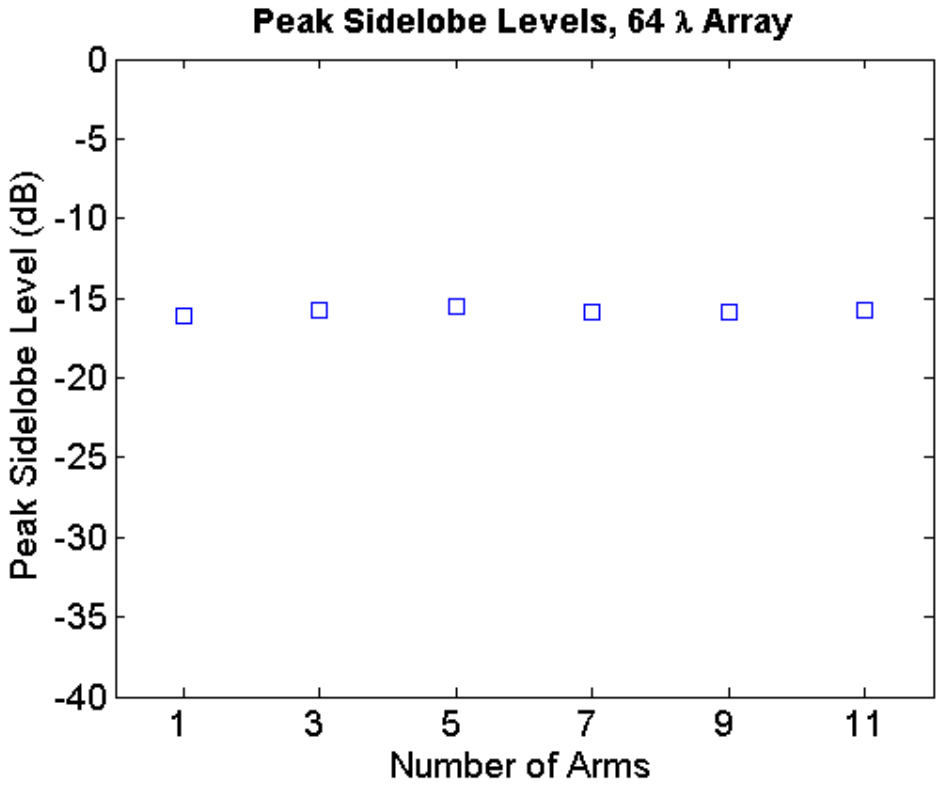

Figure 5-32 The peak sidelobe levels of the arrays shown in Figure 5-30.

Although the precise pattern of the sidelobes varies with the number of arms, the peak sidelobe level remains relatively constant, with an average of -15.8 dB. The single armed array is slightly different in that its aperture varies slightly with φ, causing a small distortion to the shape of the mainlobe. This effect is negligible for the arrays with 3 arms and above. This result suggests that the designer has freedom to choose the number of arms in the array, with little effect on sidelobe height.

To investigate whether or not sidelobe height is independent of N_{arms} for all values of array length, this simulation was repeated for lengths varying from 10 λ to 350 λ, in 10 λ steps. Odd values of N_{arms} were used, in the range 1 to 21. For each design the far field directivity was simulated, and the peak sidelobe level was recorded. The results are shown in Figure 5-33.

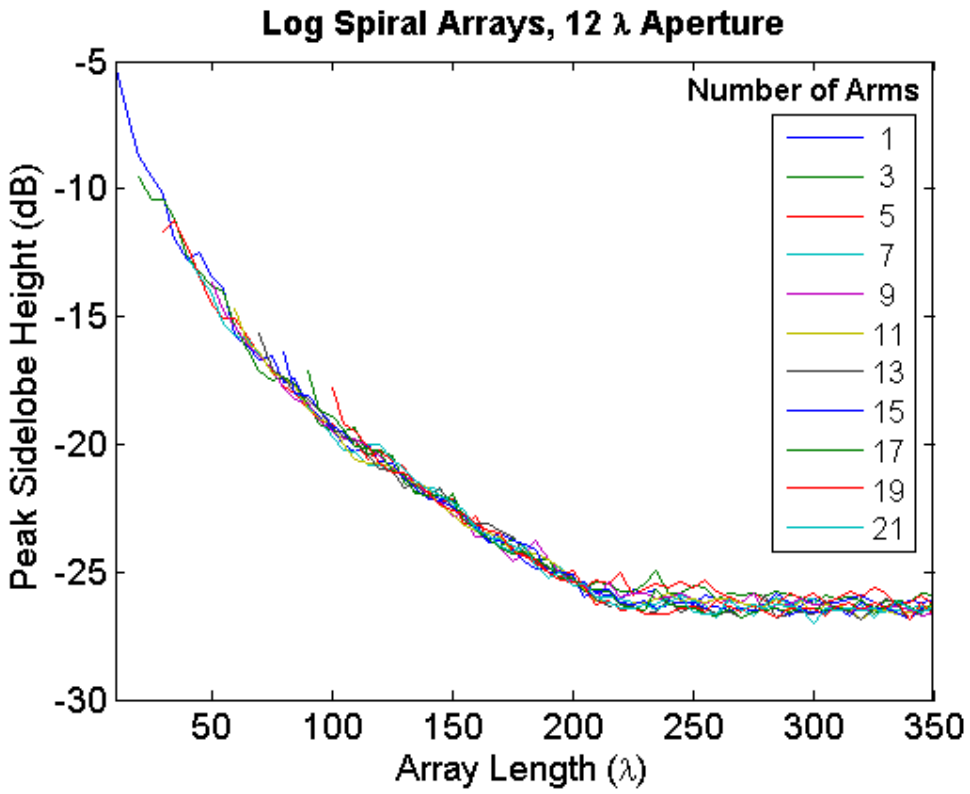

Figure 5-33 **Peak sidelobes for log spiral arrays with 12 λ aperture. Array length is varied between 10 and 350 λ, and N_{arms} takes odd values from 1 to 21.**

As with the previous example peak sidelobe level varies very little as the number of arms is changed. One possible exception to this is for the shortest arrays with 13 to 19 arms, which appear to have sidelobes which are 1 to 1.5 dB higher than the average value for that array length. It has already been shown in Section 5.5 that straight arms cause higher sidelobes, and these designs have pitches between 77 and 86 degrees, making their arms close to vertical.

As expected, the sidelobe level is heavily dependent on the length of the array. Sidelobe level decreases with length, until a length of approximately 220 λ, where it flattens off. All designs beyond this point have a peak sidelobe level of

approximately -26 dB, which corresponds to the underlying sidelobe floor of the log spiral distribution, as discussed in Section 5.7.

To characterise the best possible performance that can be achieved, the design with the lowest sidelobe level is selected for each array length. The analysis was repeated for apertures of 8, 16 and 20 λ, and the results are shown in Figure 5-34.

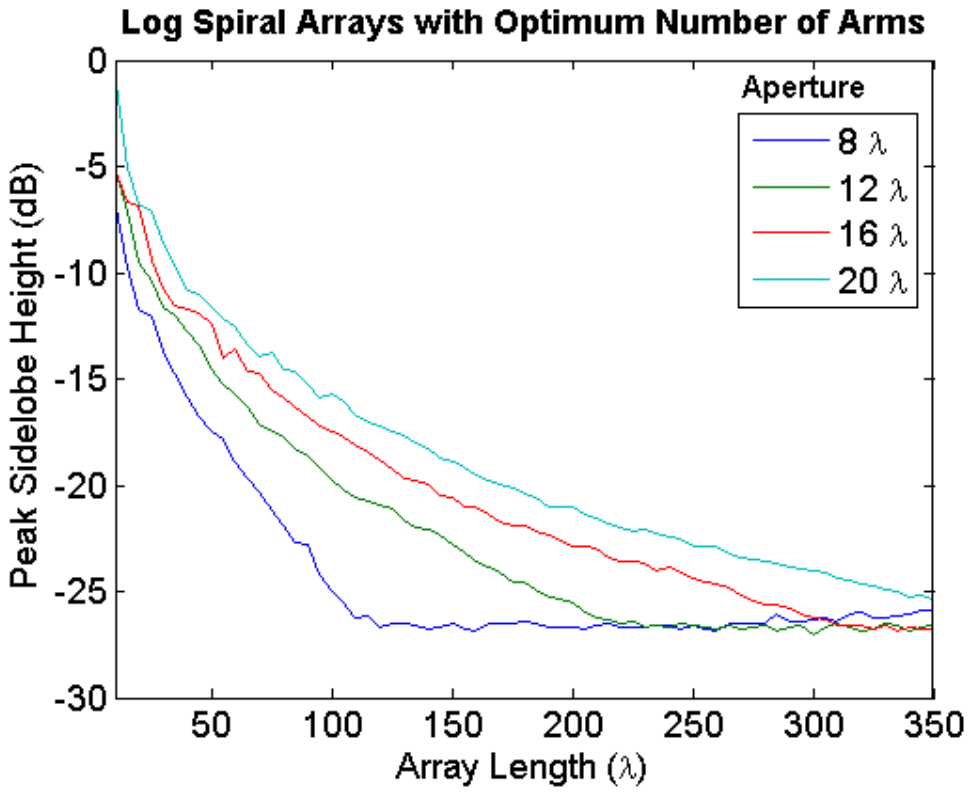

Figure 5-34 **Peak sidelobe levels for log spiral arrays of various apertures. In each case numbers of arms between 1 and 21 were simulated (odd values), and the lowest peak sidelobe plotted.**

For the results up to an aperture of 16 λ, sidelobe height decreases as the array length is increased, until a peak sidelobe height of -26 dB is reached. The graph then flattens out. The 20 λ device is still decreasing at an array length of 350 λ, indicating

that it is yet to reach the point where the sidelobes associated with the log spiral distribution become dominant. At values above -26 dB the reduction in sidelobe level is very close to an exponential decay. This can be seen clearly in with the data is re-plotted against the log of array length.

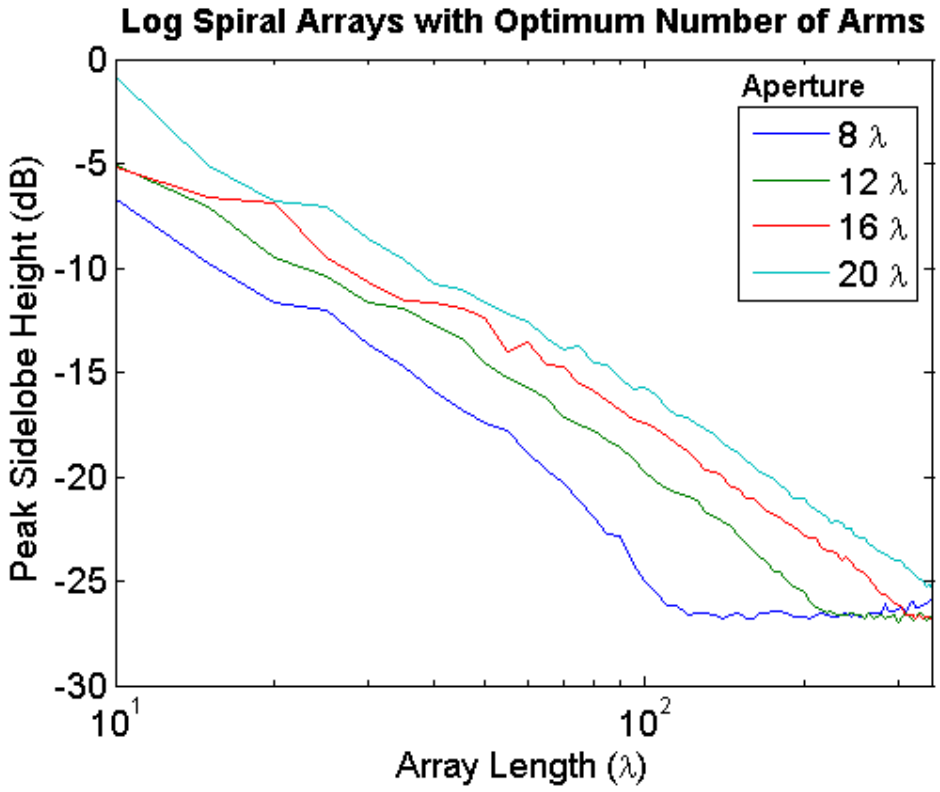

Figure 5-35 Peak sidelobe data from Figure 5-34 re-plotted against the log of array length.

The zero crossing point and the gradient of this data varies with in a non linear fashion with both array length and aperture. This means that curve fitting to this data to obtain an expression for array performance is very approximate. Overall the reduction in peak sidelobe height with increasing array length is approximately 16 dB per octave.

The results in Figure 5-34 and Figure 5-35 illustrate the performance that can be achieved using log spiral arrays. It has already been shown in Section 5.8 that when these designs are sampled with at least λ/2 spacing they can be used to create arrays with discrete elements with no degradation in performance. There are however some limitations that arise when creating practical arrays, caused by the need to avoid overlapping elements. Therefore, some additional rules are required to avoid these overlapping designs.

On first inspection there are two situations which can cause elements to overlap:

- The number of arms specified means that the first elements in adjacent arms are closer than the element width, and overlap.

- The pitch is low enough that adjacent arms are closer than the element width, and the elements overlap.

These two situations are illustrated in Figure 5-36. The separation of arms at the centre of the array, d_c, is given in Equation 5-22. If the element aperture, a, is substituted for d_c, then the equation can be arranged to give the maximum number of arms that can be used, as shown in Equation 5-23.

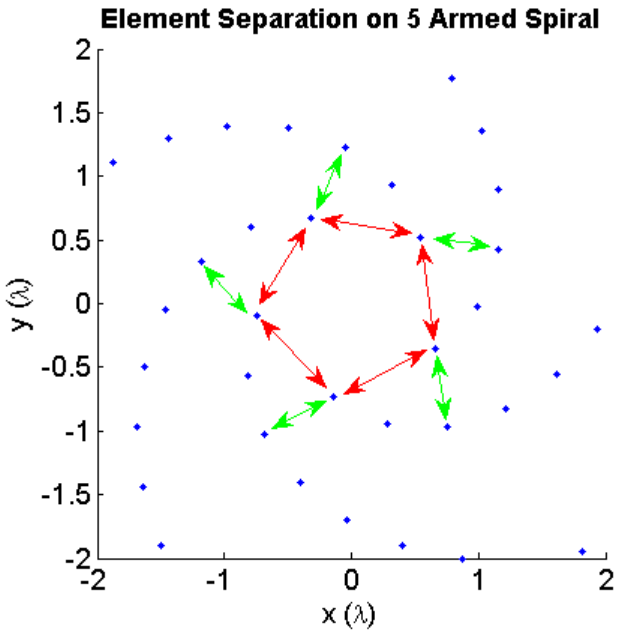

Figure 5-36 **The centre of a 5 armed spiral, with two types of critical element spacing illustrated. Shown in red is the gap between successive arms around the centre of the array. Shown in green is the gap between adjacent arms as the outer arm passes the inner arm.**

$$d_c = \frac{\pi R_{\min}^{\ 2}}{N_{arms}} \qquad (5\text{-}22)$$

$$N_{arms} = \frac{\pi R_{\min}^{\ 2}}{a} \qquad (5\text{-}23)$$

The more general problem of overlapping elements is influenced by the number of arms and also the pitch of the arms. To help avoid these overlapping designs a function was written in Matlab to display the array layout, taking into consideration the element size. An example of one of these plots is shown in Figure 5-37, showing a 7 armed array with λ/2 elements, which has no element overlap.

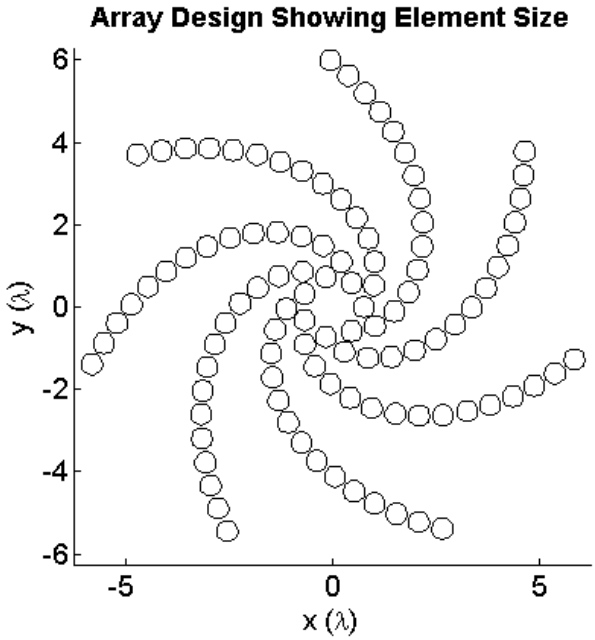

Figure 5-37 **A 7 armed log spiral array with circular elements plotted to access element overlap.**

When the design guidelines produce an array which has overlapping elements a number of techniques can be used to spread the elements out, producing a practical design:

- Increase R_{min} to provide more space at the centre of the array. Although this alters the element distribution and as a result, the fundamental minimum sidelobe heights of the array, these are often not the dominant sidelobes in the design. This will have a small effect of beamwidth, so care must be taken that the design does not deviate from specification.

- Reduce the element size. This has the benefit of increasing element acceptance angle, but will reduce the overall sensitivity of the array.

- Increase the element pitch, *d*. This will reduce the maximum steering angle.

- Increase the number of arms in the array to the maximum allowed by Equation 5-23. This has been found to achieve optimum packing for a given design.

A combination of these techniques may be use to adapt array designs to make them more practical to implement. Consider an array which is required to have an aperture of 12λ, and element spacing of 0.6 λ, and a peak sidelobe level of -19 dB. Using the standard design technique, a 9 armed array would be created, with a pitch of 28 degrees, and 180 elements. However, this approach has overlapping elements at the centre of the array, and could not be constructed in practice. The highest pitch that can be used which avoids overlapping elements is 50°, but this design has a sidelobe height of -16.1 dB, and uses only 117 elements. Both of these designs are shown in Figure 5-38.

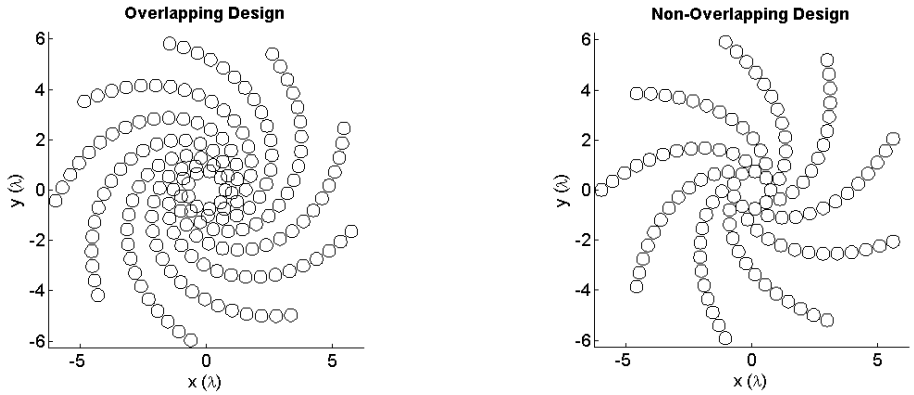

Figure 5-38 **A design with a pitch of 28°, and 180 elements can achieve the design requirement of -19 dB peak sidelobes, with a peak of -19.7 dB, but has overlapping elements. The highest performance design with no overlap has a pitch of 50°, and 117 elements, but has a higher sidelobe level of -16.1 dB, (a) overlapping design and (b) non-overlapping design**

The solution employed here is to increase R_{min} in order to allow a larger array to be constructed, with no element overlap. Figure 5-39 shows a design where R_{min} has been increased from the standard 0.75 λ calculated using Equation 5-13, to 1.5 λ. With this increase, more room is afforded at the centre of the array, and the element distribution is sufficiently smooth to avoid its inherent sidelobes from dominating. The result is an array with 11 arms, a pitch of 30°, 187 elements, and a peak sidelobe level of -19.2 dB. The array uses approximately the same number of elements as the overlapping design, indicating little reduction in efficiency due to the increase in R_{min} This technique allows higher performance arrays to be constructed than would be practical under the standard design technique.

One final adaptation to the standard design rules that have been investigated has been to place a single element at the centre of the array. This has very little effect on array performance since it is a single element, and its central position does not induce skew into the beam. However, it can be useful for alignment purposes during experimentation, and provides an increase in sensitivity, albeit small.

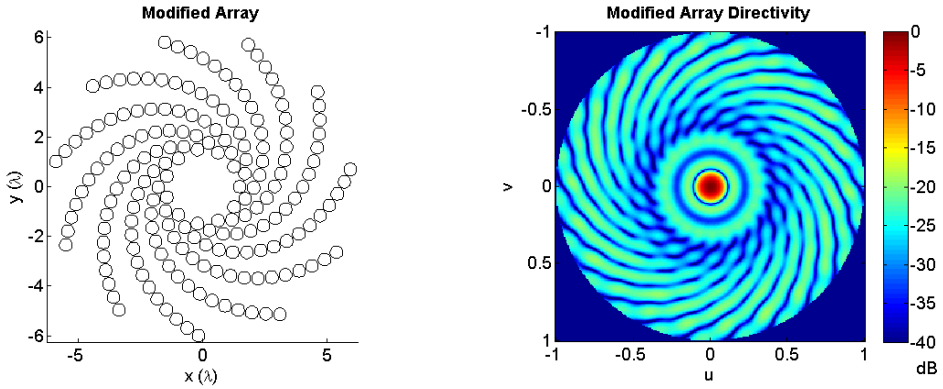

(a) (b)

Figure 5-39 **Directivity of array where R_{min} has been increased to allow both more arms to be added, and a lower pitch to be achieved, increasing the number of elements to 209. The peak sidelobe level is -19.2 dB, (a) array design and (b) array directivity.**

Key design points discussed in this section were:

- Increasing the total length of the array reduces the peak sidelobe level by 16 dB per decade.

- Sidelobe level is relatively insensitive to the number of arms in the array. This means that the number of arms can be selected purely to improve the practicality of array layout. Equation 5-23 specifies the maximum number of arms that can be used for a given element size

- Some array designs may have overlapping elements, depending on the desired element size. However, R_{min}, a, d, and N_{arms} can be adjusted to avoid overlap.

5.11 Near field Performance

To this point the analysis of log spiral array performance has focussed on the far field behaviour of the beam. However, ultrasonic imaging is often conducted in the near field, so it is important to characterise performance in that region.

In order to access near field performance the DRI model which is discussed in Chapter 4 is used to simulate the field created by the array across the *x-z* plane, which runs perpendicular to the array's surface. For each simulation the array was rotated to find the plane in which the worst case sidelobes occur to give an accurate assessment of performance. Of particular interest is any change in the near field beam pattern with the number of arms. The designs simulated here are steered to 30° in elevation, and focussed to a depth of 60 mm. The beams are formed in a simulated steel block, with a longitudinal wave velocity of 5,900 m/s.

A series of array designs are considered, each with an aperture of 12 λ, an element size of λ/2, and an inter element spacing of λ/2. The arrays are simulated under CW excitation at a frequency of 1.5 MHz. This results in a wavelength in the block of 3.9 mm, and an array aperture of 47.2 mm. A maximum number of elements of 128 was used, and designs were produced with 1, 5 and 9 arms. A summary of the designs and their far field performance, simulated using the 2D FFT method, is shown in Table 5-1. As predicted in Section 5.10 the sidelobe levels of the arrays are within 1 dB. Images of the array designs, including the element size, are shown in Figure 5-40. None of the designs have overlapping elements, so all would be practical to implement. The near field directivity of the arrays is shown in Figure 5-41.

N_{arms}	p (°)	N	S_p (dB)
1	4.75	128	-16.2
5	20	125	-15.6
9	55	126	-15.5

Table 5-1 **Summary of the 3 array designs, showing number of arms, pitch, number of elements, and peak sidelobe height.**

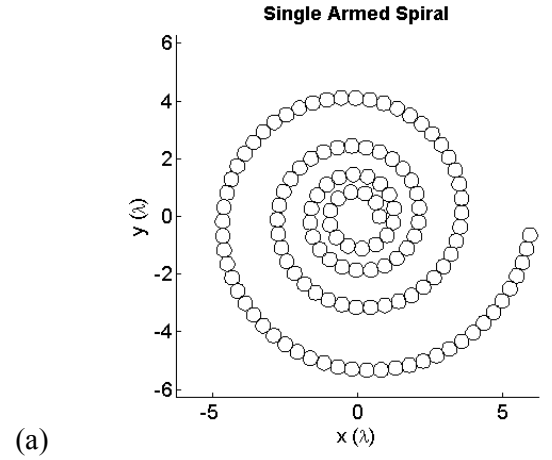

(a)

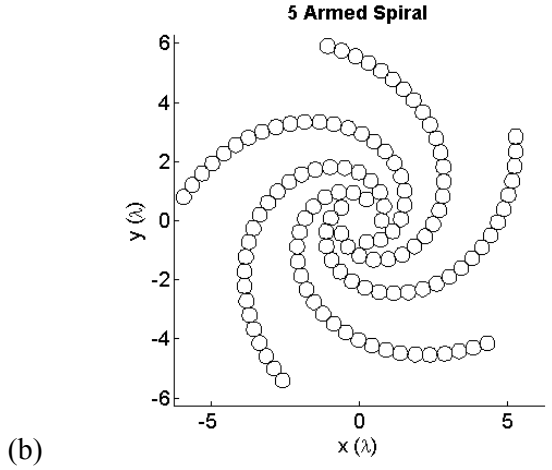

(b)

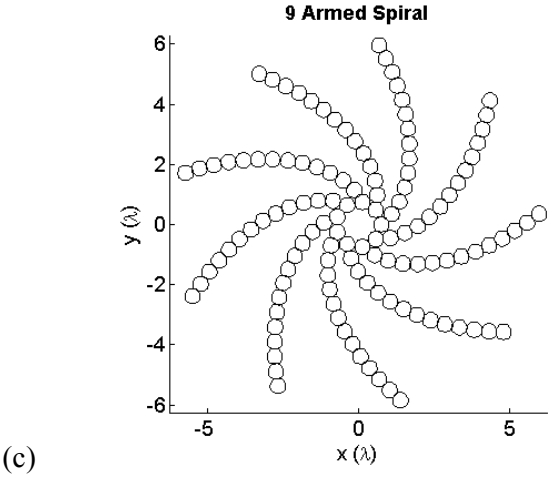

(c)

Figure 5-40 **Images log spiral designs, (a) 1 arm 128 elements, (b), 5 arms 125 elements and (c) 9 arms 126 elements.**

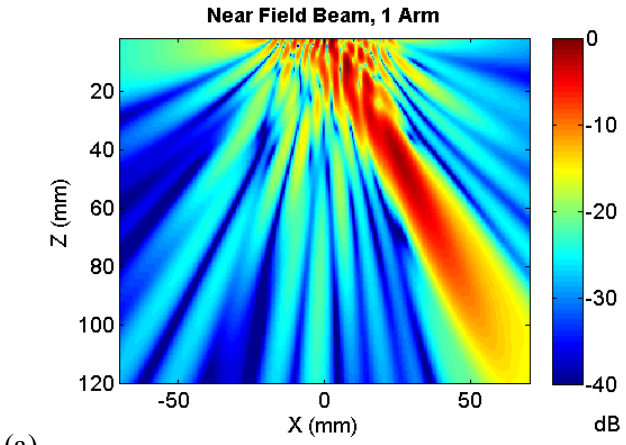

(a)

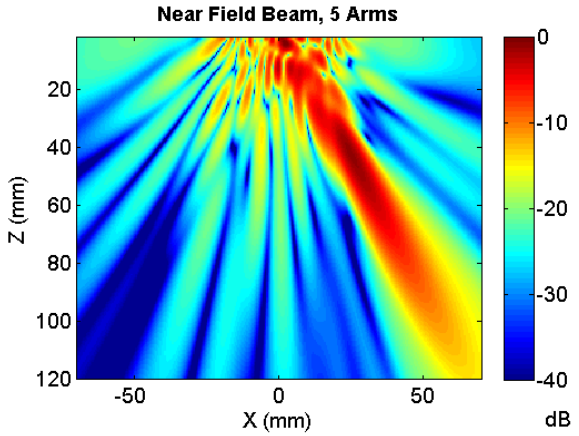

(b)

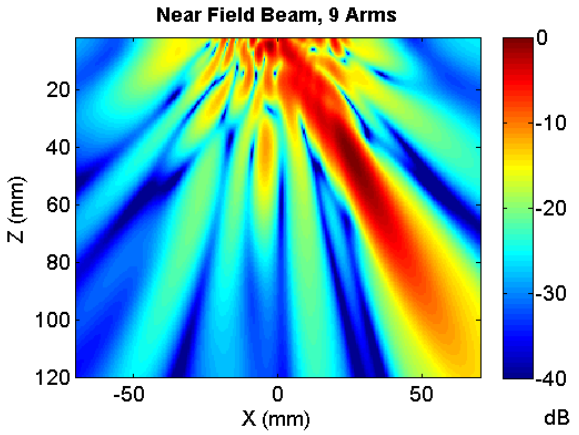

(c)

Figure 5-41 **Near field directivity of the 1, 5, and 9 armed log spiral designs in Figure 5-40 simulated in steel.**

As expected the sidelobe levels of the designs are similar, and the mainlobe has a similar focal shape. However, there are some differences in the size and distribution of sidelobes produced in the near field, before the focal point. The size of the sidelobes increases with the number of arms, and the 9 armed design appears to have a smoother axial beam in the steering direction. This is due to the more even radial distribution of elements achieved by incorporating more arms. Despite this, the 9 armed spiral has a marginally wider distribution of sidelobe energy, when compared to the 1 and 5 armed designs.

Overall there is not a clear shift in near field performance across these designs. This allows the designer to select the layout that best suits their chosen manufacturing process.

Key design points discussed in this section were:

- Focused CW near field performance does not vary dramatically with the number of arms in the log spiral, when the number of elements used is kept constant.

5.12 Summary of design method

The previous sections have outlined a series of rules to assist with the design of log spiral arrays. These are summarised in the following design process. The equations required for this design process are renamed as 'Design Equations', and are included for ease of reference.

Design Process:

1. Capture the following design requirements:

    a. The -3 dB beam width of the mainlobe, θ_w.

    b. The maximum elevation steering angle, θ_{smax}, which will be applied.

    c. The number of elements in the array, N.

    d. The peak sidelobe height, S_p.

2. Calculate the required aperture of the array, D, using Design Equation 1 (if worst case beamwidth is specified then this will give the effective aperture at θ_{smax}).

$$D = \frac{0.63}{\sin\left(\frac{\theta_w}{2}\right)} \qquad \textbf{Design Equation 1}$$

3. Calculate the minimum radius, R_{min}, using Design Equation 2.

$$R_{\min} = \frac{D}{16} \qquad \textbf{Design Equation 2}$$

4. Calculate the required element aperture, *a*, using Design Equation 3.

$$a = \frac{0.51}{\sin\left(\frac{\theta_{s\max}}{2}\right)}$$ **Design Equation 3**

5. Calculate the required element pitch, *d*, using Design Equation 4.

$$d = \frac{\lambda}{1+\sin(\theta_{s\max})}$$ **Design Equation 4**

6. Calculate the maximum number of arms, N_{arms}, that can be used, using Design Equation 5.

$$N_{arms} = \frac{\pi R_{\min}^{\ 2}}{a}$$ **Design Equation 5**

7. Calculate the maximum spiral pitch that can be achieved, using Design Equation 6 (by combining Equations 5-5, and 5-8).

$$p = \frac{\pi}{2} - \cos^{-1}\left(N_{arms} \frac{\left(\frac{D}{2} - r_{\min}\right)}{dN} \right)$$ **Design Equation 6**

8. Construct a logarithmic spiral with the calculated parameters, using Design Equations 7-10.

$$b = \frac{1}{\tan\left(\frac{\pi}{2} - p\right)}$$ **Design Equation 7**

$$L = \frac{\left(\frac{D}{2} - r_{\min}\right)}{\cos\left(\frac{\pi}{2} - p\right)}$$ **Design Equation 8**

$$r = \frac{bx}{\sqrt{1+b^2}} + R_{\min}$$ **Design Equation 9**

where x is a vector ranging from 0 to L in steps of d.

$$\gamma = \frac{1}{b}\ln(r)$$ **Design Equation 10**

9. Plot the spiral, and ensure that no elements overlap. If there are overlapping elements do one of the following:

    a. Increase R_{min}, allowing N_{arms} and/or p to be adjusted.

    b. Decrease a (decreases sensitivity).

    c. Increase d (reduces θ_{smax}).

10. Evaluate peak sidelobe level, s_p, of resulting design using DRI.

5.13 Comparison with standard designs

Now that the performance of log spiral arrays has been characterised it is useful to compare this performance to that of more standard array designs. This will be done for each of the following scenarios:

- Far field steered directivity, under CW excitation.
- Far field steered directivity, under pulsed excitation.
- Near field focused directivity, under CW excitation.
- Near field focused directivity, under pulsed excitation.

These comparisons will be carried out under constant beamwidth of 4.5°, with the peak sidelobe height plotted against the number of array elements. All arrays in the comparison will be capable of steering to a maximum elevation (θ_{smax}) of 90°, so the spacing of any periodic aspects of the arrays will be λ/2. To avoid element overlap, and to permit a wide steering, circular elements will be used, with an aperture of 0.45 λ. The array designs that will be used for comparison are:

- λ/2 spaced periodic grid.
- λ/2 spaced segmented annular.
- Random distribution.

For both periodic design methods there is only one design which will meet the specification. This is in contrast to the aperiodic design, where a wide variety of element counts can be employed, with varying performance. To illustrate this log

spiral and random arrays were designed with three different maximum element limits; 128, 256, and 512. While these numbers are all powers of 2, they also represent common channel counts available on current phased array controllers.

The spiral arrays require a larger aperture to achieve the same beamwidth as the grid, annular and random designs, which all have a uniform element distribution. The required aperture to achieve the target beamwidth of 4.5° was calculated using Equations 5-15 and 5-16. This results in an aperture of 16 λ for the log spiral designs, and 13 λ for all others.

The log spiral designs were created by first following the design guidelines in Section 5.12. The CW directivities of the resultant designs were then simulated to get the peak sidelobe levels. N_{arms} and R_{min} were then varied to investigate whether alternative designs exist with lower sidelobe levels. In each case a single element is inserted at the centre of the array to bring the number of elements used closer to that which is allowed. The resulting designs are illustrated in Figure 5-42 and Figure 5-43, with their design details shown in. Table 5-2.

Each spiral design has an element placed at the origin, in the centre of the array. The maximum element count that could be achieved for this aperture was 376, and this design is used in the 512 maximum element column. In cases where R_{min} has been modified the increase over the standard value has been recorded.

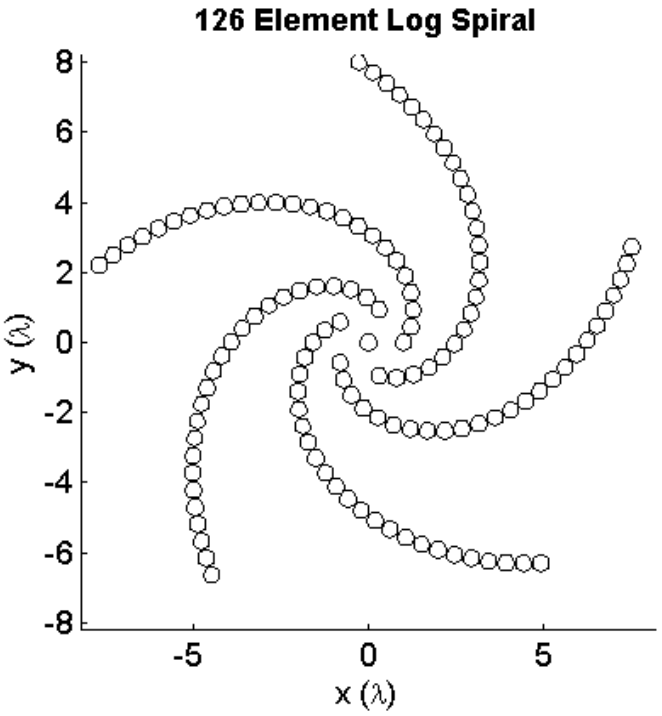

(a)

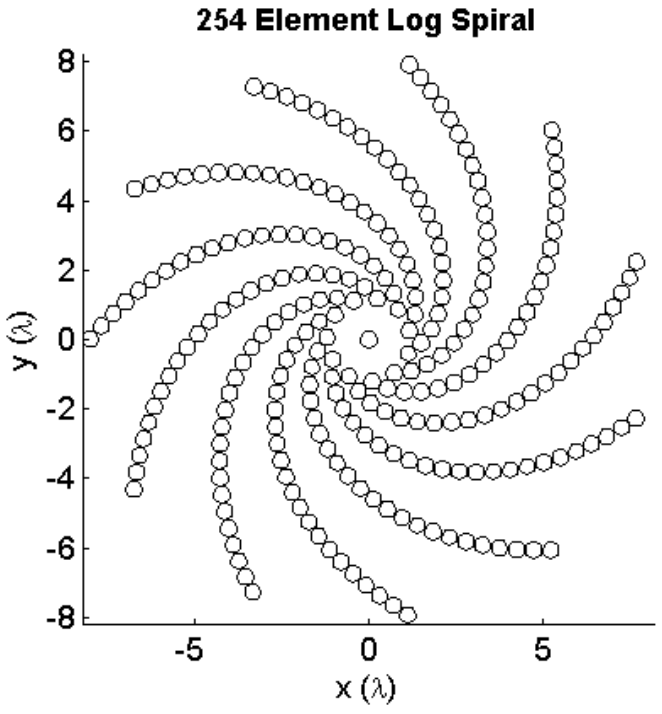

(b)

Figure 5-42 **Log spiral array designs, each with a 16λ aperture, (a) 126 element and (b) 254 element.**

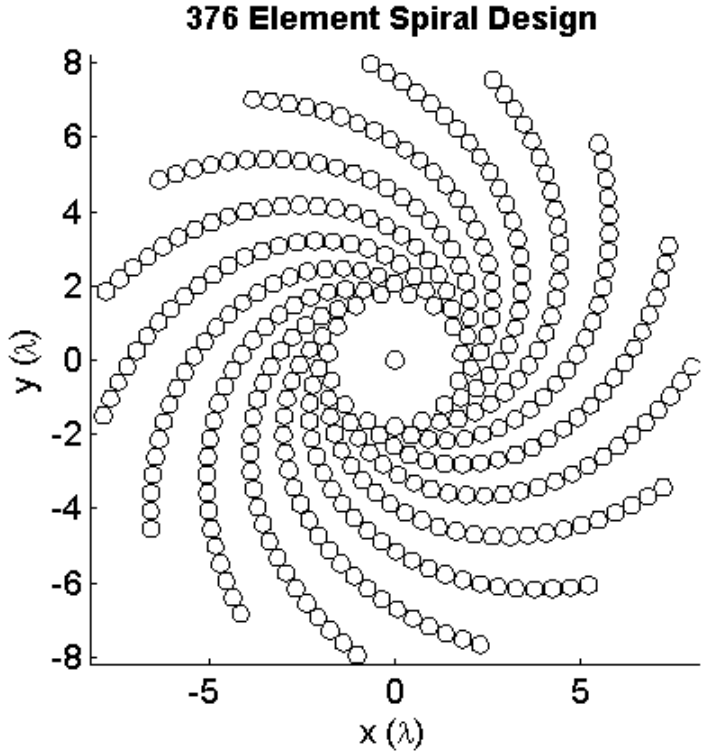

Figure 5-43 **Log spiral array design, with a 16λ aperture, and 376 elements.**

Variable	**Max Number of Elements**		
	128	**256**	**512**
N_{arms}	5	11	15
p (°)	36	39	32
R_{min} multiplier	1.0 x	1.2 x	1.8 x
N	126	254	376

Table 5-2 **Details of spiral designs used for comparison with traditional designs. The maximum number of elements that could be packed into the aperture was 376, which is less than the 512 element limit.**

For comparison random designs of 128, 256, and 512 elements were created. These designs were generated by creating a λ/2 spaced grid, with a circular aperture of 13 λ, with 540 bins. These bins were then populated at random with the appropriate number of elements, each placed at the centre of the bin. In each case 1000 designs were generated and analysed using the 2D FFT method. The design with the lowest peak sidelobe level was then selected. This method was found to be superior to the methods described in Chapter 3, which used abstract element positions, since the λ/2 spacing of the underlying grid ensures that no grating lobes are present in the beam. Images of the random array designs are shown in Figure 5-44 and Figure 5-45.

The periodic grid and annular designs also require only a 13 λ aperture, and have 540 and 579 elements respectively, as shown in Figure 5-46.

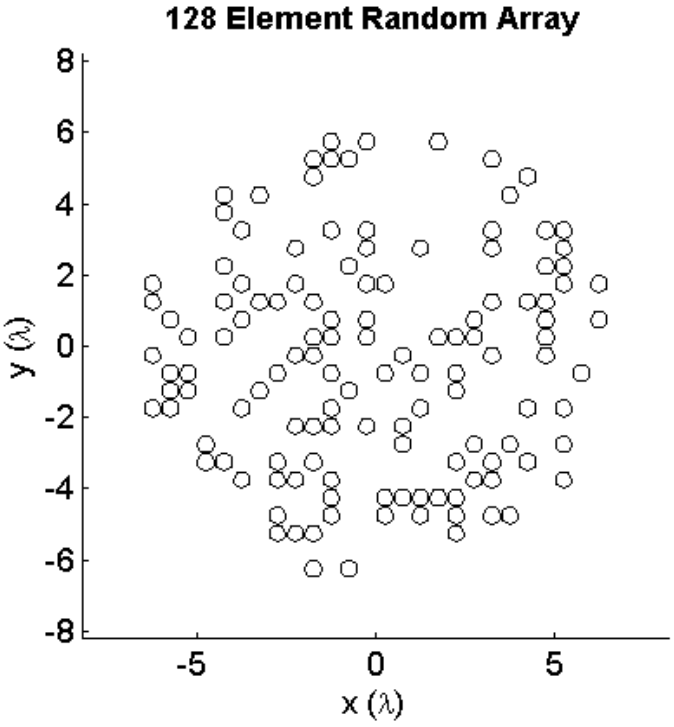

Figure 5-44 Random array design with a 16λ aperture and 128 elements.

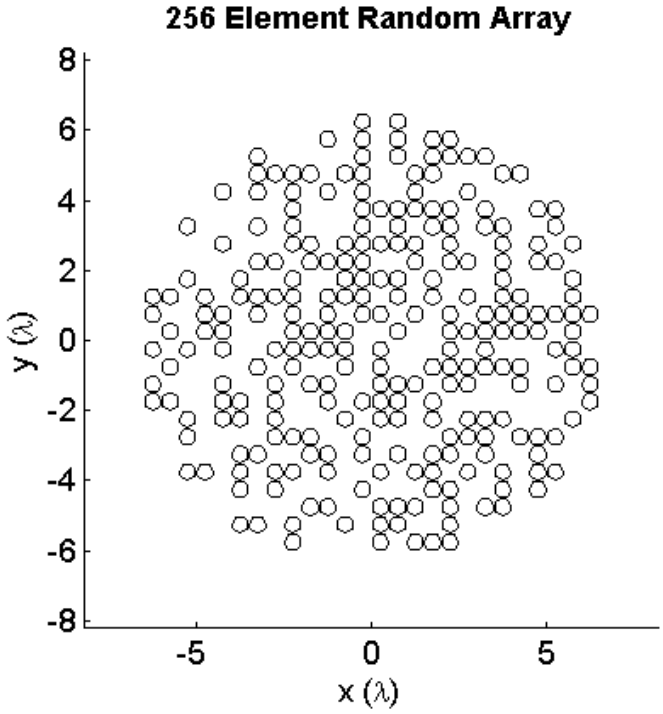

(a)

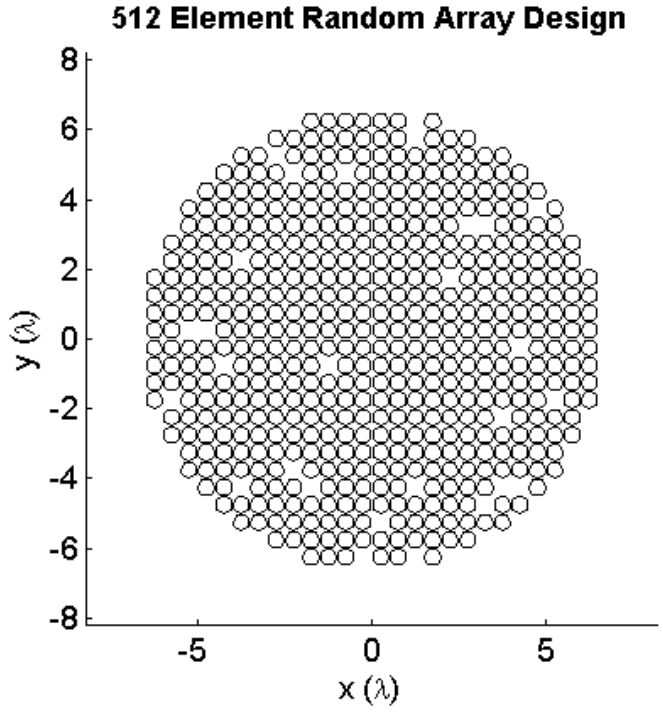

(b)

Figure 5-45 **Two random array designs each with a 16λ aperture, (a) 256 element and (b) 512 element.**

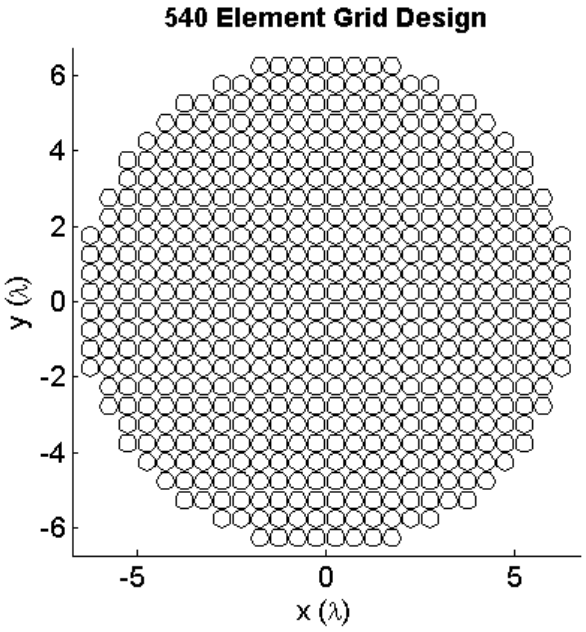

(a)

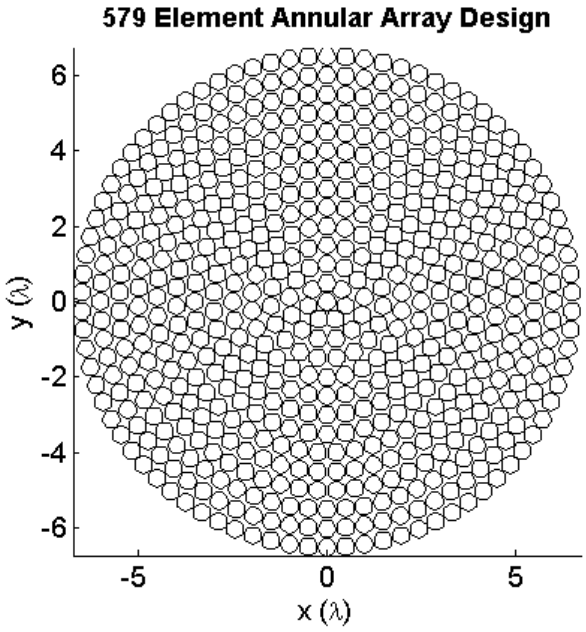

(b)

Figure 5-46 **Periodic array designs both with a 13 λ aperture, (a) λ/2 spaced periodic grid array and (b) annular array.**

5.13.1 Directivity under CW excitation

The far field CW directivity of each array design was calculated using the DRI model. This was done with no steering applied, and then repeated for θ_s=60°, φ_s=45°. The simulated beam patterns are shown in Figure 5-47, Figure 5-48 and Figure 5-49. For each array the beamwidths at -3 and -10 dB were measured, along with the peak sidelobe level, and the integrated sidelobe ratio (ISLR). ISLR measures the ratio of the total sidelobe energy, to that of the mainlobe. These were all measured in the unsteered beam. The boundary between the mainlobe and the sidelobe region was defined as -20 dB for ISLR calculations. Additionally, the peak sidelobe level was also measured in the steered beam. The results are shown in Table 5-3.

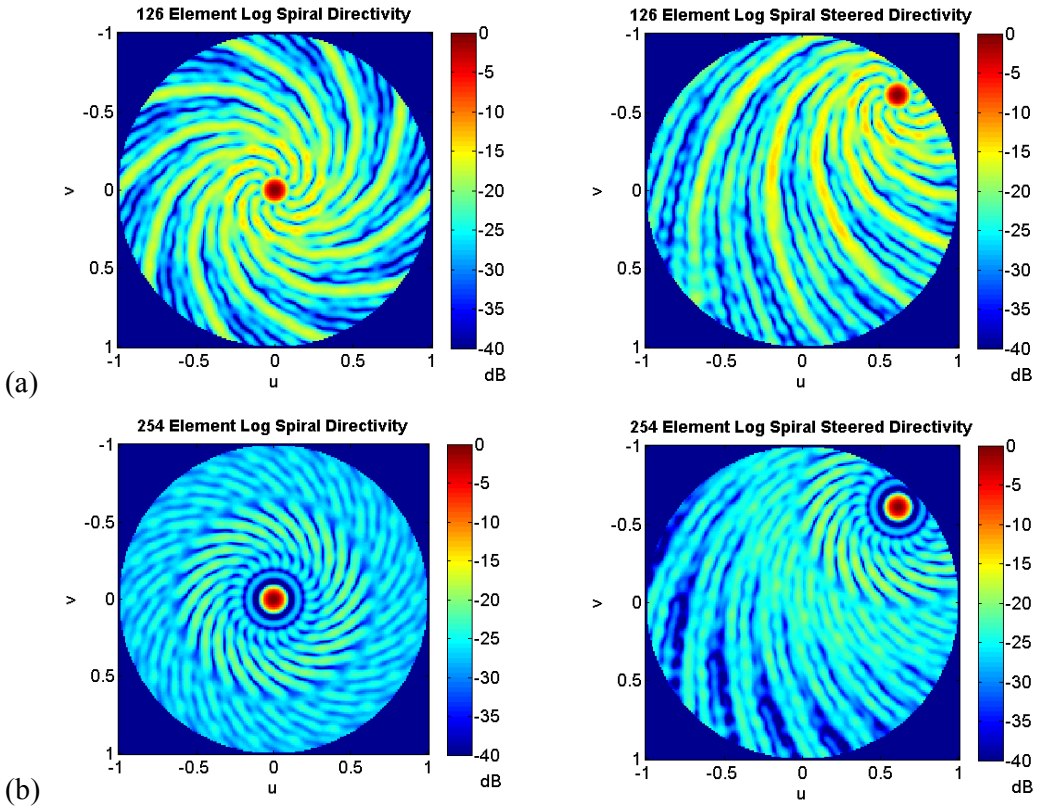

Figure 5-47 **Far field CW directivities of the 126 and 254 element log spiral arrays. Directivities in the left column are unsteered, while those in the right column are steered to θ_s=60°, φ_s=45°, (a) 126 element and (b) 254 element design.**

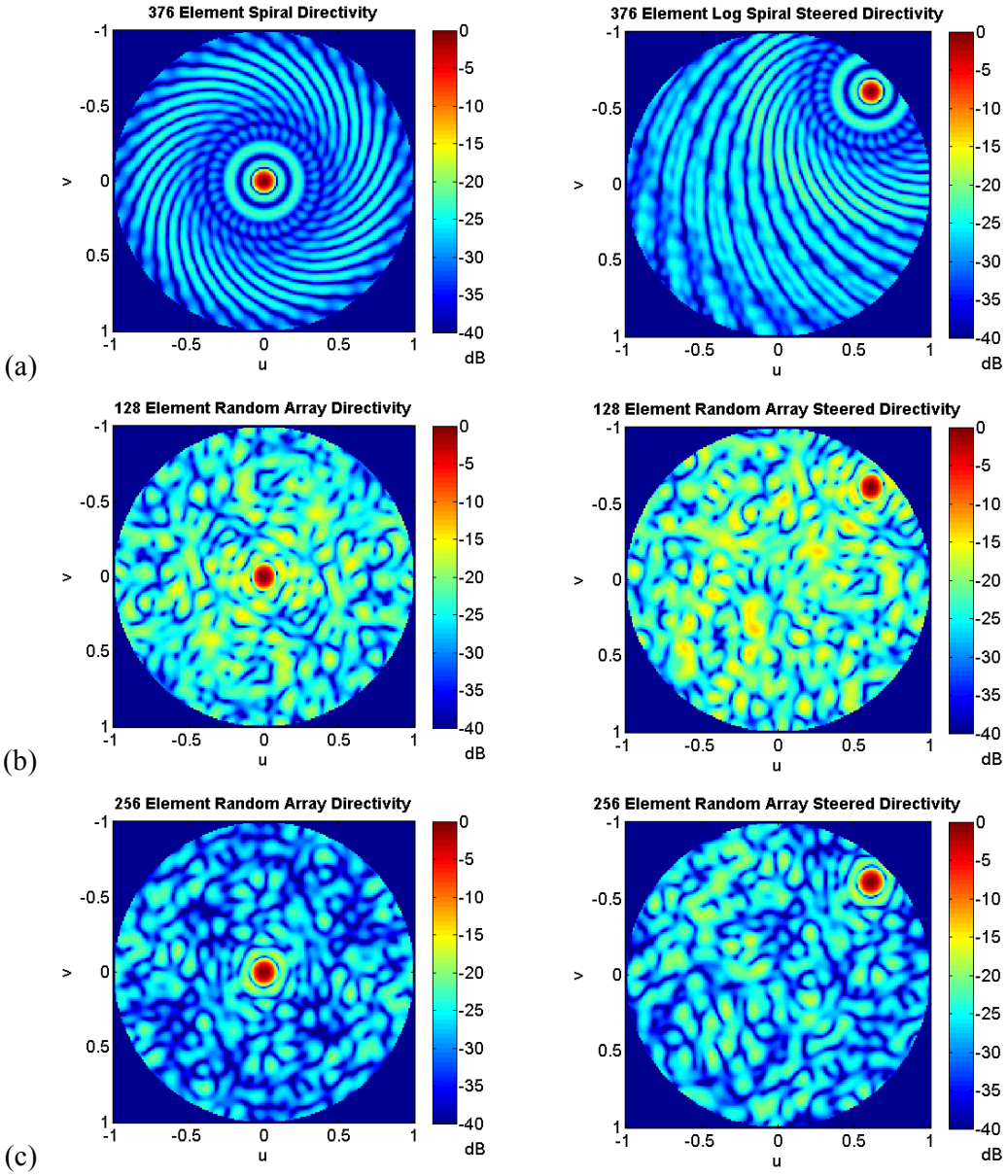

Figure 5-48 **Far field CW directivities of the 376 element log spiral array and the 128 and 256 element random arrays. Directivities in the left column are unsteered, while those in the right column are steered to θs=60°, φs=45°, (a) 376 element spiral, (b) 128 element random and (c) 256 element random design.**

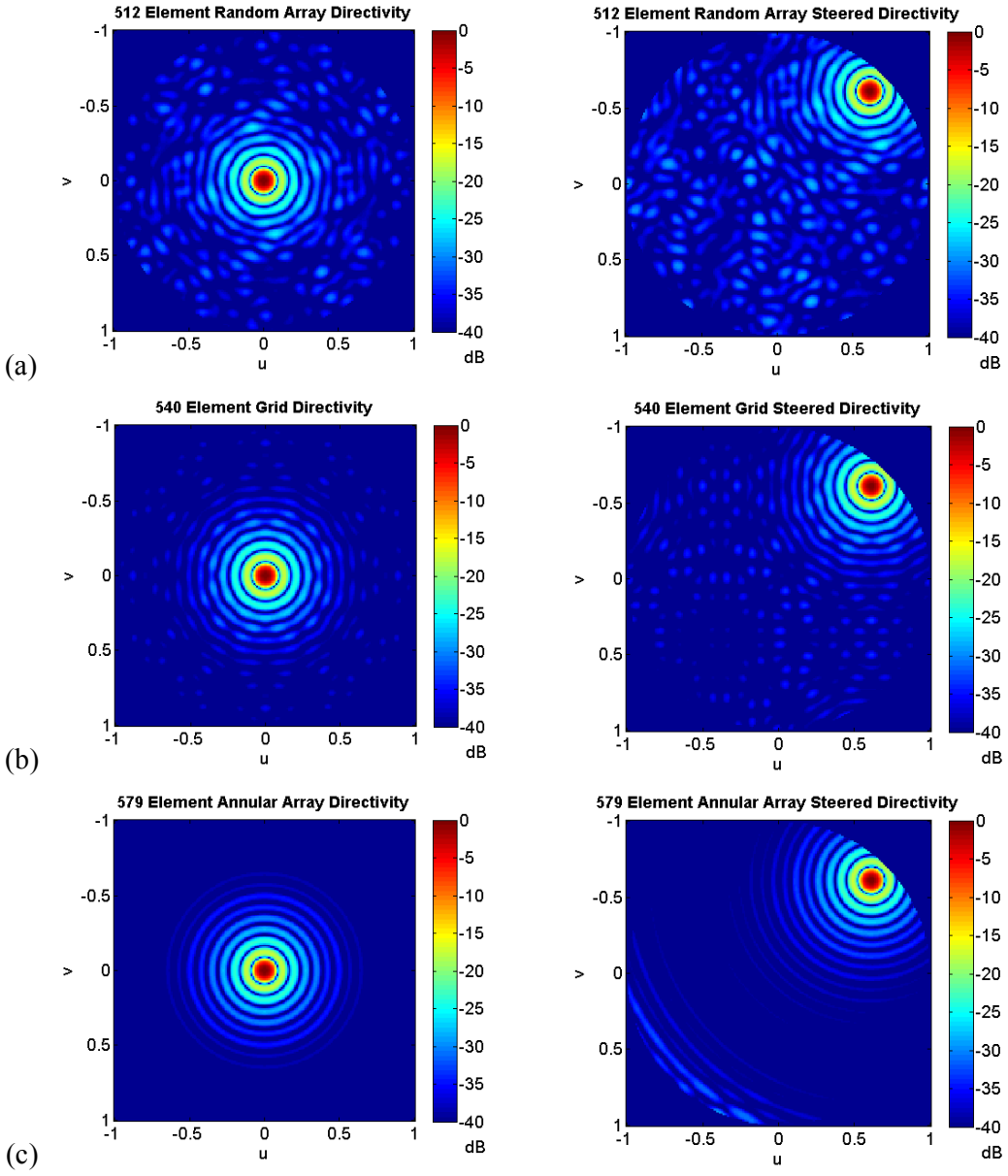

Figure 5-49 **Far field CW directivities of the 512 element random array, the 540 element grid array, and the 579 element annular array. Directivities in the left column are unsteered, while those in the right column are steered to θs=60°, φs=45°, (a) 512 element random, (b) 540 element grid and (c) 579 element annular design.**

Design	-3 dB BW (°)	-10 dB BW (°)	S_p unsteered (dB)	S_p steered (dB)	ISLR (dB)
126 Spiral	4.24	7.49	-14.10	-13.14	24.71
254 Spiral	4.16	7.30	-19.60	-17.97	23.17
376 Spiral	4.02	6.79	-21.96	-20.46	20.29
128 Random	4.30	7.30	-14.64	-13.10	23.97
256 Random	4.57	7.85	-17.75	-17.19	18.87
512 Random	4.46	7.58	-17.81	-17.37	11.05
540 Grid	4.43	7.58	-17.46	-17.10	8.76
579 Annular	4.34	7.39	-17.70	-17.34	8.88

Table 5-3 Far field CW directivity performance measurements.

All of the -3 dB beamwidths are within the design specification, with the exception of the 256 element random design, which has a beamwidth of 4.57°. The 254 and 376 element spiral designs have an increased R_{min}, which spreads their element distributions. This has the effect of decreasing their beamwidth when compared to the 126 element spiral.

The peak sidelobe levels of the arrays are shown in Figure 5-50. They are compared to the ideal spiral performance curve shown in Figure 5-34, and the probabilistic performance predictions for the random designs. A confidence interval, β of 0.1% is used, since each random array is the best of 1,000 prototype designs. The spiral designs show good agreement with the idealised curve, with small deviation on the 254 and 376 element designs due to their increased R_{min}. The unsteered sidelobe levels in the 128 and 256 element random designs are approximately 1 dB lower than the probabilistic prediction. This is expected to be partly due to the finite acceptance angle of the array elements, which is not considered in the statistical model. The

random array designs are based on a grid structure, so their performance tends to that of a dense grid as the element count is increased. This results in a departure from the probabilistic predictions, and a levelling off at approximately -17.8 dB. The 512 element random design is therefore very close to the two dense designs in terms of peak sidelobe levels, as it has 94.8% of the elements. Although the log spiral design approach was unable to achieve an element count higher than 376 elements, it achieves an unsteered sidelobe level of -21.96 dB, which is 4.59 dB lower than any of the other designs. This is despite the 376 element design having only 69.6% of the elements of the dense grid array.

The effect of steering increases the peak sidelobe level from as little as 0.36 dB on the 256 element random design, to as much as 1.63 dB on the 254 element spiral. The variation is due to the location of the worst case sidelobes in the beam. Designs with peak sidelobes far from the mainlobe, like some of the spiral designs, see a larger increase in sidelobe height, since under steering the sidelobes sit at the centre of the element directivity, and are maximised. The grid, annular, and dense random designs have peak sidelobes which are very close to the main beam, so the difference in element sensitivity under steering is minimal. This effect should be considered when selecting an array design, to ensure that the worst case sidelobe level is accommodated.

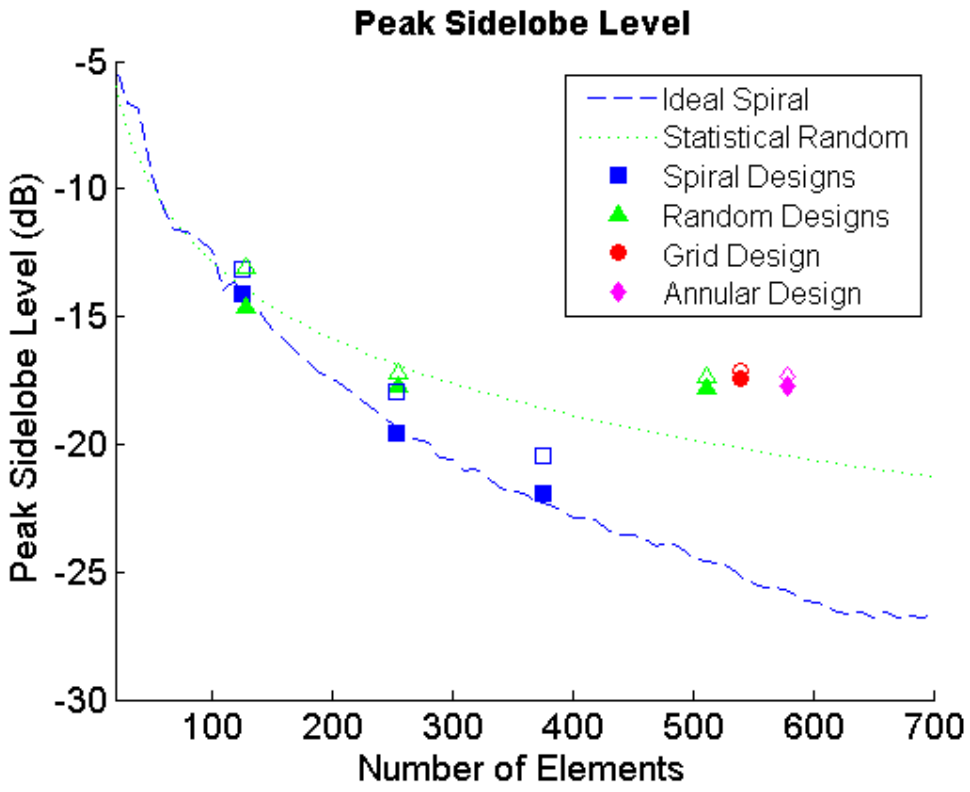

Figure 5-50 **Peak sidelobe levels in each of the simulated arrays, compared to the generalised performance predictions for log spiral and random arrays. Solid markers indicate the unsteered level, while the unfilled markers indicate steered level.**

The ISLR of each design is plotted in Figure 5-51 against the number of elements in each array. For both the spiral and random designs ISLR shows an approximately linear decrease with increasing number of elements. However, in this case the random array designs perform better than the spiral designs. As expected, the grid and annular designs have the lowest ISLRs, at 8.76 and 8.88 dB respectively. While the spiral arrays' flat sidelobe floor gives it a low peak sidelobe level, there are fewer zeros in the response when compared to the random designs. This results in the higher ISLR seen here. It suggests that spiral designs may be less suitable than random deigns for imaging in low contrast media. However, it should be considered

that the low beamwidth of the spiral designs will contribute to this result, due to the reduction in the size, and therefore power in the mainlobe.

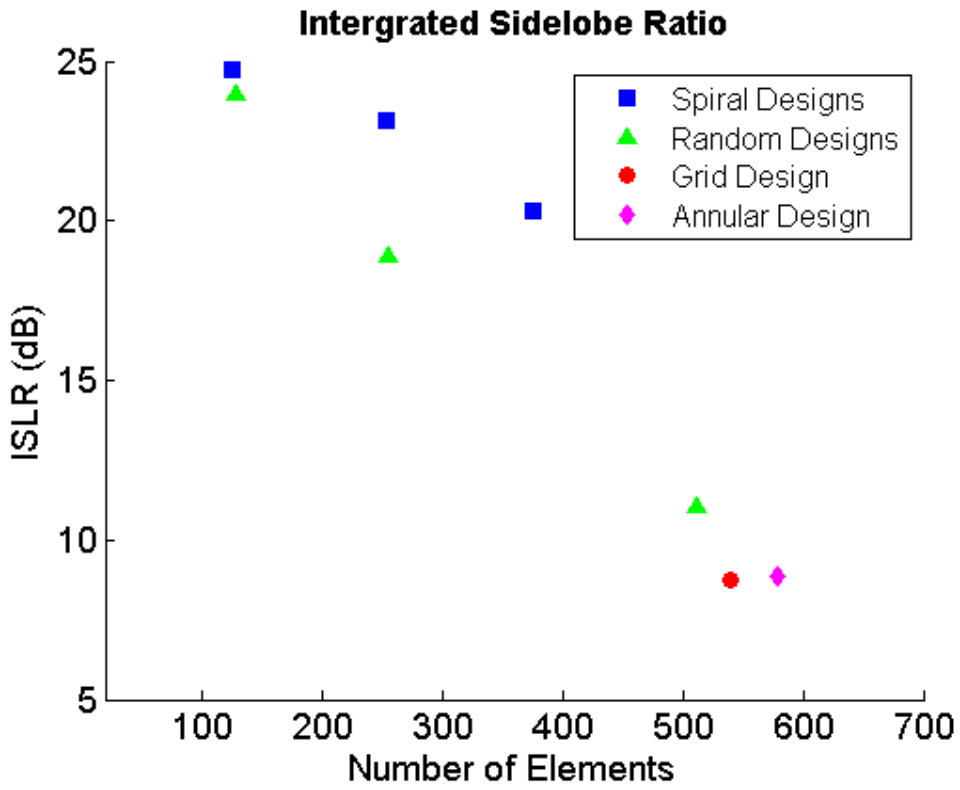

Figure 5-51 ISLR for each array design, plotted against the number of elements.

In summary, the CW directivity results demonstrate the following:

- The log spiral sidelobe levels predicted using the 2D FFT method are consistent with those predicted by the DRI model, with no overlapping elements.

- The upper limit on the density of the spiral designs is approximately 70% of the number of elements in an equivalent grid array.

- Log spiral designs have similar peak sidelobe levels to random array designs for low element densities.

- As the number of elements in the arrays is increased, the peak sidelobe height drops more quickly for log spirals than for random designs.

- Log spiral designs were able to achieve 4.59 dB lower peak sideblobes than any of the other designs investigated, reaching a level of -21.96 dB.

- Log spirals were found to have higher ISLR levels, making them less suitable for imaging in low contrast media than some other designs.

5.13.2 Directivity under pulsed excitation

While CW models are efficient and provide a good indication of array performance, most ultrasonic imaging applications use relatively short pulses of only a few cycles. To assess performance when excited with a short toneburst, the directivity simulations of Section 5.13.1 were repeated, this time using the pulsed version of the DRI model described in Chapter 4. The excitation pulse used was a 1.5 MHz, 3 cycle hamming windowed toneburst. The transducer impulse response was not modelled, to simplify the simulation. Figure 5-52 shows the excitation signal in both the time and frequency domains. As before, directivity was calculated for both unsteered and steered conditions, using the same steering parameters as for the CW simulations. The simulated beam patterns are shown in Figure 5-53, Figure 5-54 and Figure 5-55, while the key performance measurements are shown in Table 5-4.

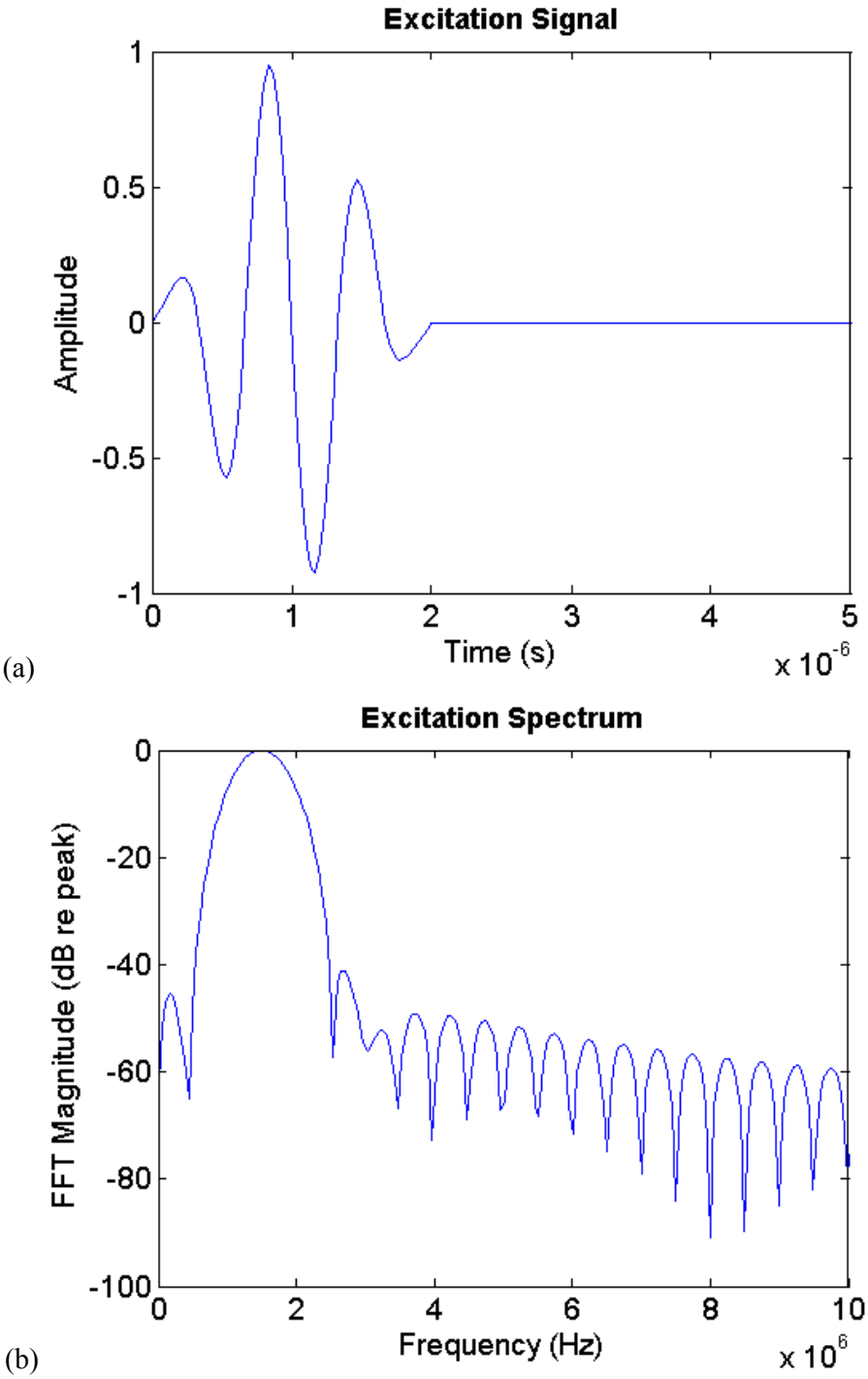

Figure 5-52 **Three cycle hamming windowed tone burst excitation signal centred at 1.5 MHz, (a) time domain and (b) frequency domain.**

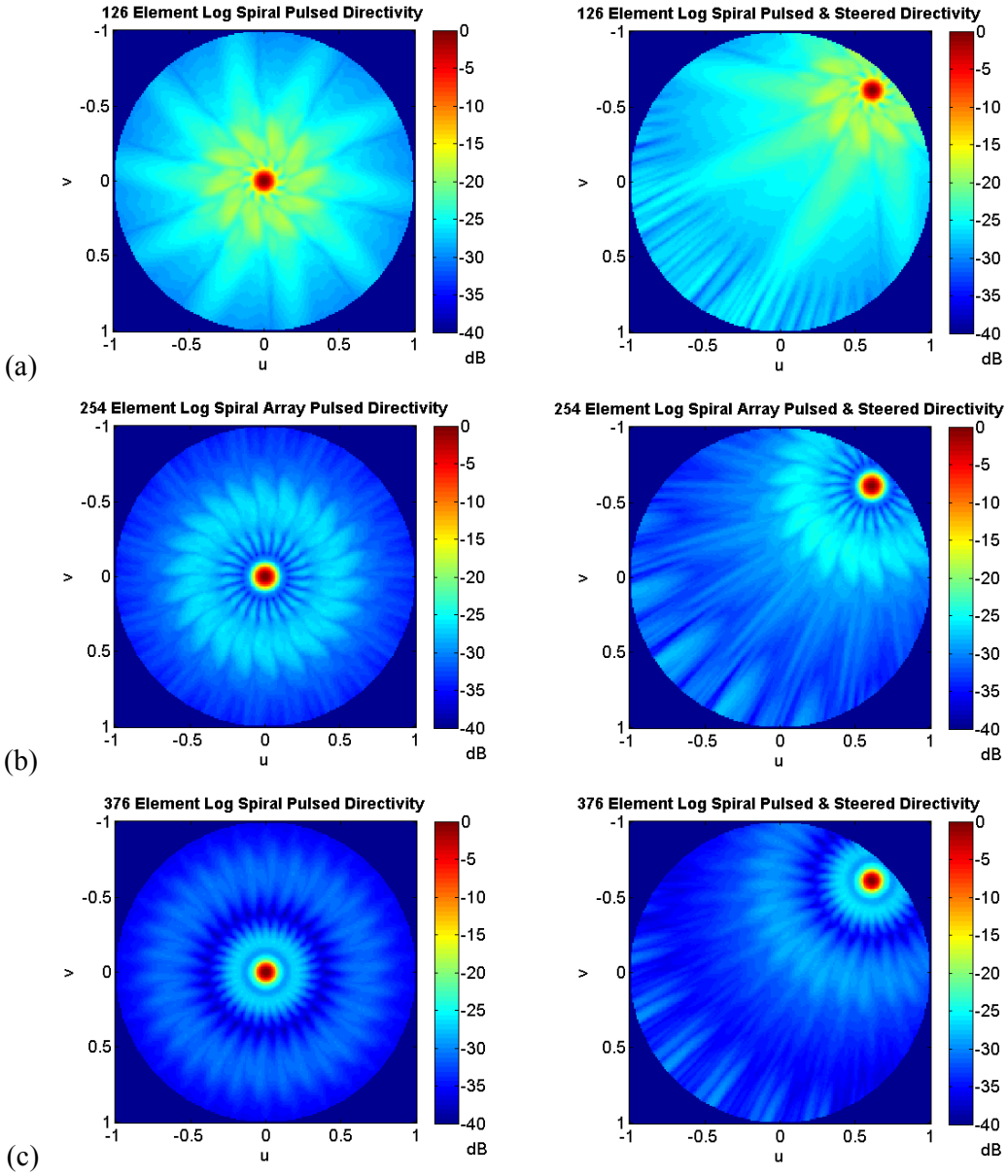

Figure 5-53 **Far field directivity with a 3 cycle, hamming windowed toneburst excitation. The unsteered field is shown in the left column, while the steered field for θ_s=60°, φ_s=45° is shown in the right column, (a) 126 element spiral, (b) 254 element spiral and (c) 376 element spiral design.**

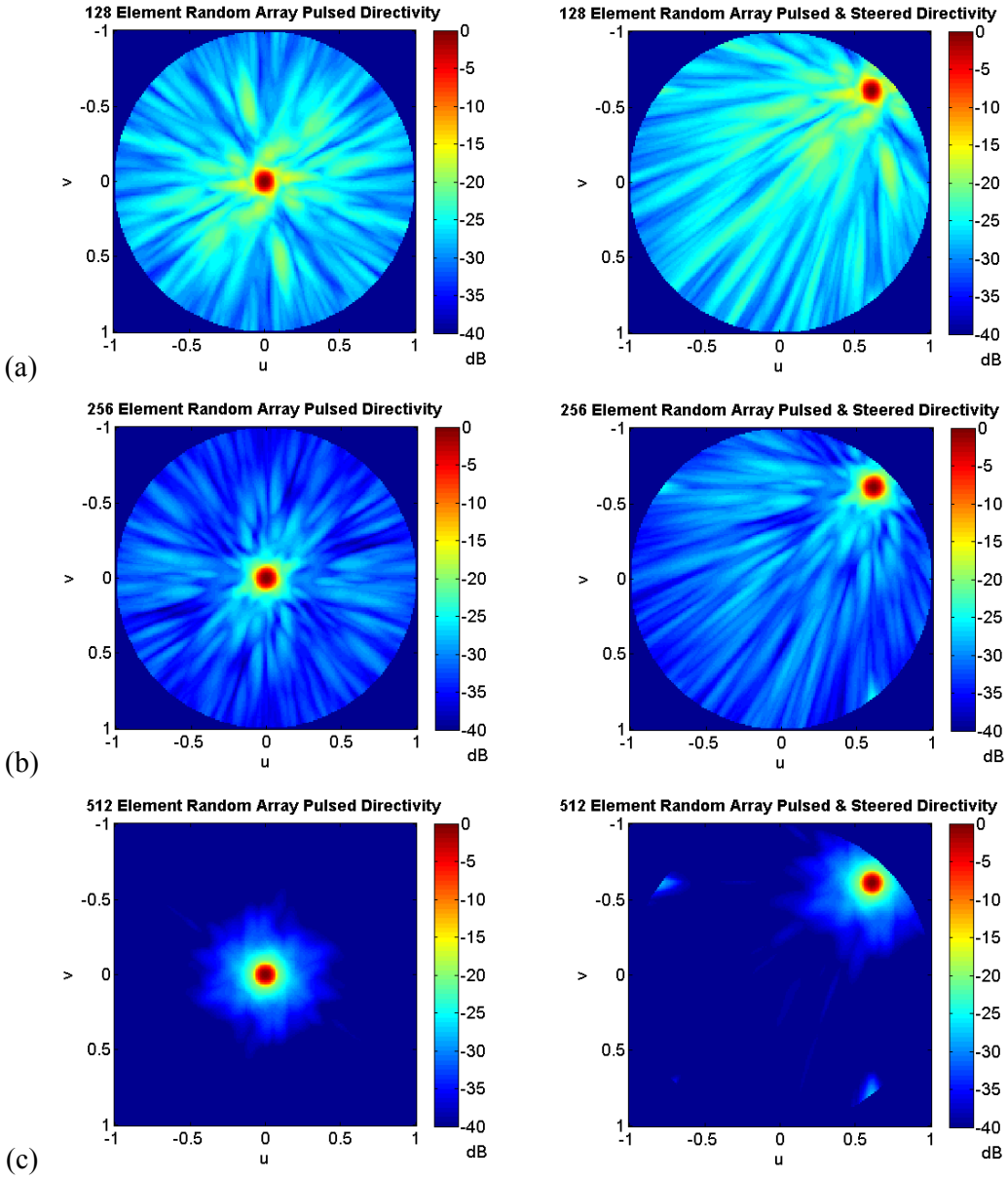

Figure 5-54 **Far field directivity with a 3 cycle, hamming windowed toneburst excitation. The unsteered field is shown in the left column, while the steered field for θs=60°, φs=45° is shown in the right column, (a) 128 element random, (b) 256 element random and (c) 512 element random design.**

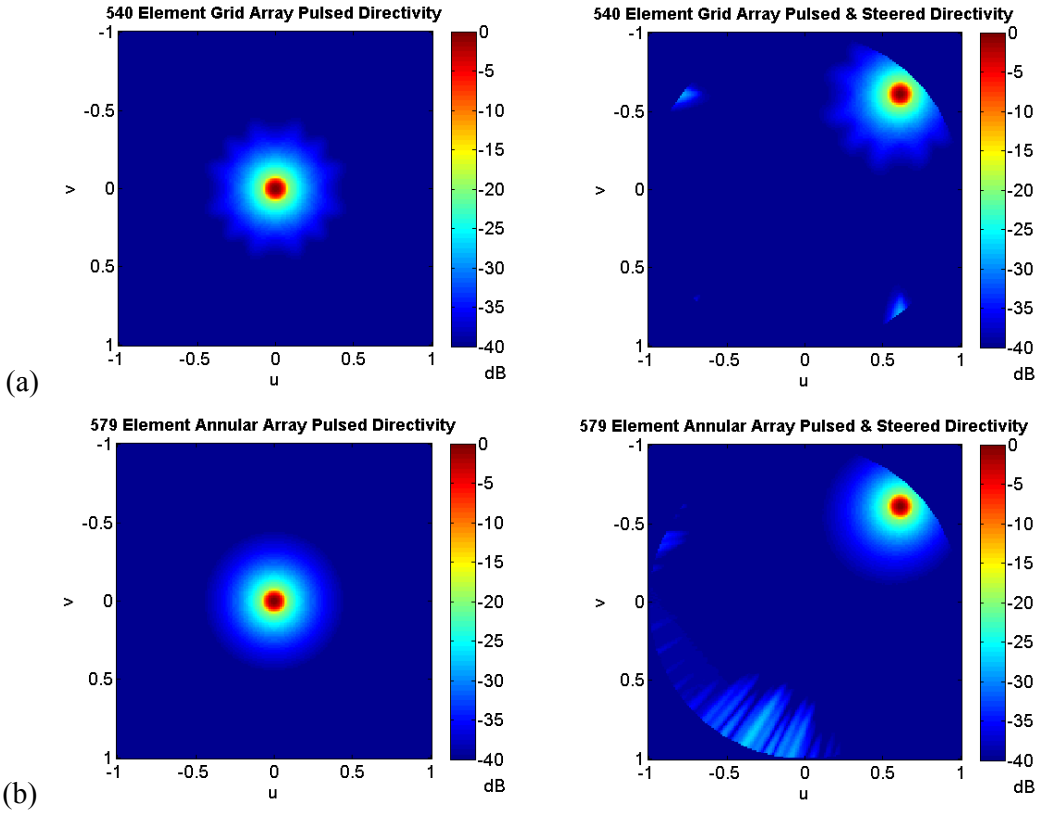

Figure 5-55 **Far field directivity with a 3 cycle, hamming windowed toneburst excitation. The unsteered field is shown in the left column, while the steered field for θs=60°, φs=45° is shown in the right column, (a) 540 element grid and (b) 579 element annular design.**

Design	-3 dB BW (°)	-10 dB BW (°)	S_p unsteered (dB)	S_p steered (dB)	ISLR (dB)
126 Spiral	3.95	7.28	-18.35	-17.14	17.34
254 Spiral	3.88	7.07	-26.05	-24.44	19.05
376 Spiral	3.68	6.59	-26.91	-26.08	17.80
128 Random	4.04	6.98	-16.51	-16.11	15.67
256 Random	4.27	7.62	-26.34	-24.51	14.90
512 Random	4.16	7.28	No lobes, -50 floor	-27.83	8.37
540 Grid	4.16	7.25	No lobes, -50 floor	-28.27	7.02
579 Annular	4.06	7.07	No lobes, -50 floor	-27.19	7.07

Table 5-4 Pulsed directivity performance.

The main difference between the pulsed results and the CW results is that sidelobe levels are much lower under pulsed excitation, by an average of 7.2 dB. This is because the short pulse does not interfere at all points in the field, but only at points were the pulses from separate array element overlap in time. The only point where all waves arrive in phase, and at their maximum amplitude is in the main beam, providing a useful reduction in sidelobe heights for other points in the field.

In all cases the -3 dB beamwidths of the arrays are reduced when compared to the data in Table 5-3, by an average of 0.29°. This narrowing of the beam is also due to the short duration of the pulses, and the lack of a perfect overlap at any point but the mainlobe. Since the effect is roughly uniform between arrays it indicates no performance advantage of any particular design. It does however indicate that the

array apertures could be made smaller to achieve the original target beamwidth of 4.5°, which would further reduce sidelobe levels due to their higher element density.

Figure 5-56 shows the peak sidelobe levels in each array, plotted against the number of elements used. In contrast with the CW results, the 126 element spiral design has a lower sidelobe height than the 128 element random array, by 1.84 dB. However, at the 256 element limit the random and spiral designs are closely matched. This variation in the change in sidelobe height is most likely due to the precise placement of the sidelobes in the beam pattern, since the amplitude of lobes at high angles is reduced by the limited acceptance angle of the array elements. The 376 element spiral offers approximately a 1 dB reduction in sidelobe hight over the 254 element design. The 512 element random design, 540 element grid design, and the 579 element annular design all lack distinct sidelobes in their beam under unsteered conditions, decaying smoothly to a floor of approximately -50 dB. Under steered conditions lobes are present at the edge of the beam, which are associated with the 0.5 λ periodicity of the arrays.

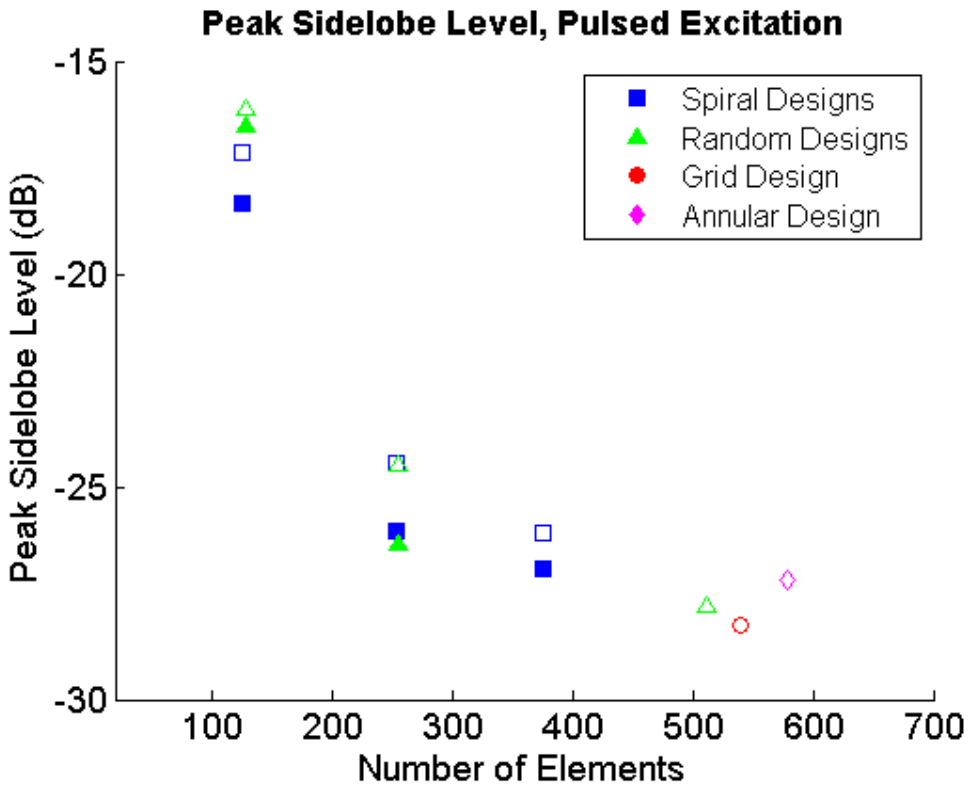

Figure 5-56 **Peak sidelobe levels in the directivities of the arrays under pulsed excitation. Solid markers denote unsteered performance, while unfilled markers denote steered performance. As no distinct lobes exist in the unsteered directivities of the 512 element random array, the 540 element grid array, and the 579 element annular array these designs are not plotted.**

Figure 5-57 shows the ISLR levels of the arrays under pulsed excitation. As with the peak sidelobe levels ISLR is lower than it was under CW excitation. Once again the spiral arrays show poorer ISLR performance than the random arrays, indicating more power in the sidelobe region. However, as with the CW results the low beamwidth of the spiral design will accentuate this shift.

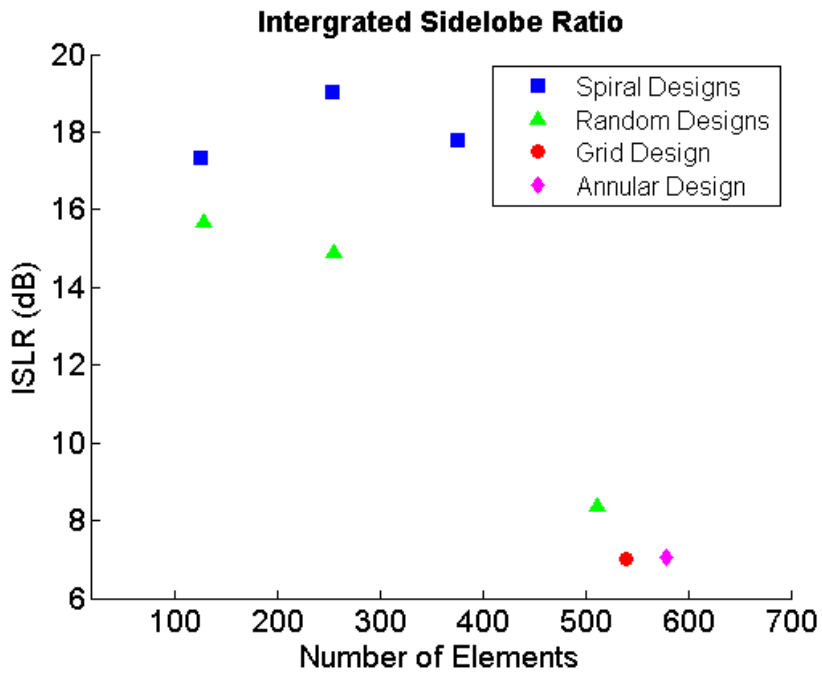

Figure 5-57 **ISLR for each array design, under pulsed excitation, plotted against the number of elements.**

In summary, the pulsed directivity results demonstrate the following:

- Peak sideleobe heights are significantly lower under pulsed excitation than under CW excitation, with an average reduction of 7.2 dB.

- The 126 element spiral design achieved lower sidelobe heights than the 128 element random design, but at 256 elements performance was similar.

- The design with the lowest sidelobes was the 540 element grid, at -28.27 dB when steered.

- Log spirals were found to have higher ISLR levels, making them less suitable for imaging in low contrast media than the other designs.

5.13.3 Near field under CW excitation

So far most of the analysis and design of the log spiral arrays has been carried out by analysing the directivity of each array pattern. However, imaging applications often demand that the beam be steered and focussed in the near field. This section will use the DRI model to analyse the near field focal performance of the arrays under CW excitation.

In each of the following simulations the arrays are excited with a 1.5 MHz sinusoid, and the beam produced in a steel load with a propagation velocity of 5,900 m/s was simulated. The beam is focused at a range of 60 mm and an angle of 20°. The simulated region of the field measures 120 mm in the *x* axis, and ranges from 20 mm to 120 mm in the *z* axis. The 20 mm deep area immediately in front of the transducer was not simulated, as this penalised the more sparse arrays due to the relative isolation of the elements, and their limited acceptance angle. This led to large sidelobe peaks directly in front of individual elements. Many practical imaging applications apply some sort of delay line, such as a Perspex wedge in NDE, so these lobes in the extreme near field do not form in the imaging media, and are not considered here.

Quantitative analysis of near field performance is more complex than that of far field performance, as there are lobes both in front and behind the focal region, which are present in even the dense grid designs. Consider the near field of the 540 element grid array shown in Figure 5-58. This $\lambda/2$ spaced grid will be used as a benchmark for other designs. To do this, a -20 dB contour was drawn around the near field beam pattern. Any interior nulls were filled to create a silhouette outside which there are no sidelobes above -20 dB. This silhouette was then applied to the other designs, and the peak sidelobe outside this region recorded as a measure of near field performance.

Since each array creates a volumetric field, it is most appropriate to plot the field in a plane which contains the worst case sidelobe. To do this, each array was rotated at

1/2° increments, with the field and peak sidelobe level calculated at each step. The arrays were rotated through their angle of rotational symmetry, which was 180° for the random designs, and the angle of separation between the arms for the spirals. The worst case plane was selected to use as a measure of array performance. The near field of each array is shown in Figure 5-59. Figure 5-60 and Figure 5-61, and the peak sidelobe levels for each design are shown in Figure 5-62, along with its rotational angle.

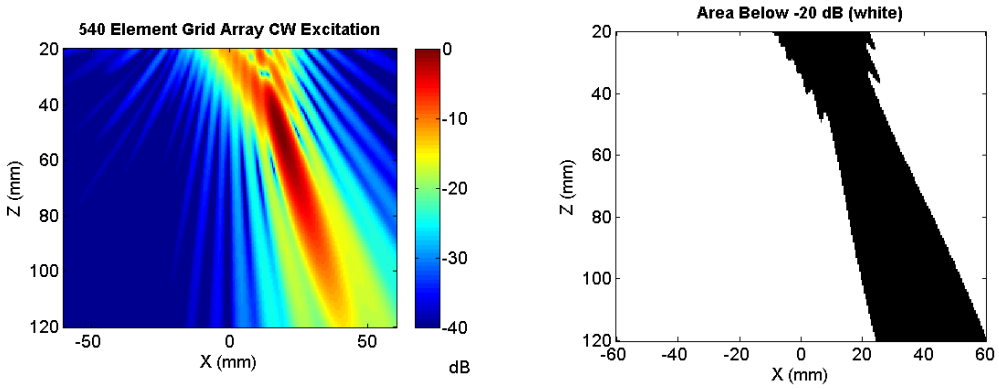

(a) (b)

Figure 5-58 **Near field of the 540 element grid under CW excitation highlighting the portion of the beam below bellow the -20 dB threshold in white, (a) near field directivity and (b) threshholded area.**

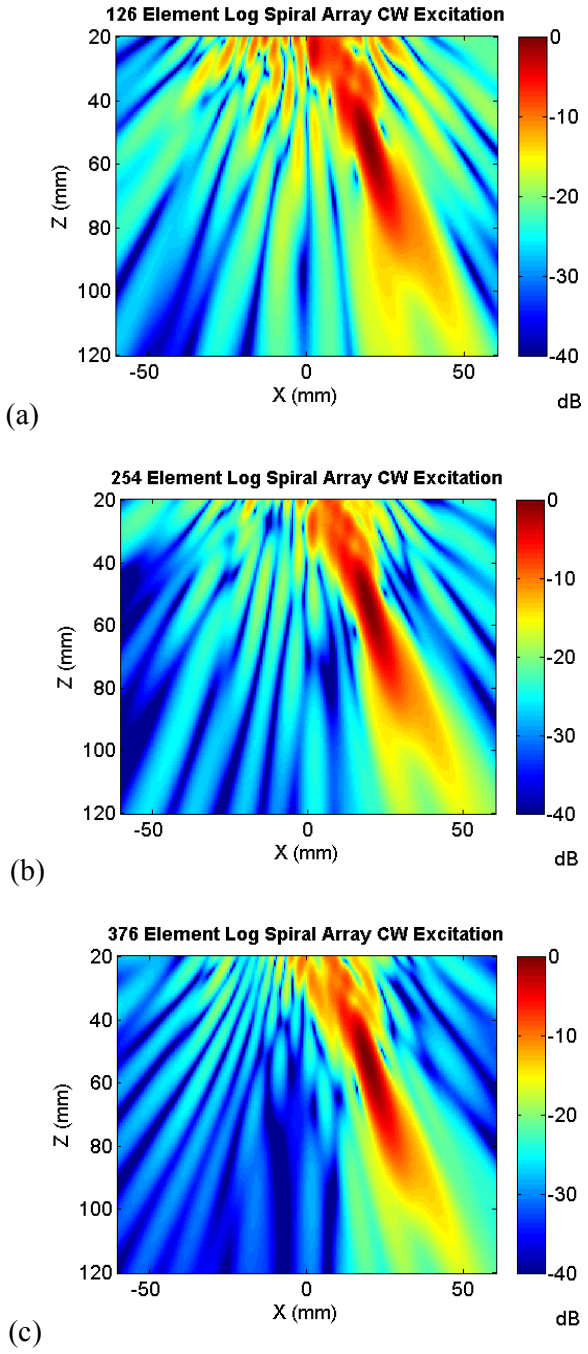

Figure 5-59 **Simulated near field of the log spiral arrays under CW excitation. The focal point is at an angle of 20°, and a distance of 60 mm, (a) 126 element spiral, (b) 254 element spiral and (c) 376 element spiral design.**

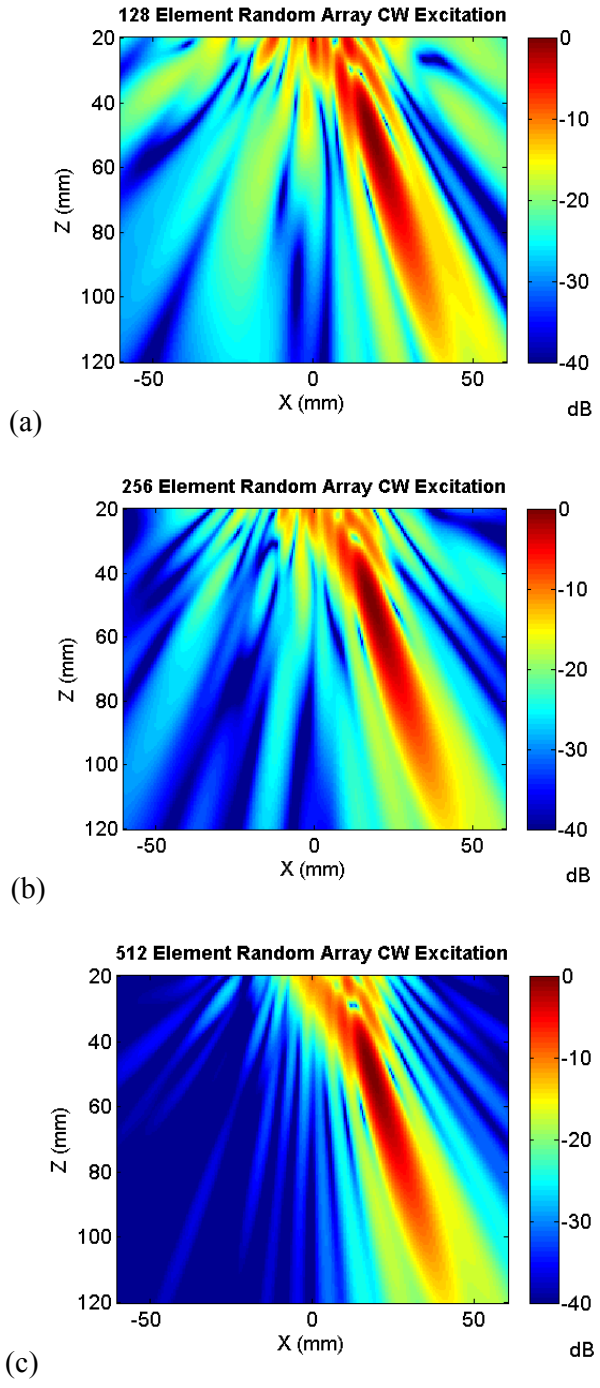

Figure 5-60 **Simulated near field of the random arrays under CW excitation. The focal point is at an angle of 20°, and a distance of 60 mm, (a) 128 element random, (b) 256 element random and (c) 512 element random design.**

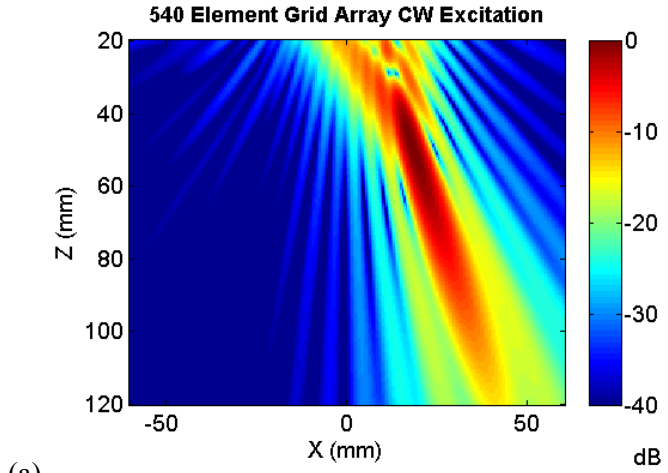

(a)

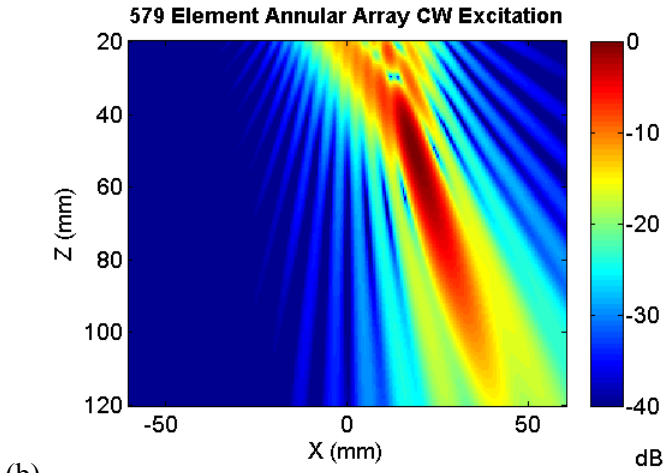

(b)

Figure 5-61 **Simulated near field of the grid and annular arrays under CW excitation. The focal point is at an angle of 20°, and a distance of 60 mm, (a) 540 element grid and (b) 579 element annular design.**

Design	Worst Case Angle (°)	Peak Sidelobe Outside Mask (dB)
126 Spiral	37.0	-7.45
254 Spiral	25.5	-12.61
376 Spiral	7.0	-13.62
128 Random	136.0	-6.98
256 Random	119.5	-10.39
512 Random	50.0	-17.42
579 Annular	0.0	-18.75

Table 5-5 **Near field sidelobe heights outside the -20 dB contour of the 540 element grid, under CW excitation.**

As with the far field results, there is a gradual improvement in array performance as the number of elements are increased. An interesting observation is that the spiral arrays appear to have a smoother axial beam profile than the random, grid and annular designs. This is desirable when imaging with techniques such as dynamic depth focussing, where one transmit pulse is used along with multiple receive focal laws to achieve a large focal region (See Chapter 2).

The peak sidelobe performance of each array is shown in Figure 5-62. As with the far field CW results the 254 element spiral has a lower sidelobe level than the equivalent random design, this time by 2.2 dB. The design with performance closest to that of the grid array was the annular design, with a peak sidelobe height of -18.75 dB.

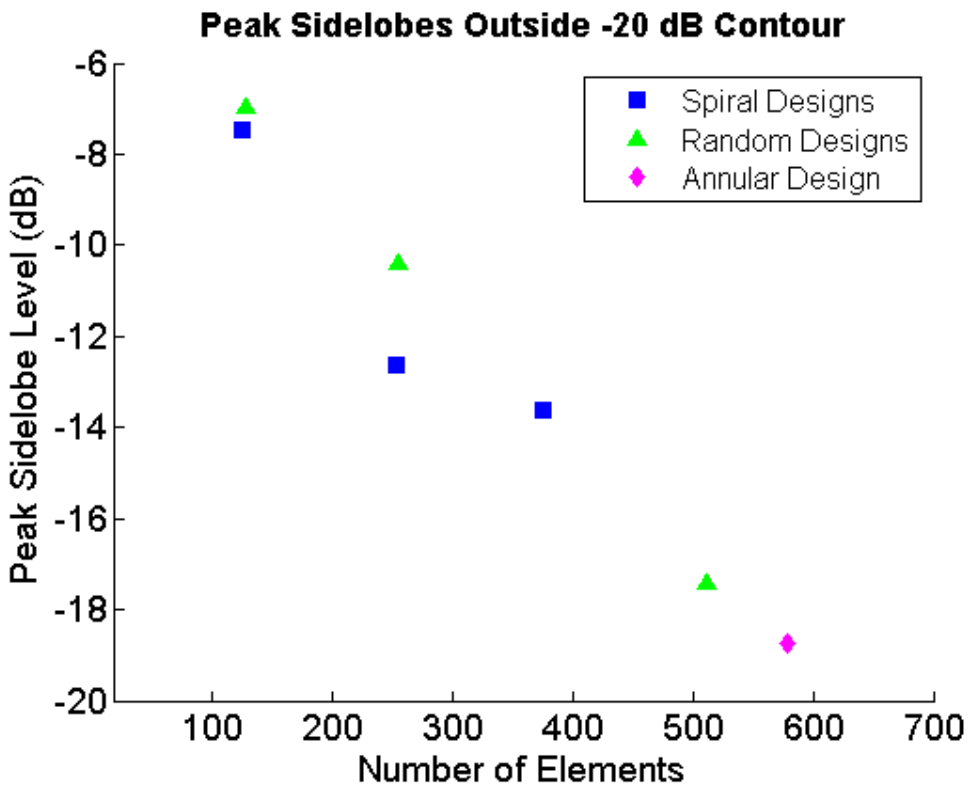

Figure 5-62 **Graph of near field sidelobe heights outside the -20 dB contour of the 540 element grid, under CW excitation.**

In summary, the CW near field results demonstrate the following:

- Near field sidelobes of the sparse arrays and the annular array are higher than that of the 540 element grid.

- The 254 element log spiral array should a 2.2 dB improvement over the 256 element random array.

5.13.4 Near field under pulsed excitation

As stated previously, most imaging applications use pulsed excitation to create images with high axial resolutions. To assess array performance under these conditions the near field simulations were repeated using the pulsed DRI beam model. As with the pulsed directivity simulations, a 3 cycle hamming windowed tone burst was used (see Figure 5-52). As with the previous near field simulations, a focal range of 60 mm was used, at an angle of 60°.

Once again a silhouette was created using the using the – 20 dB contour in the near field of the 540 element grid, as shown in Figure 5-63. For each array the profile was calculated across a field which contained the worst case sidelobe. The angles determined in the CW analysis were used (see Table 5-5). The results are shown in Figure 5-64, Figure 5-65 and Figure 5-66, while the peak sidelobe levels are shown in Table 5-6.

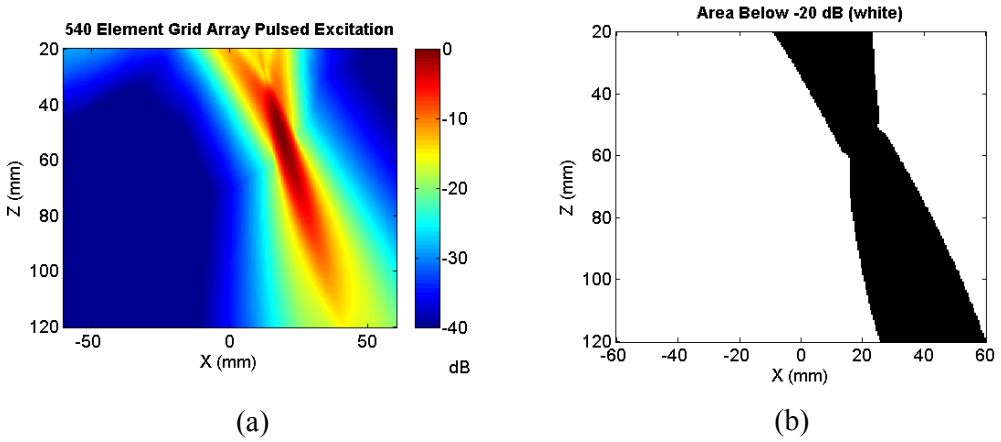

Figure 5-63 **Near field of the 540 element grid under pulsed excitation highlighting the portion of the beam below bellow the -20 dB threshold in white, (a) near field directivity and (b) threshholded area.**

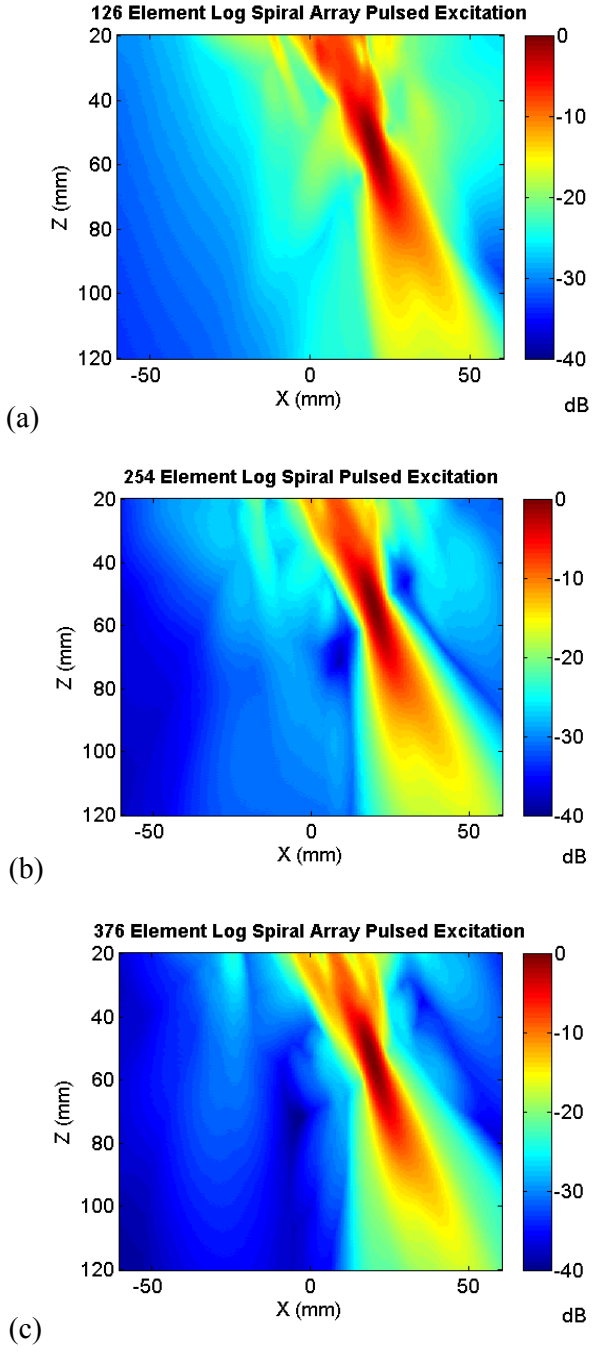

Figure 5-64 **Simulated near field of the log spiral array designs under pulsed excitation. The focal point is at an angle of 20°, and a distance of 60 mm, (a) 126 element spiral, (b) 254 element spiral and (c) 376 element spiral design.**

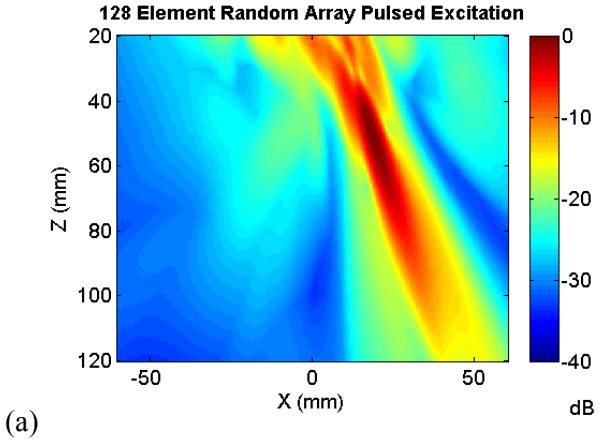

(a)

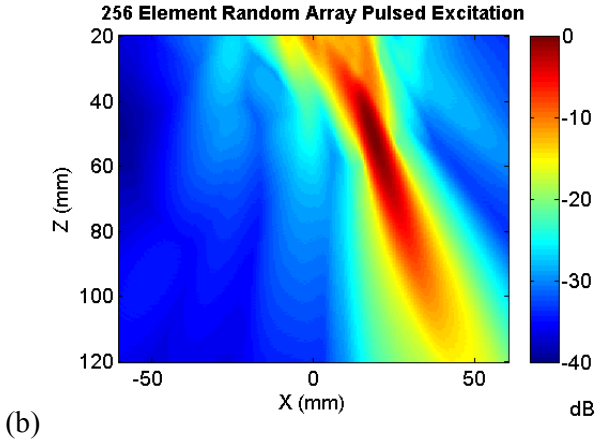

(b)

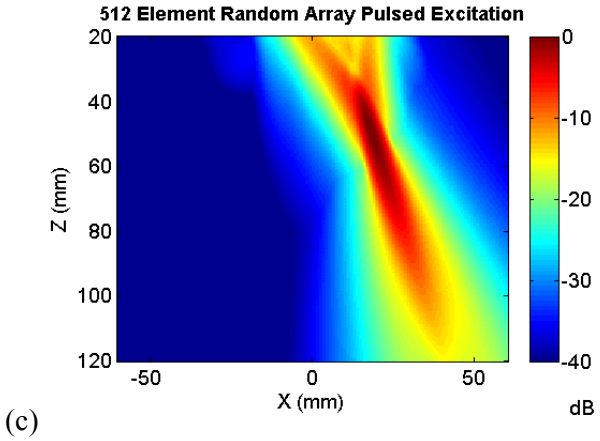

(c)

Figure 5-65 **Simulated near field of the random array designs under pulsed excitation. The focal point is at an angle of 20°, and a distance of 60 mm (a) 128 element random, (b) 256 element random and (c) 512 element random design.**

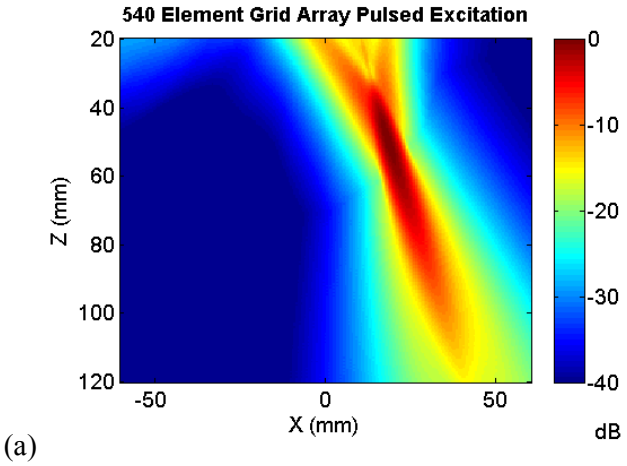

(a)

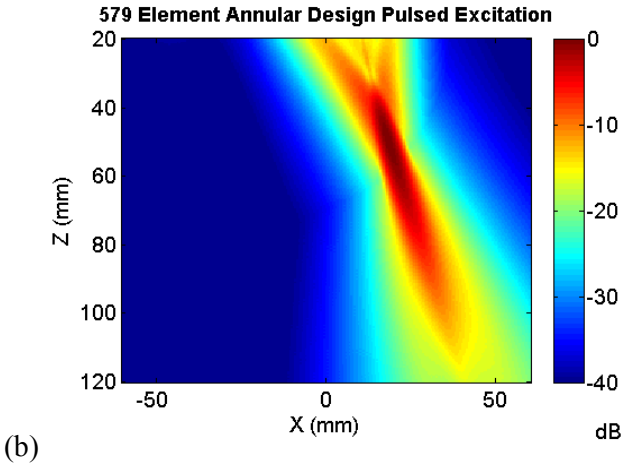

(b)

Figure 5-66 **Simulated near field of the grid and annular designs under pulsed excitation. The focal point is at an angle of 20°, and a distance of 60 mm, (a) 540 element grid and (b) 579 element annular design.**

Design	Peak Sidelobe Outside Mask (dB)
126 Spiral	-14.11
254 Spiral	-18.42
376 Spiral	-18.68
128 Random	-12.68
256 Random	-14.79
512 Random	-19.46
579 Annular	-19.71

Table 5-6 **Near field sidelobe heights outside the -20 dB contour of the 540 element grid, under pulse excitation.**

As with the far field results there is significantly less interference present in the field under pulsed excitation when compared to CW. This results in reduced sidelobe levels, with an average reduction of 4.38 dB. The most significant reductions were found in the sparse arrays, with the 126 element spiral seeing the largest change of -6.66 dB.

Figure 5-67 shows the peak sidelobe levels plotted against the number of elements in the array. Overall the spiral arrays outperformed the random designs, showing an improvement of 1.43 dB at the 128 element level, and 3.63 dB at the 256 element level. The 376 element spiral achieved a sidelobe level only 0.78 dB higher than the 512 element grid, using only 73 % of the elements.

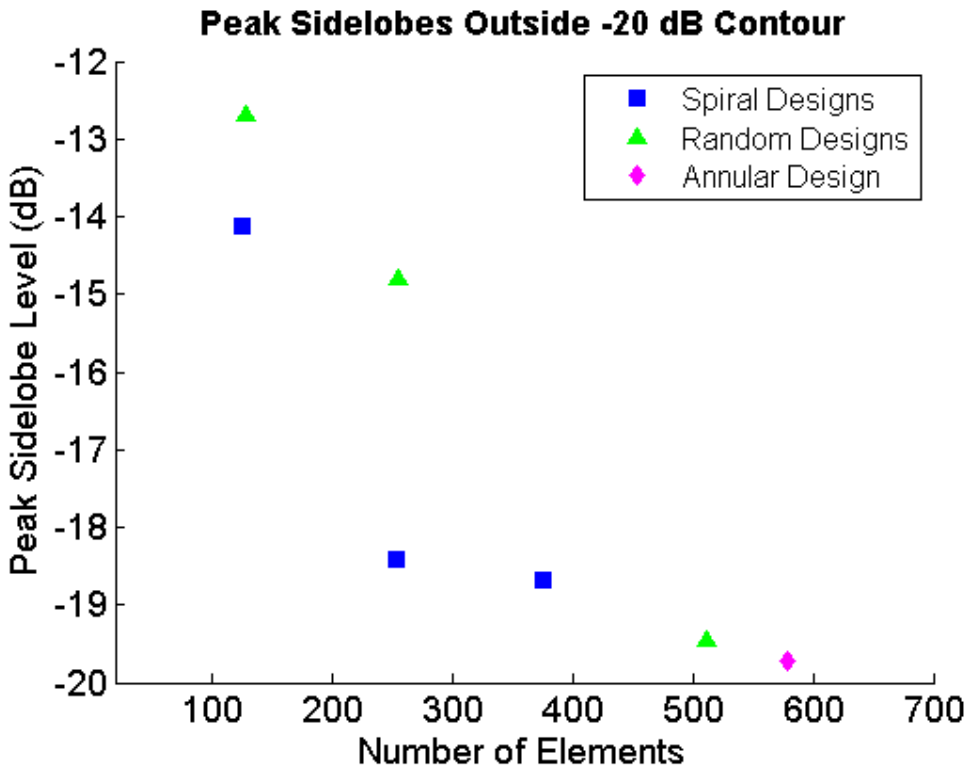

Figure 5-67 **Graph of near field sidelobe heights outside the -20 dB contour of the 540 element grid, under pulse excitation.**

In summary, the pulsed near field results demonstrate the following:

- Near field sidelobes are significantly lower under pulsed excitation than under CW excitation.

- Log spirals outperformed random designs at both 128 and 256 element levels, by 1.43 dB and 3.63 dB respectively.

5.14 Summary of Log Spiral Results

A design method for log spiral arrays has been developed, which allows common array design specifications to be translated into an array layout. The number of elements in the array can be varied, with a greater number of elements resulting in lower sidelobe levels. While in theory there is no limit to the number of elements that can be used, practical designs have been demonstrated that have between 25 and 70 % of the elements contained in a $\lambda/2$ spaced grid with a circular aperture.

The sidelobe performance of these designs was simulated, and was found to be similar to, or better than that of the equivalent random array in almost all cases. Furthermore, under CW operation a peak sidelobe level of -21.96 dB was achieved using a 376 element grid. This was 4.59 dB better than any of the designs investigated, including the 540 element dense grid, and the 579 element annular array. This is in part due to the effective apodisation that the distribution of the log spiral elements creates.

In addition to improved design flexibility, and sidelobe performance, spiral arrays have a number of advantages for fabrication. The arrangement of elements in discrete spiral arms allows space to route interconnect where they do not interfere acoustically with the array elements. This is in contrast to random, grid, and annular arrays, where there is no continuous free space in which to route interconnects.

The main trade-off with log spiral arrays is an increase in ISLR when compared to random, grid and annular arrays. This will impair their imaging performance in low contrast media, such as biomedical imaging of tissue.

In summary, log spiral arrays are suitable for a wide variety of imaging applications, under both pulsed and narrow band excitation. They offer the possibility to reduce the number of elements required when compared to grid designs, and to increase performance and manufacturability of random designs.

To demonstrate these capabilities Chapter 6 will discuss the design, manufacture and testing of a log spiral array for NDE of welds.

Chapter 6

Prototype Design, Manufacture and Testing

In Chapter 5 a design technique for log spiral 2D arrays was developed, and the performance of these arrays simulated. This chapter describes the construction and experimental testing of a prototype log spiral array, designed for the inspection of thick section dissimilar metal welds, commonly used in the nuclear industry.

Alba has been working on a Technology Strategy Board (TSB) funded project called DISSIMILAR, which is focussing on developing inspection techniques for difficult to inspect welds in the nuclear power and oil and gas sectors. The prototype log spiral array was designed to a specification produced during this project, so that its results could be compared to that of more standard periodic grid array designs.

This chapter begins by giving a brief overview of the DISSIMILAR project, and the inspection for which the prototype array was developed. The resulting array is described, and its simulated performance is shown. Finally results of experimental testing are presented.

6.1 DISSIMILAR project and weld inspection

There is growing pressure on the designers of modern electrical power plants to improve efficiency, carbon dioxide emissions, and increase power output. In order to achieve this, a wide range of materials are used to fabricate components, each tailored specifically for their particular application. This inevitably leads to issues when components fabricated from dissimilar metals have to be joined. The coarse grain structure that is created in the weld region of Dissimilar Metal Joints (DMJs) can cause scattering and distortion of ultrasonic waves, making these welds hard to inspect. The ability to steer a beam volumetrically through these welds, and potentially to correct the received wavefront for distortion is an attractive prospect. However, modern phased array controllers do not have enough channels for a dense matrix array of suitable beam width to be a viable option. Sparse 2D arrays are therefore very attractive, making DMJs an excellent application on which to measure the performance of 2D log spiral arrays.

Alba is part of a TSB funded project called DISSIMILAR, whose aim is to demonstrate improved phased array inspection capabilities in DMJs [49]. The consortium is led by TWI Ltd, who are carrying out acoustic modelling of the dissimilar welds, and have designed the inspection procedure for the project [50,51]. An 80 mm thick weld specimen, representative of safe end welds in nuclear reactors was produced, and its grain structure mapped by The University of Birmingham using electron backscatter diffraction. Alba and Peak NDT represent phased array equipment suppliers, providing the phased arrays, and phased array controllers respectively. Applied Inspection is an NDE services company who are carrying out baseline inspections using standard equipment, then comparing the results to those obtained with the novel inspection techniques. Finally, British Energy (BE), Shell, and the Health and Safety Executive (HSE) represent the plant operators, and are steering the project, and evaluating its results.

To allow Alba's prototype spiral array to be fully characterised, a customised test block was produced containing a variety of simulated defects. The material chosen for the block was 316L stainless steel, which is used in pipework in the nuclear industry, and was one of the materials used to fabricate the weld specimen in the DISSIMILAR project. The external dimensions of the block are 220x220x80 mm, and a full schematic of the block is shown in Figure 6-1. The block contains both side drilled holes (SDH) and flat bottomed holes (FBH), which act as simulated defects. While their acoustic characteristics are not identical to real world defects, they are much more cost effective to create, and are designed to have similar cross sections to commonly occurring defects. SDHs are typically used in test blocks intended for use with linear arrays, as they only scan in elevation, so the length of the hole is not of concern. In this case, they are useful as references to compare the 2D array's sensitivity and resolution to that of periodic arrays. FBHs are useful reflectors for volumetric scanning, as they can test the array's resolution in both the elevation and azimuthal scanning planes. All holes were 3 mm in diameter, slightly smaller than the operating wavelength.

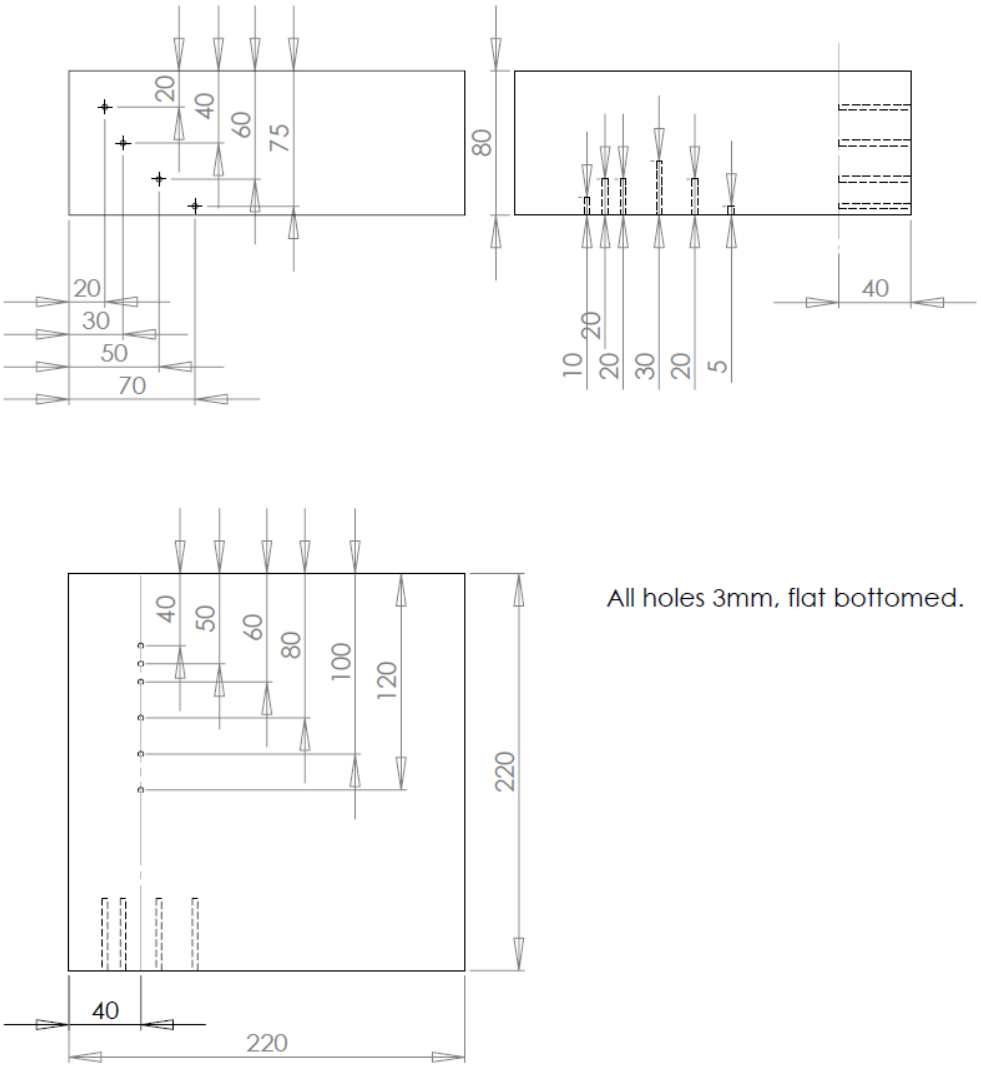

Figure 6-1 Test block schematic showing both side drilled, and flat bottomed hole defects.

A Rexolite wedge was designed and manufactured by TWI to couple sound from the array into the test piece. Rexolite is the material commonly used for ultrasonic wedges, as it has lower loss than similar plastics, and its acoustic impedance of 2.5 MRayls causes the beam to be refracted on entry into the test block, allowing the natural angle of the beam to be controlled by the design of the wedge. This is useful,

since the beam can be directed to the centre of the area to be inspected, limiting the required steering range of the array. The angle of the wedge was 18.5°, and a diagram is shown in Figure 6-2.

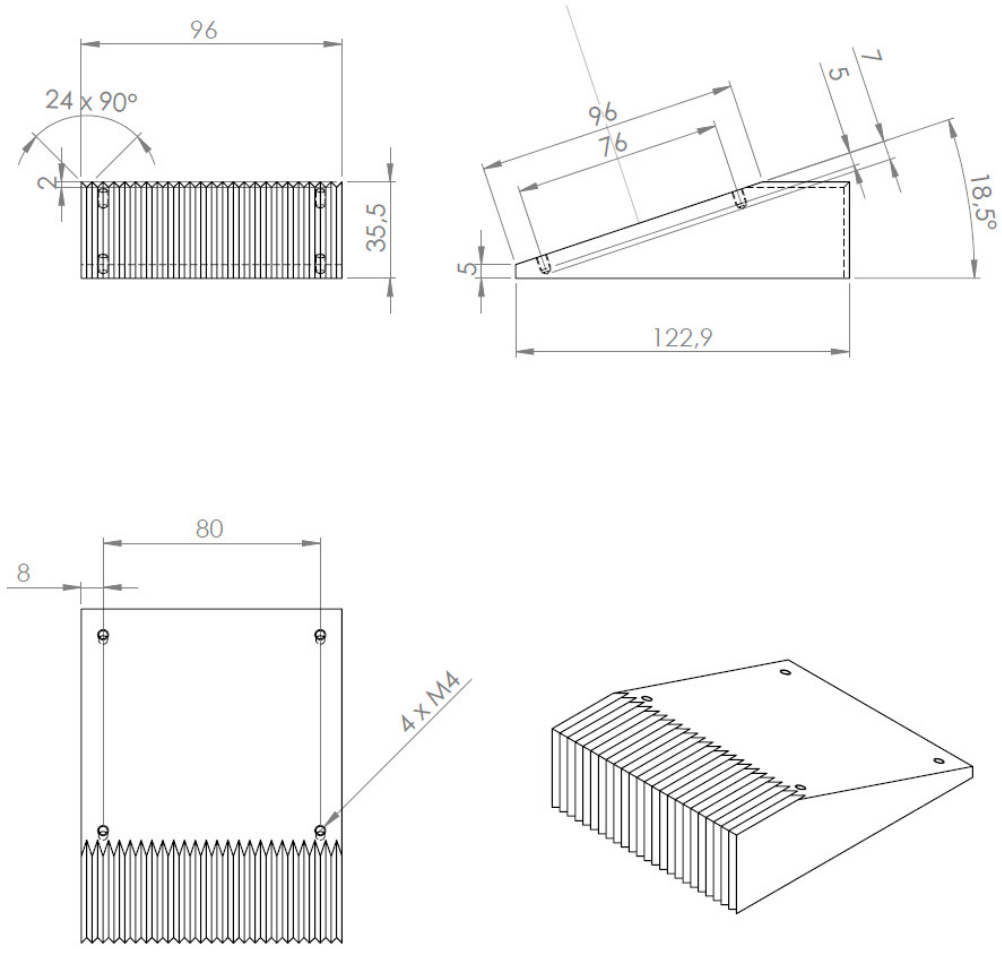

Figure 6-2 Diagram showing design of the Rexolite wedge, courtesy of TWI.

The main benefit of sparse arrays is that they require fewer elements, (and hence fewer array controller channels) than dense matrix arrays, so to illustrate this fully the array was designed to be used with a 128 channel array controller. This size of

array controller is more common than 256 or 512 channel units, and will allow the array to be evaluated by more of Alba's customers.

A 1.5 MHz 2D matrix array was designed as part of the DISSIMILAR project, to compare the performance of 2D arrays to that of linear arrays for inspecting DMJs. This device consists of 126 elements in an 18 x 7 grid, with a 3.5 x 6.4 mm pitch, as shown in Figure 6-3. The array's aperture is 63 x 44.8 mm, which was designed to be as large as possible to achieve good resolution. The array's pitch is approximately 0.88 x 1.60 λ, which is very sparse, although at its natural 50° beam angle the effective pitch is less in the primary axis due to refraction in the wedge. This large secondary axis pitch limits the out of plane steering capability of the array, to approximately ±10° before grating lobes would significantly interfere with image quality. The array has been designed to be operated with a Hamming apodisation to create a circular beam in the test piece, and lower sidelobe levels. This means that a spiral array with the same aperture will have a similar beamwidth to that of the matrix array.

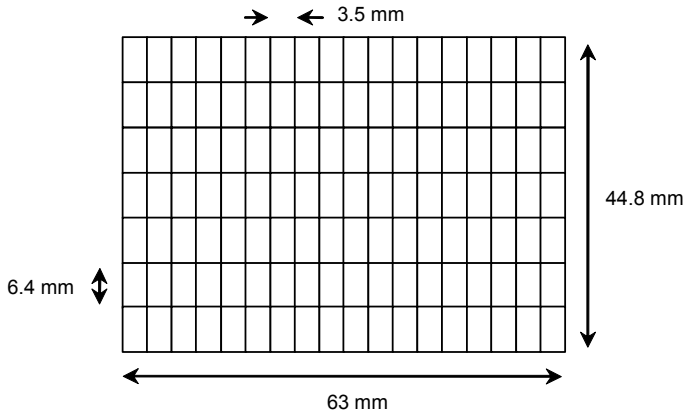

Figure 6-3 Diagram showing the layout of the 126 element 2D matrix array.

The modelled results in Section 6.2 show that the selected log spiral array performs significantly better than the 2D matrix array, allowing near volumetric steering. Building the log spiral array to a similar specification would allow back to back experimental comparison of array performance, although it was not possible to carry out this comparison during the duration of the work.

6.2 Design of array layout

The first step in designing the prototype log spiral array was to design the array layout. The array was mounted on an angled wedge to couple it into the test piece, so to achieve a circular acoustic footprint in the test block the array was stretched creating an elliptical aperture. To simplify the manufacturing process the array was designed to have approximately the same aperture as the 2D matrix prototype.

The specification for the prototype array is as follows:

- 128 elements (maximum).
- Resolution of approximately 10 mm in the weld.
- Elevation steering range of 30° up to 70° in the weld.

To achieve the steering range a natural beam angle (unsteered) of 50° was originally selected for the wedge. However, TWI had already chosen an angle of 51° for the sparse matrix array, so this angle was adopted. This angle allows the critical areas of the weld to be inspected using only +/-20° elevation steering. While these are the most critical angles, the array was designed to be capable of steering +/-60°, allowing it to steer down to 0° to get a backwall echo as a reference. The wedge angle was calculated using Snell's law, with the speed of sound in the test block and wedge 5,770 m/s, and 2,350 m/s respectively:

$$\theta_w = \sin^{-1}\left(\frac{2{,}350}{5{,}770}\sin(50)\right) = 18.45° \qquad \textbf{(6-1)}$$

This was rounded to 18.5° to simplify the construction of the wedge, resulting in a natural angle of 51.2°.

The refraction at the boundary between the wedge and the test piece causes a foreshortening of the array aperture. This means that its effective aperture as viewed from an observation point in the weld is shorter than the actual aperture, as shown in Figure 6-4. If this were not corrected for, the cross section of the ultrasonic beam would appear oval at its natural angle, rather than the expected circular cross section obtained from a circular aperture. To account for this, the design of the array was stretched, so that the effective aperture, and therefore the beam cross section are circular at the natural angle. Steering away from the natural angle still causes the beam to be distorted, but by ensuring that it is circular at the centre of the inspection the worst case distortion is minimised. To achieve this, the desired effective aperture of the array was first created using the standard design process. This array design was then stretched to create the actual array aperture to be constructed. This is an established technique, which is already used in NDE to manufacture fixed angle probes which produce beams with a circular cross section.

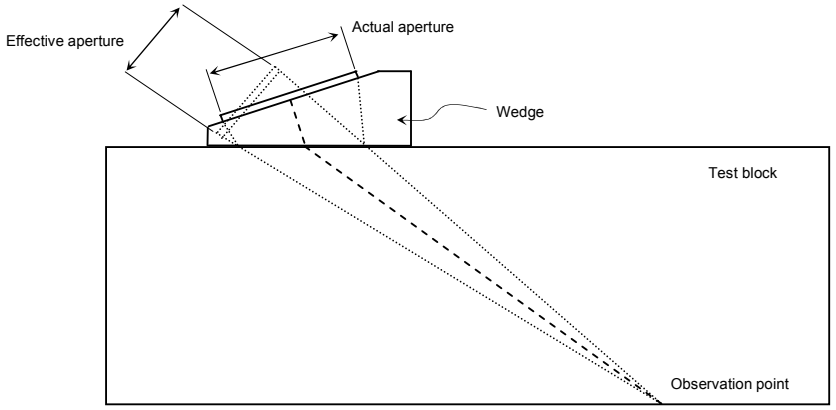

Figure 6-4 **Diagram showing the reduced effective aperture of an array mounted on an angled Rexolite wedge.**

If the observation point is far from the array the relationship between the aperture D and the effective aperture, D_e becomes:

$$\frac{D}{D_e} = \frac{\cos(\theta_w)}{\cos(\theta_t)} \qquad \textbf{(6-2)}$$

where θ_t is the natural beam angle in the test piece. The ratio D / D_e can be used to stretch the array aperture in the x axis, resulting in an elliptical array with a circular beam in the test piece. This also increases the total radiating area of the array, and the spacing between array elements, aiding manufacture. Using a wedge angle of 18.5°, and a test piece angle of 51.2°, the array was stretched by a factor of 1.51.

The target beamwidth of 10 mm equates to a beamwidth of approximately 4.6° at a distance of 125 mm. Using Design Equation 1, the required aperture to achieve this resolution is 15.76λ. However, the largest housing that could be obtained within the budget and timeframe of the project limited the maximum aperture to 10λ. This housing was a spare that had already been designed and manufactured for the 2D matrix array, and was produced with the tight flatness tolerances required (< 5 μm flatness) to manufacture a uniform array. This is a large deviation from the design rules, but one which could not be avoided. It is somewhat mitigated by driving the array with short pulses. It has already been shown in Chapter 5 that beamwidths are reduced under pulsed excitation, It was therefore decided that the reduction in aperture to 10λ was a necessary compromise. This equates to an aperture of 41.3 mm.

The element aperture was selected as λ/2 to achieve the maximum possible steering range, and to avoid element overlap. An element pitch of 0.6λ was chosen to ensure a steering range of +/-40° with no grating lobes, and to avoid element overlap. Finally, the number of arms, spiral pitch, and minimum radius were all adjusted to optimise peak sidelobe height, whilst avoiding element overlap. The resulting array design is shown in Table 6-1. Images of the array design before and after being stretched are shown in Figure 6-3.

General Parameters	**Value**
Centre frequency	1.5 MHz
Wave mode	Longitudinal
Load velocity	5,770 m/s
Wedge velocity	2,350 m/s
Wedge angle	18.5°
Load angle	51.2°
Spiral Parameters	**Value**
Number of elements	127
Centre element	Yes
Stretch factor (x axis)	1.51
Design element size	0.5 λ (unstretched)
Actual element size	3 x 2 mm
Design aperture	10.0 λ
Actual aperture	62.3 x 41.3 mm
Number of arms	9
Arm pitch	30°
Element pitch	0.6 λ (excluding stretch)
Minimum radius	2.0 λ (excluding stretch)

Table 6-1 2D log spiral prototype array design.

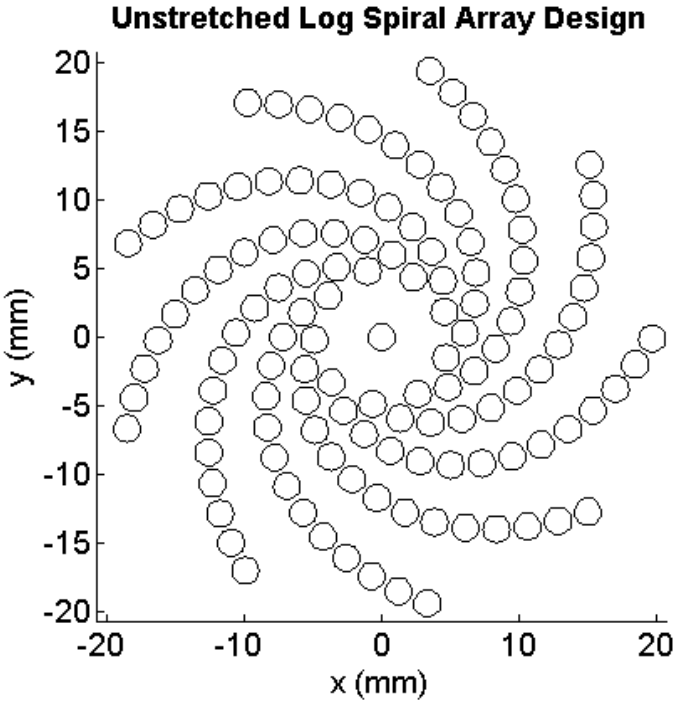

(a)

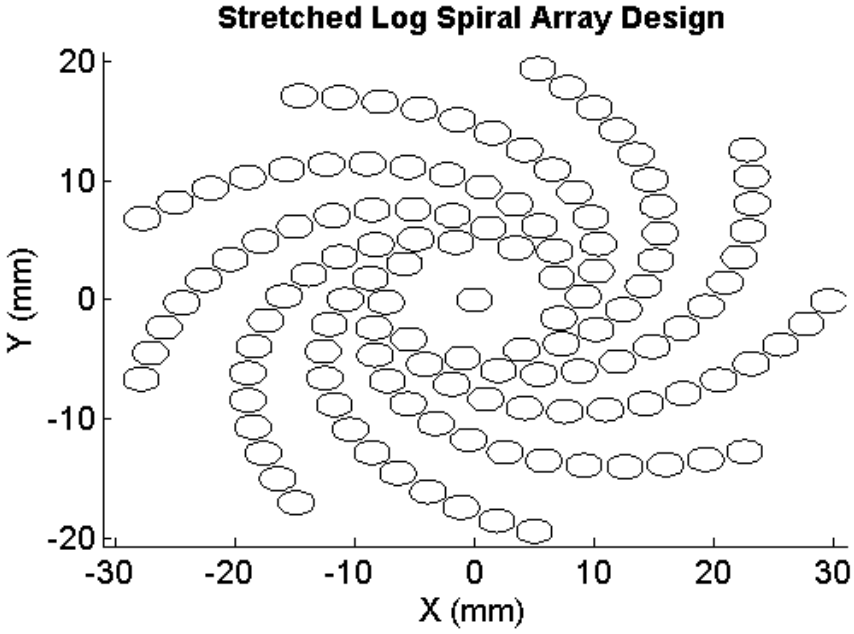

(b)

Figure 6-5 Images of the spiral array design, (a) unstretched and (b) stretched.

The CW beam produced by this array configuration was modelled using the DRI method described in Chapter 4. To provide a full assessment of array performance the model was run for three different field configurations:

- A 140 x 80 mm field running through the thickness of the test block in the *x-z* plane, showing the near field and the focal region.

- A 40 x 40 mm field perpendicular to the beam normal providing a cross section of the beam at the focal point.

- A hemispherical field in the test block to highlight any out of plane components in the beam.

These configurations are illustrated in Figure 6-6.

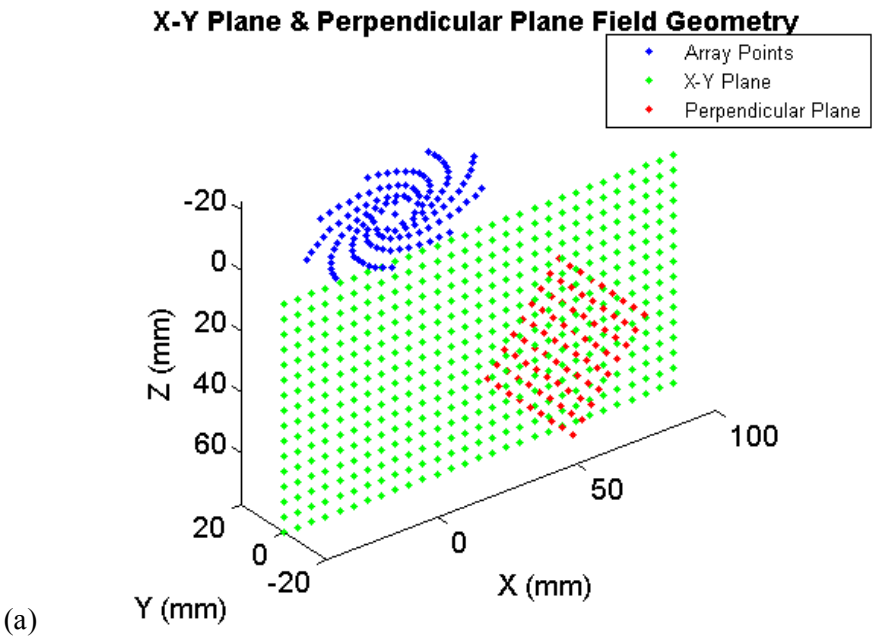

(a)

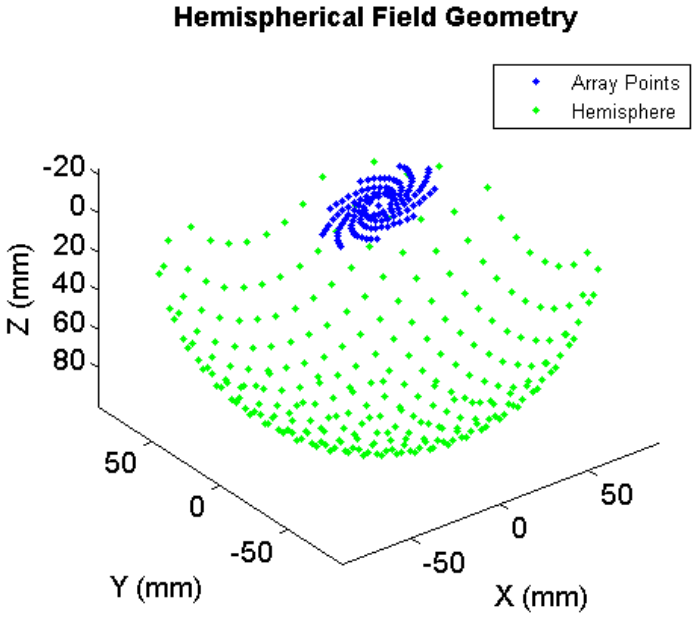

(b)

Figure 6-6 **Three field geometries used to assess the performance of the prototype array, (a) *x-y* plane and perpendicular plane and (b) hemisphere.**

The *x-y* plane was simulated with the beam focused to a range of 80 mm, and steered to angles of 0, 30, 50, and 70° in the test piece. Angles between 30 and 70° are the most important for this inspection, but simulating the 0° beam examines the array's ability to steer further, and to detect the back wall reflection. The results are shown in Figure 6-7 and Figure 6-8.

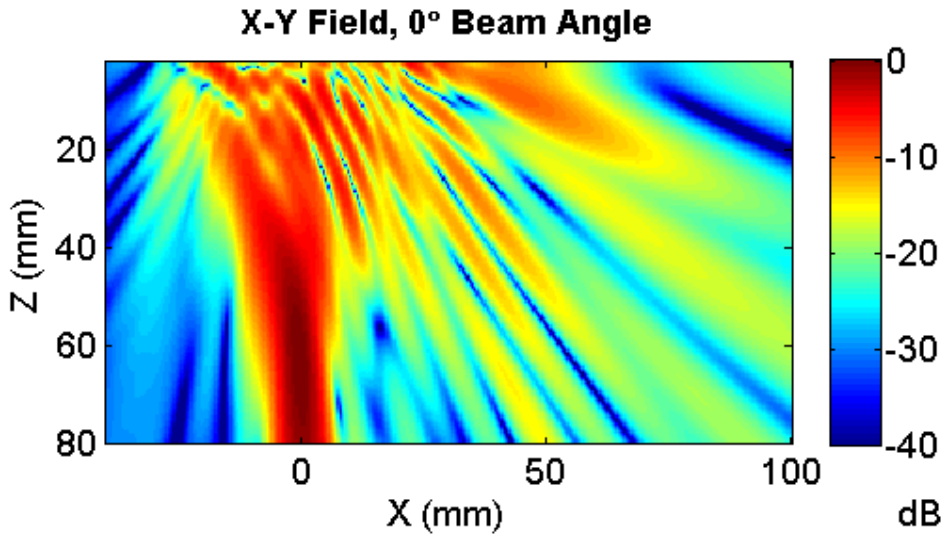

(a)

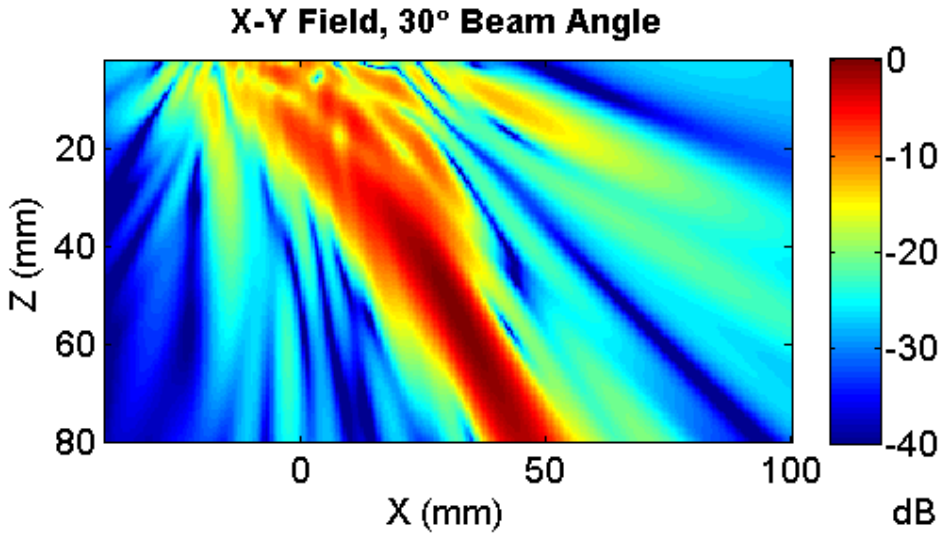

(b)

Figure 6-7 **CW simulation of the *x-y* field produced by the log spiral array design, when focussed at a range 80 mm, and steered to (a) 0° and (b) 30°.**

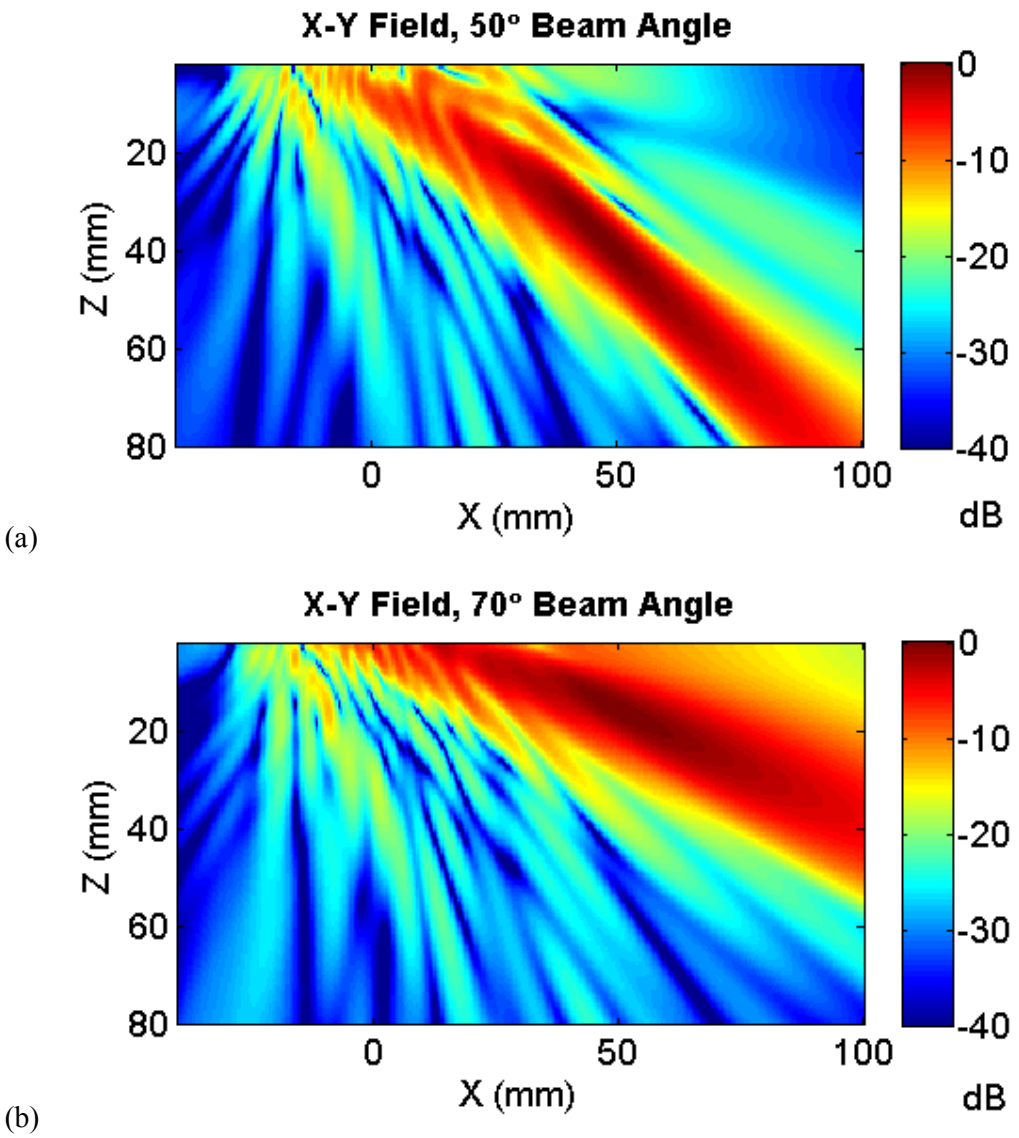

Figure 6-8 **CW simulation of the x-y field produced by the log spiral array design, when focussed at a range 80 mm, and steered to (a) 50° and (b) 70°.**

The results for the 30, 50, and 70° angles show relatively low sidelobes, around -20 dB for points at a similar range to the focus. At 70° the beam is significantly wider than other angles, due to the reduced effective aperture. When steered to 0° the array shows higher sidelobe levels, particularly at shallower depths. This will impair its

ability to detect weak signals near the backwall, but since the backwall reflection itself is relatively strong it will be detected.

The perpendicular plane was used to calculate the cross section of the beam, and measure its resolution. The field was calculated for a 51° steering angle, with the plane centred on the focal point at a range of 80 mm. The results are shown in Figure 6-9, and show that the array has a -3 dB beamwidth of 9 mm along the axis lying in the *x*-*y* plane, and 8 mm in the *y* axis. This focal spot is almost circular, showing that the array has been stretched correctly for the selected wedge angle.

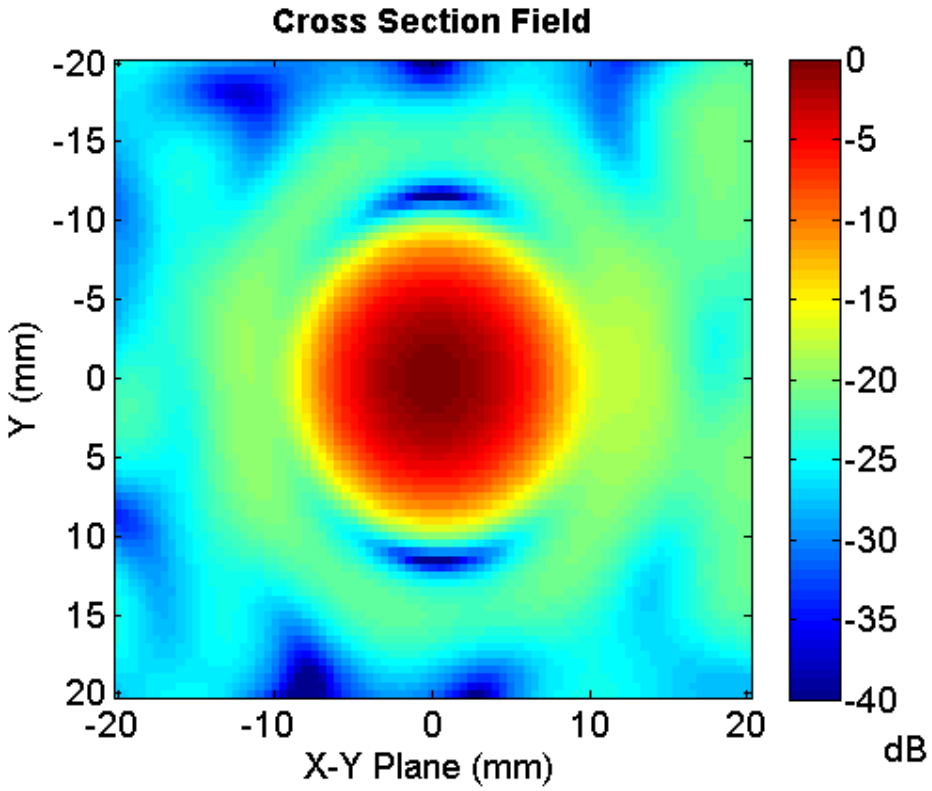

Figure 6-9 Perpendicular plane field, showing the beam cross section.

The hemispherical field was simulated in the far field, using steering, but no focussing. The elevation of the beam was maintained at its natural angle of 50° in the test piece, and the azimuthally steering angle was set to 0, 45 and 90° respectively, as shown in Figure 6-10 and Figure 6-11.

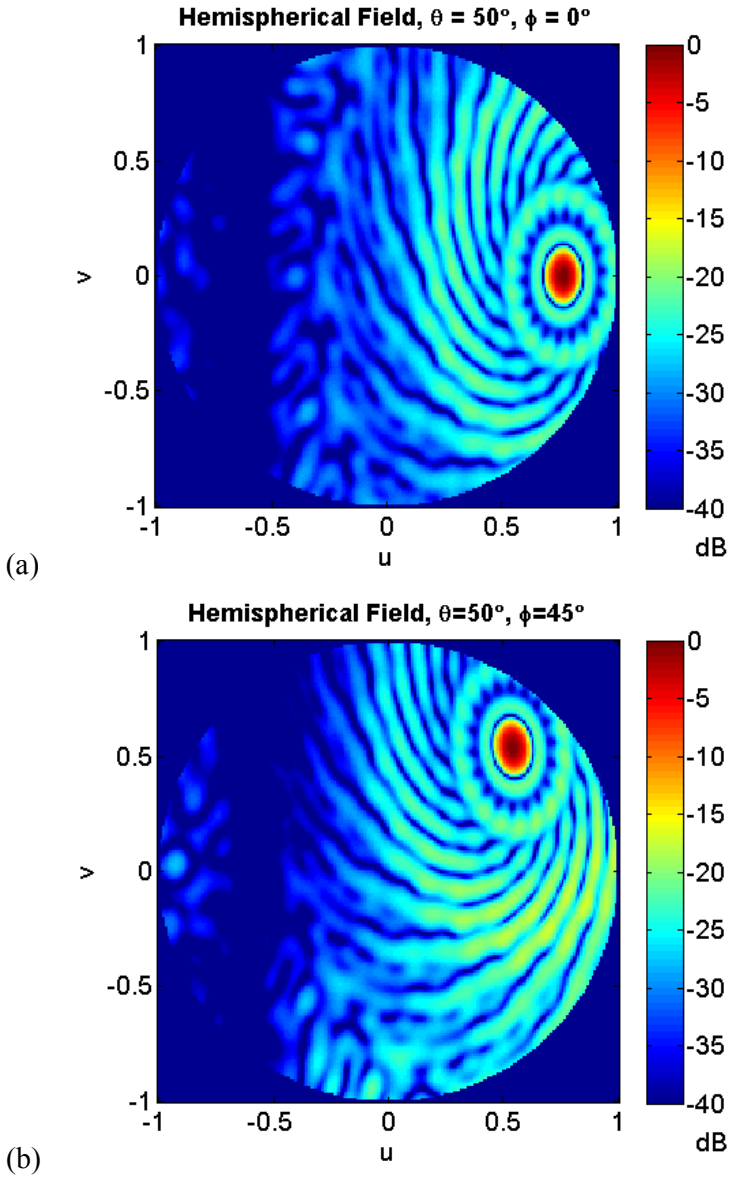

Figure 6-10 **CW Hemispherical field produced by prototype design with θ_s = 50°, (a) φ_s= 0 and (b) φ_s= 45°.**

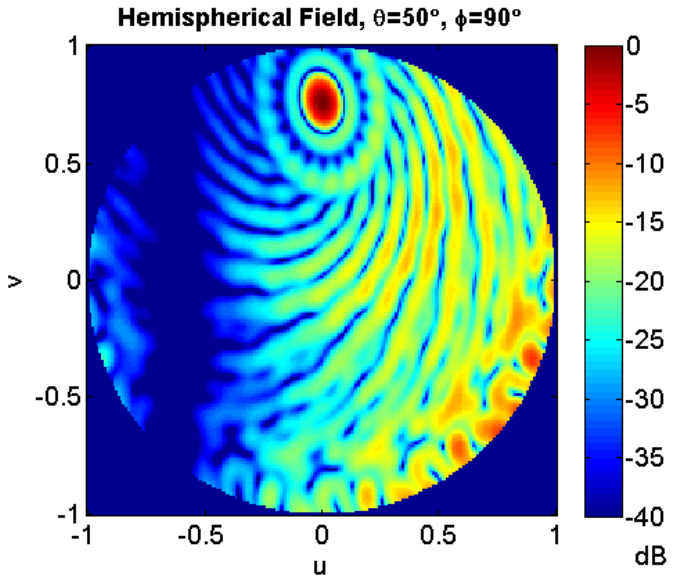

Figure 6-11 **CW Hemispherical field produced by prototype design, with θs = 50°, and φs= 90°.**

With no azimuthal steering the peak sidelobe level is approximately -21 dB. When the beam is steered to 45° off axis this level increases to -17 dB, due to the directivity of the array elements. Within this region the array should show good imaging performance. When the beam is steered perpendicular to the normal axis the sidelobe levels rise significantly to -12 dB in the centre of the beam. There is also some grating lobe energy at the edge of the beam, although in practice the non-piston like vibration of the array elements may limit sensitivity at this extreme angle. It should be noted that the lobes at the extreme left of the images are signals which have passed directly through the array structure in the model, which does not account for the structure of the array itself. In reality these signals would be blocked by the array's housing and backing block, and would not be transmitted.

These results compare favourably to the modelled far field performance of the 2D matrix array, which was shown in Figure 6-3. The design was modelled in the same wedge configuration as the log spiral design, and the elevation steering angle

maintained at 50°. Two azimuthal steering angles were simulated: 0° and 45°, and the results are shown in Figure 6-12. At 0° azimuthal steering the array produces a single main beam, with -13 dB sidelobes, characteristic of a rectangular aperture. However, when the beam is steered to 45°three grating lobes are created in the field. The strongest of these is 14 dB higher than the intended main lobe, preventing this array from forming volumetric images.

In summary, field modelling has shown that no unexpected grating lobes have been introduced by adapting the log spiral array for operation through the Rexolite wedge. The array performance exceeds both the resolution and steering range specifications, using only 127 elements. It is also expected that sidelobe levels will be further reduced when the array is excited with short pulses. In addition, modelled results for the log spiral array show a significant improvement over the more conventional matrix array considered.

The array was constructed using 1-3 piezocomposite technology, which is described in the following section.

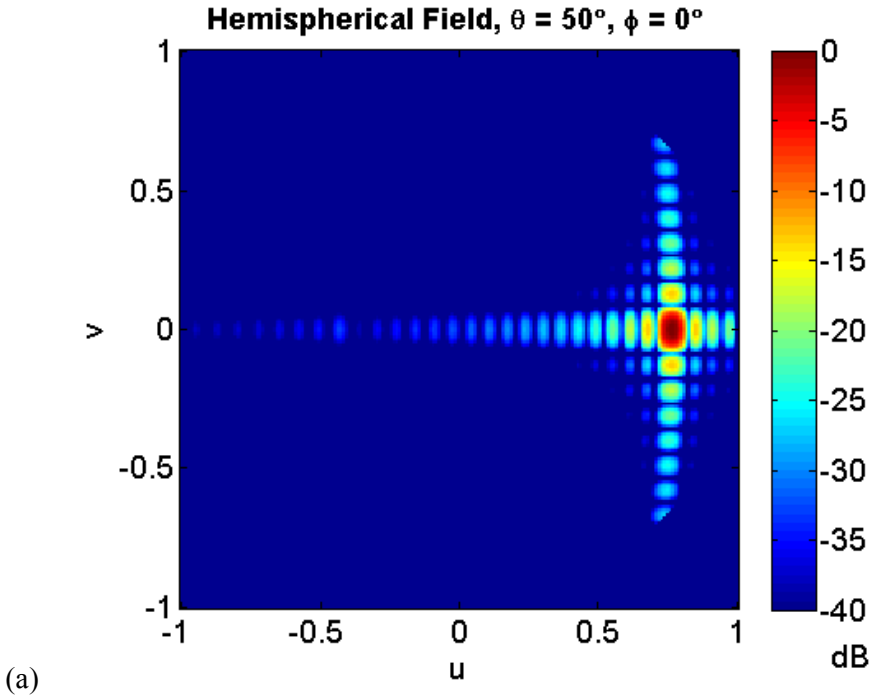

(a)

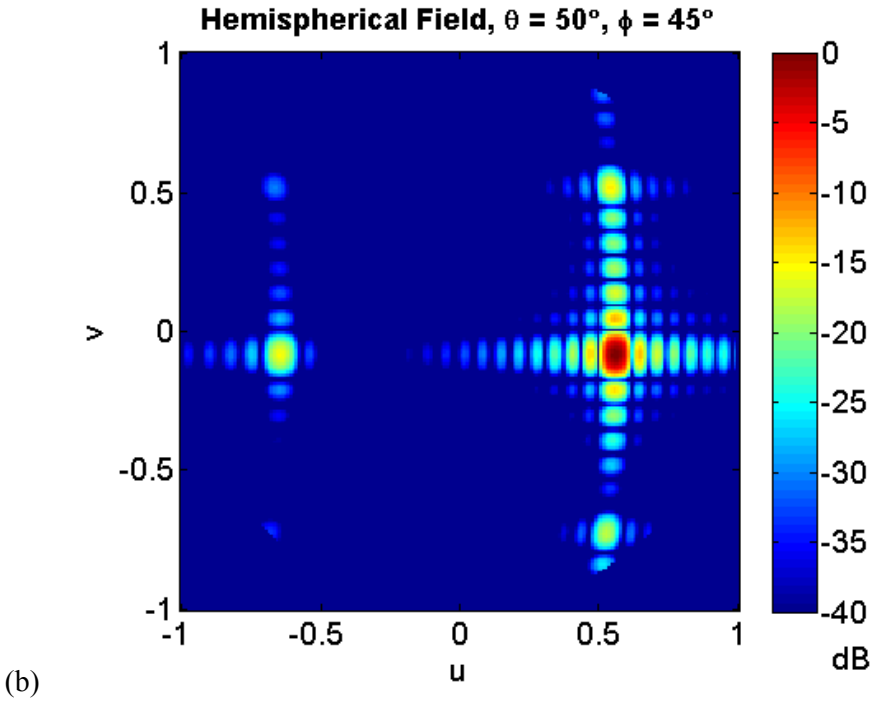

(b)

Figure 6-12 **CW hemispherical field produced by the 126 element matrix array shown in Figure 6-3 with with θ_s = 50°, (a) φ_s= 0° and (b) φ_s= 90°.**

6.3 1-3 Piezocomposites

1-3 piezocomposites are used extensively in sonar, biomedical, and NDE devices as the active material for electromechanical transduction. They are well suited for both transmit and receive modes, and allow the performance of the device to be customised. They consist of a grid of lead zirconate titanate (PZT) pillars, encapsulated in a polymer matrix, as depicted in Figure 6-13. The 1-3 prefix denotes the configuration of the active and passive components: the active PZT is continuous in only one axis, while the passive polymer is continuous in all three.

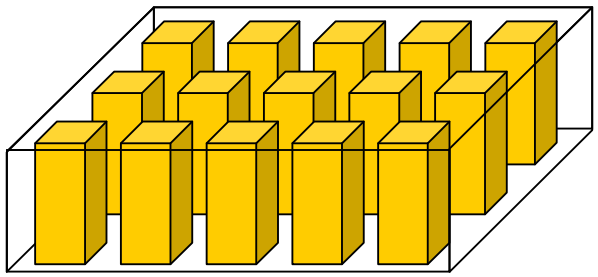

Figure 6-13 **1-3 Piezocomposite structure showing PZT pillars (gold) surrounded by a passive polymer encapsulant (transparent with outline).**

1-3 piezocomposites offer superior performance over monolithic PZT devices in a number of key areas [52]:

- Low acoustic impedance (10 – 20 MRayls, compared to ~33 MRayls for monolithic PZT), improving the acoustic match to water, and Rexolite.

- A reduction in lateral clamping, resulting in an increased electromechanical coupling coefficient (60 – 70% compared to 45 – 50% for PZT).

- Damping of lateral resonant modes such as Lamb waves, which can corrupt surface displacement, and increase crosstalk in arrays.

- The ability to tailor both the electro-acoustic performance, and the shape of a device to an application (for example curved sonar projectors).

These improvements result in unimodal devices with increased sensitivity, bandwidth, and acceptance angle, all of which improve imaging performance in array applications. However, 1-3 piezocomposites are complex to design in comparison to monolithic PZT devices, and so require advanced modelling techniques to optimise their performance.

Before personal computers were ubiquitous and capable of performing billions of calculations per second, simple models for thickness mode piezoelectric transducers were required. Examples of these are the equivalent circuits of Mason [53], and the transmission line based KLM model [54]. While these early electrical analogs proved to be useful analysis tools for transducer designers, they offered limited physical insight into device operation. A systems feedback approach, commonly referred to as LSM (Linear Systems Model), was used by Hayward, to produce a block diagram model which clearly described device operation using measurable material properties and dimensions as inputs [55]. This model was extended to consider multiple passive layers to the front and rear of the transducer [56], which allows the designer to consider multi layer acoustic matching systems, and backing blocks. To complement these models, Smith developed a method for calculating the effective material properties of a 1-3 piezocomposite device which were relevant to thickness mode oscillations [57]. This allows the material properties of the active and passive phases of the device to be converted into a single set of material properties for the composite material. While these analytical models can accurately be used to simulate thickness mode performance, they do not consider lateral resonances in the transducer structure.

As affordable desktop computers became more readily available, finite element modelling of 1-3 piezocomposite structures became possible, and this allowed the full analysis of all supported resonant modes. Hossack showed that 3D finite element modelling could be used to simulate the electro acoustic performance of 1-3 piezocomposites, achieving good agreement with both experimental results, and analytical models [58]. Finite element analysis has since been used to model a wide range of transducer configurations and phenomena, including Lamb wave propagation in arrays [59 , 60], novel polymer materials [61 , 62], 2D array configurations [63], and flexible devices [64,65]. The use of time domain finite element modelling is attractive, as it allows non adjacent elements to be decoupled, greatly reducing the time required to run large models. A general overview of finite element modelling of piezoelectric devices is given in [66].

To design a suitable composite for constructing the log spiral array prototype a number of areas need to be addressed:

6.3.1 Ceramic material

High sensitivity and bandwidth is required for imaging applications, and it is normal to choose a soft ceramic, with a high coupling coefficient and electrical permittivity. PZT 5H meets these criteria, and was used as the active component in the prototype composite.

6.3.2 Filler material

Choice of filler material for phased arrays is always a compromise. Low stiffness and high acoustic attenuation are often associated with each other, providing a high coupling coefficient and low mechanical crosstalk respectively. However, high attenuation reduces sensitivity, and very low stiffness can result in poor surface dilation quality. A medium-set epoxy achieves a good compromise, and it has been

used in Alba to produce linear arrays with a thickness coupling coefficient of 65%, and crosstalk between adjacent elements of less than -40 dB.

6.3.3 Pillar aspect ratio

A pillar aspect ratio (width to height) of 0.25 or lower is desirable to achieve a high electromechanical coupling coefficient, and suppress lateral resonance modes [57,58]. Analysis using a Linear Systems Model (LSM) [56] implemented in Matlab shows that to achieve the target centre frequency of 1.5 MHz, a piezocomposite thickness of 1.05 mm is required. Therefore, a pillar width of approximately 200 μm, with an aspect ratio of 0.20 would be suitable.

6.3.4 Ceramic volume fraction

The ceramic volume fraction of a device can have a significant effect on its performance. For pulse echo transducers, a volume fraction between 30% and 70% yields the greatest transmit-receive sensitivity [56]. The composite layout is shown in Figure 6-14, showing the pillar width, pitch, and the kerf between adjacent pillars, labled as p_{comp}, d_{comp}, and k_{comp} respectively. Alba creates 1-3 piezocomposites using the dice and fill method, where a block of ceramic is first diced into a fine pillar structure using a diamond saw, and the vacant area is encapsulated with polymer. It is therefore important to know the required pitch and kerf of the composite, to properly set up the saw.

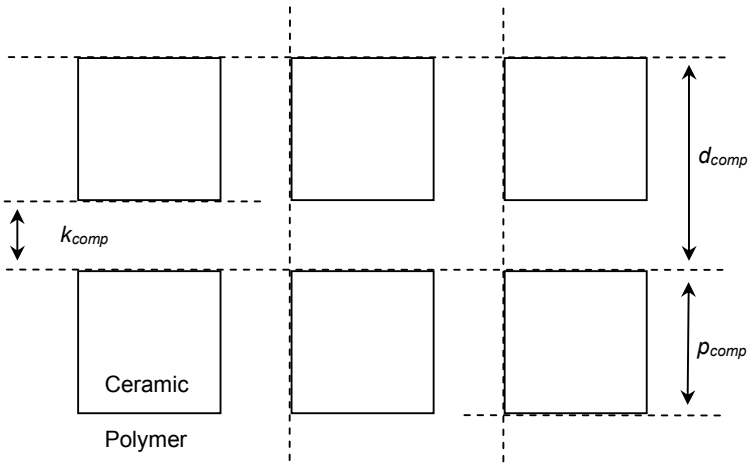

Figure 6-14 **Diagram of the piezocomposite microstructure, showing the inter pillar pitch, d_{comp}, the pillar width, p_{comp}, and the kerf, k_{comp}.**

The volume fraction of ceramic in a composite is given by the following equation:

$$V = \frac{{p_{comp}}^2}{{d_{comp}}^2} \qquad \textbf{(6-3)}$$

Alba has a variety of diamond blades for its saws, and the most suitable blade for this job has a kerf of 100 μm. If this were used to produce 200 μm wide pillars, the resulting inter pillar pitch would be 300 μm. Using Equation 6-3, this gives a volume fraction of 44.4%. This is a good compromise between optimum electromechanical coupling and minimised acoustic impedance, making this design well suited for optimised transmit-receive sensitivity [57].

6.3.5 Number of pillars under array element

One final consideration for the design of piezocomposites for 2D arrays is that there is a sufficient number of pillars under the array element for it to vibrate in an approximately piston like manner. There is a discontinuity at the edge of the element, where active pillars sit adjacent to inactive pillars. This unequal loading can change their vibrational response, introducing parasitic modes. It has been shown in the literature that 2D array can be constructed with as little as 9 pillars under each element [63].

Simple analysis of the log spiral design shows that there are many more pillars than this under each element. Figure 6-15 shows a 3 x 2 mm electrode superimposed on the pillar structure, completely covering 44 pillars. The alignment of the element relative to the microstructure varies throughout the array, but it is not anticipated that this will significantly affect the performance of the design.

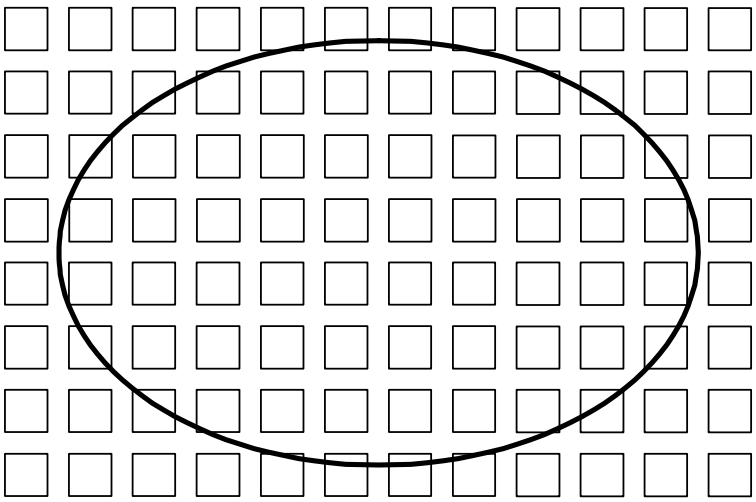

Figure 6-15 Plan of log spiral array element showing 44 full pillars under the electrode.

6.4 Construction of prototype

The prototype log spiral array was constructed in Alba. Many of the manufacturing techniques required to do this were developed as part of the Engineering Doctorate Programme, having been developed from Alba's existing sonar array manufacturing capability. An overview of the prototype design and this manufacturing process is given in this section.

Figure 6-16 shows a cross sectional diagram of the prototype transducer, with its key components annotated.

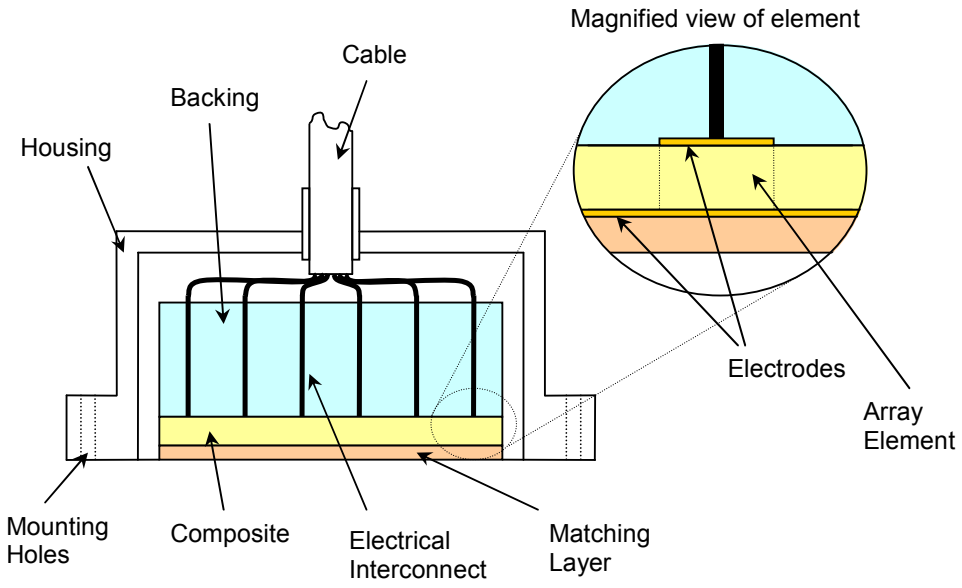

Figure 6-16 **Cross sectional diagram of the array prototype showing the key components. The pillar structure of the piezocomposite is omitted for clarity.**

The design of the piezocomposite microstructure is described in Section 6.3. The construction of the composite began with a monolithic block of PZT. This was diced through both the *x* and *y* directions using a high speed dicing saw fitted with a

diamond blade. The resulting pillar structure was then encapsulated using a two part epoxy system. The excess epoxy and the ceramic stock were then removed from the structure using a surface grinder. The composite was then lapped to its final thickness of 1.05 mm to achieve a surface roughness of < 1 μm R_a (roughness average).

Copper electrodes were applied to the front and rear faces of the device, and patterned using a proprietary Alba process. The electroded rear face of the composite is shown in Figure 6-17. These electrodes were electrically connected to an external cable, consisting of 127 individual micro-coaxial cables. The use of coaxial cables ensures electrical crosstalk is < -60 dB, ensuring it has a negligible effect on array performance. The other end of the cable was soldered to a 128 pin Hypertronics connector, which is compatible with many commercial array controllers, including CUE's Zetec DYNARAY.

Figure 6-17 **Rear face of the piezocomposite immediately after having its electrode applied. While there is some discoloration at the edge of the outer elements, these areas were still found to be conductive; the discoloration was an unwanted optical effect caused by the sputter process, and with further process development can now be avoided. The substrate is 70 x 50 mm, and the elements are 3 x 2 mm.**

A customised acoustic backing material was created, both to acoustically damp the array elements, and to mechanically support them. It consists of a mineral filled polymer material, with an acoustic impedance of approximately 6 MRayls, and a high acoustic attenuation. The polymer used gives a compromise between high acoustic attenuation, and the mechanical stiffness required to support the device during machining of the matching layer. The mineral filler adds mass, increasing the acoustic impedance of the backing to increase the bandwidth of the device. 6 MRayls was chosen as a compromise between bandwidth and sensitivity. The

mineral filler was also specially design to avoid settling during the curing process, to provide a uniform acoustic performance throughout its thickness. The acoustic backing was fitted to the rear of the composite.

A quarter wave acoustic matching layer was bonded to the front of the device, to improve the acoustic matching into the Rexolite wedge. The acoustic impedance of the matching layer was designed to be approximately the geometric mean of the piezocomposite and a water load [67]. This optimises device bandwidth when operating into water, but is not ideal for matching to the Rexolie wedge. This is a compromise, since a material with a high enough impedance for optimum matching to Rexolite was not available from Alba's material suppliers. The matching layer improves both the sensitivity, and the bandwidth of the device [67], and also acts as a protective front layer.

A stainless steel housing was designed in Alba, and manufactured by a local subcontractor. Key datum surfaces on the housing were ground to achieve flatness tolerances of ±5 μm, ensuring that planarity of the key acoustic components was maintained.

The completed prototype log spiral array is shown in Figure 6-18. The following section describes the testing that was carried out on the array, and the experimental results that were obtained.

(a)

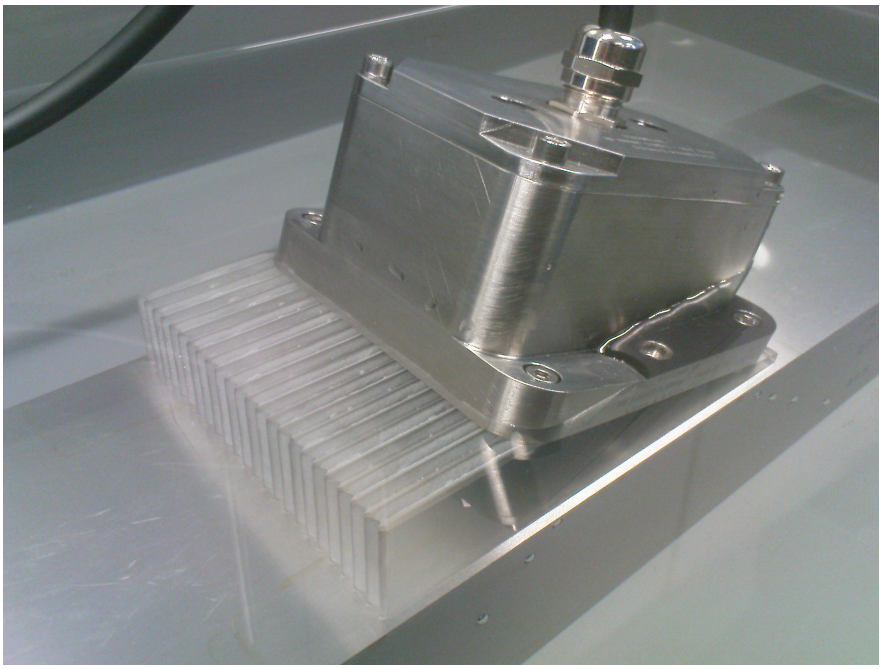

(b)

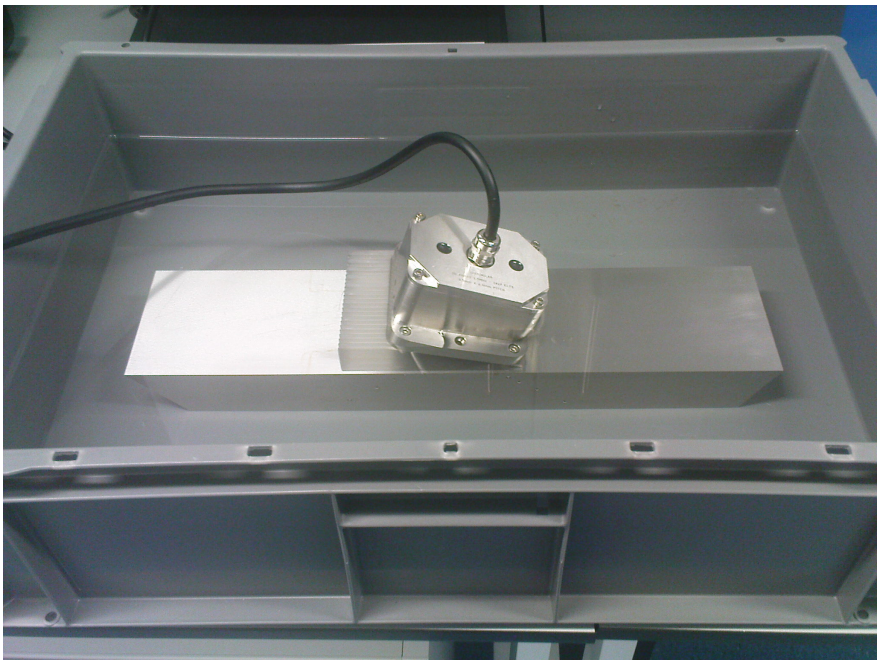

Figure 6-18 **Images of the log spiral array prototype, (a) mounted on its Rexolite wedge and (b) used in an immersion inspection of a test block.**

6.5 Experimental results

The following sections describe the experimental results obtained from the log spiral array prototype.

6.5.1 Electrical impedance

The electrical impedance of the array was measured prior to casting the backing and matching layers. At this stage the front and back faces of the piezocomposite were air loaded, and are therefore relatively undamped. The impedance magnitude of all 127 array elements is shown in Figure 6-19. The uniformity of the impedance indicates that the composite microstructure is in good condition, and that the varied positioning of the electrodes has not introduced variation in electrical performance. The electrical resonant frequency was 1.42 MHz, which later increased to 1.54 MHz after the addition of the backing and matching layers. The mean impedance at electrical resonance was 327 ohms.

This uniformity is further evidenced by the low frequency capacitance of the elements, which is shown in Figure 6-20, where over 90% of the elements are within +/- 5% of the mean value, which was 64.2 pF.

The impedance of the array elements was modelled using the linear systems model. As this is an analytical model it is very quick to run (< 1s), and it is very useful for comparing post process impedance results with theory during manufacture. This helps to monitor the manufacturing process, ensuring the composite is performing as expected at all times. The modelled and experimental results are shown in Figure 6-21, and good correlation is achieved.

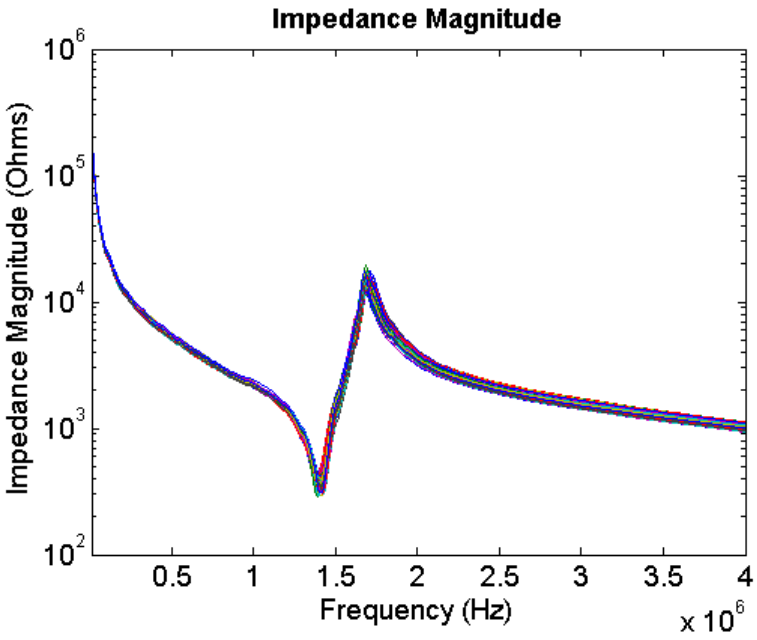

Figure 6-19 **Impedance magnitude of all array elements.**

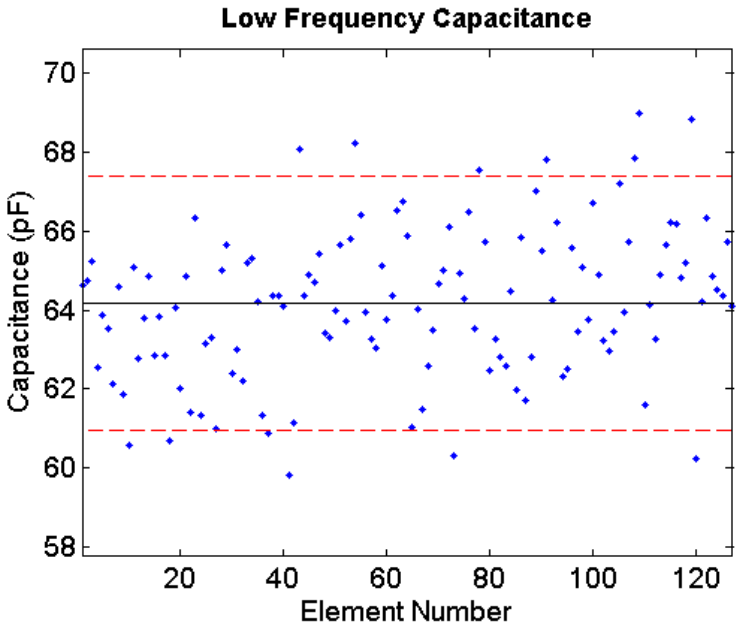

Figure 6-20 **Low frequency capacitance of array elements, with error bars at ± 5% of mean value.**

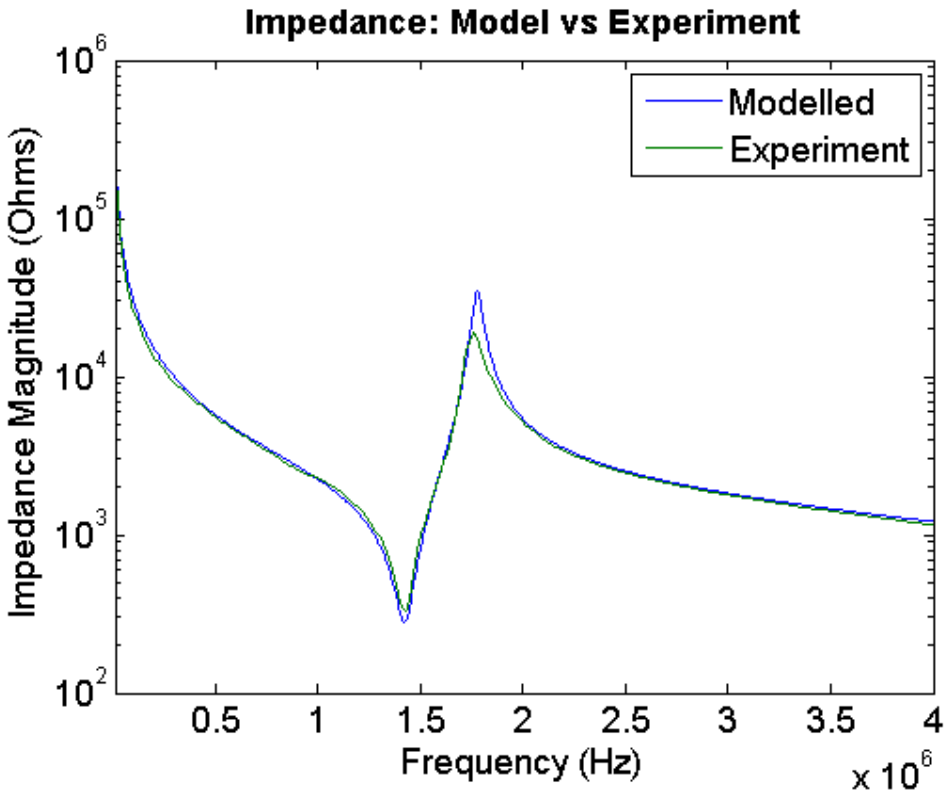

Figure 6-21 **Modelled impedance of an array element, calculated using the analytical linear systems model, compared to the measured impedance of an array element.**

6.5.2 Laser vibrometry

The surface displacement of the completed array was measured in air under CW excitation using a Polytec scanning laser vibrometer in the CUE laboratory. This instrument uses a laser interferometer to measure minute surface displacements, and monitor how they vary with time. A tilting mirror is used to scan the laser in the *x*-*y* axis, allowing relatively large surfaces to be interrogated quickly.

Two scans were carried out: firstly a detailed scan of the centre array element was performed to assess the dilation quality of an individual array element; secondly the whole array surface was scanned, to measure the uniformity of the displacement across its surface.

For each experiment the array was driven under CW excitation using a function generator, with a frequency of 1.5 MHz. In both cases the amplitude was set to 20 V, however when driving all array elements in parallel only 2.5 V could be achieved across the elements due to the large capacitance of the coaxial cables. In order to improve the signal to noise ratio 8 measurements were averaged for each scan point. For both scans a median filter was applied to de-noise the resulting image.

For the scan of the centre element a resolution of 56 μm was used. Figure 6-22 shows both the magnitude and phase of the measured surface displacement. While the matching layer prevents the observation of the microstructure's movement, the result shows a relatively uniform displacement, with a flat phase response over the element surface area. A peak displacement of 127 pm/V was observed close to the centre of the element. Cross talk is worse in the vertical axis, where the longer side of the element is exposed. The peak crosstalk outside of the minimum element spacing distance of 0.6λ (2.34 mm) is -15.8 dB. It should be noted that the centre element is well isolated from other elements, and it is expected that the elements in the arms will experience higher crosstalk. However, the imaging performance of the array demonstrated in Section 6.5.8 is testament to the fact that cross-talk has been kept at manageable levels.

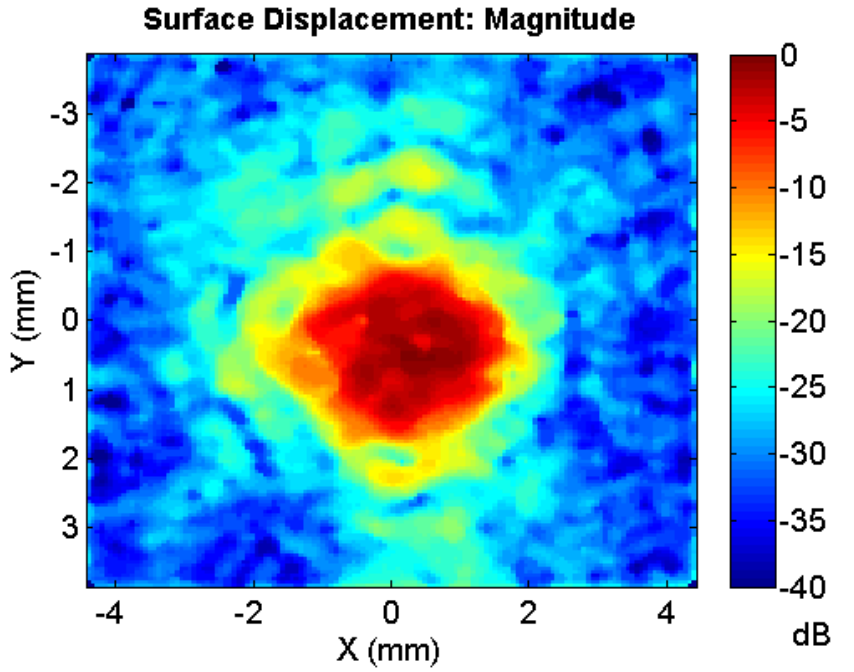

(a)

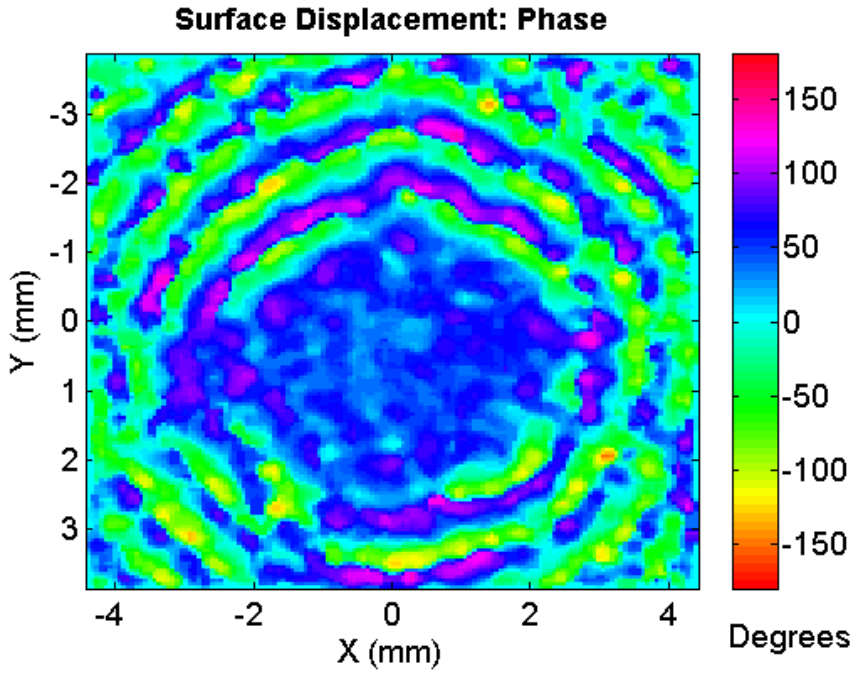

(b)

Figure 6-22 **Surface displacement of the centre array element under CW excitation at 1.5 MHz, (a) magnitude and (b) phase.**

The scan of the whole array used a coarser resolution of 287 μm and contains approximately 35,000 scan points. The magnitude and phase of the surface displacement are shown in Figure 6-23. The magnitude plot clearly shows that the array elements are positioned as intended in the design, and that all are resonating. The variation in displacement across the array is 3.9 dB, which is particularly uniform for a first of type prototype. There is very little phase variation across the array despite its large aperture, indicating that good flatness was achieved with the selected manufacturing process. 90% of the elements were within ±15° of phase.

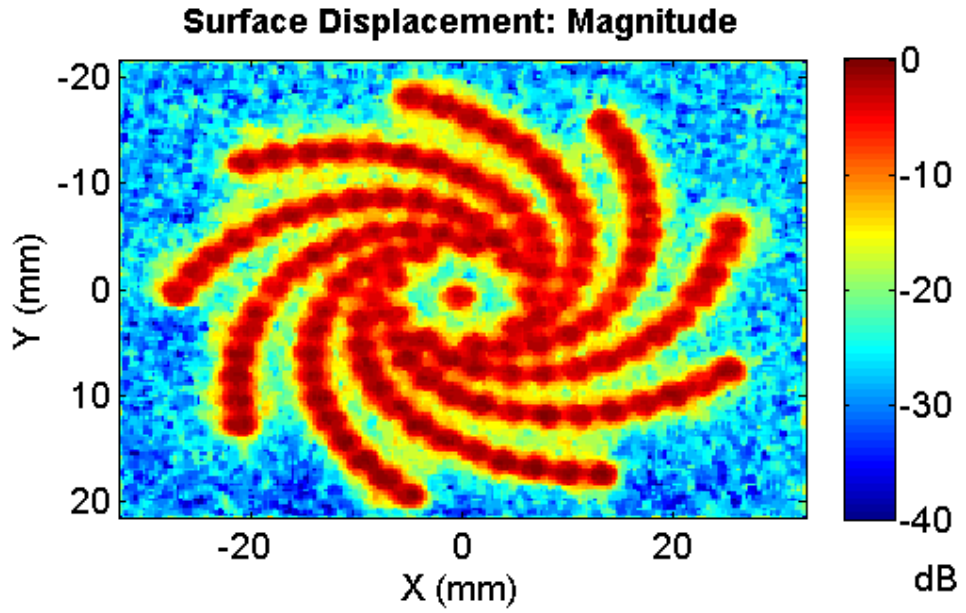

(a)

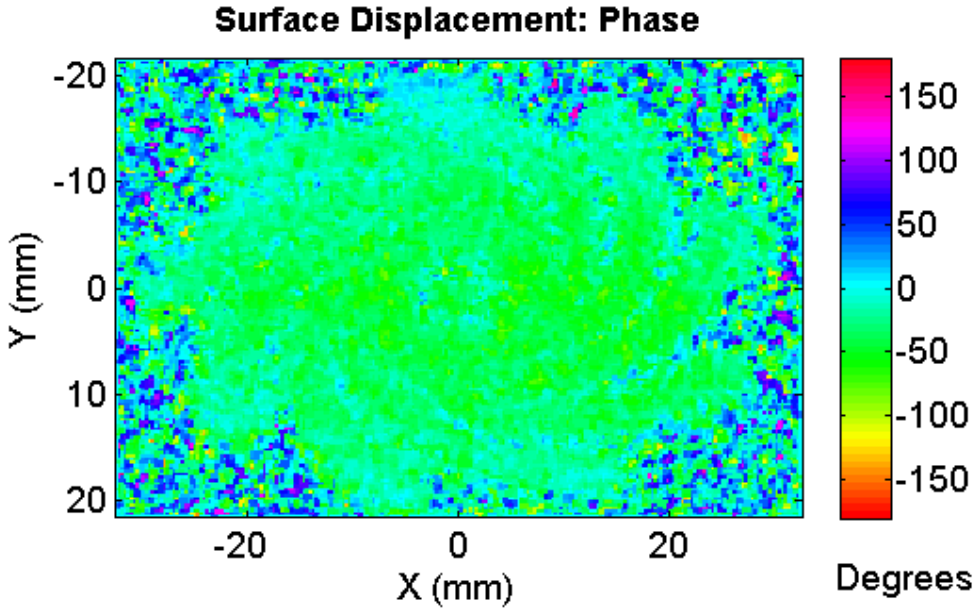

(b)

Figure 6-23 **Surface displacement of the prototype array with all elements in parallel under CW excitation at 1.5 MHz, (a) magnitude and (b) phase.**

6.5.3 Pulse echo testing

To test the functional performance of the array elements a simple pulse-echo test was carried out in a tank of water. The array was placed on top of a flat metal plate, supported by two metal slips, so that its front face was parallel with the plate. This arrangement is shown in Figure 6-24. An array controller was used to pulse each channel with a rectangular function, with an amplitude of 40 V and a duration of 190 ns. This pulse length was chosen to provide sufficient bandwidth to excite the array elements at their fundamental resonance, but to avoid exciting their third harmonic. The received pulse-echo response of the centre element is shown in Figure 6-25, along with the received spectrum, which was calculated using an FFT.

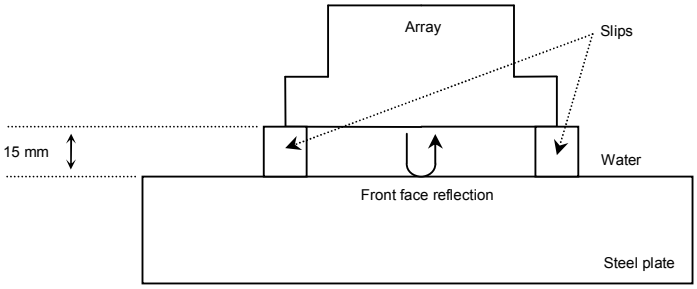

Figure 6-24 Pulse echo test setup.

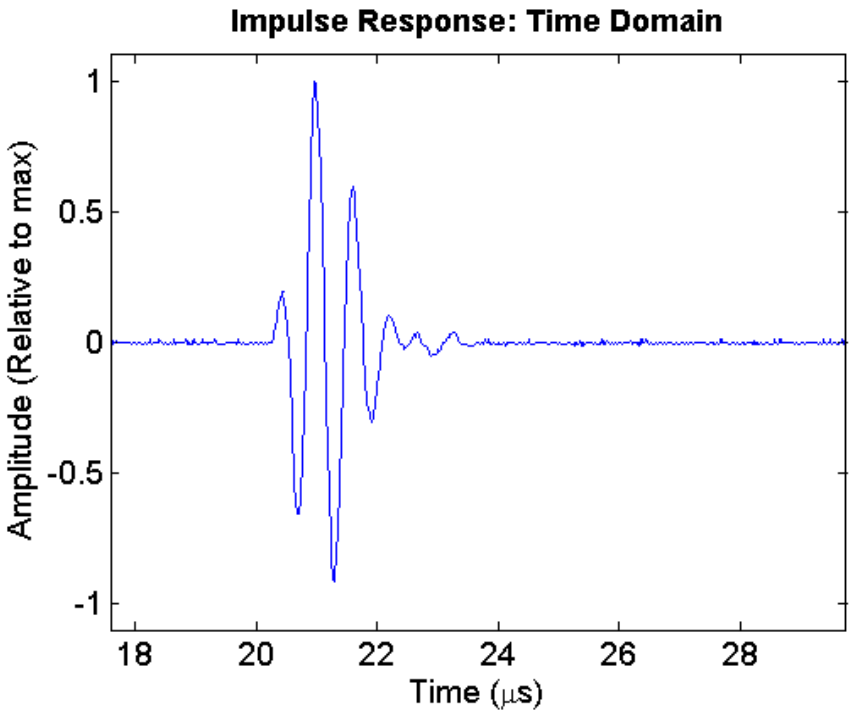

(a)

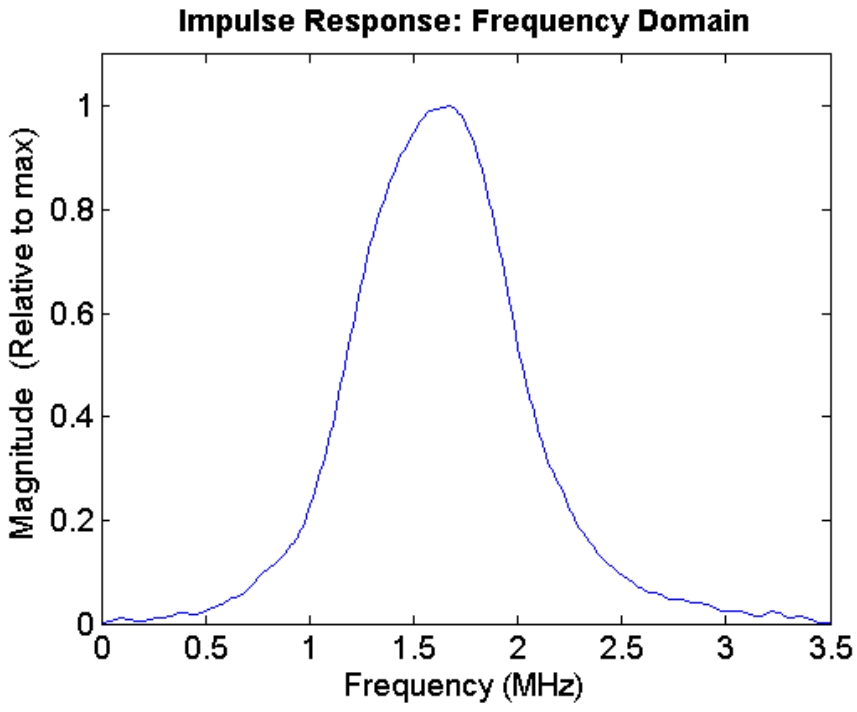

(b)

Figure 6-25 **Pulse echo response of the centre element, (a) time domain and (b) frequency domain.**

The centre frequency of the array is 1.6 MHz, slightly higher than the design frequency of 1.5 MHz. This is due to a small error in the thickness of the matching layer. The bandwidth of the array is 0.85 MHz, resulting in a fractional bandwidth of 53%. This is lower than has been achieved by Alba on similar array designs, and is thought to be due to the unusual shape of the elements. The mismatched loading on pillars at the edge of the element can result in bending modes being introduced, and these modes can cause the element to ring for longer, reducing bandwidth. Future work will look at optimising the microstructure of the array to reduce these effects, and is described in Chapter 7.

The pulse echo response of a transducer element is compared to that of a modelled response in Figure 6-26. The modelled response was generated in LSM, so does not consider any of the lateral modes that may occur across the element. The model is centred at 1.5 MHz, and has a bandwidth of 0.99 MHz, giving it a fractional bandwidth of 66%.

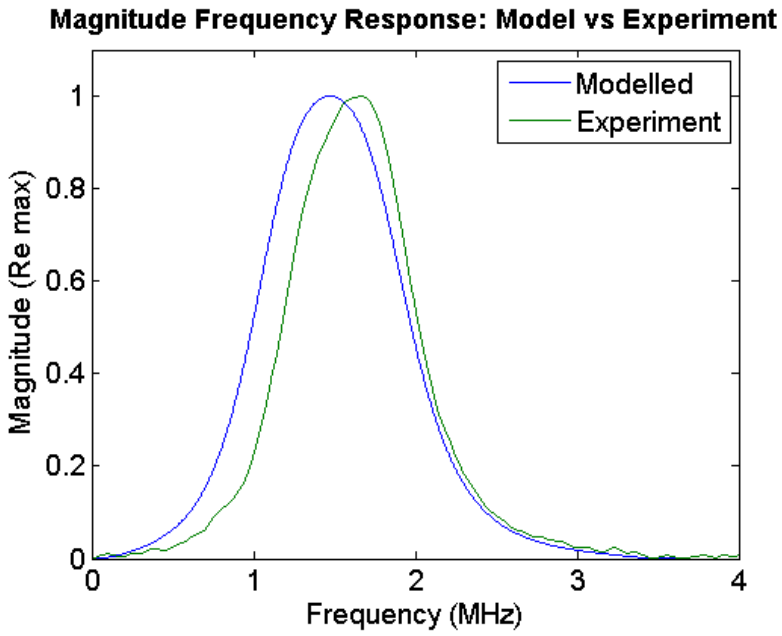

Figure 6-26 **Modelled magnitude frequency response using LSM compared to that of the experimental result.**

To test their uniformity and flatness, the array elements were fired successively, and the rectified A-scans placed side by side to form a B-scan image of the plate, as shown in Figure 6-27.

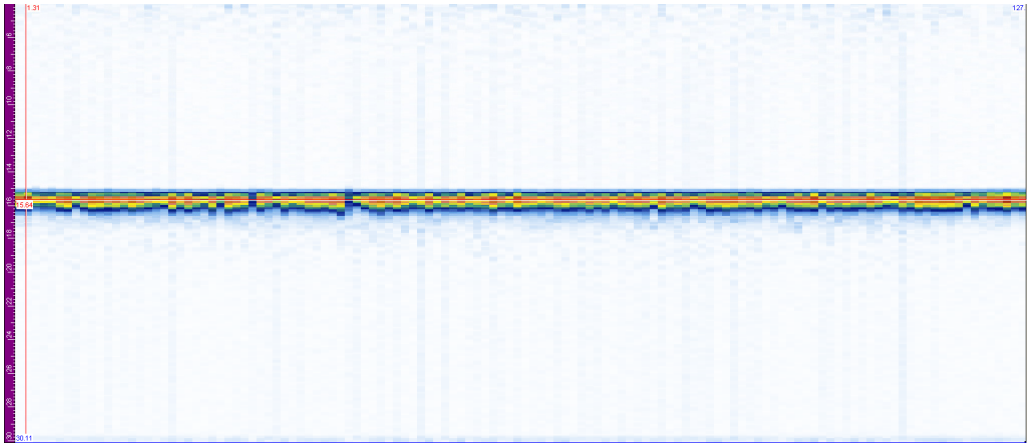

Figure 6-27 **Rectified b-scan of the front face reflection from the block, with element 1 on the left and element 127 on the right. The vertical scale is round trip distance in water (mm).**

In general the sensitivity of the array elements is uniform, as predicted by the electrical impedance, and the laser vibrometry. The arrival time of the echo is also consistent, indicating that the array is flat, and parallel to the block.

These tests indicate that, while the array's performance is not a perfect match for theory, it is functioning well within what could be expected for an initial prototype of a new design. The next stage is to perform functional inspections to test the imaging capability of the array.

6.5.4 Array controller configuration

Modern phased array controllers are designed to be capable of carrying out a wide range of inspections, and as such, offer the user a wide variety of configuration options. However, they typically only have a limited number of default options for the layout of the array in use. The user can generally select between 1D and 2D arrays, and then specify the number of elements, and pitch in each axis, with the controller assuming that 2D designs are laid out in a simple grid pattern. Due to this limitation in the user interface, focal laws for arbitrary arrays must be calculated externally, and then loaded into the instrument by means of a configuration file.

The Zetec Dynarray used in the work accepts customised focal laws in file format with the extension *.law*. Each delay law is defined by a series of transmit and receive delays, one for each element in the array. The file also contains information on the delay experienced in the wedge, and the point that the beam enters the test piece (referred to as the index point). A number of focal laws can be defined in one file, and the instrument displays these laws together to create a scan of the test piece.

A Matlab script was written to generate *.law* files for arbitrary arrays, and was used to test the prototype spiral array. The software allows the user to define sweeps in both elevation and azimuth (referred to as skew by Zetec), and offers three focal modes:

- Range, where focal points are created at a constant range in the test piece, creating an arc (or hemisphere) of focal points.

- Depth, where focal points are created at a constant depth in the test piece, creating points in the *x-y* plane. This is useful for inspecting defects close to the back wall.

- Distance, where focal points are created at a constant x distance in the test piece, creating points in the y-z plane. This is useful for inspecting defects on the end face of a component.

These modes are similar to those found on most modern array controllers, allowing the user to tailor the scan for a specific inspection. Examples of each of these modes are shown in Figure 6-28. In each case, the array element locations (array points), focal points, and index points are plotted.

Similar software has been written for the Micopulse 5 PA phased array controller by Peak NDT, meaning that the inspections carried out here are not limited to a single platform. As this software allows users to program delay laws for completely arbitrary array designs, and can be deployed on current array controllers, it shows that novel arrays such as log spirals can be used in industrial inspections. However, full support for log spiral arrays from standard array controller software would be advantageous. It would make it easier for potential customers to adopt log spiral arrays, removing the need for them to develop custom software. This is discussed further in Chapter 7.

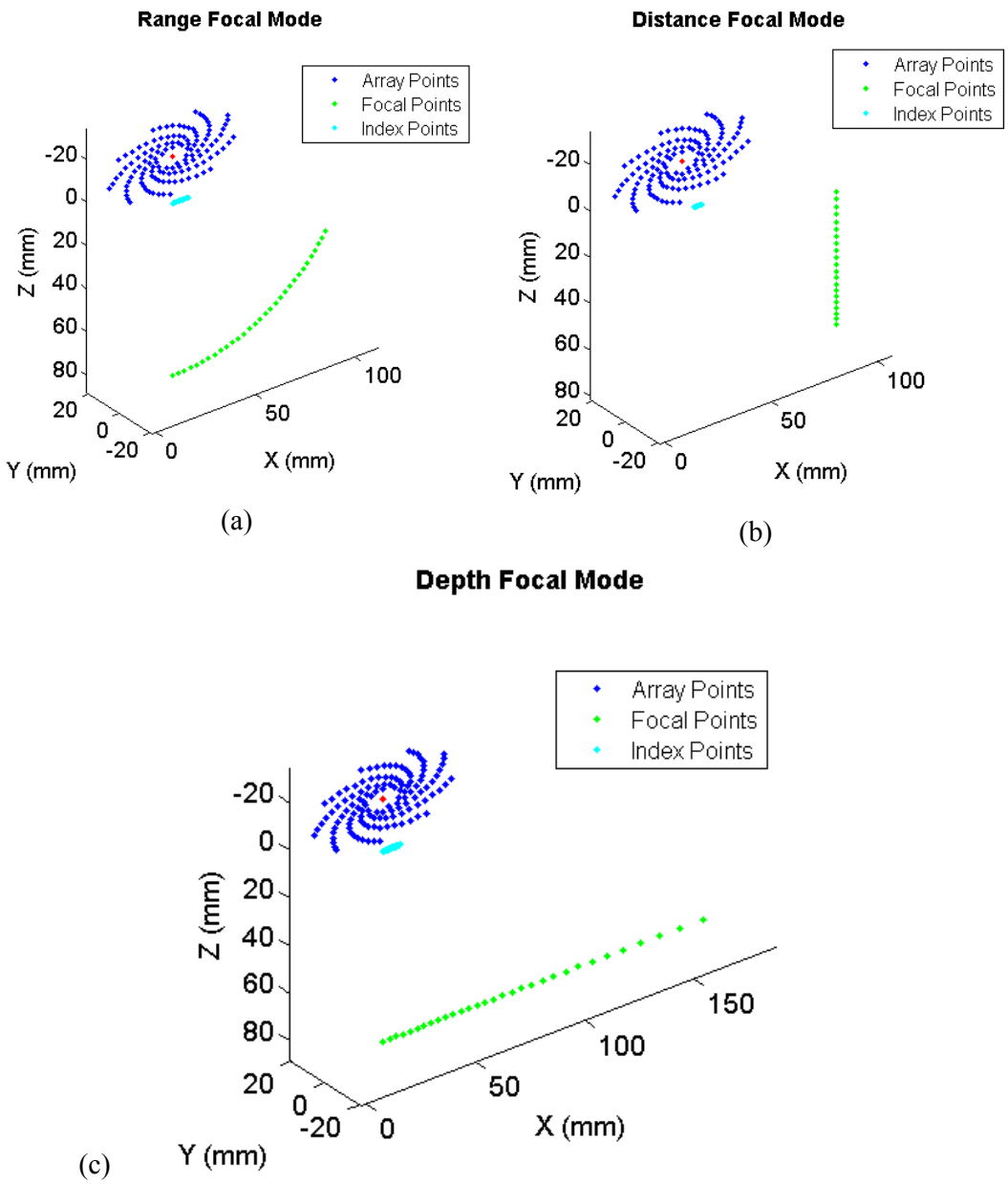

Figure 6-28 **Illustrations of the three focal modes, all setup to perform elevation scanning with a focal range of 80 mm, and an angular step of 2°, (a) range mode, sweeping from 0° to 70°, (b) distance mode, sweeping from 40° to 80° and (c) depth mode, sweeping from 0° to 70°.**

6.5.5 Sector scans of SDHs

The initial scans performed on the test block were simple focused sector scans. The array was coupled to the Rexolite wedge using coupling gel, and the two components were then screwed together. The test block was immersed in a water tank to ensure good coupling between the wedge and the test piece, and the wedge/array assembly was placed on top of the test block on top of the area with the SDHs. The locations of the SDHs in the test block are shown in Figure 6-29. These defects will be referred to as SDH 1 – 4, with SDH 1 being the 75 mm deep hole, and SDH 4 being the 20 mm deep hole.

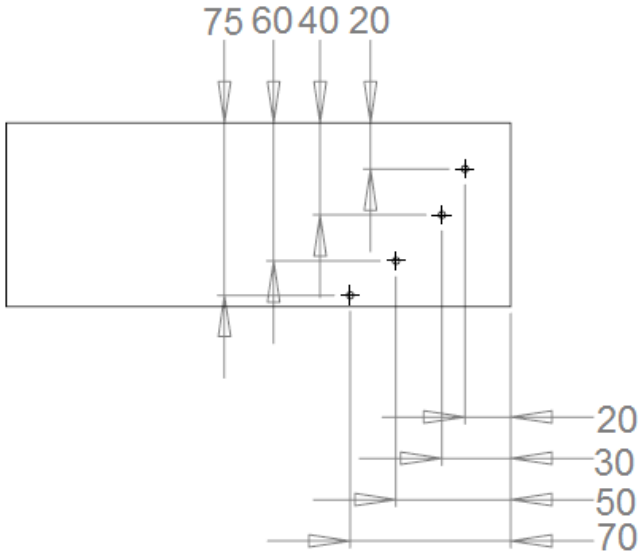

Figure 6-29 **Locations of the SDHs one the test block. All holes are 3 mm in diameter, and 40 mm deep.**

The array controller was programmed to perform an elevation sweep between 0 and 70 degrees, in 0.25° steps, and focussing at a range of 55 mm. This produced a scan with 281 focal laws, and focal points located as shown in Figure 6-30. In all scans

the excitation setting is 40 V, and the gain is adjusted so that the signal of interest is 80% full screen height.

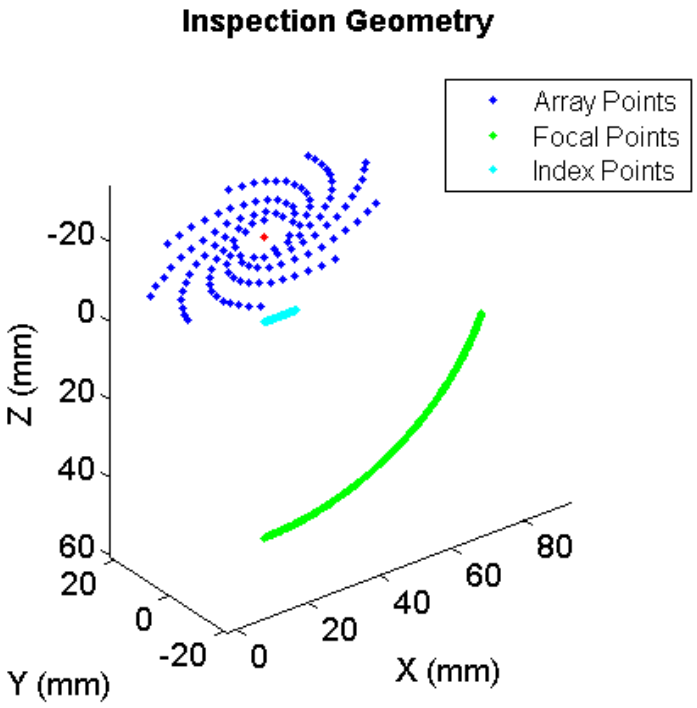

Figure 6-30 Focal points of 55 mm range sector scan.

The array was positioned so that all four SDHs were visible in the scan, with the array almost directly above the 75 mm deep hole. The array controller was set up to display a-scan data on the left half of the screen, with a sector scan on the right half. A drop down menu on the interface allows the user to select which of the 281 a-scans is displayed, and this A-scan is highlighted on the sector scan with a black line. Cursors are available to measure the location of points in the image in mm. Figure 6-31 shows the resulting image, with the 0° A-scan selected.

The image clearly shows the upper two holes in yellow / red, while the lower two holes are much fainter. This is because the directivity of the array elements means

that the array is much more sensitive close to its natural angle of 50.9°. The back wall is visible at the base of the image, and the A-scan indicates that the strength of its reflection is 9.9%. The depth of the reflection is 79.7 mm, which is very close to the actual 80 mm thickness of the block. This difference is due to small differences between the speed of sound in the wedge and test piece, and the values which are used by the software to plot the image.

There is a sixth indication to the upper right of the image, which is a standing echo in the array / wedge assembly. This can be determined by moving the array across the test block, and observing how the image changes. While indications relating to reflections from within the block change as the array is moved, this reflection remains in the same position. Therefore, it is concluded that this is a reflection from the end of the wedge.

Figure 6-32 to Figure 6-35 show the A-scans which intersect SDH 1 to 4 respectively, with the position of each defect highlighted with the red cursor on the sector scan. The position, range, and reflection strength of each defect is given in Table 6-2. The software measures the distance to the defect from the rear of the array, meaning that the 0° beam is positioned at 24 mm. This value has been subtracted from the results in the table to give a more intuitive measure of position.

Reflector	**Angle (°)**	**Distance (mm)**	**Depth (mm)**	**Range (mm)**	**Strength (%)**
Back wall	0	0	79.7	79.7	9.9
SDH 1	2.5	3.5	72.9	72.9	4.8
SDH 2	18.75	22.5	57.7	61.0	21.3
SDH 3	42.75	41.4	38.0	51.8	84.0
SDH 4	64.75	50.2	19.5	45.9	64.6

Table 6-2 Position, range, and signal strength of each reflector in the sector scan.

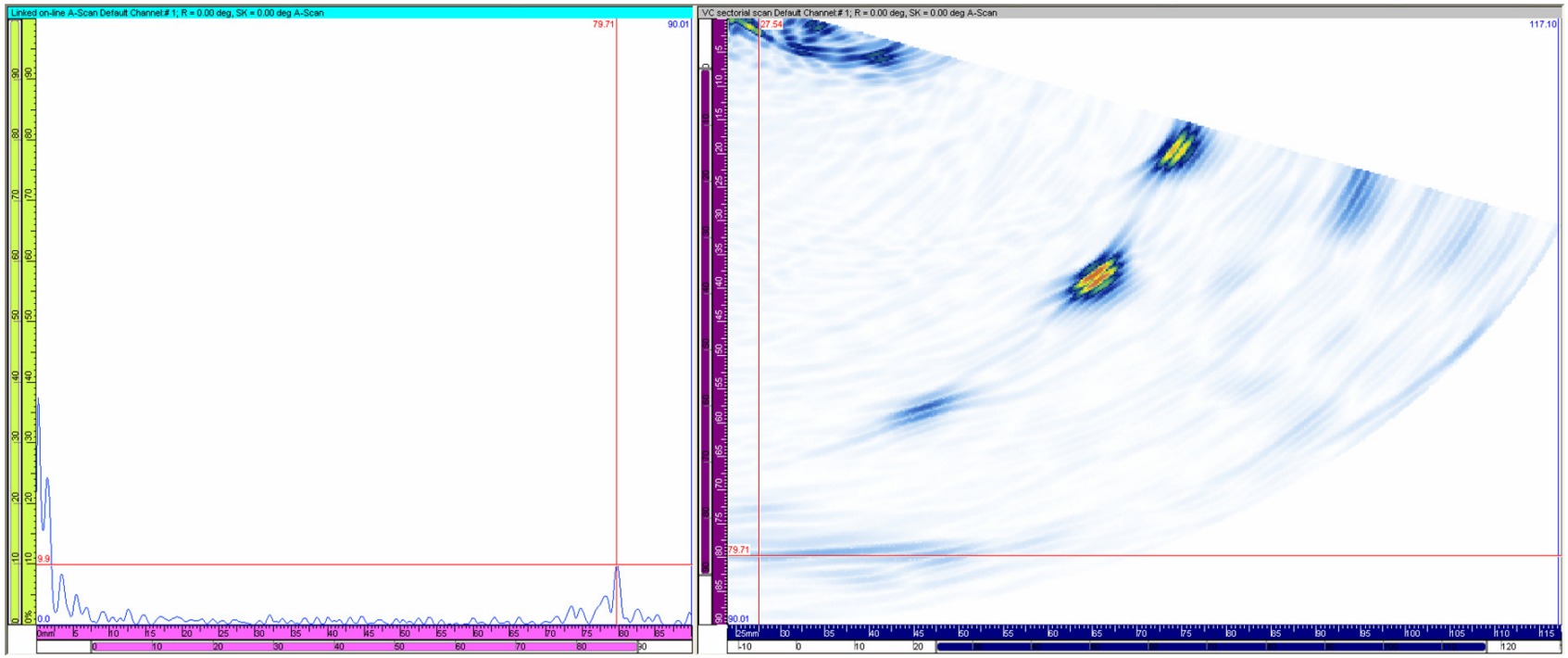

Figure 6-31 **A-scan (left) and sector scan (right) of the SDHs in the test block, with a 55 mm focal range. The A-scan shown is the 0° beam, with the back wall reflection highlighted at 79.7 mm. Gain is 47 dB, making SDH 3 approximately 80% full screen height.**

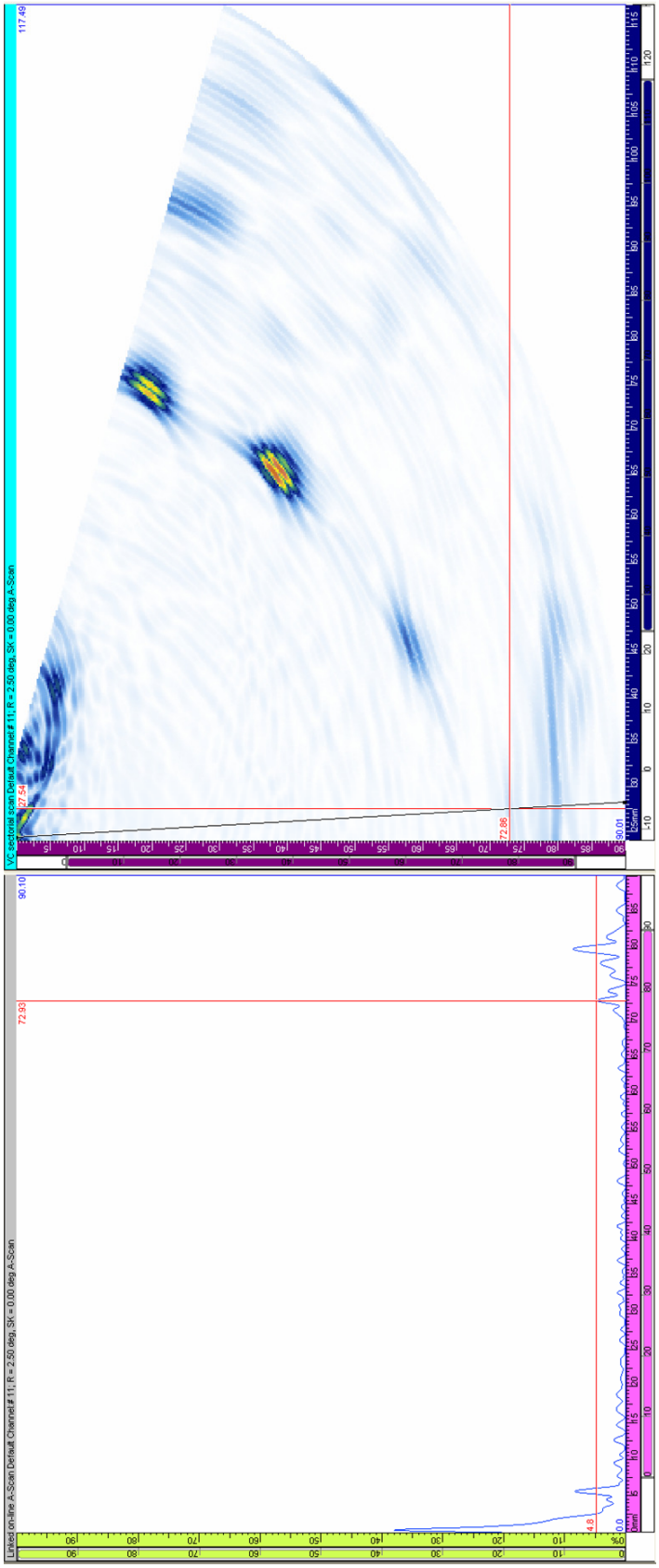

Figure 6-32 **A-scan (left) and sector scan (right) of the SDHs in the test block, with a 55 mm focal range. The A-scan shown is the 2.5° beam, with the reflection from SDH 1 highlighted.**

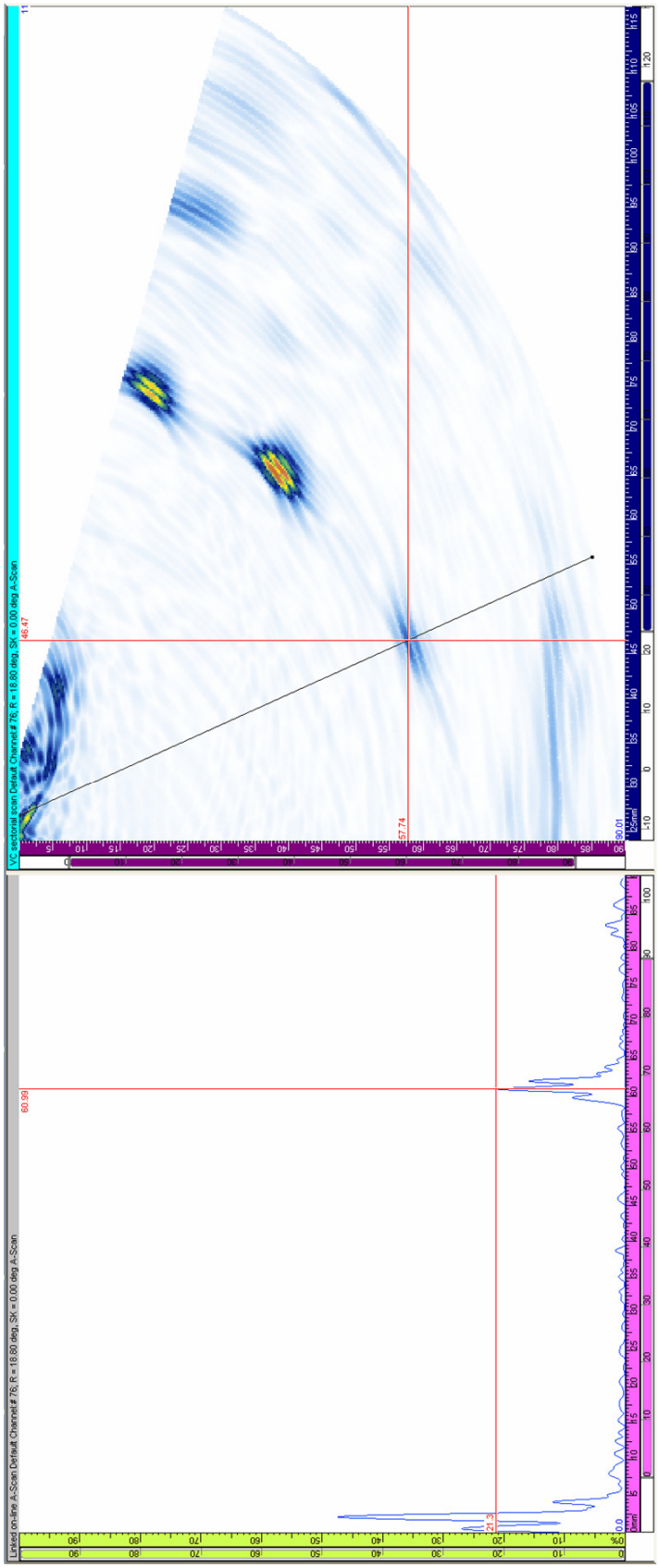

Figure 6-33 **A-scan (left) and sector scan (right) of the SDHs in the test block, with a 55 mm focal range. The A-scan shown is the 18.75° beam, with the reflection from SDH 2 highlighted.**

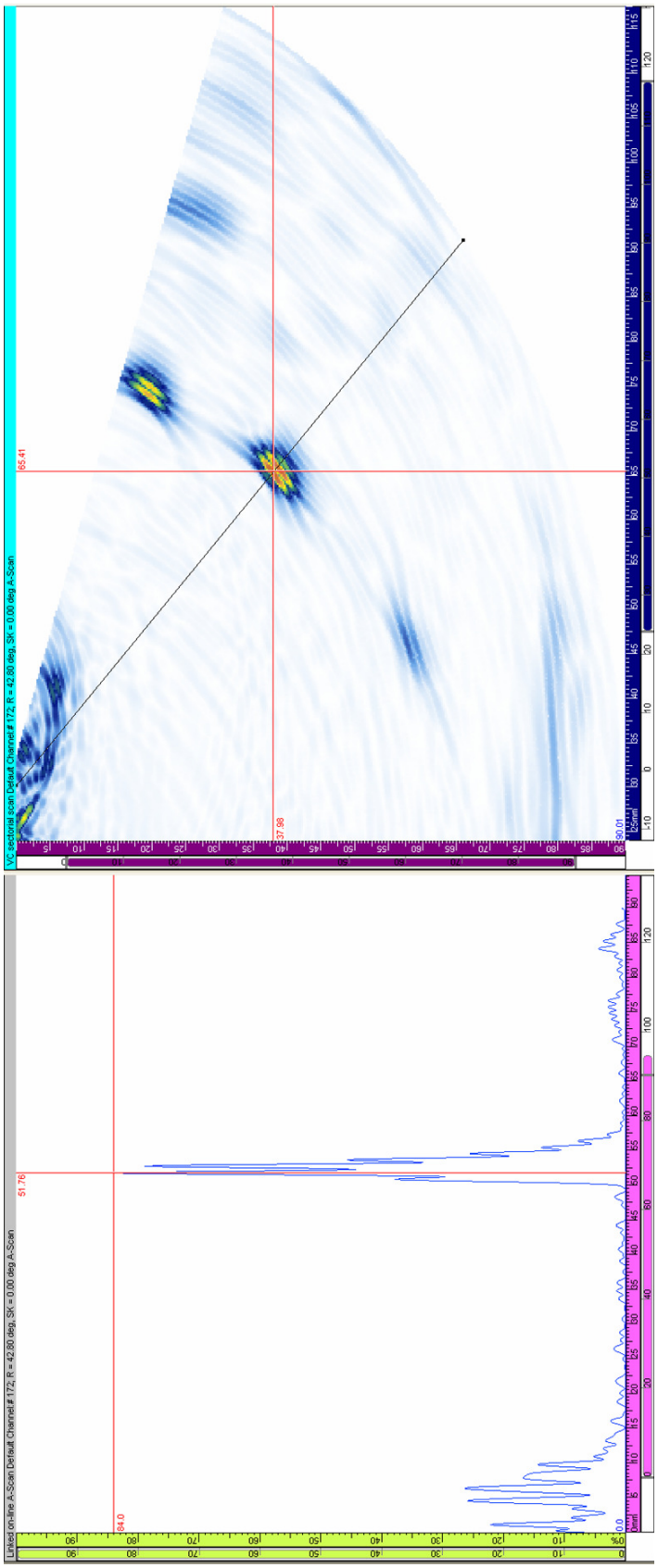

Figure 6-34 **A-scan (left) and sector scan (right) of the SDHs in the test block, with a 55 mm focal range. The A-scan shown is the 42.75° beam, with the reflection from SDH 3 highlighted.**

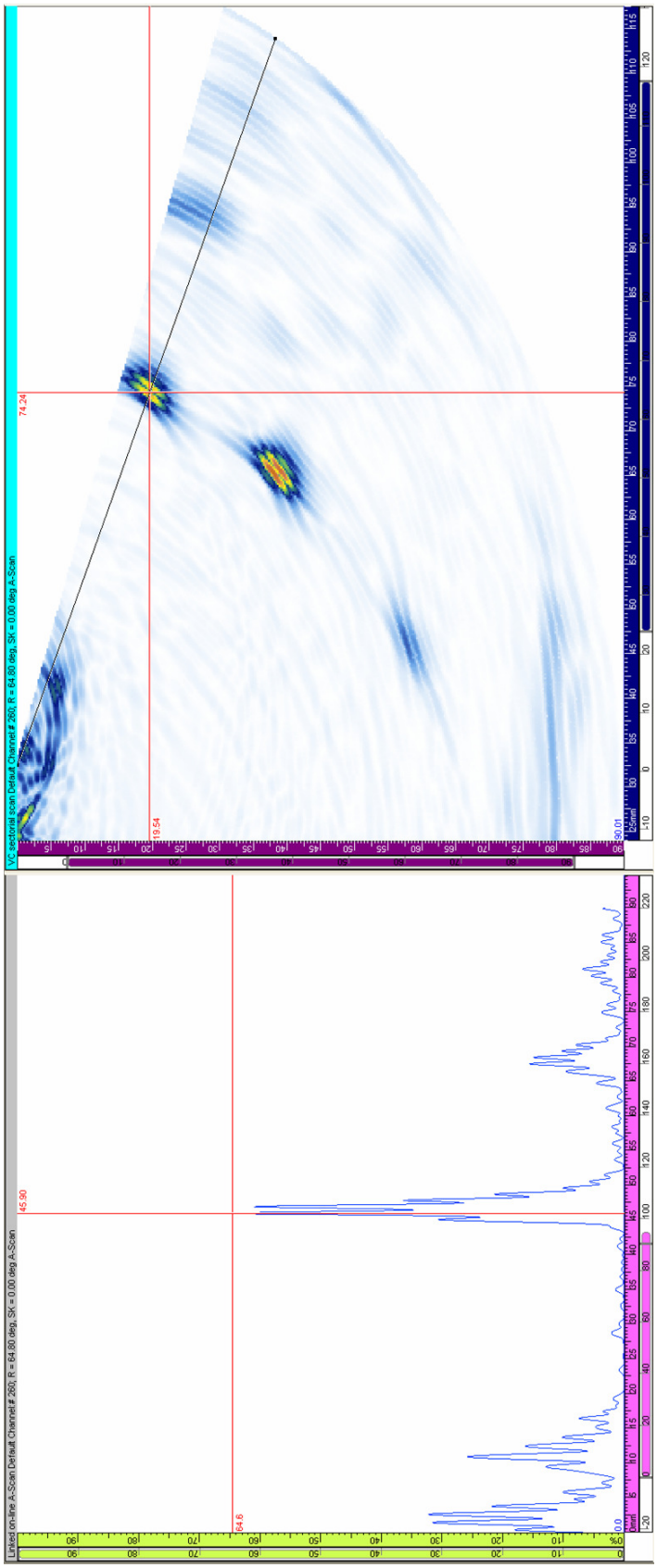

Figure 6-35 **A-scan (left) and sector scan (right) of the SDHs in the test block, with a 55 mm focal range. The A-scan shown is the 64.75° beam, with the reflection from SDH 4 highlighted.**

While the array was not designed to steer the beam down to 0°, the weak back wall reflection is very useful, since it not only provides a positional reference, but also gives a relative measure of the signal strength from the SDHs. SDH 1 is at a similar angle and range as the back wall, and the reflection strength 6.3 dB lower. Both are further away than the focal range of the scan, and this and their angle contribute to their weak signal strengths.

The focal range was set to 55 mm to ensure that SDHs 2 – 4 were all close to being in focus. The difference in reflection strengths indicate the directivity of the array elements, since SDH 2 is 11.9 dB lower than SDH 3.

The positions of the defects from the image are compared to their actual positions in Figure 6-36. Here, the along scan distance of SDH 1 is used as a reference for the actual points. The maximum positional error is 3.3 mm for SDH4, with the error increasing with steered angle. These errors are thought to be due to inaccuracy in the wedge angle, and small differences in the speed of sound in the wedge and test block from their datasheet values.

One other source of inaccuracy is the lack of a low frequency smoothing filter in the array controller. After rectification, a smoothing function is typically used to give the signal a smooth envelope, which not only improves the clarity of the images, but makes sizing easier. The array controller can only smooth waveforms down to 2 MHz, which is why the defects in the image are double peaked.

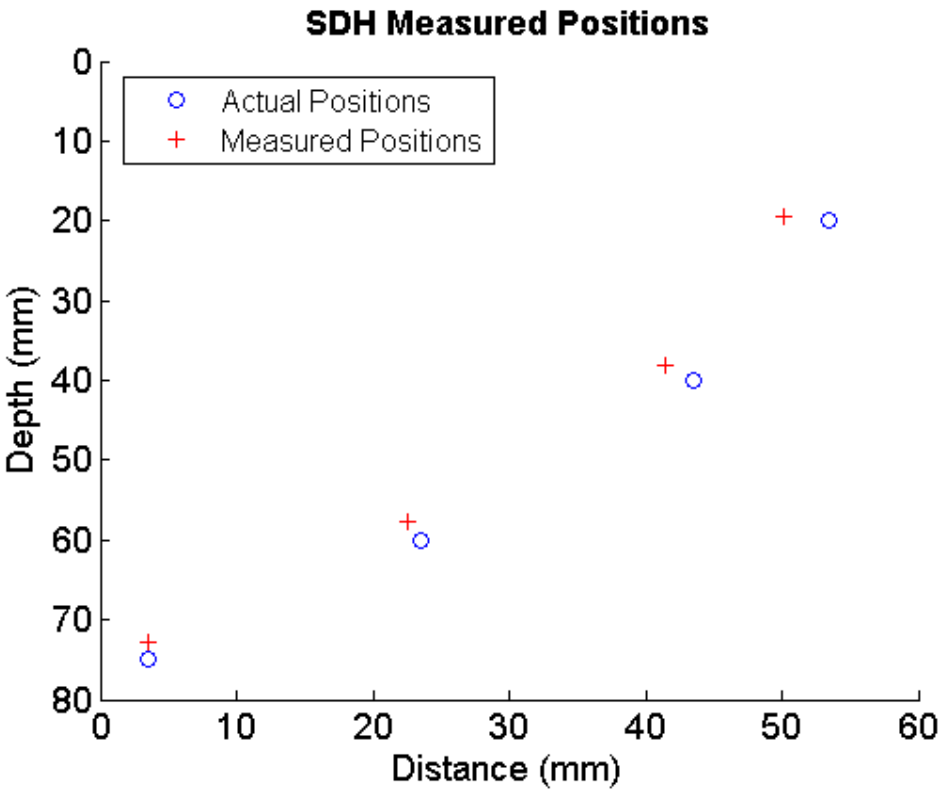

Figure 6-36 **Defect positions (blue circles) compared to the positions measured in the sector scan (red crosses).**

While this scan detected all of the defects, it would be useful to get a clearer image of SDH 1 given its close proximity to the back wall. A new sector scan was created, this time focusing at a range of 75 mm. The array was repositioned so that SDHs 1-3 were within the scan area, and the gain was increased to 49 dB to set the reflection from SDH 2 to approximately 80% full screen height. The resulting images are shown in Figure 6-37 to Figure 6-40. Cursors have been used to size SDH 2 and 3 at their -6 dB points.

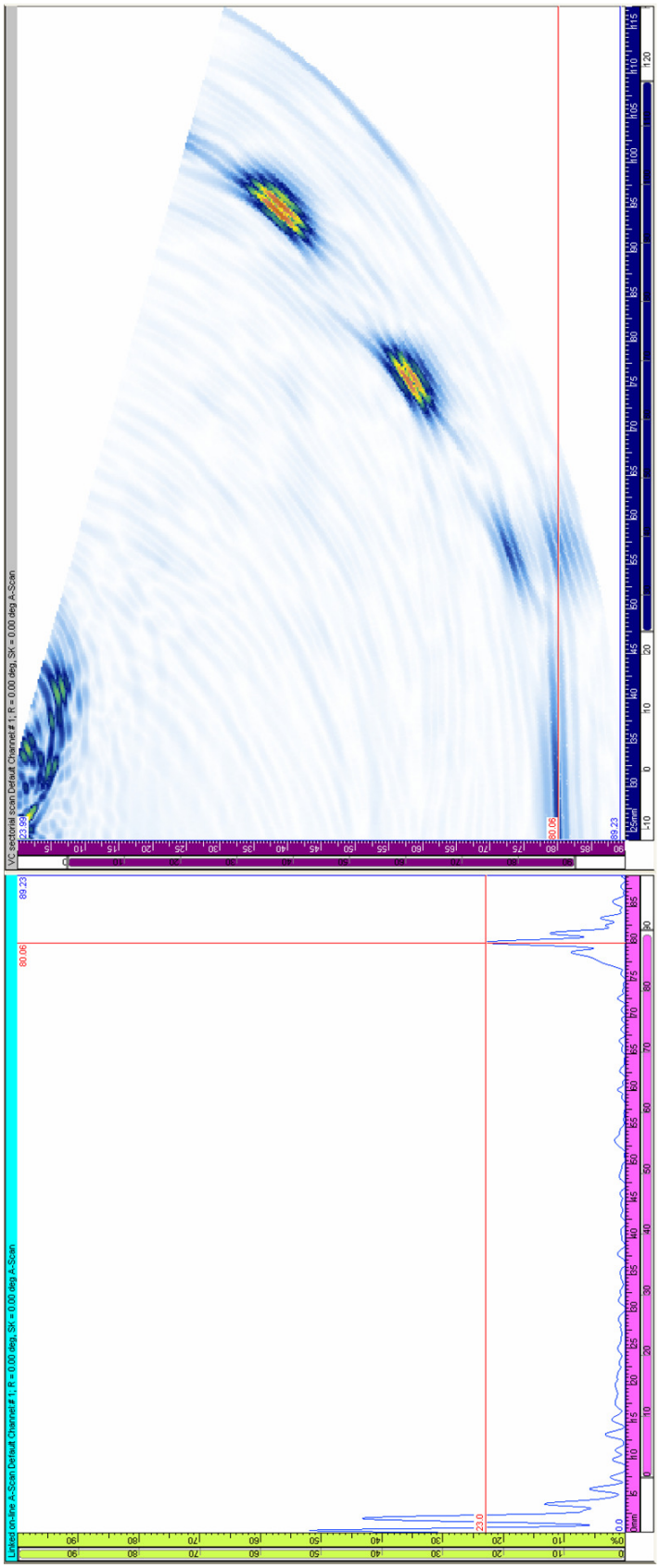

Figure 6-37 **A-scan (left) and sector scan (right) of SDH 1 - 3 in the test block, with a 75 mm focal range. The A-scan shown is the 0° beam, with the reflection from the back wall highlighted.**

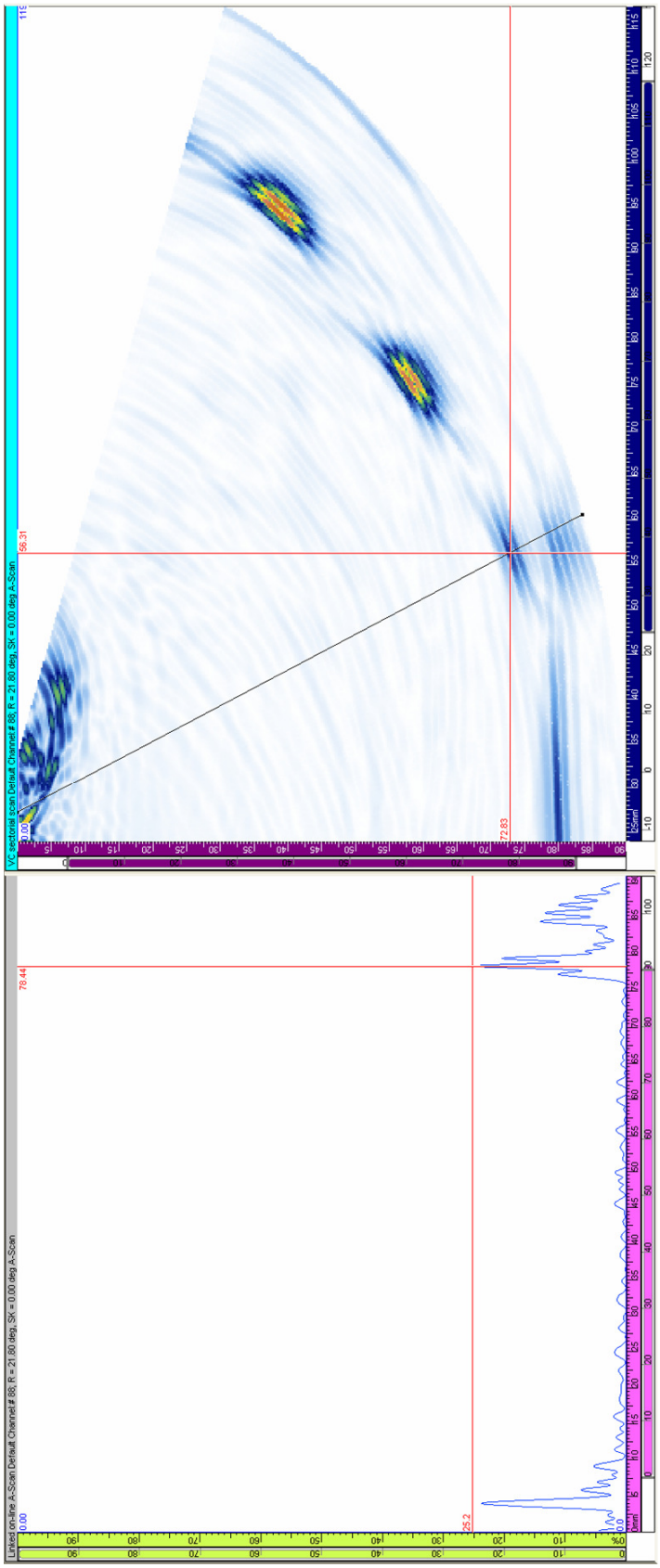

Figure 6-38 **A-scan (left) and sector scan (right) of SDH 1 - 3 in the test block, with a 75 mm focal range. The A-scan shown is the 21.75° beam, with the reflection from SDH 1 highlighted.**

Figure 6-38

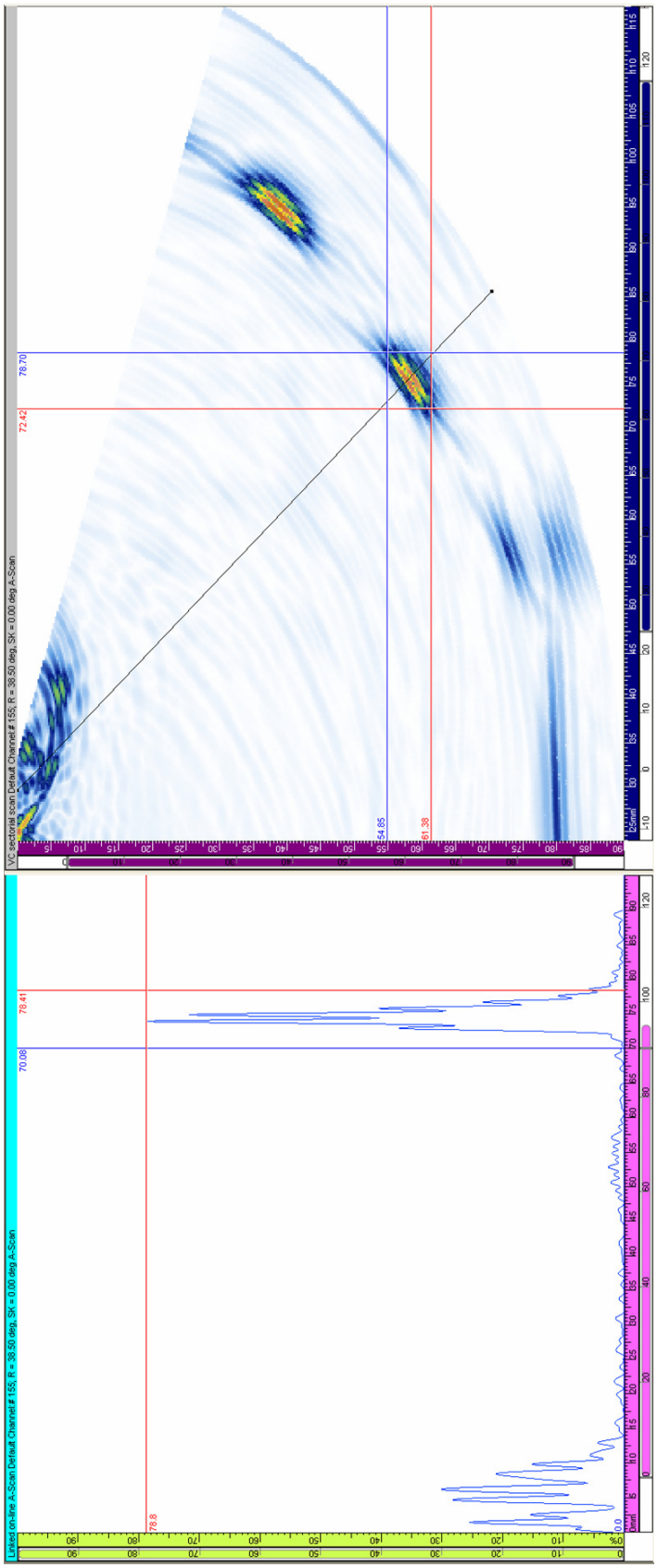

Figure 6-39 **A-scan (left) and sector scan (right) of SDH 1 - 3 in the test block, with a 75 mm focal range. The A-scan shown is the 38.5° beam, with the reflection from SDH 2 highlighted, and sized.**

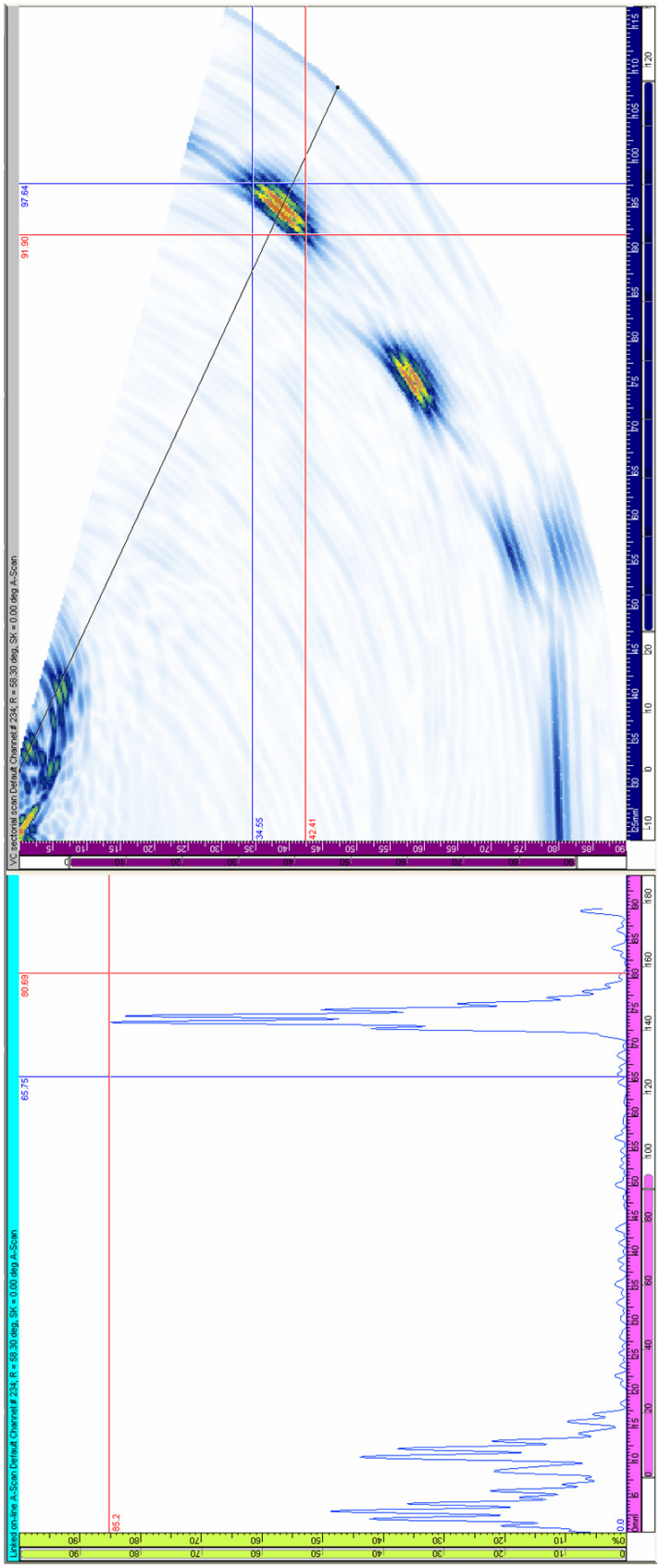

Figure 6-40 **A-scan (left) and sector scan (right) of SDH 1 - 3 in the test block, with a 75 mm focal range. The A-scan shown is the 58.25° beam, with the reflection from SDH 3 highlighted, and sized.**

In this scan all three defects are in focus at the same time, as they have ranges of 78.4, 73.8, and 73.6 mm respectively. Once again the reflection of SDH 1 is much weaker than the other defects due to its shallow beam angle of 21.75°. However, it is easily distinguished from back wall reflection, despite its close proximity.

The reflections from SDH 2 and 3 were approximately the same strength, as both detection angles were within 15° of the wedge's natural angle. These reflections were used to measure the resolution of the array, by using the cursors in the array controller's software. The -6 dB height and width of the reflections are displayed in Table 6-3, and these were then used to calculate lateral resolution. Axial resolution was measured in the A-scans and is also displayed.

Defect	Width (mm)	Height (mm)	Lateral (mm)	Axial (mm)
SDH 2	6.3	6.5	9.0	2.5
SDH 3	5.7	7.9	9.7	2.3

Table 6-3 Resolution of the array in the 75 mm focal range sector scan.

The lateral resolution of the array exceeds the original design specification of 10 mm, and is very close to the modelled result shown in Figure 6-9, which predicted a lateral beam width of 9 mm. The axial resolution of the array is much higher at 2.3 – 2.5 mm. This width varies from scan to scan as the lack of a low frequency smoothing function creates peaks in the signal envelope, which affect the measured width.

These initial sector scans show that the array is performing as expected, and is capable of detecting side drilled holes smaller than the beam width of the array. The next stage was to verify the array's ability to detect flat bottom holes, which have a lower target strength.

6.5.6 Sector scans of FBHs

Flat bottom holes drilled from the bottom of the test block are a good way of testing the array's volumetric steering performance, since the end of the hole appears as a point source, reflecting sound in all directions. Because they present a smaller cross section to the array they have a lower target strength than side drilled holes. A diagram showing the location of the 6 FBHs in the test block is shown in Figure 6-41. The holes are numbered from left to right, beginning at the 10 mm deep hole.

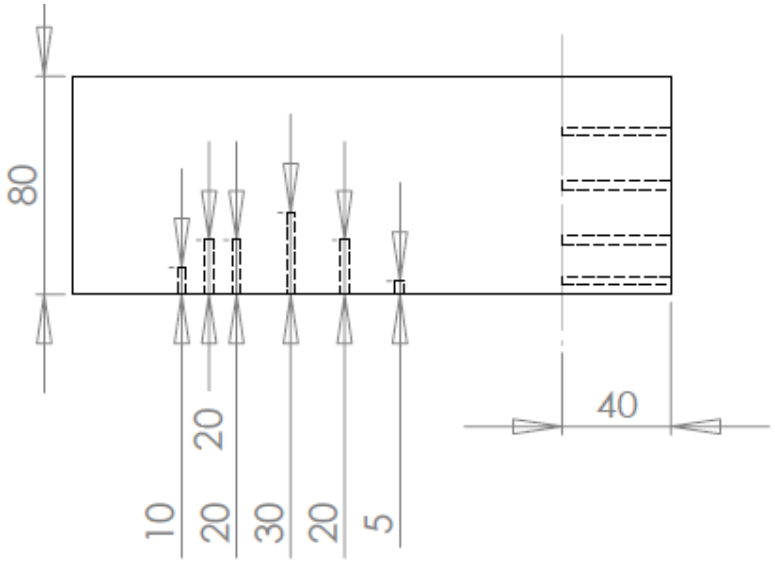

Figure 6-41 **Diagram showing the depth of the FBHs in the test piece. The first 3 holes are separated by 10 mm, while the second 3 are separated by 20 mm.**

Before attempting to image these holes using a volumetric scan, a focused sector scan was used to determine if they could be detected. As in the previous section, the beam was swept from 0° to 70° in 0.25° steps, but this time a depth focal law was used, with a depth of 65 mm. The gain was increased to 60 dB, making the back wall reflection 95% full screen height. The array was positioned so that the scanning plane was perpendicular to the line of defects, so that only one defect would appear

in each scan, as shown in Figure 6-42. The array was then manually aligned to produce images of each of the defects, and these are shown in Figure 6-43 to Figure 6-49.

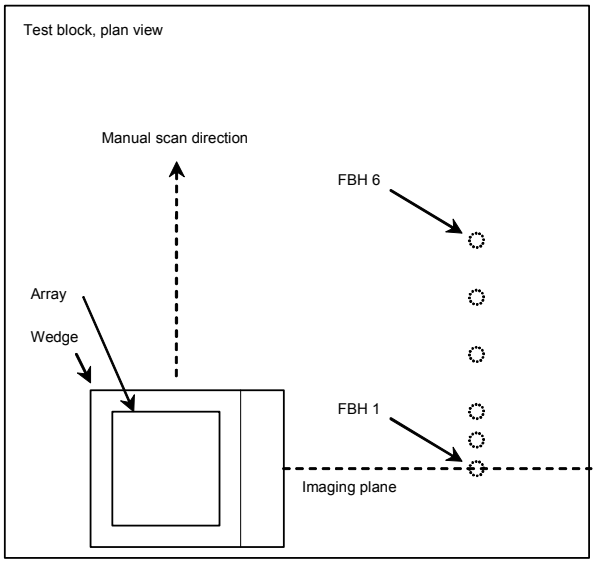

Figure 6-42 Diagram of the sector scan used to detect the flat bottomed holes.

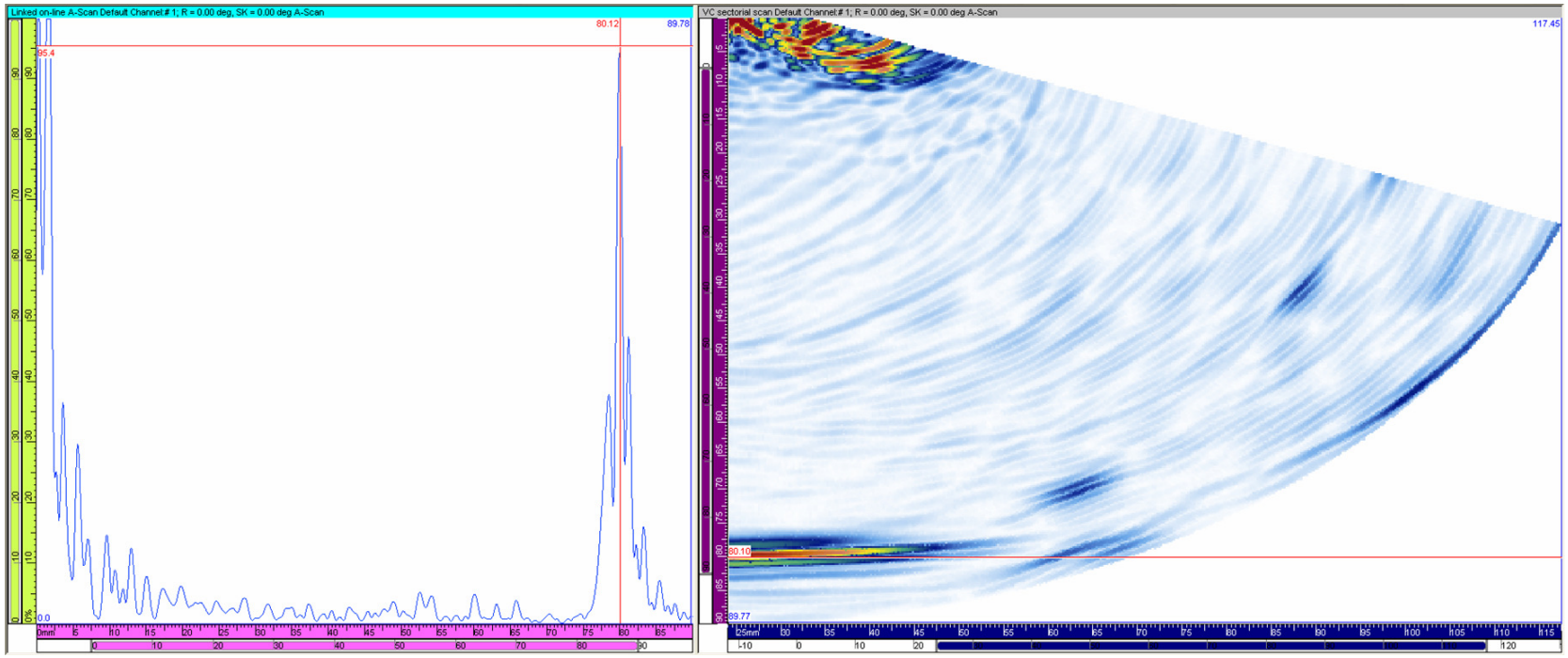

Figure 6-43 **A-scan (left) and sector scan (right) of FBH 1 in the test block, with a 65 mm focal depth. The A-scan shown is the 0° beam, with the reflection from the back wall highlighted.**

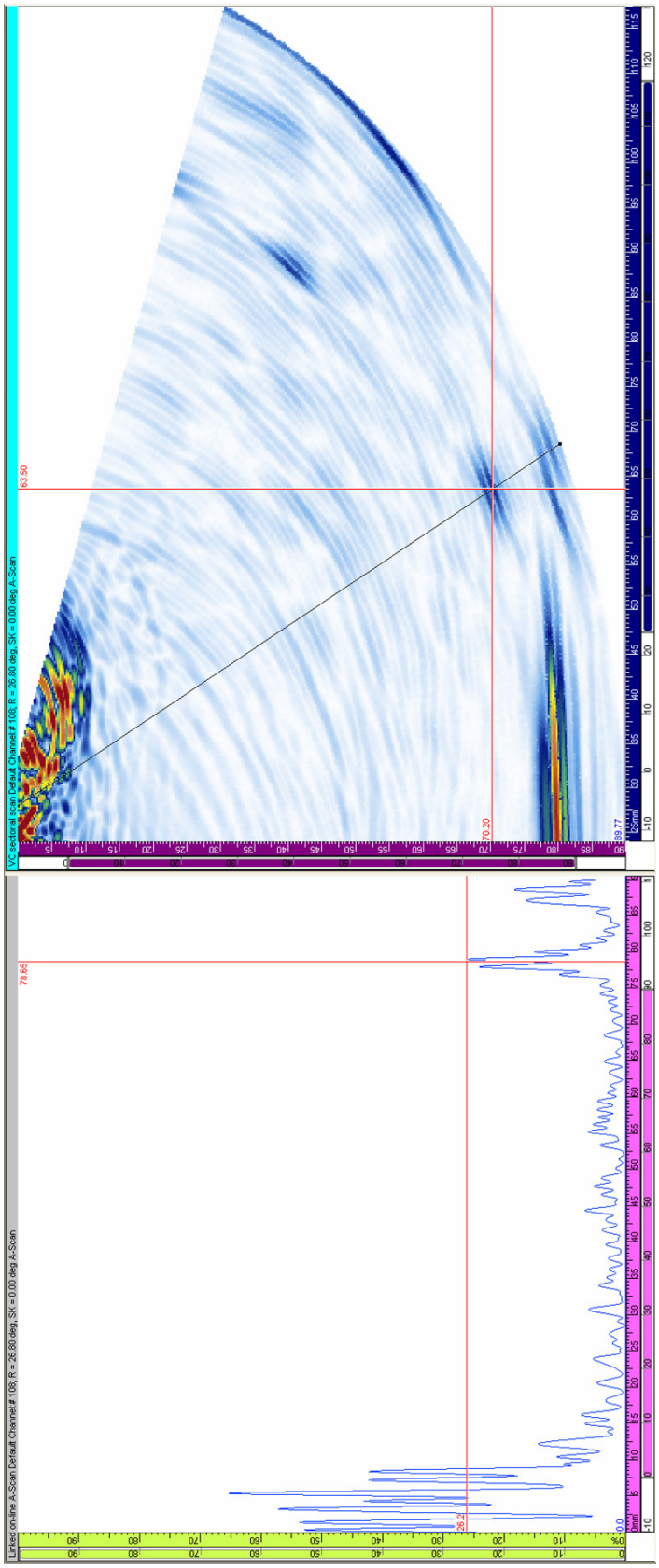

Figure 6-44 **A-scan (left) and sector scan (right) of FBH 1 in the test block, with a 65 mm focal depth. The A-scan shown is the 26.75° beam, with the reflection from FBH 1 highlighted.**

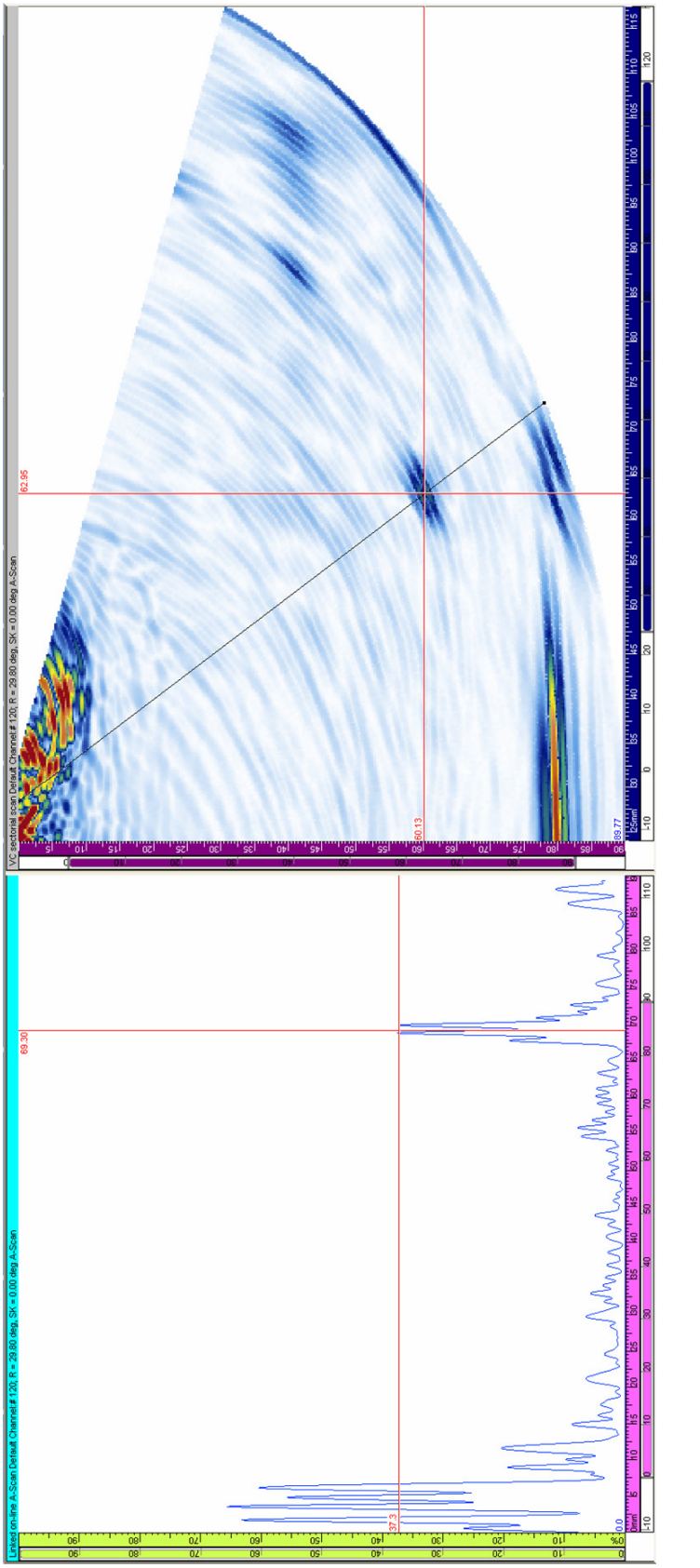

Figure 6-45 **A-scan (left) and sector scan (right) of FBH 2 in the test block, with a 65 mm focal depth. The A-scan shown is the 29.75° beam, with the reflection from FBH 2 highlighted.**

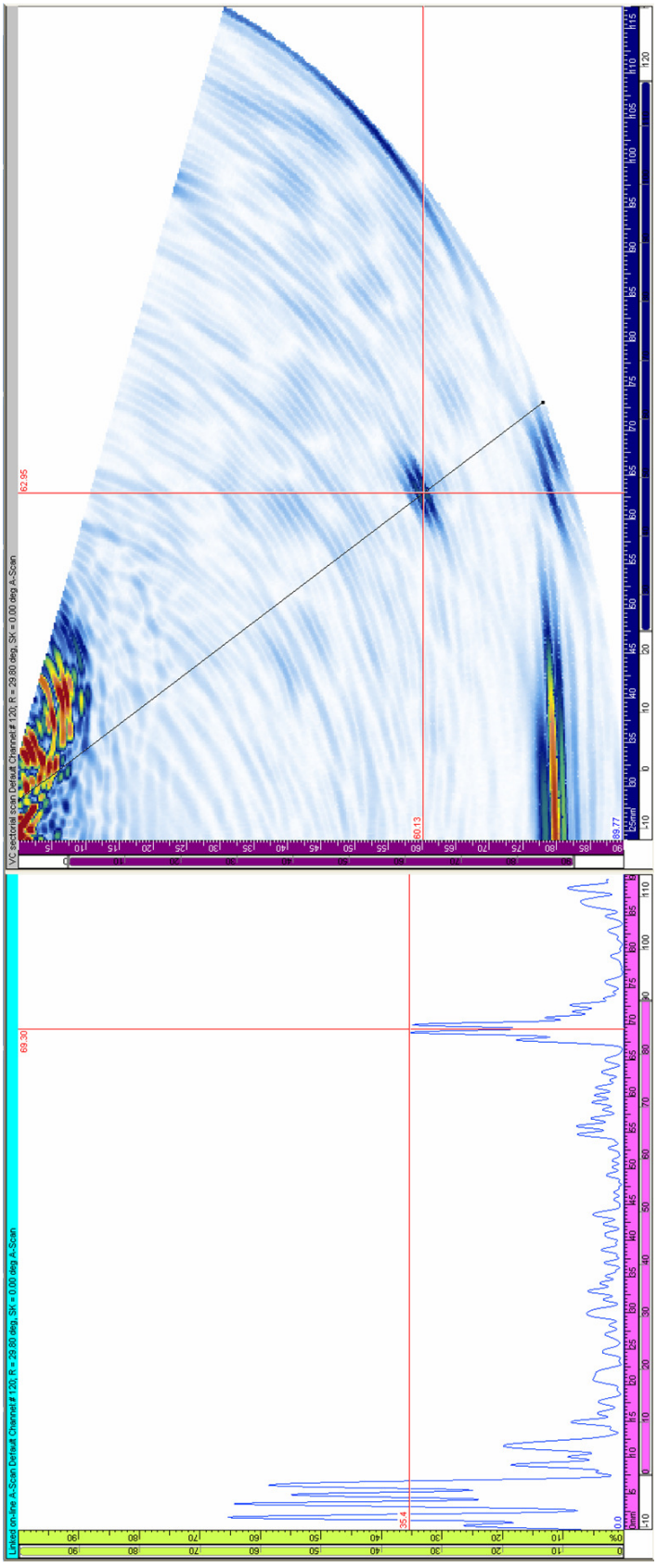

Figure 6-46 **A-scan (left) and sector scan (right) of FBH 3 in the test block, with a 65 mm focal depth. The A-scan shown is the 29.75° beam, with the reflection from FBH 3 highlighted.**

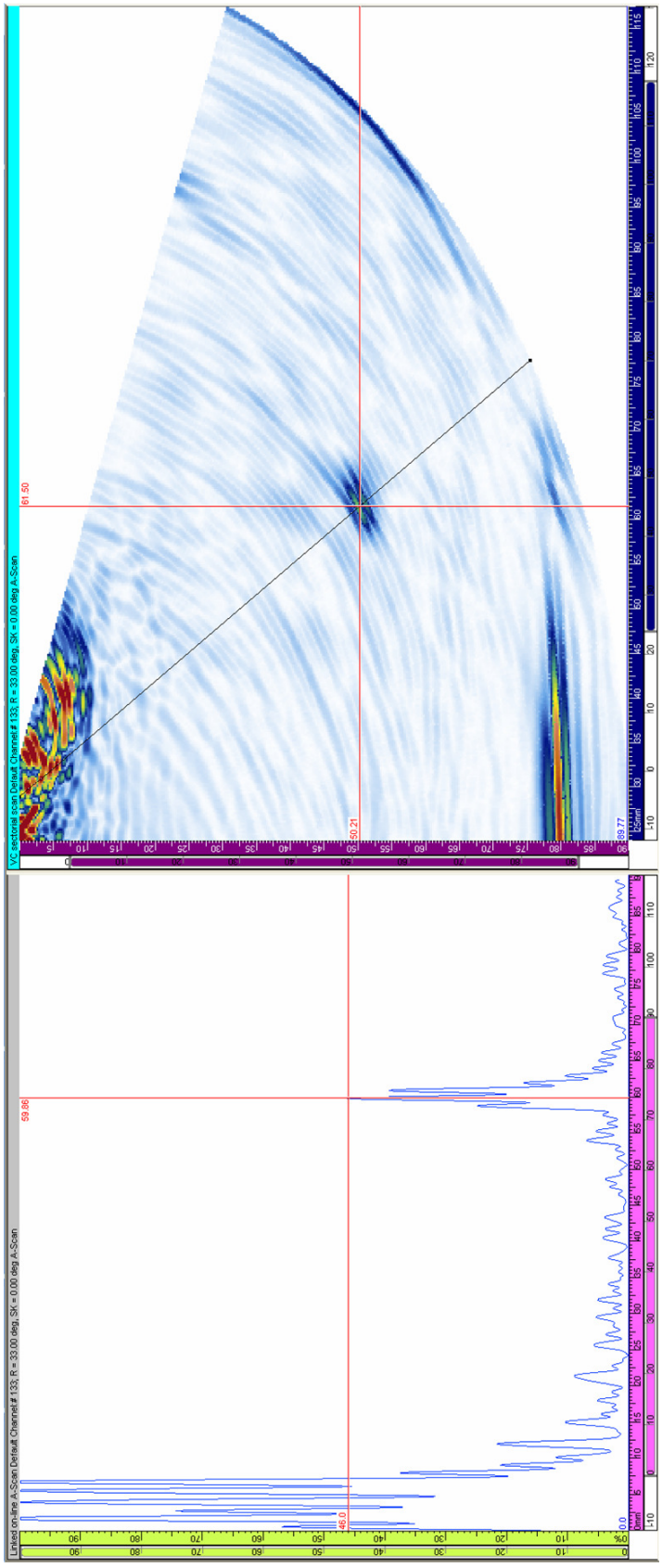

Figure 6-47 **A-scan (left) and sector scan (right) of FBH 4 in the test block, with a 65 mm focal depth. The A-scan shown is the 33.0° beam, with the reflection from FBH 4 highlighted.**

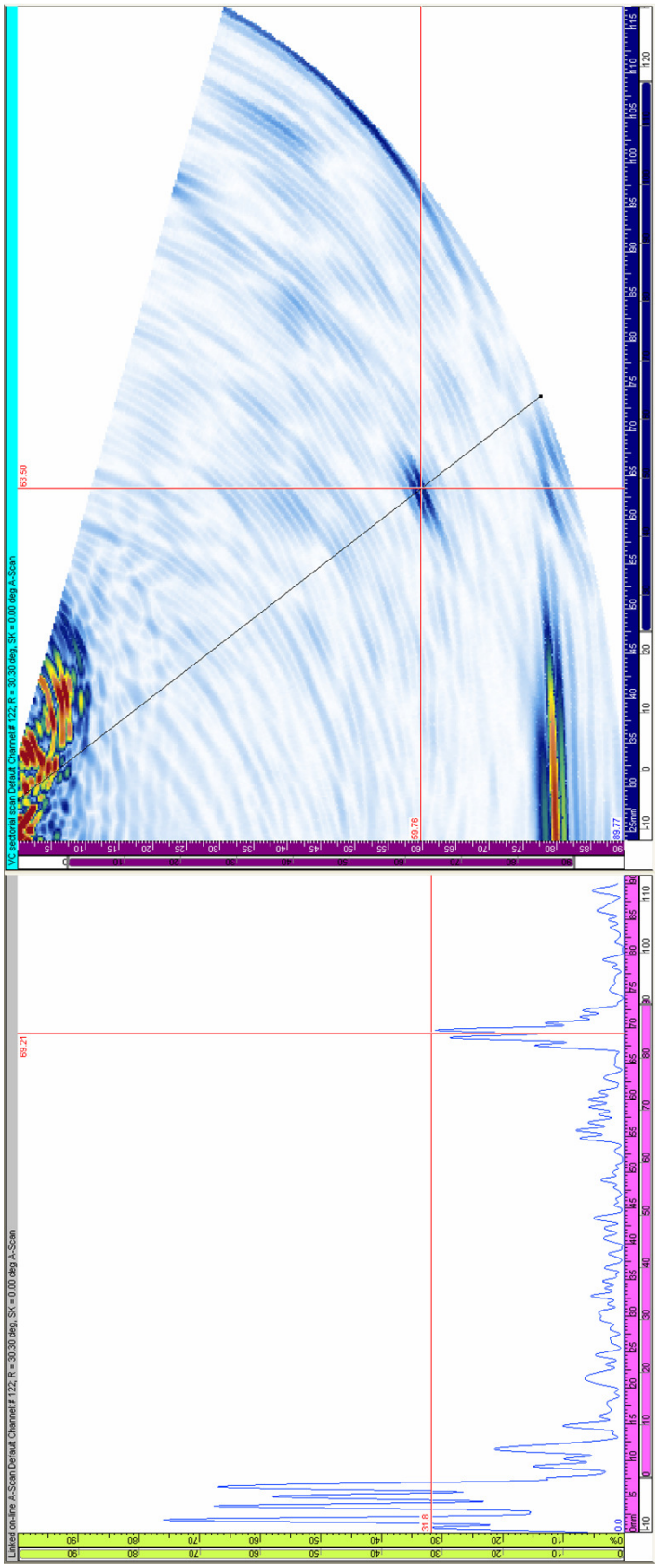

Figure 6-48 **A-scan (left) and sector scan (right) of FBH 5 in the test block, with a 65 mm focal depth. The A-scan shown is the 30.3° beam, with the reflection from FBH 5 highlighted.**

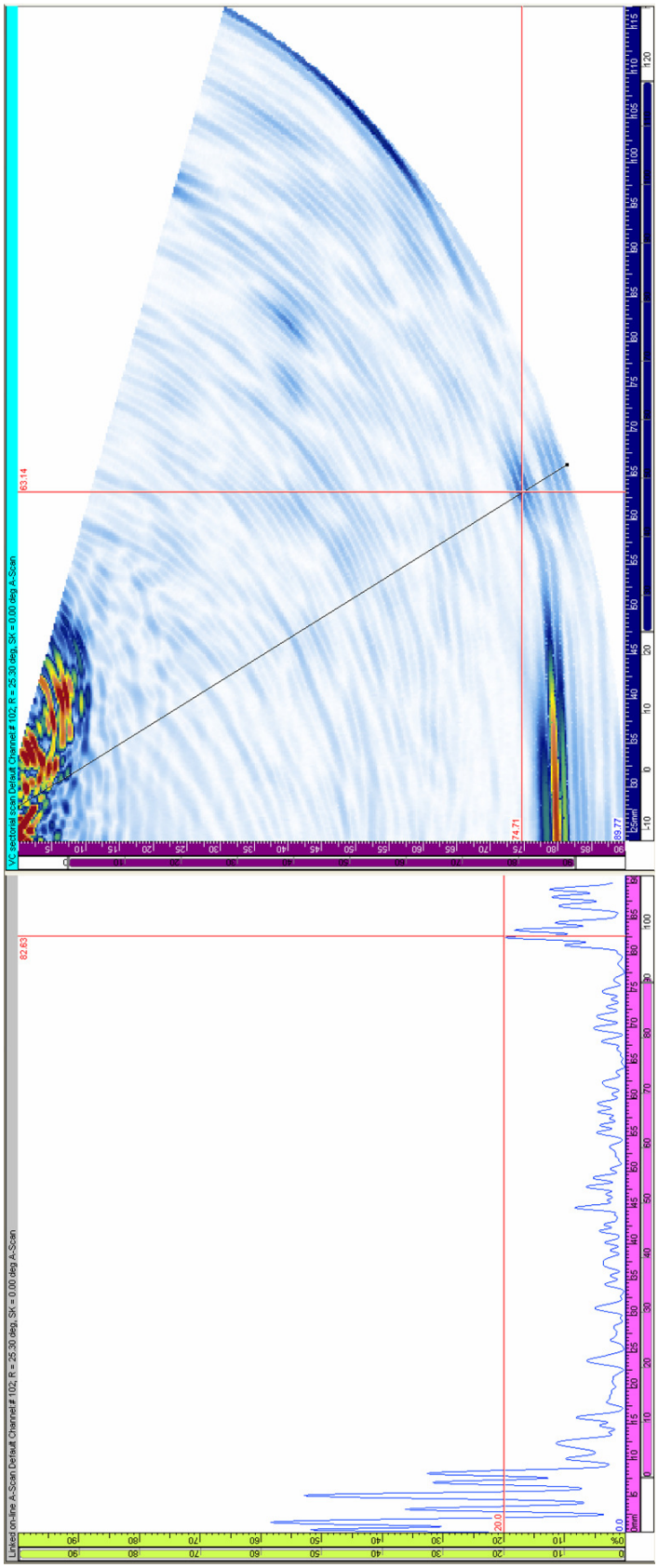

Figure 6-49 **A-scan (left) and sector scan (right) of FBH 6 in the test block, with a 65 mm focal depth. The A-scan shown is the 25.3° beam, with the reflection from FBH 6 highlighted.**

The angle, depth, and signal strength of the detected defects is shown in Table 6-4. While the reflections from the FBHs are of lower strength than the SDHs, all are clearly detectable above the coherent backscatter noise floor. The strongest reflection was from FBH 4, as its beam angle of 33° is closest to the natural angle of the array. This reflection is still 6.3 dB lower than that of the back wall reflection, despite the back wall being at 0°, where the array is significantly less sensitive.

On each scan there is also an echo visible at the base of each FBH, where sound has reflected from the rim of the hole. In a real inspection, these reflections are a clear indication that the defects are not merely voids in the components, but extend through to the back wall of the block. The depth of each defect was recorded, and in all cases accuracy was within 0.3 mm.

Each image shows a large reflection to the far right, which is the wedge reflection noted from previous inspections, however the images of FBH 1 and 2 show additional indications to the right of the image, around (40,85). It is thought that these indications are from unplanned defects in the block, since they do not occur in the other scans, and were detected from multiple angles, appearing at the same point.

Reflector	**Angle (°)**	**Depth (mm)**	**Strength (%)**
Back wall	0	80.1	95.4
FBH 1	26.75	70.2	26.2
FBH 2	29.75	60.13	37.3
FBH 3	29.75	60.13	35.4
FBH 4	33.0	50.2	46.0
FBH 5	30.25	59.8	31.8
FBH 6	25.25	74.7	20.0

Table 6-4 Measured position and signal strength of FBHs in sector scan.

The array successfully detected all of the defects in the test block. The next stage was to skew the beam out of plane in order to simulate the detection of misoriented defects, and test the azimuthally steering ability of the array.

6.5.7 Skewed sector scans

In the previous sections the prototype array has been used to perform focused sector scans, but these scans could have been carried out with a linear array. This section demonstrates the array's ability to steer the beam volumetrically, by creating skewed sector scans. These scans were used to detect the SDHs in the test block, with the array mechanically rotated to a variety of angles.

The alignment of the array in these scans is shown in Figure 6-50. Here the beam has been skewed out of the normal imaging plane by an azimuthally steering angle of φ. By doing so the array should be capable of detecting the SDHs even when it is not aligned normal to them.

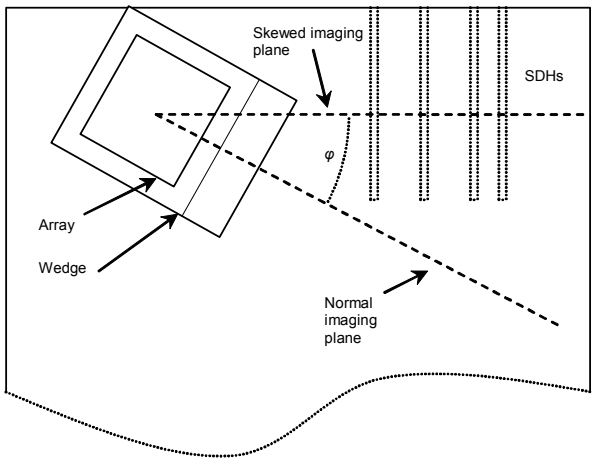

Figure 6-50 Diagram showing the position of the array during the skewed sector scan.

The array was positioned so that the holes were at a range of approximately 65 mm, and the array controller was programmed to produce a beam focused at a 65 mm range, sweeping in elevation from 0 to 70° in 0.25° steps. The array was then mechanically rotated by 20°, and the beam steered by the same amount in azimuth, and the scan was repeated. This process was repeated for skew angle of 40 and 60°. The beams produced during this experiment are shown in Figure 6-51. The sector scans captured are shown in Figure 6-52 to Figure 6-55, with the reflection from SDH 3 highlighted. A gain of 46 dB was used to give an amplitude of approximately 80% full screen height from SHD 3.

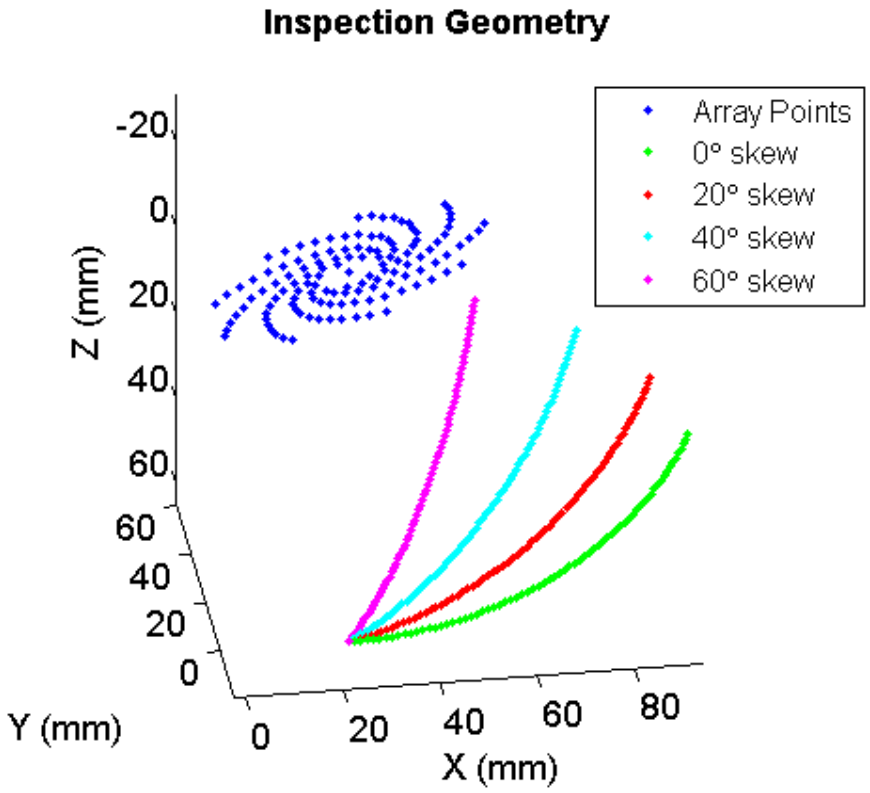

Figure 6-51 Diagram showing the focal points generated during the four scans.

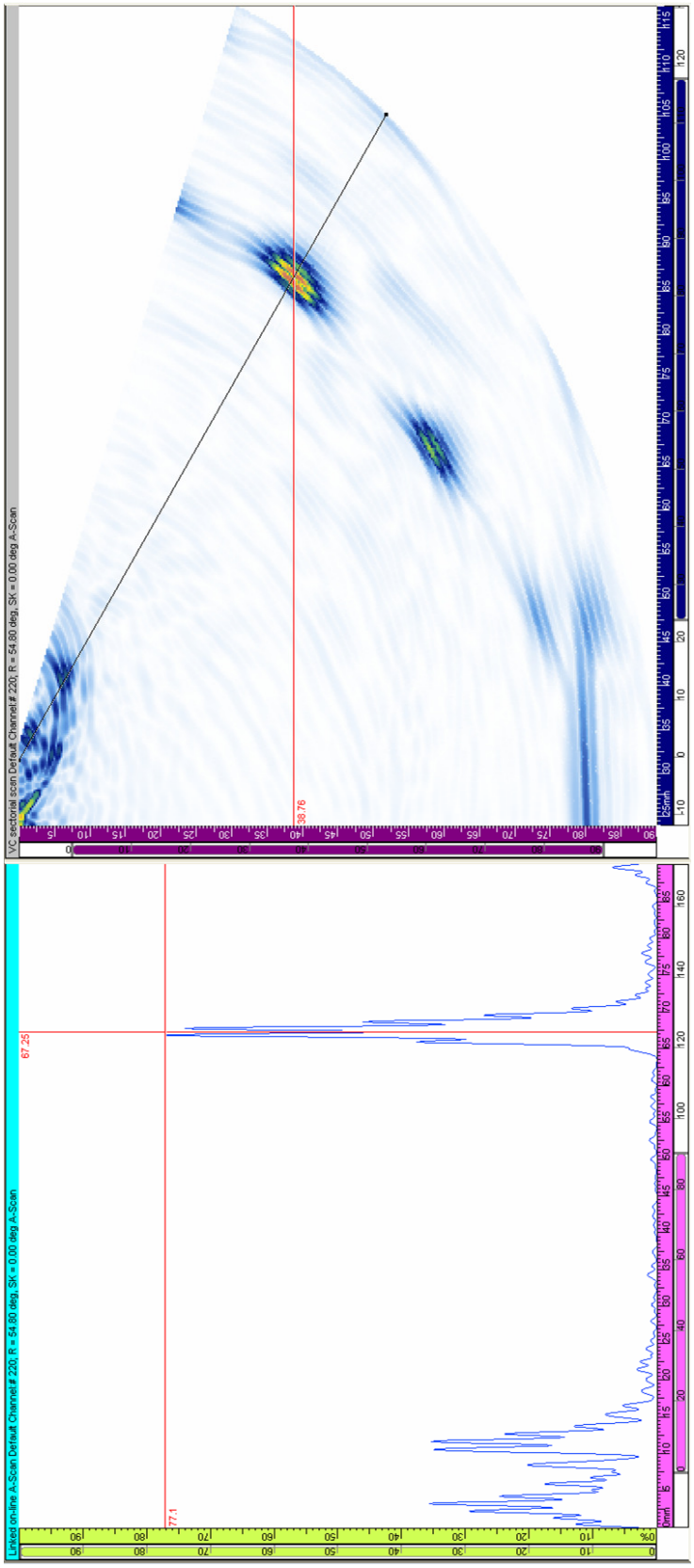

Figure 6-52 **A-scan (left) and sector scan (right) of SDH 1 - 3, with a 65 mm focal range and 0° skew. The A-scan shown is the 54.75° beam, with the reflection from SDH3 highlighted.**

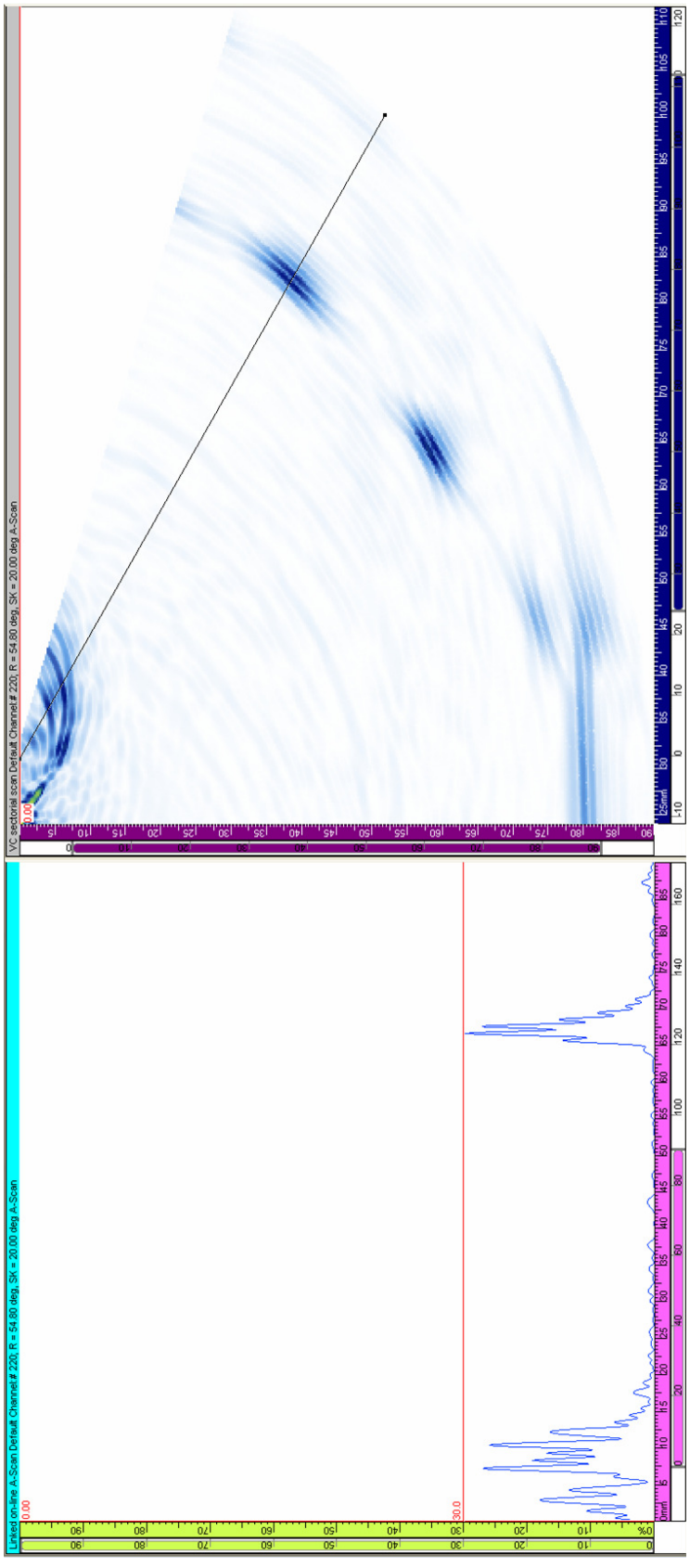

Figure 6-53 **A-scan (left) and sector scan (right) of SDH 1 - 3, with a 65 mm focal range and 20° skew. The A-scan shown is the 54.75° beam, with the reflection from SDH3 highlighted.**

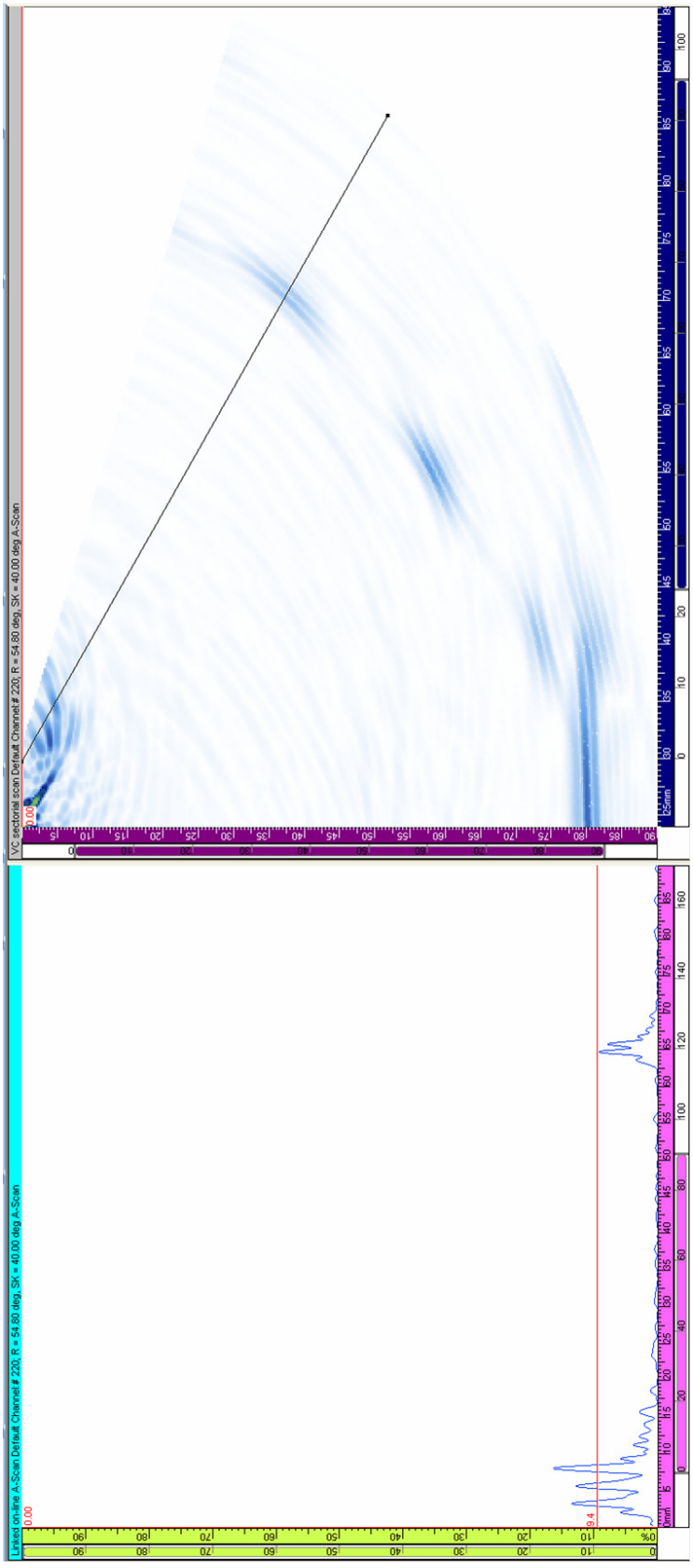

Figure 6-54 **A-scan (left) and sector scan (right) of SDH 1 - 3, with a 65 mm focal range and 40° skew. The A-scan shown is the 54.75° beam, with the reflection from SDH3 highlighted.**

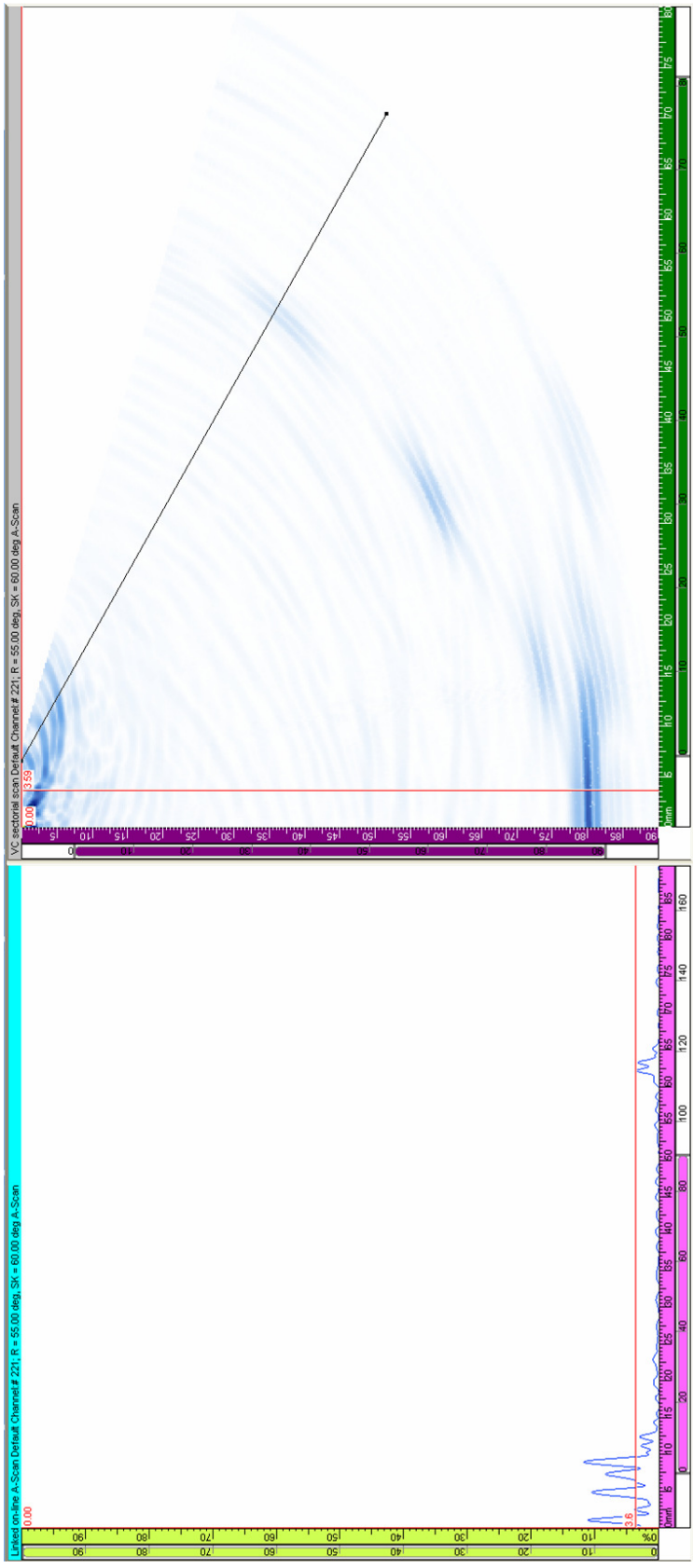

Figure 6-55 **A-scan (left) and sector scan (right) of SDH 1 - 3, with a 65 mm focal range and 60° skew. The A-scan shown is the 54.75° beam, with the reflection from SDH3 highlighted.**

Even at highest azimuthal steering angle of 60° the defects remain visible, demonstrating the true volumetric steering capability of the design. In addition, there is no evidence of spurious reflections due to grating lobes being introduced. The strength of the signal drops of from 77.1% at 0° skew, to 3.6% at 60° skew, a 26.6 dB drop. This is likely to limit the steering range in some inspections, where reflections from small defects may become masked below the coherent noise floor. However, in this case all of the defects are easily detected, as the noise floor is ~1% full screen height. The reflected signal strength at each skew angle is shown in Table 6-5.

Skew Angle (°)	**Signal Strength (%)**
0	77.1
20	30.0
40	9.4
60	3.6

Table 6-5 Variation of signal strength from SDH 3 as skew angle is varied.

This result is significant, as it proves that the design is capable of steering the beam in both elevation and azimuth. Furthermore, the steering ability is not limited by grating lobes, only by the SNR of the inspection. The next section focuses on quantifying the drop off in sensitivity that occurs as the beam is skewed.

6.5.8 Azimuthal steering test

A simple test was carried out to analyse the variation in signal strength with azimuthal steering angle. The array/wedge assembly was placed on the test block, with the front edge of the wedge collinear with the edge of the test block. The angle between the wedge and the test block was then varied between -60 and 60°, in 10° steps, as shown in Figure 6-56. At each angle a volumetric scan was performed, and the reflection from the bottom edge of the test block was recorded, as shown in Figure 6-57.

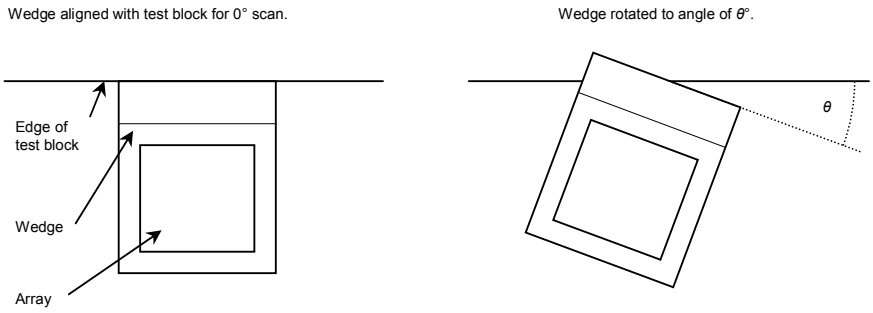

Figure 6-56 **Plan view illustrating the alignment of the wedge, array and test block during the test.**

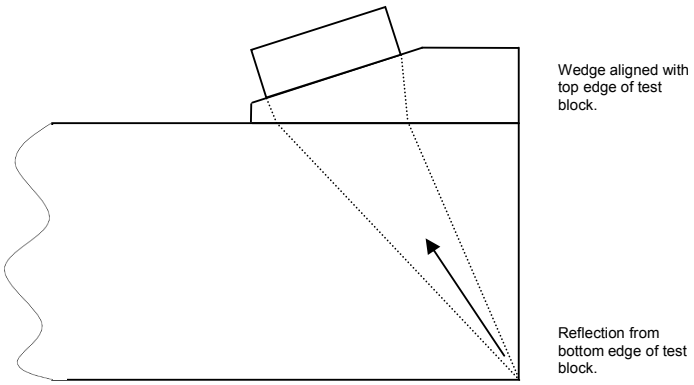

Figure 6-57 **Illustration of the reflection from the bottom edge of the block.**

The array controller was configured to scan the beam from 0 to 70° in elevation in 2° steps, and from -60 to 60° in azimuth in 5° steps. A constant depth focal law, with a focal depth of 80 mm was used. This allowed a tight focus to be maintained on the edge of the block, regardless of the orientation of the array. This configuration used 900 different focal laws, and the focal points are illustrated in Figure 6-58.

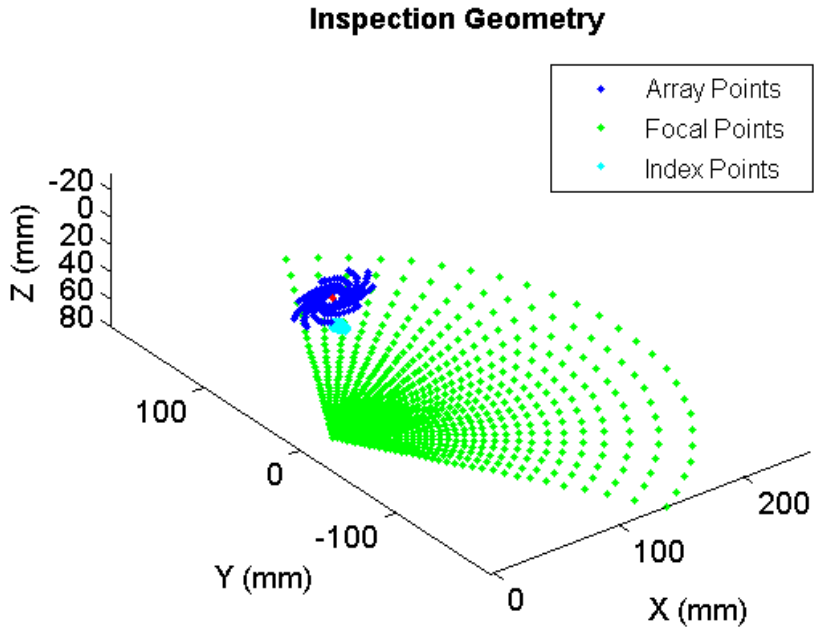

Figure 6-58 **Inspection geometry of the azimuthally steering test, showing, array points, beam index points, and the focal points.**

The edge reflection was detected in all of the configurations, indicating that the array is capable of volumetrically steering a beam over a wide range of angles. Images of the defect obtained at 0°, 20°, 40°, and 60° skew are shown in Figure 6-59 to Figure 6-62 respectively. For each skew angle the A-scan was used to measure the signal strength of the edge reflection, and this data is presented in Figure 6-63.

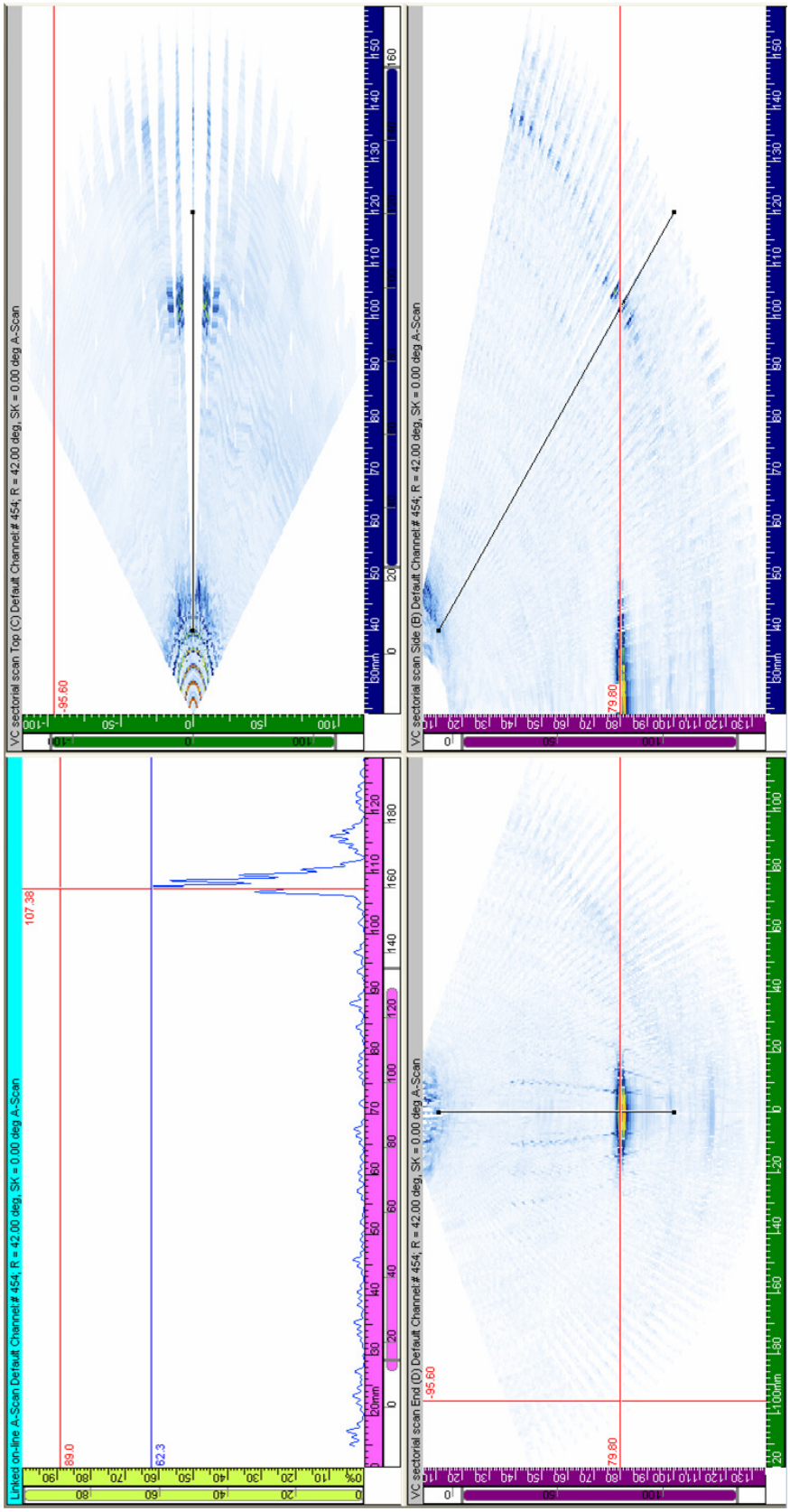

Figure 6-59 Scan showing the reflection from the edge of the test block at 0°. The scan shows an A-scan (upper left), plan view (or c-scan, upper right), end view (lower left), and side view (or sector scan, lower right). The large reflection directly below the array is from the back wall.

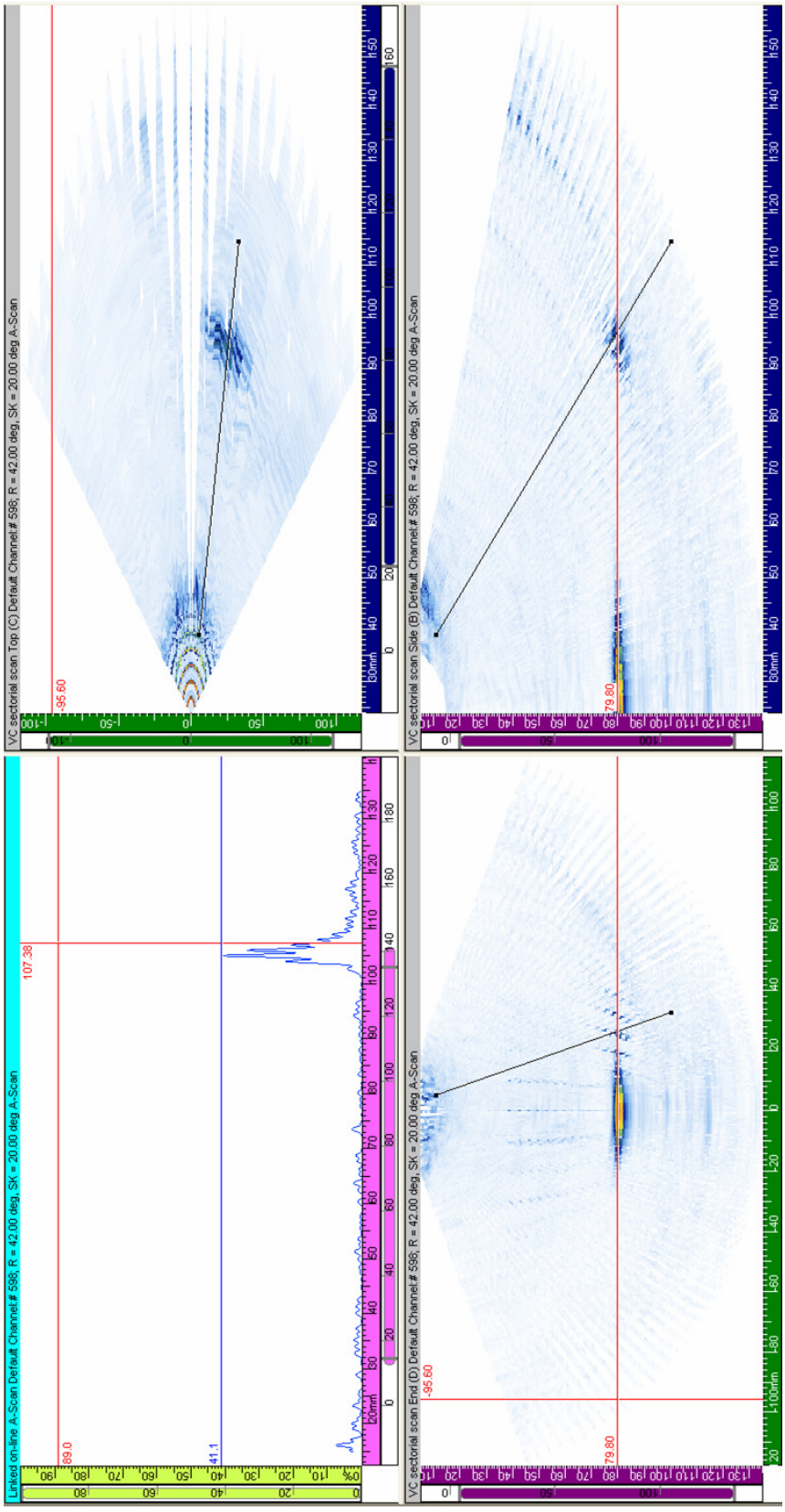

Figure 6-60 Scan showing the reflection from the edge of the test block at 20°. The layout is as in Figure 6-59. The large reflection directly below the array is from the back wall.

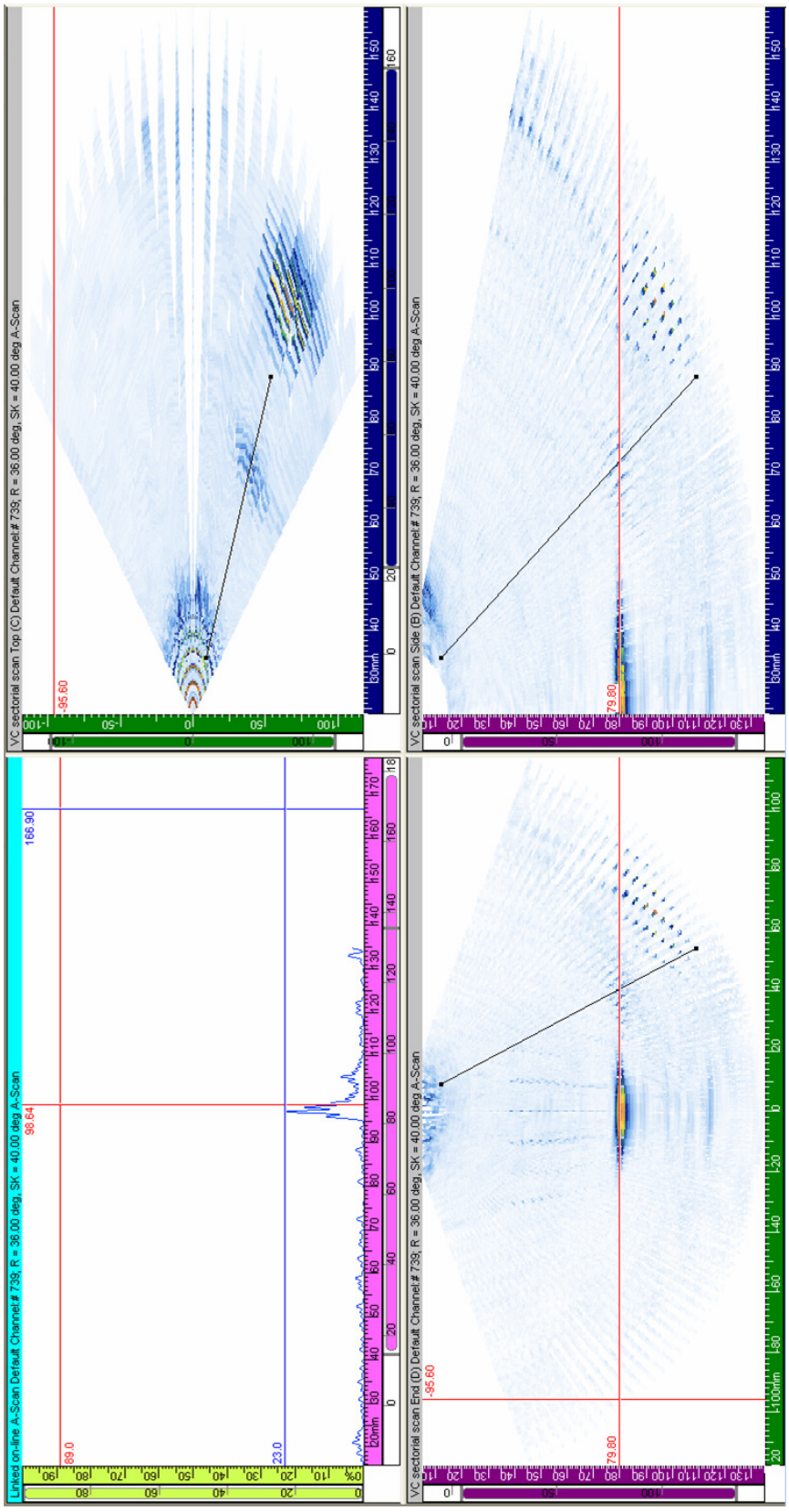

Figure 6-61 **Scan showing the reflection from the edge of the test block at 40°. The scan shows an A-scan (upper left), plan view (or c-scan, upper right), end view (lower left), and side view (or sector scan, lower right). The reflection at 105, 70, 105 mm (x-y-z) is a corner reflection from the Rexolite wedge, which is plotted deeper into the image due to the slow speed of sound in the wedge.**

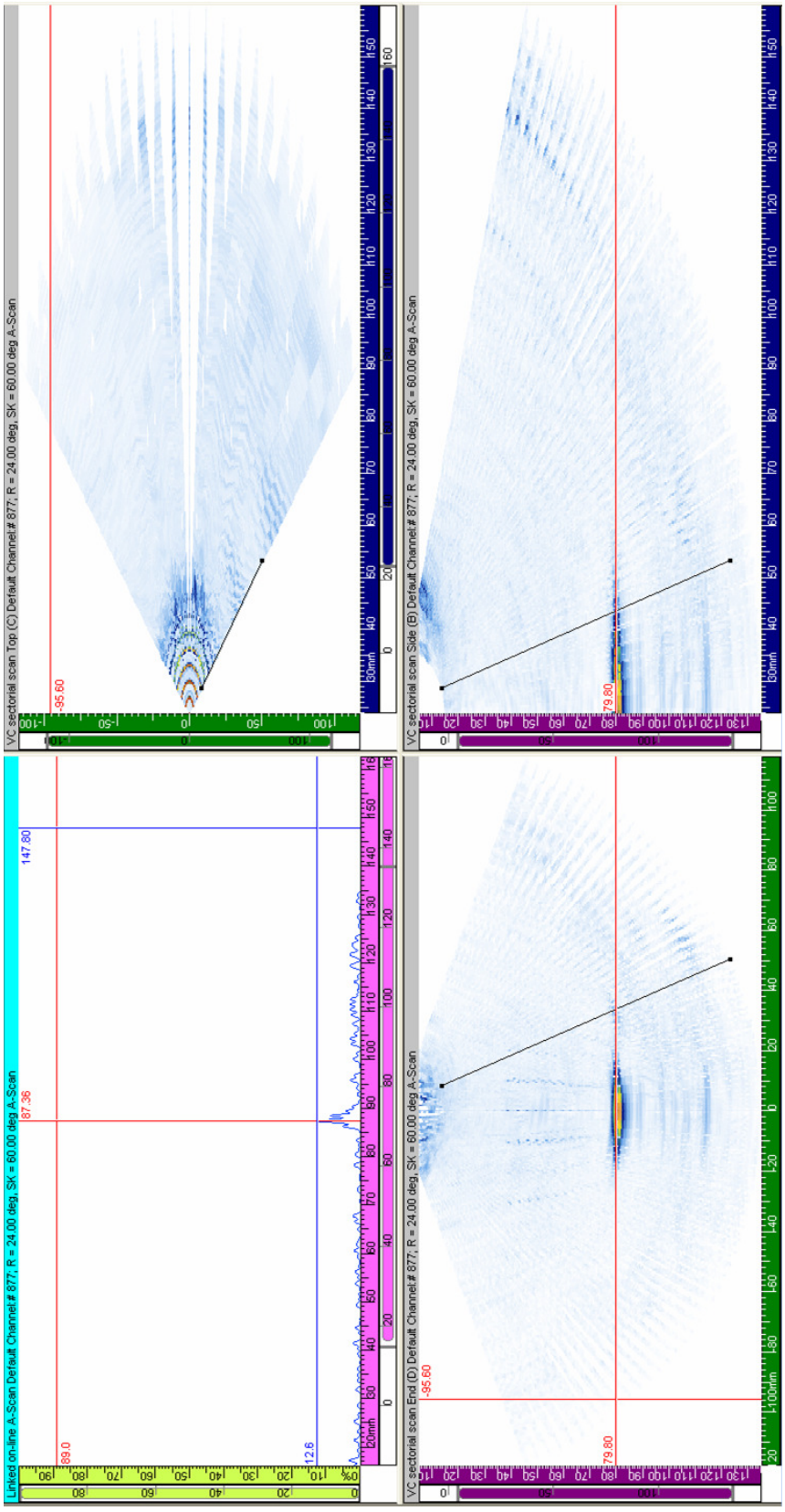

Figure 6-62 Scan showing the reflection from the edge of the test block at 60°. The scan shows an A-scan (upper left), plan view (or c-scan, upper right), end view (lower left), and side view (or sector scan, lower right).

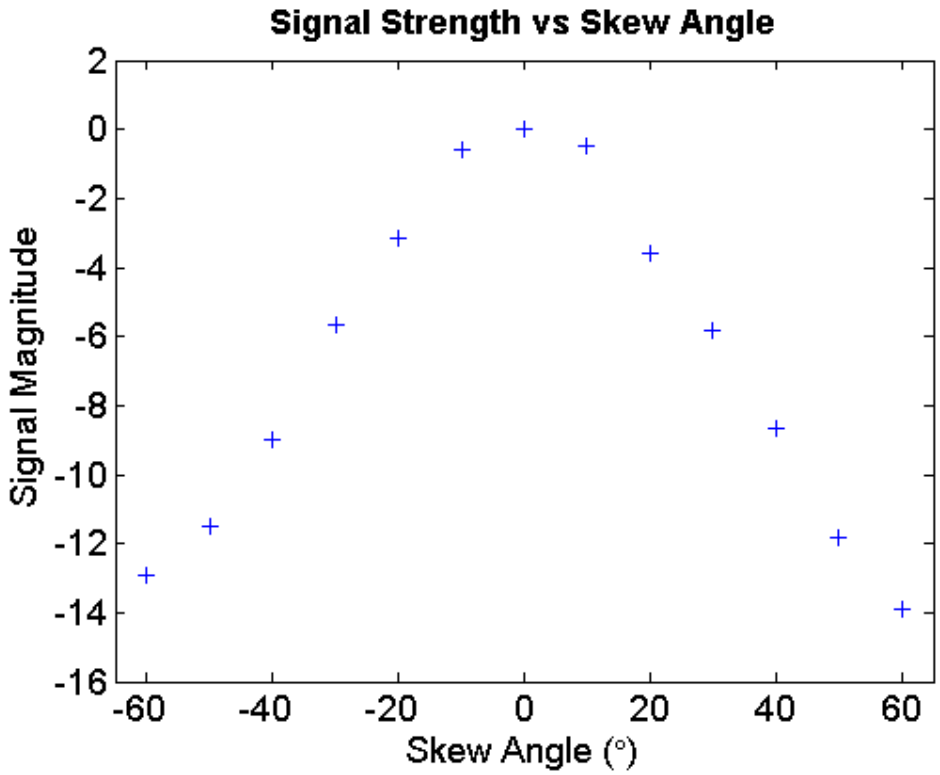

Figure 6-63 **Signal strength of the block edge reflection versus skew angle. The signal strength rolls off uniformly with skew angle, and is symmetrical about 0°.**

The array controller was set up to display a three aspect view of the scan, along with the raw A-scan data. As well as the side view which has been used previously to display sector scans, an end view and plan view of the data is displayed. Displaying the data in this way makes it easier to detect defects, which may otherwise be masked by other reflections, since the array controller software plots the brightest point through any given cross section of the data.

The edge reflection was detected in each of the scan positions, and is easiest to defects in the plan view, since it is not masked by other reflections. In total the signal dropped by 13 dB at 60°. This is not as large a drop as seen in the test in Section 0, because this time the beam does not pass close to the natural wedge angle, where the array is most sensitive. Instead the 0° skew scan has an elevation of 42°,

resulting in a lower total drop. The fact that there is a smooth drop in signal with angle, and that the graph, if approximately symmetrical about its centre is encouraging. In practice beam patterns often have spurious lobes, and can be lopsided, especially those from devices with small elements, whose surface displacements are often non-uniform.

As with previous scans there is an additional echo from inside the wedge that appears in the top right of the side view. In addition to this however, there is a large reflection that appears in both the -40 and 40° scans, just below the back wall of the block, and at a range of approximately 100 mm. By damping various parts of the array-wedge assembly with a wet cloth it was determined that this is a reflection from one of the upper corners of the Rexolite wedge. When the elevation and azimuth are both approximately 40° the sound reflects off the wedge – steel boundary, and travels into the upper corner of the wedge, where it is directly reflected back along the same path. This reflection has a relatively high signal strength, but fortunately plots outside the area of the test block due to the lower velocity of sound in Rexolite when compared to steel. As with the previously noted reflections, this could be addressed with careful choice of materials and geometry in the design of the wedge.

While the performance of the array is very promising, it became clear during testing that the quality of the volumetric images that could be produced would be limited by the array controller and PC being used. When performing scans with 800+ laws the performance of the PC and controller was sluggish, with scans taking many minutes to download to the hardware, and the software often became unstable during these periods. This limited the number of delay laws that could be used in a single scan. As can be seen from the images, the relatively coarse steps of 2° in elevation, and 5° in azimuth produce a discontinuous, banded, image, that is difficult to interpret. This is particularly true in the plan and end views, where there are blank areas between many of the scan lines. Furthermore, in the 40° skew side and end view the wedge echo appears discontinuous, making it difficult to identify as a reflection from a single source. In addition, since the software plots the strongest value through any

given cross section, stronger reflections from the front face, or the back wall often mask defects. An example of this is the side view of the 60° skew scan, where the back wall partially masks the edge reflection.

With these limitations in mind, it was decided to perform subsequent scans of the block in sections, where the array remains stationary, and multiple scans are set up to cover the area of interest. This technique is used in the next section to perform a volumetric scan of the FBHs in the test block.

6.5.9 Volumetric scans

It is clear from the scans shown in the previous section that a higher resolution will be required to successfully detect the weak reflections from the FBHs. To achieve this, the scan was split into two sections, each using 1,001 focal laws. Both scans used an elevation sweep from 28 to 38° in 1° steps. Scan 1 swept from 0 to 45° in azimuth, while scan 2 swept from 0 to -45°, both in 0.5° steps. The smaller step size in azimuth was selected, since the banding in previous scans appeared to be worse in the plan view. The array was positioned so that reflections from the defects appeared at a range of approximately 70 mm, as shown in Figure 6-64, and the focal depth was set to 65 mm, as a compromise between the various defect heights. This scan area did not cover FBH 6, which was not inspected. The gain was set to 70 dB to give as good a contrast as possible between the defects and the noise floor.

Results are shown in Figure 6-65 to Figure 6-69, with each of the defects highlighted and their positions measured.

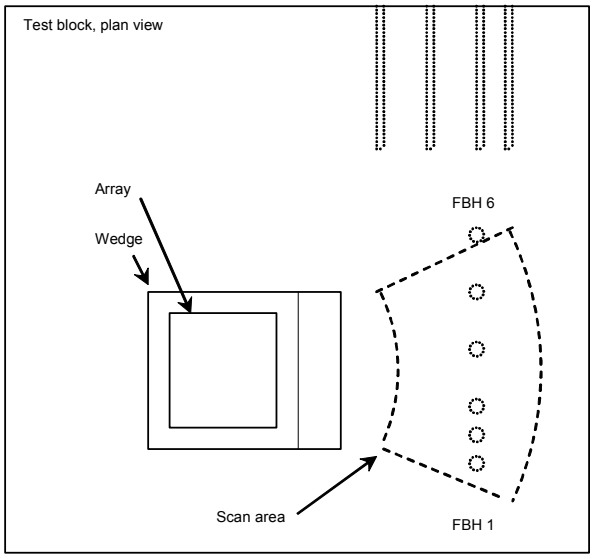

Figure 6-64 Diagram showing the layout of the volumetric scan.

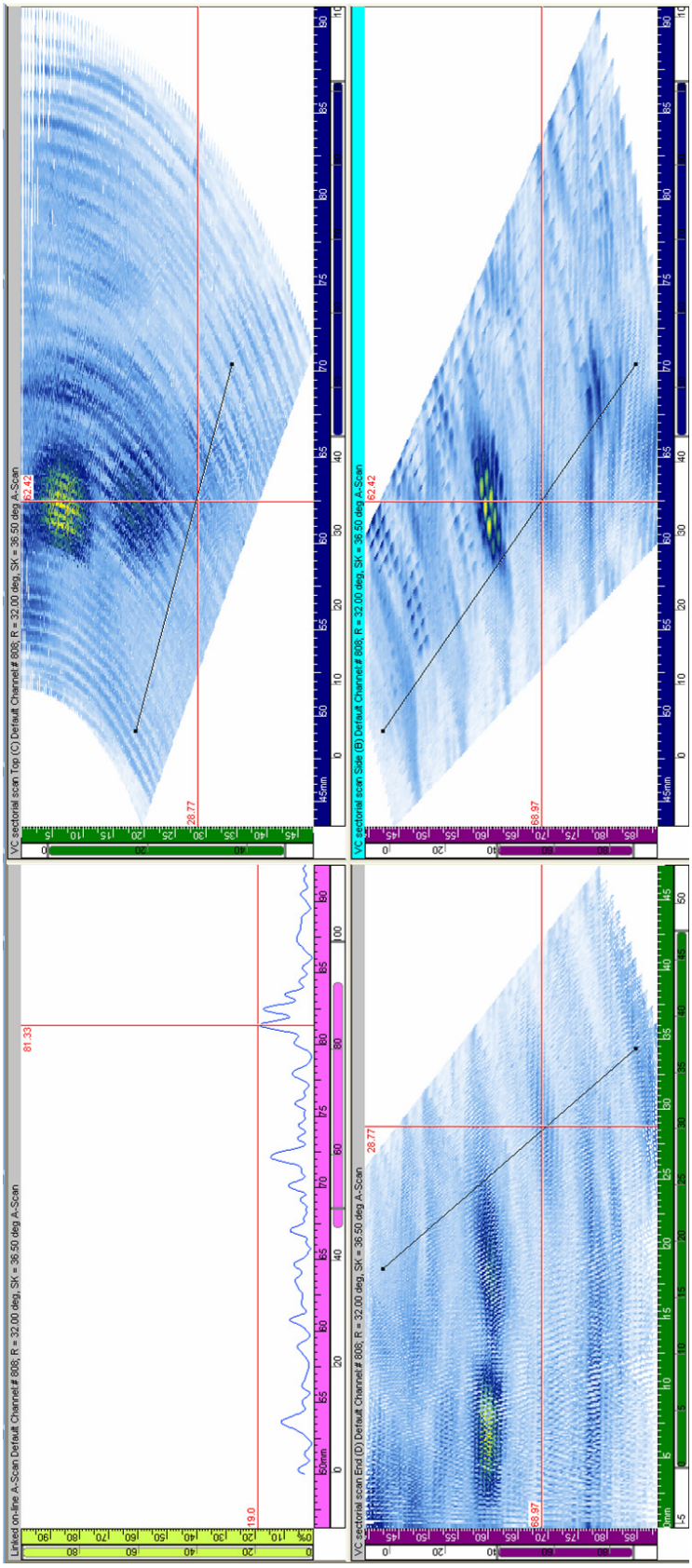

Figure 6-65 **Scan 1 showing FBH 1 - 3. The scan shows an A-scan (upper left), plan view (or c-scan, upper right), end view (lower left), and side view (or sector scan, lower right). The reflection from FBH 1 is highlighted.**

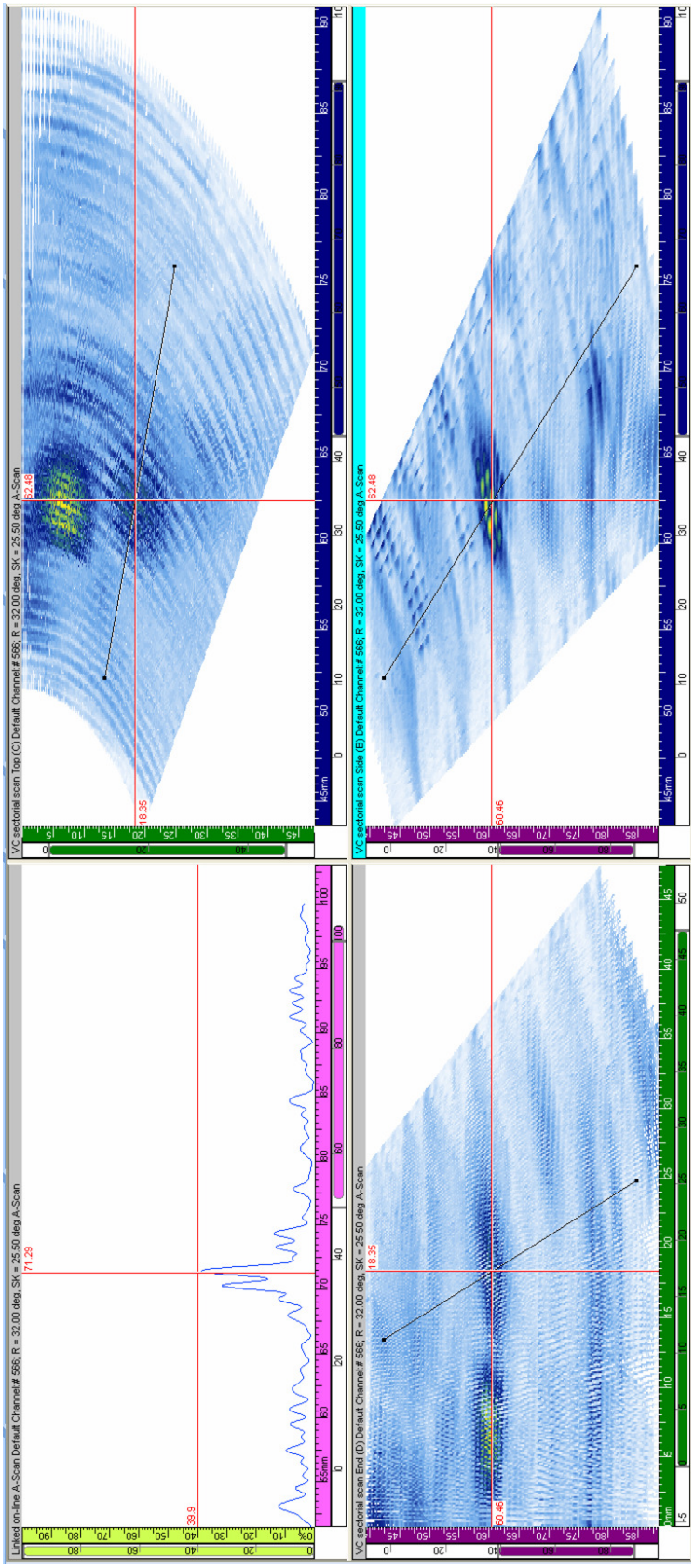

Figure 6-66 Scan 1 showing FBH 1 - 3. The scan shows an A-scan (upper left), plan view (or c-scan, upper right), end view (lower left), and side view (or sector scan, lower right). The reflection from FBH 2 is highlighted.

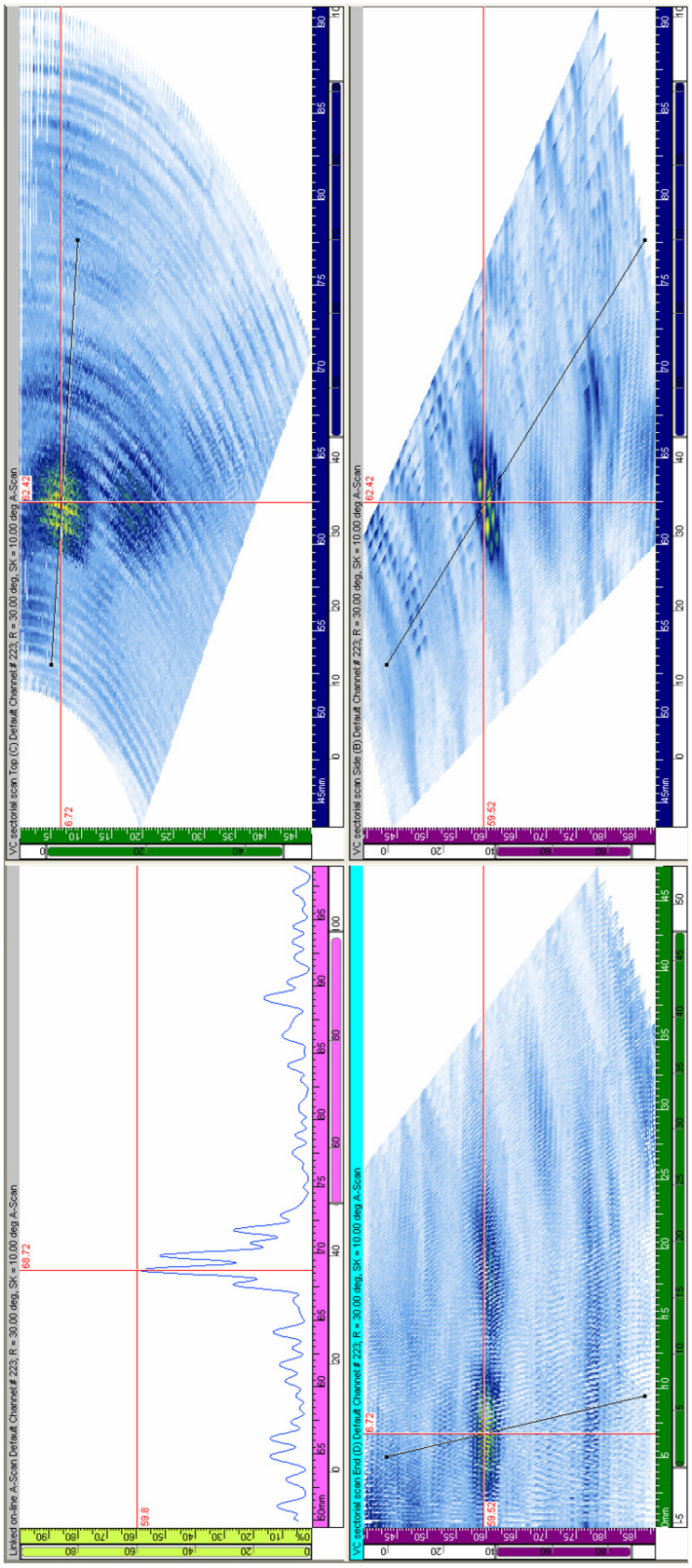

Figure 6-67 **Scan 1 showing FBH 1 - 3. The scan shows an A-scan (upper left), plan view (or c-scan, upper right), end view (lower left), and side view (or sector scan, lower right). The reflection from FBH 3 is highlighted.**

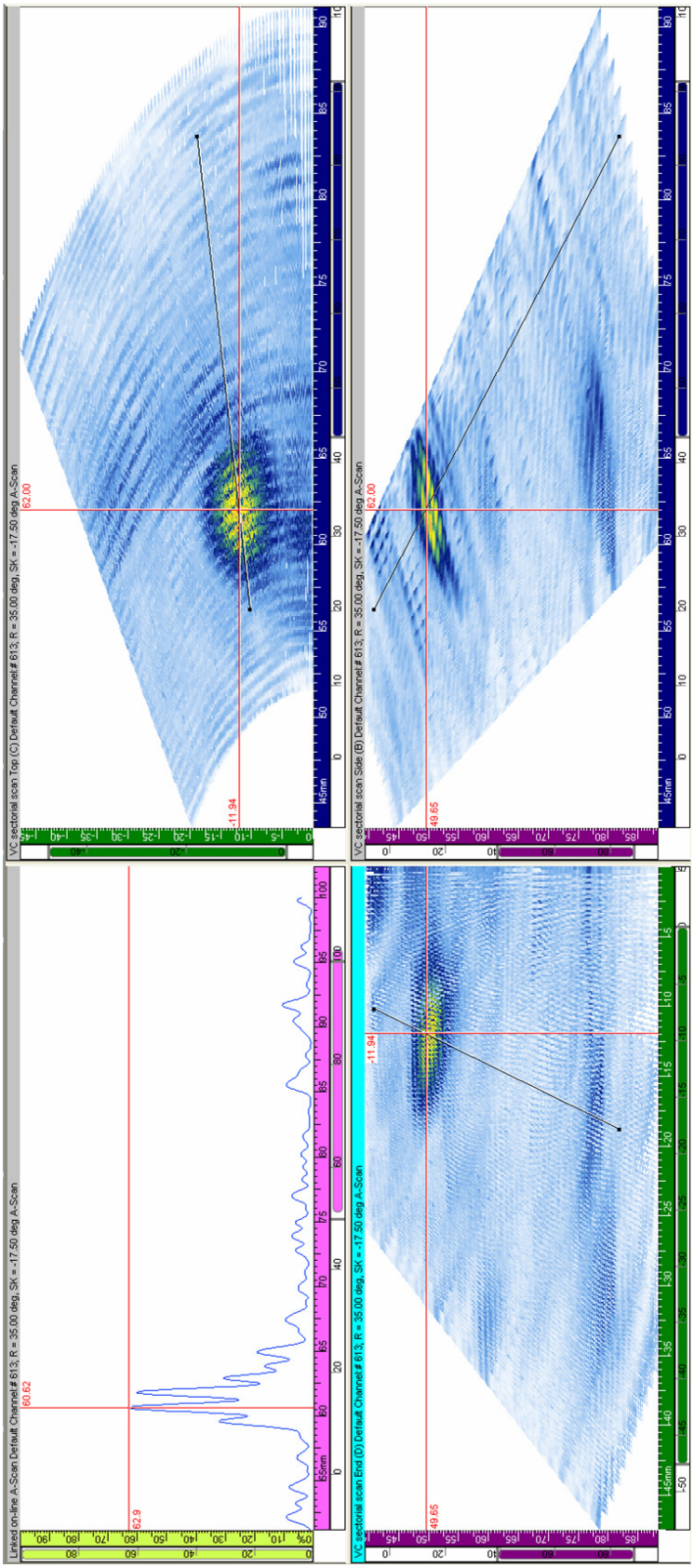

Figure 6-68 **Scan 2 showing FBH 4 and 5. The scan shows an A-scan (upper left), plan view (or c-scan, upper right), end view (lower left), and side view (or sector scan, lower right). The reflection from FBH 4 is highlighted.**

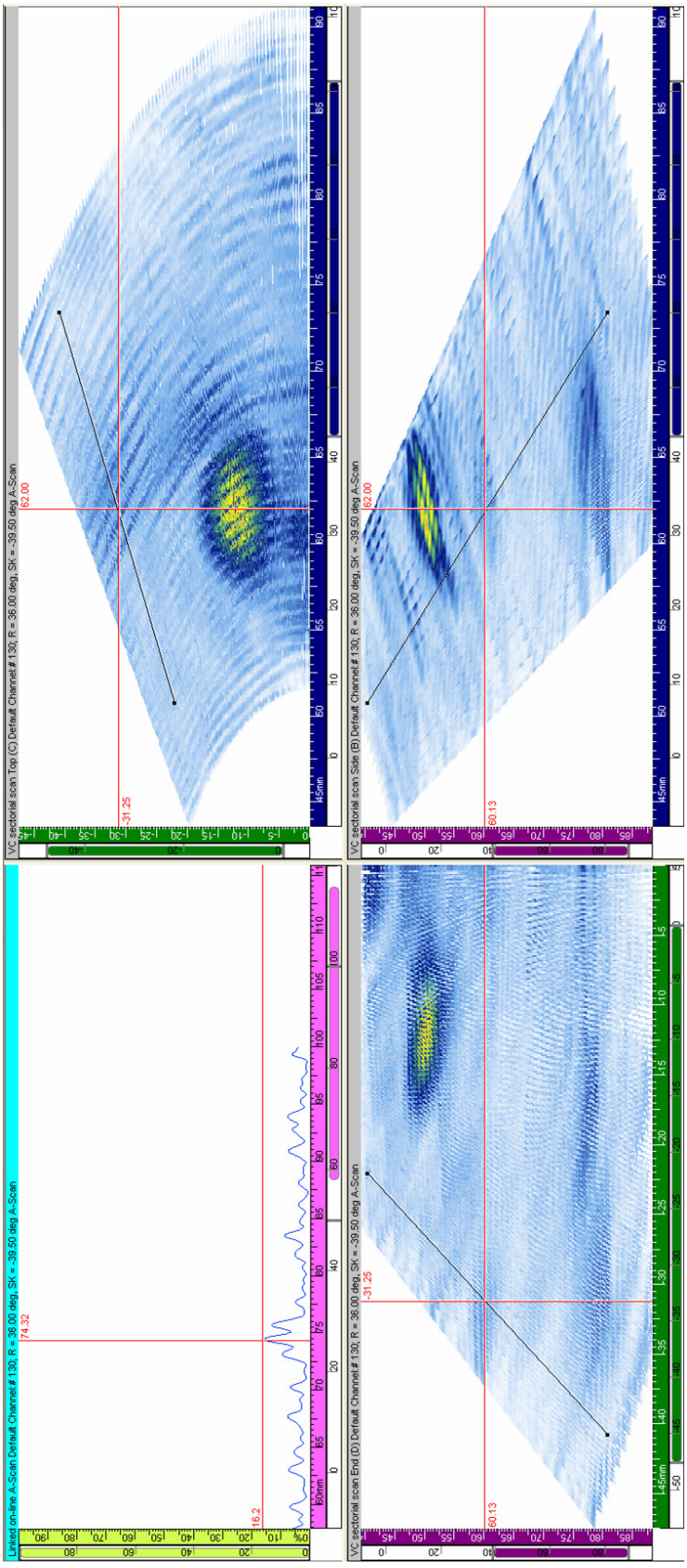

Figure 6-69 **Scan 2 showing FBH 4 and 5. The scan shows an A-scan (upper left), plan view (or c-scan, upper right), end view (lower left), and side view (or sector scan, lower right). The reflection from FBH 5 is highlighted.**

Table 6-6 shows the position, detection angle, and signal strength for each of the defects.

While the quality of the volumetric scan images has been improved by increasing the scan resolution, the results are still relatively difficult to interpret. In particular the outer two holes, FBH 1 and 5 have a lower signal strength, and are difficult to differentiate from the background echoes. However, despite this, all five holes were successfully detected, with no mechanical movement of the array, demonstrating the potential of the design.

FBH 5 had the weakest echo, which was mainly due to the high azimuthally steering angle of -39.5° which was required to detect it. This signal was only 6 dB above the noise floor, which would make it difficult to detect in a practical inspection of a component. The drop between the strongest (FBH 4) and weakest (FBH 5) echoes was 11.8 dB, once again, due to the change in azimuthally steering angle.

The positional accuracy of the scan was high in all axes, with a maximum error in x, y, and z of 0.5, 2, and 1.0 mm respectively. Furthermore, FBH 2 and 3 were clearly distinguishable, despite being only 10 mm apart, and at the same height in the block.

Defect	**X (mm)**	**Y (mm)**	**Z (mm)**	**θ (°)**	**φ (°)**	**Strength (%)**
FBH 1	62.4	26.8	69.0	32.0	36.5	19.0
FBH 2	62.5	18.4	60.5	32.0	25.5	39.9
FBH 3	62.4	6.7	59.5	30.0	10.0	59.0
FBH 4	62.0	-11.9	49.7	35.0	-17.5	62.9
FBH 5	62.0	-31.3	60.1	36.0	-39.5	16.2

Table 6-6 **Measured positions, detection angles, and signal strengths for each of the 5 defects inspected.**

This result clearly demonstrates that volumetric scanning is made possible using log spiral arrays. Indeed, given that this array is an initial prototype, and has been successful in detecting sub wavelength defects in stainless steel, there are many less challenging applications where the technique would be even more powerful. Having demonstrated the imaging capability of the array, in the next section measurements are made on the sidelobe level.

6.5.10 Sidelobe level

So far the resolution and steering performance of the array has been measured, and have been shown to meet the specification set out at the design stage. The final task is to measure the sidelobe height of the prototype, to understand it's dynamic range performance, and whether or not it performs as well as predicted by the model.

In Section 6.2 the sidelobe level of the array was predicted to be approximately -17 dB in the steering range used in the previous experiments under CW transmission simulation. This would translate to -34 dB in pulse echo. In the experimental inspections the array has been driven under pulsed excitation, and has been focused, but these simulated values still give an estimate of what could be expected from the design.

Measuring sidelobe heights of NDE arrays is more difficult than with sonar arrays, as there is no straight forward way to directly measure the field structure inside the test block in which it is designed to operate; in sonar a hydrophone can simply be placed into the water. The solution used here was to use the back wall of a test block as a reflector, and to electronically scan the beam in order to detect any reflections picked up on the array's sidelobes. The back wall is a strong reflector, so this will ensure that the amplitude of any sidelobe reflecting from it is as easy as possible to detect.

The procedure was carried out as follows:

1. The array and wedge were placed on a 60 mm thick stainless steel test block, in an area with no defects.

2. The array controller was programmed to produce a sector scan, sweeping in elevation from 0 to 70° in 0.25° steps. The scan was focussed at a range of 60 mm to achieve a strong reflection from the back wall. The gain was set to 53 dB, so that the back wall reflection was 80.7% full screen height. An image of this scan is shown in Figure 6-70.

3. The gain was then increased to 80 dB to bring the background area of the scan to ~50% full screen height. An image was captured, and is shown in Figure 6-71. The image shown a series of peaks, which may arise from a combination of sidelobes, wedge reflections, and backscatter from the metal.

4. The array and wedge were then moved to the 80 mm thick test block, and placed on an area with no defects. No scan settings were changed, and the gain remained at 80 dB. As before, the noise floor of the image was visible, and is shown in Figure 6-72.

5. The structure of the noise pattern in Figure 6-71 and Figure 6-72 were then compared to determine if the peaks arose from the wedge, or from sidelobes from the back wall.

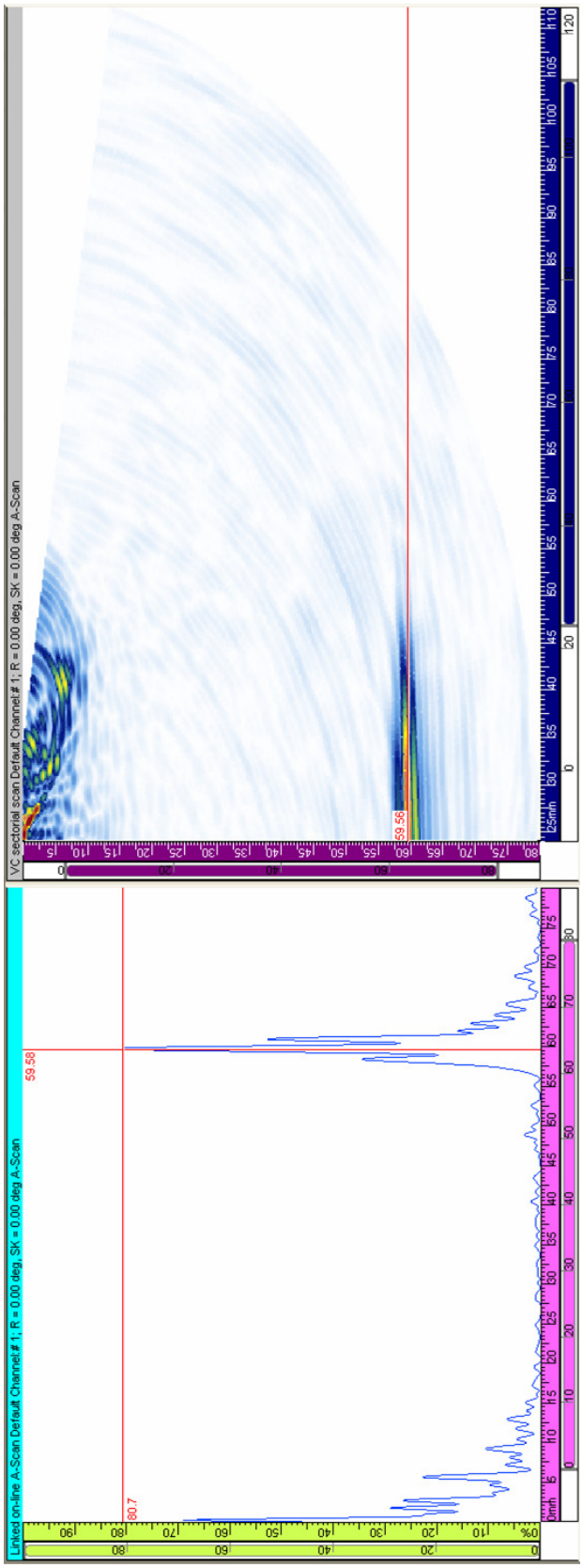

Figure 6-70 **Sector scan of a 60 mm thick steel block, with no defects. The beam was swept in elevation from 0 to 70°, in 0.25°, and was focused at a range of 60 mm. A gain of 53 dB was used. The back wall reflection is visible at 59.6 mm depth.**

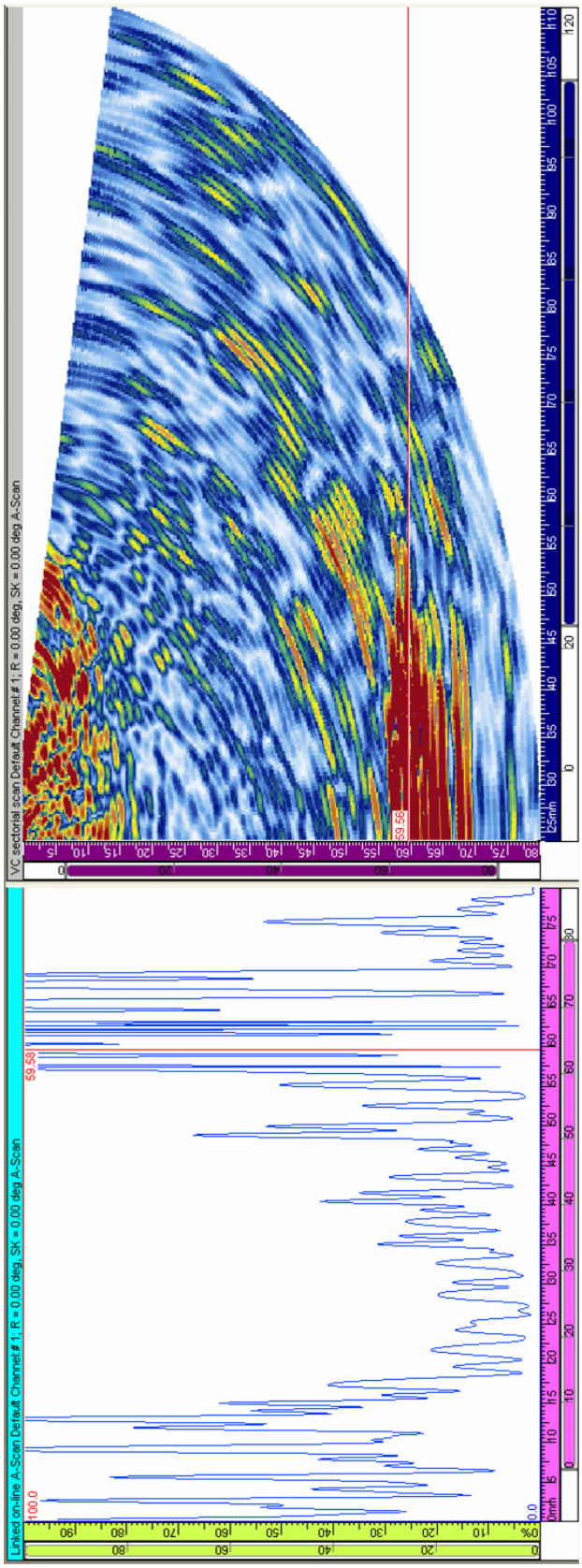

Figure 6-71 **Sector scan using the same setup as Figure 6-70, but with the gain increased to 80 dB. The back wall reflection is now saturated, and many other bright spots are now visible in the image.**

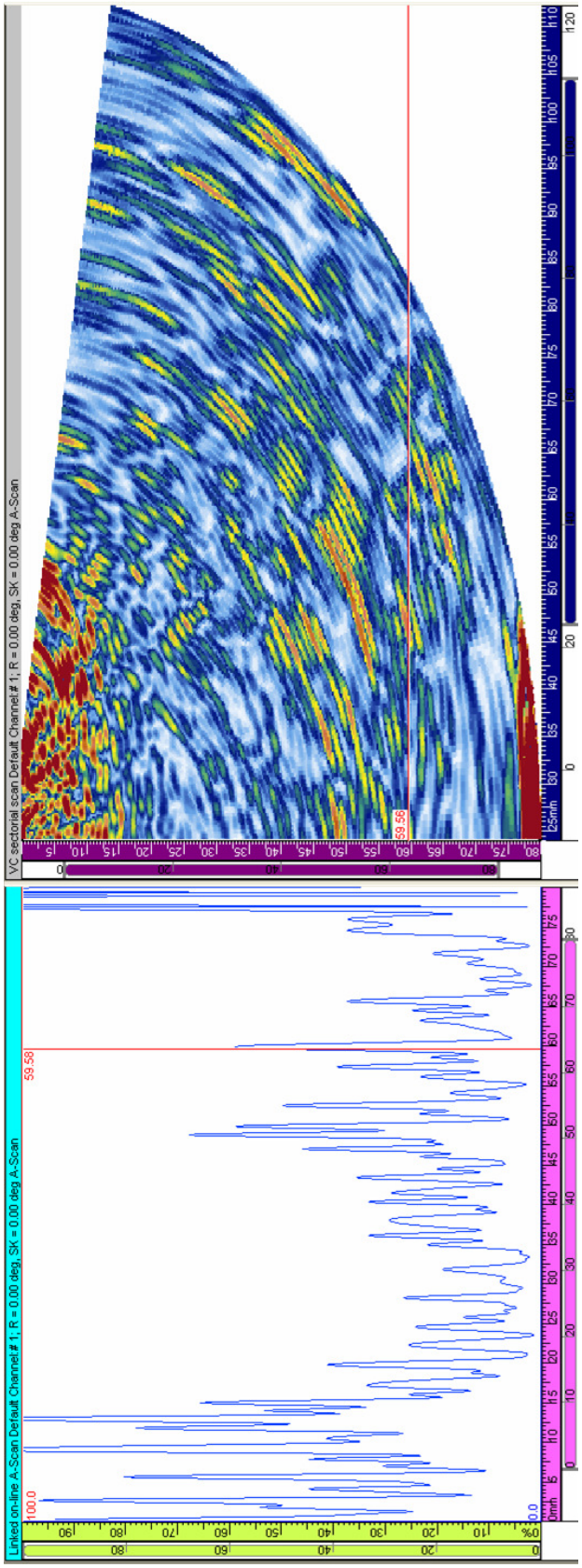

Figure 6-72 **Sector scan with the same settings as Figure 6-71, but moved to an 80 mm thick block with no defects. The saturated back wall reflection is now visible at the bottom of the image.**

To make the data easier to manipulate it was read into Matlab. There are no export options in the Zetec software, so this had to be done directly from the captured images. By using Zectec's colour scale as a reference the images were reconstructed into their original amplitude scales. The images were coded using 8 bits, so the resulting amplitude plots range from 0 to 255, and are shown in Figure 6-73.

A difference image was created by subtracting the 80 mm block image from the 60 mm block image, resulting in a range of values from -255 to 255. As expected, the back wall reflections have a large difference value, since they are in different locations. A positive value indicates a lobe which is present in the 60 mm image, but not in the 80 mm image, and therefore a potential sidelobe reflection from the back wall. The difference image is shown in Figure 6-74.

In general the images are similar, indicating that many of the reflections occur within the wedge. For example, there is a strong reflection that appears at (54,48) in both images, which is not visible in the difference image. However, there is a peak at (77,34) in the difference image, which has an amplitude of 131. It is also at a range of approximately 60 mm, indicating that it is a similar distance away as the back wall reflection from the 60 mm block. A value of 130 is equivalent to a strength of 51.0% full screen height in the A-scan window. The original back wall reflection was 80.7% full screen height, with a 53 dB gain. Taking into account both the change in gain settings, and the change in signal amplitude, the relative level of the reflection is:

$$(53-80)-20\times\log_{10}\left(\frac{51.0}{80.7}\right)=-31.0dB \qquad \textbf{(6-4)}$$

This is close to the value of -34 dB predicted by the model. The difference is thought to be due to the elements having a narrower acceptance angle, due to their non ideal surface displacement. The lobe occurred at an angle of 56.7°.

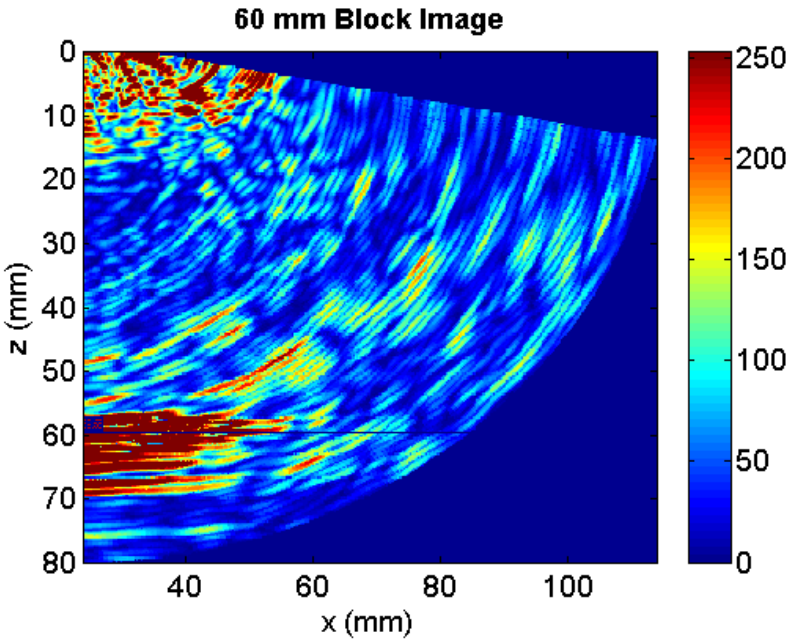

(a)

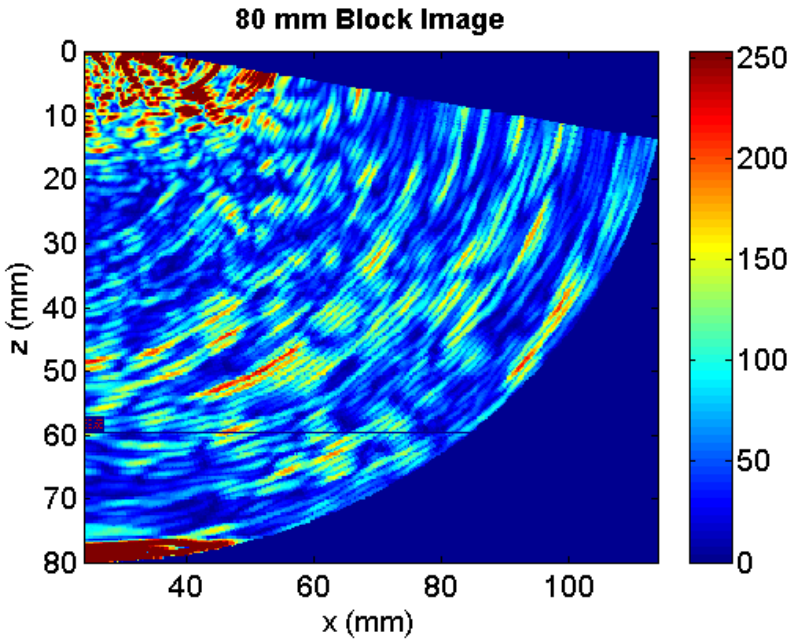

(b)

Figure 6-73 **80 dB gain images of the test blocks, having been read into Matlab. The lines from the cursors are visible as a line at 60 mm depth, but do not significantly corrupt the data, (a) 60 mm block and (b) 80 mm block**

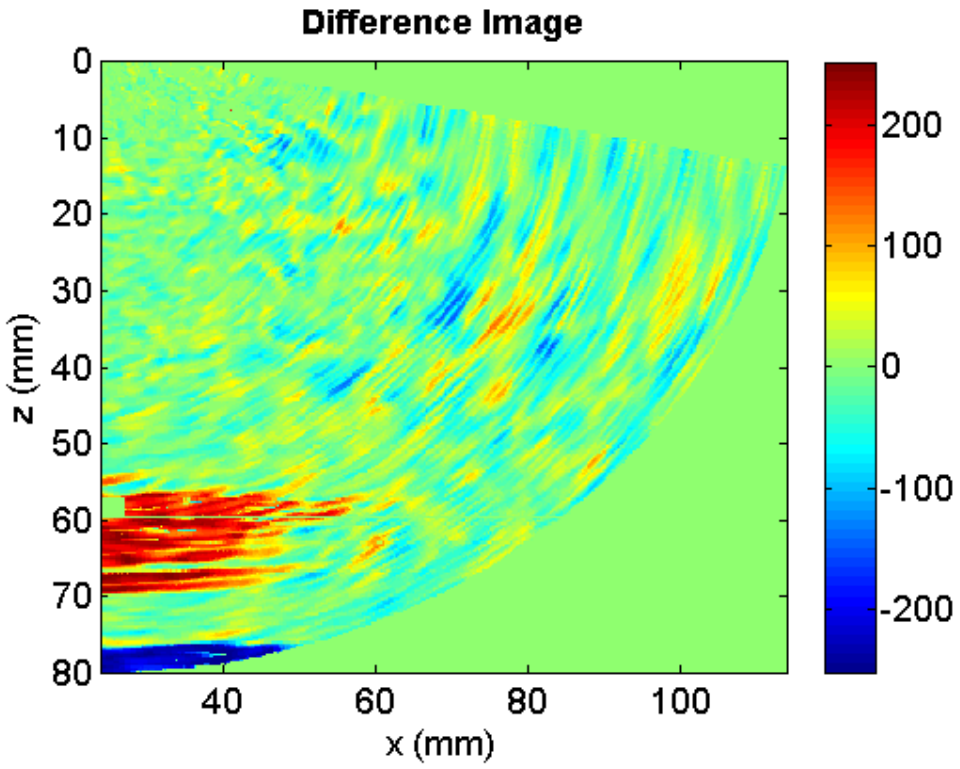

Figure 6-74 **Difference image created by subtracting the 80 mm block data from the 60 mm block data.**

The sidelobe height achieved gives the array a dynamic range of greater than 30 dB, which is in excess of what is required for most NDE inspections. Furthermore, the log spiral array design equations allow for the dynamic range to be increased for applications which require it, at the expense of additional elements, or a smaller range of steering.

6.6 Analysis of array performance

The test results presented in the previous sections of this chapter have shown that log spiral arrays are a practical solution for volumetric NDE imaging. In addition to proving the concept of the log spiral array was sound, the prototype array performed well, demonstrating that Alba has the manufacturing processes to create these devices.

The electrical impedance tests showed that the prototype elements are unimodal, and that the performance of the elements across the array was uniform. This uniformity was further demonstrated by the laser vibrometry results, which also demonstrated good phase uniformity across the array. This, in turn, was backed up by the pulse echo tests, which also measured the bandwidth of the array. While the bandwidth of the array was lower than predicted by modelling, the resulting axial resolution was still higher than the lateral resolution. Focused sector scans showed that this lateral resolution was in line with that predicted by the acoustic field model, and that sub wavelength side drilled and flat bottomed holes could be detected. The scans allowed the position of the holes to be measured accurately. The peak sidelobe height was measured, and was close to the modelled value. Finally volumetric scans were conducted, which showed that a large volume of the test piece could be inspected from a single array position, and demonstrated the azimuthally steering range of the array. Table 6-7 summarises the array performance, comparing the results to modelling where applicable.

Measurement	Experimental	Modelled / Specification
Element low frequency capacitance uniformity	90% within +/- 5% of mean (64.2 pF)	52.5 pF
Centre frequency	1.6 MHz	1.5 MHz
Fractional bandwidth	53%	66%
Lateral beamwidth	9.35 mm (mean)	9.0 mm
Peak sidelobe height	-31.0 dB	-34.0 dB
Practical elevation steering range	0° to 70°	30° to 70°
Practical azimuthal steering range	-60° to 60°	As high as achievable

Table 6-7 Comparison of experimental results with modelled / specified values.

There were a number of factors, some external, which limited the imaging performance of the array:

- Sound reflected back from the edges of the Rexolite wedge created artefacts in the image. Using finite element software to model these reflections would allow the wedge to be redesigned, altering the geometry and adding attenuative materials to reduce the severity of these reflections.

- The array controller lacked a smoothing function which covered the frequency range of interest, and was unable to recreate the envelope of the acoustic signal. This made both the A-scans and the images multi peaked, which made defect location and sizing more difficult. It should be straight forward for Zetec to modify their software / hardware to add a smoothing function which operated at 1.5 MHz.

- The array controller and PC became unstable when scans containing over 800 focal laws were loaded. This may have been due to the performance of the PC running the controller software, and upgrading the PC may alleviate this.

- While the array was capable of detecting defects at skew angle of up to 60°, the drop in signal strength at high skew angle made defects difficult to detect, and images difficult to interpret due to their large dynamic range. Programming the array controller to increase its gain at high scan angle would be a possible solution. Alternatively, the images could be plotted on a logarithmic amplitude scale.

Overall, the prototype array was successful in demonstrating the theoretical concepts set out in the main body of the work.

The next section discusses future work which is planned to further develop the log spiral array concept.

Chapter 7

Future Work

The work which has been presented in this thesis shows that logarithmic spiral arrays hold great promise for reducing the number of elements required to create a practical 2D ultrasonic array. There is a great deal of future work which could be carried out, both to improve the performance of the arrays, and to improve the array design process. The most important of these areas are discussed in this section as a guide for future research in the field.

7.1 Increasing array density

One limitation of log spiral arrays that has been demonstrated is the limited array density that can be achieved, while avoiding overlap of elements. Higher density arrays would allow the designs to cover a wider range of array performance, affording the designer more flexibility. Chapter 5 outlined a number of approaches which can be used to avoid overlap, including reducing the size of the array elements, but this is done at the expense of reduced array sensitivity. A maximum element density of approximately 70% was demonstrated, while maintaining $\lambda/2$ sized elements. However, in applications where more system channels are available, it may be desirable to increase the number of elements above this density level, thereby reducing peak sidelobe level.

Two methods of achieving this increase in density are proposed for future work:

- Adding a group of elements to the empty space at the centre of the array.

- Adding additional spiral arms in the gaps between existing spiral arms, toward the outside of the array.

Both of these methods exploit free space in the array structure, and attempt to fill these areas to further reduce sidelobe levels. The areas where elements could be added are illustrated in Figure 7-1.

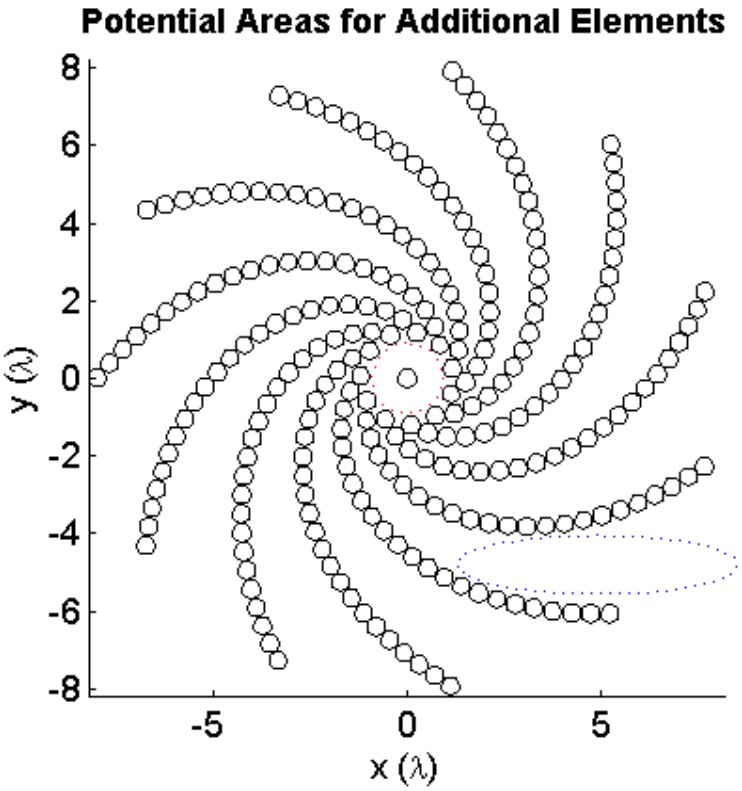

Figure 7-1 **Areas where additional elements could be placed to increase array density include the centre of the array (red), and the areas between the spiral arms (blue).**

The idea of adding elements to the centre of the array has already suggested in Chapter 5, where a single element was placed at the centre of the array designs under analysis. A wide number of strategies could be employed for sampling this area, including a dense grid pattern, a miniature spiral, or even a random distribution. However, while adding elements to this area would reduce sidelobe heights, the element distribution of the array would become highly biased toward the centre. This would mean a larger aperture would be required to achieve a specified beamwidth, which would be undesirable in applications where aperture is limited.

Perhaps a more attractive method of increasing array density would be to add additional spiral arms, which run between the existing arms, and have a larger R_{min} to avoid overlap at the centre. This would have the opposite effect to adding elements to the centre, since the element distribution of the array would be shifted outwards. This may have the result in increasing the minimum sidelobe level that could be achieved, but the exact radial placement of the arms would allow the designer to adjust this at will. Designs could then be tailored for application where aperture is limited, but the number of channels available allows for an array with more elements. The angular placing of the additional arms would also be important. Adding arms to an array with an odd number of arms would result in an array with an even number of arms. It was shown in Chapter 5 that sidelobes in even armed arrays overlap, which is undesirable when the design aim is to suppress sidelobes. One solution may be to avoid placing the additional arms directly between existing arms, but instead rotate them by some amount which avoids directly overlapping sidelobes.

There are clearly a number of approaches which could be taken to create denser spiral arrays, and to adjust the element distribution. This would increase the range of array densities for which spiral arrays can be used, allowing the designer to alter performance across a continuous scale from the very sparse to approaching fully dense.

7.2 Spiral arm sampling

In Chapter 5 two methods for sampling log spiral arms were investigated: periodic sampling and logarithmic sampling. It was decided that since λ/2 periodic sampling could be used to avoid grating lobes, or heightened sidelobes in the beam, it would be used for much of the investigation. However, for applications where higher sidelobes are acceptable a more economical sampling method could be used.

Potential sampling methods which could be used are:

- Geometric series: This method could be designed to spread sidelobe energy evenly through the field, in a similar way that the log spiral structure spreads sidelobes.

- Random: The spiral arms could be sampled in a random aperiodic manner, which would also achieve a flat sidelobe floor.

Either of these methods could be used to lower the element density of log spiral arrays even further. It is unclear whether this would be advantageous to creating a less dense spiral design, which was periodically sampled with a λ/2 spacing. This trade off should be assessed to determine whether or not spiral designs which are more sparsely sampled are of use.

By investigating new sampling methods, the performance of log spiral arrays could be further tailored for use in applications which require ultra sparse arrays.

7.3 Finite element analysis of piezocomposite and wedge

This thesis has focussed on optimising the layout of sparse 2D arrays to reduce sidelobe levels. However, the layout of a piezocomposite array also has an impact on the design and performance of the individual composite elements. For example, cross-talk in more densely packed areas near the centre of the array may be higher than near the outside of the array. Furthermore, small elements with λ/2 apertures often have non uniform displacement profiles, which can affect acceptance angle and sensitivity. It is therefore interesting to analyse the impact of composite design on spiral array performance.

The layout of log spiral arrays is expected to offer some benefits when compared to more traditional designs:

- The large average spacing between elements reduces the level of crosstalk between elements.

- The inactive areas of the array surface could be filled with a lossy material to further attenuate acoustic waves travelling between elements.

- The aperiodic nature of the array avoids the excitation of Lamb modes, which can be excited in periodic array layouts, creating high levels of crosstalk, and degrading surface displacement [59,60].

Finite element analysis could be used to create a 3D model of the array structure, including the underlying composite. This would then provide simulated information on electrical impedance, surface displacement, mechanical crosstalk, and element acceptance angle, to name but a few important measurables. The design of the piezo composite structure could then be tailored to take advantage of these favourable characteristics of the log spiral layout.

In addition to this, the experimental results obtained from the prototype array contained reflections from within the Rexolite wedge. The basic design of the wedge meant that at some angles sound was directly reflected back to the array from the edges and corners of the wedge. Using modelling as a guide, the design of the wedge could be altered to reduce the severity of these reflections. The following strategies could be employed:

- Altering the geometry of the wedge so that it does not present a normal surface, edge, or corner to the beam, all of which cause direct reflections. This is difficult to accomplish across the whole design, but could shape the basic concept of the design.

- Add an additional attenuative material to the outside of the wedge, to damp reflections. This material should be a close acoustic impedance match for Rexolite to minimise the reflection coefficient at the material boundary. Alba uses highly attenuative, flexible epoxies which could be loaded with minerals to tune their acoustic impedance to that of Rexolite.

These strategies would reduce the strength of internal wedge reflections, and ultimately improve the quality of the ultrasonic image.

7.4 Development of design aids

In Chapter 5 a design process for log spiral array was presented, to guide those seeking to design sparse arrays. Guidelines for array performance were outlined, indicating that peak sidelobe levels roll off at approximately 16 dB per decade increase in the number of array elements. While these guidelines are useful, a design tool which could not only select the optimum design for a given array specification, but predict its peak sidelobe level would be of great benefit to the designer.

Currently, when designs which produce overlapping array elements are encountered, the designer must adjust a number of array design parameters iteratively, until a non overlapping design is found. Additionally, this is not likely to be the only design solution, but one of many possibilities, and finding the design with the lowest sidelobe level could prove time consuming. To avoid this, a design tool with an analytical expression for minimum element separation in a log spiral design could be developed. This could immediately rule out any designs with overlapping elements, saving the designer a great deal of time. If this could be combined with an analytical expression for peak sidelobe height in log spiral arrays, the design tool could immediately select the highest performance design. In addition to this, the designer could specify other criteria, to aid the manufacture of the design, such as minimum element separation, or minimum arm pitch. This could lead to designs which are not only optimised for acoustic performance, but also for manufacture.

In addition to these new developments, the documentation and robustness of the current design rules and modelling tools needs to be improved. This will not only improve the effectiveness of the tools, but also reduce the risk inherent in Alba's growing reliance on new technology. The following steps will be taken to ensure that the tools are fully developed and integrated into the company:

- Complete the documentation of the field modelling software, by producing a user manual, and a fully documented and controlled copy of the code.

- Complete further testing of the log spiral array design rules, to ensure that they reliably produce designs which meet the intended specification.

- Produce a user manual to allow Alba's design staff to be trained to design and model log spiral arrays. This will sumarise the trade-offs when compared to dense arrays, the design process, and the manufacturing process.

- Include an entry in the design training matrix to track the members of staff who have been trained in using both the field modelling software, and the log spiral design process.

It is recognised that even with the design guidelines presented in this thesis, the design of log spiral arrays is still more complex than that of 2D matrix arrays. As Therefore, the development of tools would be a useful avenue for future research.

7.5 Analysis of sidelobe positions in log spiral arrays

In Chapter 5 it was demonstrated that log spiral arrays produce arrays with superior performance to that of Archimedes spiral arrays. This is due to the aperiodic spacing between successive turns of the log spiral arm. It was also demonstrated that the sidelobe peaks produced by log spiral arrays follow the pattern of the arms in the array. A deeper understanding of the mathematical properties that produce this effect would be useful, not only for log spiral array design, but could potentially lead to even more efficient array designs.

One potential approach would be to examine the Fourier Transform of a log spiral arm analytically, rather than by using the numerical approach pursued in the work. The following objectives could be pursued:

- Develop an analytical solution for the peak sidelobe levels and positions created by a log spiral array.

- Investigate the effect of array performance when the base of the spiral design is varied to values other than *e*.

- Determine whether other functions exist which also distribute sidelobes evenly, and if they can do so more efficiently than the log spiral.

- Investigate alternative designs which trade off ISLR against peak sidelobe height, which may be useful for some low contrast imaging applications.

It is clear that further analysis of log spiral array properties would be of use to supplement the findings in the work.

7.6 Development of log spiral arrays in Alba

As stated in Chapter 1 the major impact of the work is to provide Alba with a competitive advantage in the market for 2D NDE arrays, employing 128 – 256 elements. Currently, ultrasonic array contollers of 32 up to 512 channels are used in the industry, however these contollers are not large enough to accommodate periodic grid arrays capable of volumetric steering. Log spiral arrays will allow customers to carry out volumetric inspections, without having to invest in even larger phased array contollers.

Currently, state of the art 2D NDE array range from 1 – 10 MHz, and contain up to 256 elements arranged in either a periodic grid, or segmented annular layout. These units retail from £10k to £30k. The annual UK market for large (128 element plus) ultrasonic phased arrays is estimated to be approximately £600k - £800k, with approximately £200k of this being 2D arrays. This market is expected to grow significantly, with continued emphasis on extending the life of existing plant, and the construction of new nuclear power generation plant in the UK. Since the imaging performance of 2D arrays is commonly limited by the number of array contoller channels available, this is a market where log spiral arrays give Alba a competitive advantage.

Alba has already had enquirys from two RCNDE members about producing prototype log spiral arrays to evaluate their performance, with two additional companies also expressing interest. Through its contacts in the RCNDE and Brittish Instiute for NDT (BINDT), Alba is already in contact with many potential customers, who have expressed an interest in working with a UK based array supplier, who can offer bespoke designs. It is proposed that Alba uses these links to trail its log spiral arrays on UK plant, before looking further afield to the growing markets in Europe and the US.

Accounting for parts, labour, and sub contracted services, the initial log spiral prototype cost £8k to develop. It is estimated that with some value engineering, and

the appropriate tooling this could be reduced to approximately £5k, including company overheads, since a large portion of this cost was labour. In order to offer a range of 2D arrays up to 10 MHz, Alba would have to invest in developing new processes and tooling to create thin, flat matching layers, and new processes for fine wire attachment. This process would take approximately 12 months to complete, and is estimated to cost ~£100k, including labour, parts, sub contract and tooling. Since this work is novel, designed to increase reveue for the company, and would lead to new jobs in Glasgow, the company will look to seek matched funding support for this work from local enterprise agencies. This would reduce the risk, and the cost to the company for the work.

Current lead time for a new device would be 8 weeks from date of purchase. The development work would seek to reduce this to 5 weeks, to be competitive with current market conditions. Over the next 12 months Alba would have capacity for approximately 5 log spiral arrays, but it is likely that only 2 initial orders could be secured.

Over the next 5 years, Alba will seek to expand its intrest in the NDE business in two ways:

- Further develop and increase sales of log spiral 2D arrays. As volumes increase, the manufacturing processes for log spiral arrays will be further developed, reducing not only their cost, but the cost of other high frequency devices.

- Use this reduction in manufacturing costs to move into the lower cost, higher volume market for linear arrays. The market price for 128 element linear arrays is approximately £4k to £6k, and Alba will seek to drop its manufacturing costs to £3k for these devices.

Another critical area is the support for log spiral arrays from array contoller manufacturers. While it is possible to program many array contollers to control arbitrary arrays, it would be desirable to have functionality for contolling log spiral arrays built into the instrument. The most effective way to do this would be for Alba to partner with an array controller manufacturer. The instrument manufacturer would benefit from offering improved inspection capability, and Alba would benefit from a better support for its devices. Alba has already contacted instrument manufacturers about setting up this relationship, and will pursue them further over the next year.

Based on these figures, a projected 5 year cashflow is shown in Table 7-1. This assumes slow but steady growth of 2D array sales over the 5 years, with linear arrays introduced in year 4 once manufacturing costs have fallen sufficiently. It also assumes matched funding for the initial development phase. These figures show the venture breaking even in year 3, with a 5 year profit of £278k, £160k in the final year, and a final year turnover of £690k. This represents a return on the initial investment of £100k (funding paid in arrears) of 278%. The final year would see Alba produce a total of 8 2D arrays and 40 linear arrays. This would require a staff of approximately 5 technicians, and 2 engineerings to sustain, creating a total of 6 new jobs over the period.

While this opportunity offers a clear incentive to the company, a number of risks are apparent:

- Failure to secure local enterprise funding for the development project.
- NDE industry does not choose to adopt log spiral arrays.
- Target manufacturing costs cannot be achieved.

Failure to obtain funding would leave the company exposed to significantly more financial risk than planned, and so the pursuit of the project should be conditional on securing this. Lack of uptake from the NDE industry would likely be apparent in the second year of the project, when orders could dry up after the initial sales. At this point the company would be close to break-even, and could write the venture off as useful development, utilising the manufacturing lessons learned in its high frequency sonar devices. Failure to achieve target manufacturing costs is seen as unlikely, but would hurt profits if it occurred.

Subject to obtaining funding, the risk on the project appears manageable, and Alba plan to pursue it further. As such, prioritised tasks for the business are as follows:

1. Obtain funding support to develop more cost effective manufacturing processes for log spiral arrays.

2. Speak to RCNDE members who have already expressed interest about trialing prototype arrays on plant.

3. Seek a partnership with an instrument manufacturer to improve instrument support for log spiral arrays.

Development of spiral arrays not only represents an opportunity for Alba to move into a new market, but a vehicle for further developing its manufacturing techniques. This will benefit the whole company, and makes the project an attractive venture.

	Income	**Expenditure**
Year 1		
Development project		£100,000
Development funding	£50,000	
2D array sales	£20,000	
2D array costs		£16,000
Year 2		
2D array sales	£50,000	
2D array costs		£24,000
Year 3		
2D array sales	£80,000	
2D array costs		£30,000
Year 4		
2D array sales	£120,000	
2D array manufacture		£40,000
Linear array sales	£50,000	
Linear array costs		£42,000
Year 5		
2D array sales	£120,000	
2D array manufacture		£40,000
Linear array sales	£200,000	
Linear array costs		£120,000
TOTAL	**£690,000**	**£412,000**
PROFIT	**£278,000**	

Table 7-1 Projected 5 year cashflow for Alba's NDE business.

Chapter 8

Concluding Remarks

The original goals of the engineering doctorate project were outlined in Chapter 1:

- Investigate the design of 2D sparse arrays, with the objective of reducing the number of elements required to meet a given acoustic specification.

- Create a design process for such arrays that would allow Alba to rapidly convert a customer specification into a practical array design.

- Develop Alba's acoustic modelling capability to model the performance of these arrays.

- Develop Alba's manufacturing capability for high frequency 2D NDE arrays, and build a prototype to evaluate its performance.

A thorough investigation of sparse 2D array design techniques was carried out, and logarithmic spiral based designs were selected as the most promising. These designs produce a flat sidelobe floor, which minimises the peak sidelobe height for a specified number of elements. They allow the density of the array to be varied between 25 and 70% of that of a $\lambda/2$ spaced grid array. The performance of these designs was simulated in both the near and far fields, under both CW and pulsed drive conditions, and peak sidelobe height was found to be lower than statistically random arrays, in some cases by as much as 4.6 dB. This performance was achieved at the sacrifice of ISLR, which was poorer than the statistically random arrays. In addition to its superb peak sidelobe performance, the logarithmic spiral design simplifies the process of electrically connecting to the array elements, resulting in a more cost effective manufacturing process.

A design process was created for logarithmic spiral arrays, to allow an array specification to be efficiently translated into an array design. The process was tested through the design of a prototype array, and the simulated performance of the resulting design was successfully shown to match the original specification.

A series of new acoustic beam models were written to allow the design of novel arrays. Many of these models are now used routinely in the design of Alba's sonar devices. Simulated results from these models have been shown to match experimental results over a wide variety of array configurations, including linear arrays, curved arrays, and 2D arrays. This modelling capability has allowed the company to take on more complex designs, with one example being arrays with apodised elements. In addition, the models have allowed the company to model the near field performance of its prototype NDE phased arrays.

A wide range of new manufacturing techniques were investigated to allow the company to produce large 2D arrays, with abstract element patterns. These were put into effect, and used to produce a prototype 2D log spiral array. This device was thoroughly tested, and the results showed that the array was capable of performing volumetric steering in an NDE inspection with only 127 elements, 23.5% of a dense matrix array. The array was capable of detecting sub wavelength side drilled, and flat bottomed holes, at azimuthal steering angles of up to 60°. A peak sidelobe level of -31 dB was achieved.

The following conclusions can be drawn from the work:

- Log spiral layouts allow a dramatic reduction in the number of array elements required in an ultrasonic volumetric imaging system, over traditional designs.

- The pulse-echo sidelobe levels afforded by these designs are low enough to satisfy the dynamic range required for NDE imaging.

- The one way sidelobe heights are low enough to be used in forward look imaging systems in the sonar industry.

- The designs are not well suited for mainstream biomedical imaging, due to their lack of contrast. However, there may be niche biomedical markets with

lower dynamic range requirements in which they would be useful, for example the imaging of bone structures.

The major advantages of logarithmic spiral arrays are as follows:

- They allow fully volumetric inspections to be carried out with existing phased array contollers, by reducing the number of active channels required. This will offer a more complete coverage of test pieces than is currently possible with periodic grid arrays.

- Their peak sidelobe levels are lower than that of equivalent random array layouts, resulting in higher quality images.

- They allow the designer to tade off the number of active elements, and therefore array controller channels, against peak sidelobe height. This represents a significant cost reduction, since cheaper array contollers can be used.

- The deterministic layout of log spiral arrays allows a series of simple design rules to be used to design arrays, avoiding lengthy mathematical optimisation based design required for random arrays.

- The structured layout of log spiral arrays allows manufacturing processes to be simplified and standardised when compared to random arrays.

The disadvantages of log spiral arrays are:

- Higher ISLR when compared to equivalent random arrays, resulting in poorer imaging performance in low contrast media.

- A marginally larger aperture than required for periodic grid, or random arrays, due to a narrower element distribution.

Through its participation in the engineering doctorate programme, Alba has developed the capability to design and manufacture large novel 2D arrays for the NDE industry. These designs are unique within the industry, and offer the company a significant advantage over its competitors. A prototype logarithmic spiral array was demonstrated at an industrial seminar, and generated interest from attendees in the conventional power, nuclear power, and oil and gas industries. Furthermore, the initial cashflow projections indicate that the devices could form a profitable addition to Alba's business within 5 years. The company is in the process of preparing a more detailed business plan to exploit these opportunities, which will be put into action in 2011.

Publications Arising from this Work

The following publications were contributed to by the author as part of this work:

[1] S. N. Ramadas, A. Tweedie, R. L. O' Leary, and G. Hayward, "A rule based design optimisation tool for ultrasonic transducers and arrays," Proceedings of the International Congress on Ultrasonics, Vienna, Paper ID 1091, 2007.

[2] A. Tweedie, R. L. O'Leary, G Harvey, A. Gachagan, C. Holmes, P. D Wilcox and B. W. Drinkwater, "Total Focussing Method for Volumetric Imaging in Immersion Non Destructive Evaluation," Proceedings of the IEEE Ultrasonics Symposium, 2007, pp. 1017-1020.

[3] A. Tweedie, V. Murray and G. Hayward, "Aperiodic and Deterministic 2D Phased Array Structures for Ultrasonic Imaging," Proceedings of the IEEE Ultrasonics Symposium, 2009, pp. 406-409.

[4] G. Harvey, A. Tweedie, C. Carpentier and P. Reynolds, "Finite Element Analysis of Ultrasonic Phased Array Inspections on Anisotropic Welds," Proceedings of the QNDE Annual conference, 2010.

[5] A. Tweedie, G. Hayward and V. Murray, "Aperiodic and Deterministic 2D Ultrasonic Phased Array Structures for Ultrasonic Imaging," U.S. Navy Workshop on Acoustic Transduction, Penn State University, 2009, (oral presentation and poster session).

[6] A Tweedie, G Harvey, R. L. O'Leary, A Gachagan, C Holmes, P. D. Wilcox and B. W. Drinkwater, "Application of Total Focussing Method in Immersion Ultrasound NDE," Brittish Institue of Non Destructive Testing Annual Conference, Glasgow, 2007, (oral presentation).

Bibliography

[1] T. S. Sumanaweera, J. Swartz and D. Napolitano, "A spiral 2D phased array for 3D imaging," Proceedings of the IEEE Ultrasonics Symposium, 1999, pp. 1271-1274.

[2] P. E. Dewdney, P. J. Hall, R. T. Schilizzi, T. Joseph and L. W. Lazio, " The square kilometre array," Proceedings of the IEEE, Volume 97, No. 8, 2009, pp. 1482-1496.

[3] P. J. Napier, A. R. Thompson and R. D. Ekers, "The very large array: design and performance of a modern synthesis radio telescope," Proceedings of the IEEE, Volume 71, No. 11, 1983, pp. 1295-1320.

[4] J. Krautkramer, "Ultrasonic Testing of Materials, 4th Revision, 1990, Springer.

[5] O. T Von Ramm and S. W. Smith, "Beam Steering with Linear Arrays," IEEE Transactions on Biomedical Engineering, Volume BME-30, 1983, pp. 438 – 452.

[6] B. D. Steinberg, "Principles of Aperture and Array System Design," New York: Wiley, 1976, p. 54.

[7] D. H. Turnbull and F. S. Foster, "Beam Steering with Pulsed Two-Dimensional Transducer Arrays," IEEE Transactions on Ultrasonics Ferroelectrics and Frequency Control, Vol. 38, No. 4, 1991, pp. 320-333.

[8] J. L. Schwartz and B. D. Steinberg, "Ultrasparse, Ultrawideband Arrays," IEEE Transactions on Ultrasonics Ferroelectrics and Frequency Control, Vol. 45, No. 2, 1998, pp. 376-393.

[9] P. J. 't Hoen, “Aperture apodization to reduce the off-axis intensity of the pulsed-mode directivity function of linear arrays,” Ultrasonics, Vol. 20, issue 5, September 1982, Pages 231-236.

[10] G. Hayward, R. Hamilton, B. Kanani and D. Reilly, "A Thin Film Technique for Spatial Apodisation of Disc-Shaped Piezoceramic Transducers", Journal of the Acoustical Society of America, Vol, 4, Pt.1, 1991, pp1808-1815.

[11] J. N. Wright, “Resolution issues in medical ultrasound,” Proceedings of the IEEE Ultrasonics Symposium, 1985, pp. 793-799.

[12] S. W. Smith, G. E. Trahey and O.T. von Ramm, “Two-Dimensional Arrays For Medical Ultrasound,” Proceedings of the IEEE Ultrasonics Symposium, 1991, Vol. 1, pp. 625-628.

[13] C. W. Sherwin, J. P. Ruina and R. D. Rawcliffe, “Some Early Developments in Synthetic Aperture Radar Systems,” IRE Transactions on Military Electronics, 1962, pp. 111-115.

[14] G. R. Lockwood and F. S. Foster, “Design of Sparse Array Imaging Systems,” IEEE Ultrasonics Symposium, 1995, pp. 1237-1243.

[15] C. Holmes, B. W. Drinkwater and P. D. Wilcox, “Post-processing of the full matrix capture of ultrasonic transmit-receive array data for non-destructive evaluation,” Nondestructive Testing and Evaluation International, vol. 38, no. 8, 2005, pp. 701–711.

[16] A. Tweedie, R. L. O’Leary, G Harvey, A. Gachagan, C. Holmes, P. D Wilcox and B. W. Drinkwater, “Total Focussing Method for Volumetric Imaging in Immersion Non Destructive Evaluation,” Proceedings of the IEEE Ultrasonics Symposium, 2007, pp. 1017-1020.

[17] A. Austeng and S. Holm, “Sparse 2-D arrays for 3-D phased array imaging – design methods,” IEEE Transactions on Ultrasonics Ferroelectrics and Frequency Control, Vol. 49, No. 8, 2002, pp. 1087-1093.

[18] A. Austeng and S. Holm, “Sparse 2-D arrays for 3-D phased array imaging – experimental validation,” IEEE Transactions on Ultrasonics Ferroelectrics and Frequency Control, Vol. 49, No. 8, 2002, pp. 1073-1086.

[19] O. Martinez, G. Godoy, M. A. G. Izquierdo and L. G. Ullate, “ Application of vernier thinning techniques to segmented annular arrays,” Ultrasonics, 42, 2004, pp. 977-982.

[20] G. R. Lockwood and F. S. Foster, “Optimising sparse two-dimensional transducer arrays using an effective aperture approach,” Proceedings of the IEEE Ultrasonics Symposium, 1994, pp. 1497-1501.

[21] S. I. Nikolov and J. A. Jensen, “Application of different spatial sampling patterns for sparse array transducer design,” Ultrasonics, 37, 2000, pp. 667-671.

[22] B. D Steinberg, “The peak sidelobe of the phased array having randomly located elements,” IEEE Transactions on Antennas and Propagation, Vol AP-20, No. 2, 1972.

[23] W. J. Hendricks, “The totally random versus the bin approach for random arrays,” IEEE Transactions on Antennas and Propagation, Vol 39, No. 12, 1991.

[24] J. D. Dyson, “The equiangular spiral antenna,” IRE Transactions on Antennas and Propagation, Volume 7, Issue 2, 1959, pp. 181-187.

[25] R. Bawer and J. Wolfe, “The spiral antenna,” IRE International Convention Record, Volume 8, Part 1, 1960, pp. 84-95.

[26] N. G. de Bruijn, “Algebraic theory of Penrose’s non-periodic tilings of the plane,” Indagationes Mathematicae, 43, 1981 pp. 39–66.

[27] S. M. Kirkup, “Computation of the acoustic field surrounding a baffled panel by the Rayleigh integral method,” Appl. Math. Modelling, 1994, Vol 18, pp. 403-407.

[28] S. I. Warshaw, “Time-domain acoustic pressure fields from axisymetric impulse sources by Rayleigh’s Integral,” Proceedings of Acoustics Paris, pp. 5953 – 5957, 2008.

[29] J. W. Wind, Y H. Wijnant and A. de Boer, “Fast evaluation of the Rayleigh integral and applications to inverse acoustics,” International Congress on Sound and Vibration, 2006.

[30] S. Kirup, “Fortran Codes For Computing The Acoustic Field Surrounding A Vibrating Plate By The Rayleigh Integral Method,” Proceedings of the 10th WSEAS international conference on Mathematical methods, computational techniques and intelligent systems, 2008, pp. 364-369.

[31] J. A. Jensen, “A New Approach to Calculating Spatial Impulse Responses,” IEEE Ultrasonics Symposium, 1997, pp. 1755-1759.

[32] J.W. Goodman, “Introduction to Fourier Optics,” McGraw-Hill, New York, 1968.

[33] M. E. Schafer, “Transducer Surface Velocity Reconstructions Using The Angular Spectrum Method,” IEEE Ultrasonics Symposium, 1988, pp. 669-672.

[34] G. L. Wojcik, D. K. Vaughan, N. Abboud, J. Mould Jr, “Electromechanical Modeling Using Explicit Time-Domain Finite Elements,” IEEE Ultrasonics Symposium, 1993.

[35] PZFlex, Weidlinger Associates, 299 E El Camino Real, Mountain View, CA.

[36] M. N. Jackson, G. Hayward, “A New Three-Port Model of the Thickness Mode Piezoelectric Transducer,” Proceedings of the IEEE Ultrasonics Symposium, 1983, pp. 878-882.

[37] R.S. Longhurs, “Geometrical and Physical Optics,” 2nd Edition, 1968, Longmans.

[38] C. Holmes, B. W. Drinkwater and P. D. Wilcox, “Post-processing of the full matrix capture of ultrasonic transmit-receive array data for non-destructive evaluation,” Nondestructive Testing and Evaluation International, Vol. 38, no. 8, pp. 701–711, 2005.

[39] L. E. Kinsler, A. R. Frey, A. B. Coppens and J. V. Sanders, “Fundamentals of Acoustics,” 4th Edition, 2000, John Wiley & Sons.

[40] T. L. Heath, “A History of Greek Mathematics,” p. 64, Boston: Adamant Media Corporation, 1921.

[41] M. Iye, S. Okamura, M. Hamabe and M. Watanabe, “Spectral analysis of the asymmetric spiral pattern of NGC 4254,” The Astronomical Journal, 256, 1982, 103-111.

[42] V. A. Tucker, “Gliding Flight: Drag And Torque of a Hawk and a Falcon with Straight and Turned Heads, and a Lower Value for the Parasite Drag Coefficient,” The Journal of Experimental Biology, 203, 2000, 3733-3744.

[43] J. J. Rehmeyer, “Mathematical lives of plants,” Science News, 172 no. 3, 2007.

[44] B. B. Mandelbrot, “Fractal aspects of the iteration of $z \rightarrow \lambda z(1- z)$ for complex λ and z,” Annals of the New York Academy of Sciences, Vol. 357, NonLinear Dynamics, pp. 249 – 259, 1980.

[45] H. Nyquist, “Certain topics in telegraph transmission theory,” Proceedings of the IEEE, Vol. 90, Iss. 2, p. 280, 2002 (reprint).

[46] C. Page, “Applications of the Fourier Integral in Physical Science,” Vol. 2, Iss. 3, pp. 231 – 237, 1955.

[47] J. Radon, “On the Determination of Functions from Their Integral Values along Certain Manifolds,” IEEE Transactions on Medical Imaging, Vol. 5, Iss. 4, pp. 170 – 176, 1986 (translated reprint).

[48] D. T. Blackstock, “Fundamentals of Physical Acoustics,” 2000, John. Wiley & Sons Ltd, pp 451.

[49] DISSIMILAR project website, http://www.dissimilarweld.co.uk.

[50] C. Nageswaran, C. Carpentier and Y. Y. Tse, “Improving phased array ultrasonic testing using models to overcome austenitic weld distortion,” Proc 7th Int. Conf. on NDE in Relation to Structural Integrity for Nuclear and Pressurised Components, 2009.

[51] C. Nageswaran, C. Carpentier and Y. Y. Tse, “Microstructural quantification, modelling and array ultrasonics to improve the inspection of austenitic welds,” Insight, Vol. 51 No. 12, 2009.

[52] W. Smith, "The Application Of 1-3 Piezocomposites In Acoustic Transducers," Proceedings of the IEEE 7th International Symposium on Ferroelectrics, 1990, pp. 145-152.

[53] W. P. Mason, Electromechanical Transducers and Wave Filters, Princeton, NJ, Van Nostrand, 1948.

[54] D. A. Leedom, R. Krimholtz and G. L. Matthei, "Equivalent circuits for transducers having arbitrary even-or-odd symmetry piezoelectric excitation," IEEE Trans. Sonics Ultruron, vol. SU-18, pp. 128-141,1971.

[55] G. Hayward, C. J. Macleod and T. S. Durrani, "A systems model of the thickness-mode piezoelectric transducer," J. Acoust. Soc. Amer., Vol. 76, No. 2, pp. 369-382, 1984.

[56] G. Hayward and M. Jackson, "A Lattice Model of the Thickness-Mode Piezoelectric Transducer," IEEE Transactions on Ultrasonics Ferroelectrics and Frequency Control, Vol. 33 Iss. 1, 1986, pp. 41-50.

[57] W. A. Smith and B. A. Auld, "Modeling 1-3 Composite Piezoelectrics: Thickness-Mode Oscillations" IEEE Transactions on Ultrasonics Ferroelectrics and Frequency Control, Vol. 38 Iss. 1, 1991, pp. 41-47.

[58] J. A. Hossack and G. Hayward, "Finite-Element Analysis of 1-3 Composite Transducers," IEEE Transactions on Ultrasonics Ferroelectrics and Frequency Control, Vol. 38 No. 6, 1991, pp. 618-629.

[59] G. Hayward and J. Hyslop, "Determination of Lamb Wave Dispersion Data in Lossy Anisotropic Plates Using Time Domain Finite Element Analysis. Part I: Theory and Experimental Verification," IEEE Transactions on

Ultrasonics Ferroelectrics and Frequency Control, Vol. 53 No. 2, 2006, pp. 443-448.

[60] G. Hayward and J. Hyslop, "Determination of Lamb Wave Dispersion Data in Lossy Anisotropic Plates Using Time Domain Finite Element Analysis. Part II: Application to 2-2 and 1-3 Piezoelectric Composite Transducer Arrays," IEEE Transactions on Ultrasonics Ferroelectrics and Frequency Control, Vol. 53 No. 2, 2006, pp. 449-455.

[61] R. L. O'Leary and G. Hayward, "Investigation Into the Effects of Modification of the Passive Phase for Improved Manufacture of 1-3 Connectivity Piezocomposite Transducers," IEEE Transactions on Ultrasonics Ferroelectrics and Frequency Control, Vol. 46 No. 3, 1999, pp. 511-516.

[62] R.L. O'Leary, A.C.S. Parr, G. Hayward, A. Trogé and R.A. Pethrick, "Experimental Assessment of Periodic Piezoelectric Composite Arrays Incorporating an Anisotropic Passive Phase," Proceedings of the IEEE Ultrasonic Symposium, 2006, pp. 1907-1910.

[63] D. Hall, G. Hayward and Y. Gorfu, "Theoretical and Experimental Evaluation of a Two-Dimensional Composite Matrix Array," IEEE Transactions on Ultrasonics Ferroelectrics and Frequency Control, Vol. 40 No. 6, 1993, pp. 704-709.

[64] A. Gachagan, G. Hayward and R. Banks, "A Flexible Piezoelectric Transducer Design for Efficient Generation and Reception of Ultrasonic Lamb Waves," IEEE Transactions on Ultrasonics Ferroelectrics and Frequency Control, Vol. 52 No. 7, 2005, pp. 1175-1182.

[65] G. Harvey, A Gachagan, J. Mackersie, T. McCunnie and R. Banks, "Flexible Ultrasonic Transducers Incorporating Piezoelectric Fibres," IEEE

Transactions on Ultrasonics Ferroelectrics and Frequency Control, Vol. 56 No. 9, 2009, pp. 1999-2009.

[66] N. Abboud, G. Wojcik, D. Vaughan, J. Mould, D. Powell and L. Nikodym, "Finite Element Modeling for Ultrasonic Transducers," Proc. SPIE Int. Symp. Medical Imaging, 1998, pp. 19-42.

[67] C. S. Desilets, J. D. Fraser and G. S. Kino, "The Design of Efficient Broad-Band Piezoelectric Transducers," IEEE Transactions on Sonics and Ultrasonics, Vol. 25 , Iss: 3, 1978, pp. 115-125.